SOME ASPECTS OF

THE MICROSTRUCTURE AND FRACTURE TOUGHNESS

OF THE WELD HEAT AFFECTED ZONE OF A

MARTENSITIC PRECIPITATION HARDENED STAINLESS STEEL

by

J.M.Wright,   B.Sc.,   M.Sc.

A thesis submitted for the degree of Doctor of
Philosophy of the University of Aston in Birmingham.

June, 1978.

SOME ASPECTS OF THE MICROSTRUCTURE AND FRACTURE TOUGHNESS OF THE WELD HEAT AFFECTED ZONE OF A MARTENSITIC PRECIPITATION HARDENED STAINLESS STEEL

JOHN MALCOLM WRIGHT

Ph.D   1978

SUMMARY

The fracture toughness and microstructure of the weld heat-affected zone of a high strength stainless steel, FV520B, have been investigated. Work has concentrated on the conditions prevailing in single pass, full penetration butt welds. These conditions have been reproduced by a simulation technique based on experimental techniques and heat flow theory. This approach has been shown to provide acceptable microstructure and property correlations in this material.

Strength increases were due to a number of precipitates, Nb(C,N) and -copper being significant among them. Unwelded airmelted plate showed COD fracture toughness values of about 0.050mm, vacuum remelting increasing this figure to about 0.070mm; fracture toughness tended to increase with rising ageing temperature.

Two regions of softness in the weld HAZ were examined. The first, occurring around $785^{\circ}C$ was attributable to austenite; the second, at around $1250^{\circ}C$ was due to structure coarsening and delta ferrite formation. In neither case was the fracture toughness radically altered.

Pre- and post-weld heat treatments had little effect compared to plate type and orientation. Fracture toughness of transverse airmelted plate was consistently low; vacuum remelting was of great benefit.

An examination of the various fracture toughness parameters postulated for high toughness materials has also been made. These show a reasonable amount of correlation for the specimen geometry considered. Optical methods of test measurement have not been as successful as mechanical methods in this respect.

KEY-WORDS	MICROSTRUCTURE
	FRACTURE TOUGHNESS
	HEAT-AFFECTED ZONE

CONTENTS

1   INTRODUCTION

Stainless maraging steels are a logical development of the iron-nickel maraging steels developed in the 1950's to allow their use in hostile environments. The original stainless precipitation hardening steels contained up to 0.2% carbon and as such were liable to problems such as weld decay and low toughness. Maraging steels, deriving their name from the metallurgical class 'martensitic age-hardening', heralded a new type of material showing exceptional toughness and strength whilst suffering from no adverse precipitation effects. This was due to the extremely low carbon martensite matrix, the dimensional stability of which during ageing further increases its attractiveness. Due to the extremely poor corrosion resistance of these steels attention was turned to developing a stainless version on the same basis, i.e. very low carbon martensite. Several such steels have been developed in the U.S.A., being generally classified as 15/7 PH steels, but only one equivalent British steel has made its appearance, this being the FV520 series made by Firth-Vickers Ltd. Two types of steel are produced, FV520 B being a martensitic steel suitable for bar and forgings, while FV520 S is a controlled transformation steel with extra ductility for forming being supplied in sheet form. Again very high strengths and toughness can be obtained, enabling thinner sections to be used than hitherto with consequent weight savings. This led to many applications in transport engineering, especially the aerospace industry, being originally specified for the now-abandoned TSR-2 project.

The welding of FV520 B not surprisingly presents some problems in fabrication since the processes adopted invariably involve appreciable heating of the whole weld zone with inevitable loss in weld properties. However, as with other heat treatable alloys, acceptable weld properties have been obtained by appropriate choice of as-welded condition and post-weld heat treatment. Thus welding is either carried out in the annealed

(solution treated) or overaged 550°C condition. A subsequent low temperature heat treatment then suffices to raise the general level of properties of the weld and its heat affected zone (HAZ) to those of the parent material. Stress relief is unnecessary as this is achieved during the ageing treatment; neither is preheat to avoid weld cracking required unless very heavy sections are involved. Any tendency to retain austenite is minimised by composition control and the low carbon content means that no peak hardening is experienced in the HAZ. The low carbon content also means that any tendency to precipitate coarse chromium carbides is removed and hence 'weld decay' is not a problem.

The HAZ and weld metal are subject to a wide variety of temperatures and heating and cooling rates with associated strain due to thermal expansion and contraction. Inevitably this results in material with a very wide range of structures and properties being concentrated into the narrow weld zones. It is essential that this situation does not lead to failure after welding, especially in applications where human life is at risk, such as aircraft. In order to ensure that this will not be the case detailed study of welds and heat affected zones is clearly essential. Only when this information is available can these materials be used in practical situations with complete confidence.

The fact that FV520 has not found wider use in fabrications may be in some part due to reluctance to use a material with largely unknown welding properties. Minimal work has been conducted on this aspect to date, and such as has been carried out has been directed towards resistance to hydrogen induced cracking and high temperature cracking in FV520 B. As one of the main attractions of this steel is its high toughness it is anticipated that its major applications will be in fields where this is of paramount importance. The British Aircraft Corporation, showing an interest in this material, tried to attach fracture toughness values to 75mm bars of

FV520 B heat-treated to different strength levels, but found that even this thickness of bar was insufficient to obtain a valid result for overaged conditions. Thick sections are not necessarily representative of the sections to be used in service and hence a different approach is required to obtain fracture toughness values in thin sections. The present investigation set out to examine the microstructure and its effect on fracture toughness in parent material and heat affected zones of FV520 B to eliminate the complete lack of data in this area. The high toughness values anticipated meant that the research would be moving into a testing field of expanding interest and variation of opinion. To obtain reproducible, but at the same time representative, results a simulative approach to heat affected zones was adopted. This enabled a sufficiently large consistent sample of each type of HAZ microstructure to be tested and the influence of the structure on the result established.

The wide range of welding processes, and resulting thermal cycles, employed in welding these and similar steels meant that some narrowing of the field had to take place to bring testing within practical limits. By firstly carrying out a MIG weld it was intended to study the thermal cycles obtained in the real situation, employ these for the simulation, and as a check on the validity of the simulation approach, to check the correlation between real and simulated HAZ microstructures. Further expansion of the simulated thermal cycles by heat flow relationships then allowed testing representative of other welding processes. In each case the fracture toughness value obtained was compared to that of parent material to ascertain whether any detrimental effects were evident.

2. LITERATURE REVIEW

In this review an examination is made of the background topics which are relevant to FV520 B and its weldability. Thus an outline of the general area of precipitation hardening is given together with its application to stainless steel and in particular to FV520 B. A survey is made of the effects of welding on this type of alloy, largely on the basis of published work on maraging and other steels since little has been reported on FV520 B itself. Since a major research tool in the investigation involves weld thermal simulation this technique is also examined and its correlation with real weld heat affected zones is explored. Finally the field of fracture toughness testing is reviewed. Owing to the known high fracture toughness value of FV520 B most emphasis is placed on the parameters most relevant to general yield fracture mechanics, i.e. COD and J contour values.

2.1. PRECIPITATION HARDENING

2.1.1. Introduction

Precipitation hardening, or age-hardening as it is alternatively known, finds great practical use as a relatively simple method of increasing the strength and hardness of both ferrous and non-ferrous metals. To find suitability as a precipitation hardening system there should be decreasing solid solubility of one phase within another as the temperature drops, (FIG.1). As the alloy of composition X is cooled from $700^{\circ}C$ β will precipitate out of the solid solution of α. If the rate of cooling is fast enough the β precipitate will not have time to separate out, resulting in an unstable supersaturated solid solution. Precipitation will lower the free energy of this solution and so may be expected to occur spontaneously under suitable conditions of temperature. By careful control of heat treat-

ment times and temperatures the nature of the precipitate derived can be finely adjusted to give a wide range of mechanical properties. Hence the normal procedure of events for precipitation hardening alloys is to heat to a high enough temperature to dissolve all the precipitates (solution treatment), rapid cool to room temperature, then ageing at an intermediate temperature.

Current precipitation hardening theory is based on the principles of Guinier and Prestons original work [1]. Initial hardening, and indeed a primary hardening peak, is usually obtained without any evidence of a change in microstructure when viewed in a light microscope. Guinier and Preston used X-ray diffraction techniques to detect sub-microscopic changes, and in modern times electron microscopes are used to the same effect. The hardening is a nucleation and growth process and hence the number of suitable nucleation sites is important.

2.1.2. Nucleation

Nucleii form most easily at lattice defects e.g. along dislocations, at impurity particles, grain boundaries and on slip planes such as provided by the austenite-martensite shear transformation [2]. Smallman [3] states that in very low carbon alloy steels (<0.05%C) dislocations are the preferred sites. Spontaneous nucleation due to concentration fluctuations is difficult (due to surface energy considerations) where no lattice defects exist. Precipitation and rapid growth at grain boundaries can deplete the matrix of solute before nucleation has occurred within the grains. This results in a band of unhardened material either side of the grain boundary, or worse still no precipitation at all within the grains, fine grained metals being more likely to exhibit this. The precipitates may weaken the grain boundaries but can be beneficial in pegging boundaries together to prevent high temperature creep.

2.1.3. Diffusion

Once nucleation has taken place diffusion of atoms to the nucleus takes place, although further nucleation will continue to occur. The rate of atomic diffusion is greatly accelerated when many vacancies are present as these provide suitable paths for migration. For this reason many precipitation hardening alloys are quenched after the solution treatment to trap in as many vacancies as possible, and at the same time retain a fine solute dispersion. The initial precipitate growth is rapid but gradually slows, this being consistent with the elimination of vacancies; thus processes which eliminate vacancies, e.g. cold working, should be avoided between solution treatment and ageing.

2.1.4. Ageing

Selection of ageing temperature plays an important part in the final properties of a precipitation hardening alloy. At low temperatures diffusion is very slow, resulting in long ageing times. At a temperature just below the limit of solid solubility nucleation is slow as the decrease in free energy occurring is low. Suitable ageing temperatures are those which lie between these extremes, i.e. ageing takes place within a reasonable time. Maximum hardening is obtained at the lower end of the temperature range, the temperatures at which the precipitate is fine. At the higher end of the temperature range small precipitates redissolve and diffuse to larger precipitates, resulting in a wider dispersion of particles, which in turn results in a softer structure.

The ageing process is generally believed to take place in two stages, the first stage being the formation of an intermediate precipitate. These precipitates, too fine to be seen by light microscopy, consist of clusters of solute atoms forming zones in the matrix lattice. The hardening effect derived is due to the coherency of the cluster with matrix, causing lattice strains (Fig.2). During the second stage of precipitation a new

precipitate is formed of different composition, frequently changing its morphology to flat or elongated particles on specific crystallographic planes to reduce energy effects. This naturally leads to a loss of coherency between precipitate and matrix, but further precipitation strengthening takes place.

2.1.5. Mechanisms of hardening

The three main types of hardening resulting from precipitation are;

(1) internal strain hardening;

(2) chemical hardening;

(3) dispersion hardening.

2.1.5.1. Internal strain hardening. For deformation to occur dislocations must either pass between or through precipitates which lie in their path. There is a minimum radius to which dislocations can bend and according to the theory of Orowan [4] maximum hardening occurs when precipitates or coherent precipitate strain fields are spaced at approximately twice this radius. If the precipitate is more finely dispersed the dislocation line cannot bow sufficiently to avoid all the associated strain fields and the resultant stresses on the line cancel each other, letting it move fairly easily. When the spacing between particles is large the dislocation line can bow between them quite easily with little hindrance, thus appearing soft (over-aged condition). The effect of dislocations bowing between precipitates can be seen in Fig.3, where successive lines leave loops around the particles, increasing their effective size (due to strain effects), and causing increasing obstruction to following dislocations.

2.1.5.2. Chemical hardening. If a dislocation actually cuts through a precipitate work has to be done in forming a new surface.

precipitate is formed of different composition, frequently changing its morphology to flat or elongated particles on specific crystallographic planes to reduce energy effects. This naturally leads to a loss of coherency between precipitate and matrix, but further precipitation strengthening takes place.

2.1.5. Mechanisms of hardening

The three main types of hardening resulting from precipitation are;

    (1) internal strain hardening;

    (2) chemical hardening;

    (3) dispersion hardening.

2.1.5.1. Internal strain hardening.   For deformation to occur dislocations must either pass between or through precipitates which lie in their path. There is a minimum radius to which dislocations can bend and according to the theory of Orowan [4] maximum hardening occurs when precipitates or coherent precipitate strain fields are spaced at approximately twice this radius. If the precipitate is more finely dispersed the dislocation line cannot bow sufficiently to avoid all the associated strain fields and the resultant stresses on the line cancel each other, letting it move fairly easily. When the spacing between particles is large the dislocation line can bow between them quite easily with little hindrance, thus appearing soft (over-aged condition). The effect of dislocations bowing between precipitates can be seen in Fig.3, where successive lines leave loops around the particles, increasing their effective size (due to strain effects), and causing increasing obstruction to following dislocations.

2.1.5.2. Chemical hardening.   If a dislocation actually cuts through a precipitate work has to be done in forming a new surface.

2.1.5.3. Dispersion hardening. When the precipitate becomes incoherent with the matrix the internal strains are removed and dislocations can again move between particles by the Orowan bowing mechanism. As the effective size is reduced by loss of the strain field a greater volume of precipitate is required, the higher this volume the greater the strengthening which occurs.

2.2. MARTENSITIC STAINLESS STEELS

Examination of a Schaeffler diagram [5] shows that a martensitic structure can be obtained with chromium contents up to 22%, but above 8% undesirable delta ferrite starts to form unless increasing nickel additions are made (Fig.4). Delta ferrite reduces the hardenability of the steel and increases the directionality of mechanical properties; in addition severely reduced ductilities may be experienced in the heat affected zones of welded joints. Alloys which fall within the mixed austenite – martensite region can, with selected alloy additions, be made to transform to a wholly martensitic structure by a low temperature heat treatment (semi-austenitic or controlled transformation steels). The chromium content increases hardenability with the result that medium carbon alloys are air-hardenable over 5% chromium.

From the iron-chromium equilibrium phase diagram in Fig.5, [6], it can be seen that the γ loop is closed when the chromium content exceeds 12%, extending to 18% as the carbon content increases. At least 12% chromium is required for stainlessness in mildly corrosive conditions, but such a large percentage ties up much of the carbon, reducing the amount of hardening. To overcome this an austenite stabiliser is added, nickel, which has an extra beneficial effect in increasing corrosion resistance and high temperature strength.

2.3. PRECIPITATION HARDENING STEELS

Wholly martensitic precipitation hardening stainless steels

(stainless maraging) are limited to 17% chromium, so to increase corrosion resistance small amounts of copper and molybdenum are added, these also conferring some solid solution hardening effect. A very low carbon content ensures good weldability and impact resistance.

2.3.1. Precipitating phases.

The phases regarded as causing the hardening effect are varied. The effect is well documented for non-stainless maraging steels, namely Ni_3Mo, Ni_3Ti and Fe_2Mo. As the steel under examination in this investigation was niobium stabilised, precipitates based on titanium can be ignored. Other precipitates identified in maraging steels include Mo_2C, MoC, $(Cr,Mo)C$ at low temperatures and Cr_7C_3 at higher temperatures.[7]. Lambert et al [8] found σ —FeMo and Fe_7Mo_6 predominated in low nickel maraging steels. Among the niobium stabilised steels several workers [9,10] have found NiNb to be significant. Shlyamneva also indicates a superiority of niobium stabilised steels to resist softening at elevated temperatures in comparison to titanium stabilised counterparts. At temperatures above $700^{\circ}C$ NbN and NbC may precipitate out at phase boundaries [11]. Vowles and West [12] found a $(Fe,Cr)_2Nb$ precipitate in a straight Fe-Cr-Nb alloy, the speed of precipitation being increased by increasing the complexity of the alloy; this was attributed to a faster diffusion rate of niobium. This Laves phase is similar to the $(Fe,Cr)_2Mo$ phase identified by Kimoshita et al in a maraging steel [13]. Pseudo-precipitates of elemental niobium in clusters up to 100Å diameter are claimed to be responsible for lowering the yield strength of some high strength steels [14]. These clusters segregate when cooling from the melt but can be redissolved by heating to 900° - $1300^{\circ}C$. Similar precipitation of copper has been found by Rack and Kalish [15] in a 17Cr-4Ni precipitation hardening stainless steel. This initially forms as coherent clusters but later breaks away to precipitate as f.c.c. ϵ — Cu; the copper also reduces the optimum ageing temperature for maximum strength

to around 450°C [10]. In common with many classes of steel it appears that these types of stainless steels exhibit carbide precipitation of the type $M_{23}C_6$ [16,17]. Some balancing of strength effects occurs as the strengthening by carbide precipitation is reduced by matrix alloy depletion. This type of precipitation does tend to predominate at grain boundaries rather than on dislocations within the grain, and this may have a deleterious effect on mechanical properties.

2.3.2. Austenite reversion

High alloy steels which are nominally martensitic are frequently susceptible to the effects of a small amount of austenite resulting from alloy segregation. The austenite can be formed in two ways; firstly due to interdendritic segregation in the molten state giving rise to retained austenite at room temperature; and secondly, due to the diffusion of certain alloying elements during the heating of high alloy martensite, local enrichment causes 'reverted' austenite to form which is stable on cooling again to room temperature. Whilst retained austenite is a well-known phenomena in a wide range of steels, reverted austenite seems to manifest itself particularly in stainless and precipitation hardening steels of high and often complex alloy content. It is possible to control the amount of austenite to quite well defined amounts to give beneficial mechanical properties in martensitic steels, and for this reason it would appear that a small amount of austenite is not detrimental [18].

If the reversion process is diffusion controlled the rate of heating and cooling will greatly affect the amount of reversion. Beresnev et al [19] found that, with a maraging steel, a slow heating rate increased heterogeneity between the martensitic and austenitic phases which inhibited recrystallisation for up to 150°C above the normal recrystallisation temperature. To obtain complete austenitization excessively high temperatures were required which gave rise to a coarse grain size. Sedriks and Craig [20],

again working with maraging steel, showed how the amount of reverted austenite reached a maximum at approximately 600°C (Fig.6) decreasing to zero at approximately 550°C. This is somewhat higher than onset of reversion found in an 18/10 stainless steel [21].

Reverted austenite appears to inherit some properties from the martensite from which it formed, resulting in a higher mechanical strength than retained austenite [22,23]. The reverted austenite contains a large number of stacking faults and a high dislocation density upon which precipitation can take place. However precipitation only occurred after very long ageing times, appearing as elongated $M_{23}C_6$ particles. The high dislocation density is attributed to the difference in modulus between austenite and $M_{23}C_6$ particles and thermal contraction differences with surrounding martensite. Refrigerating this austenite transforms the structure to a lath martensite, in contrast to the 'massive' martensite which forms after ageing. The stability of the austenite is increased by the presence of delta ferrite 10 , although the latter is undesirable from its tendency to cause directional properties.

2.4. FV520B

2.4.1.   Recent trends in the development of aerospace vehicles have brought to light the need for a stainless steel which overcomes some of the difficulties of the popular austenitic and martensitic types. The austenitic (En58) types can be cold-worked to high strengths at the expense of ductility, but this means that complex parts may have to be resoftened during working and any welding on a finished part results in softening by the welding heat. The martensitic (En56) types are easily formed in the softened condition but the high austenitizing temperature and hardening procedure leads to severe oxidation and distortion, and only the low carbon varieties are easily welded.

Further development resulted in a class of martensitic precipitation hardening stainless steels showing the following desirable properties to some extent;

1) a low carbon martensitic matrix;

2) a wide range of strengths obtained by simple low temperature treatments;

3) a very low δ-ferrite content to stop directional properties and low weld ductilities;

4) good ductility, both hardened and softened;

5) easily welded, with the heat affected zone having the same response as the parent metal;

6) good corrosion and stress corrosion resistance.

The normal way of providing a range of strengths in steels is to change the carbon content and vary the tempering treatment. High carbon levels are undesirable from fabrication aspects and so precipitation of various compounds is employed to increase strength, this avoiding weld bead cracking and stable austenite formation which is resistant to refrigerant transformation. The nickel-chromium system shows a slight precipitation effect during ageing, but this can be greatly increased by additions of small amounts of Al, Co, Cu, Mo, Nb and Ti. Varying the ageing temperature and time enables different strengths to be obtained due to the differing speed of ageing response of each element and variation in the size of the precipitate. The Ni-Ti precipitate utilised in the maraging systems is unsuccessful in stainless steels as the lower nickel content results in a smaller shift of the m_s and m_f temperatures. Niobium, together with titanium and aluminium, have the disadvantage of promoting δ-ferrite formation both in their own right and, in the case of the former two, by tying up carbon which is a δ-ferrite suppressor [24]. Hull [25] has investigated the relationship between alloy additions and δ-ferrite

formation in stainless steels and expressed it mathematically as

$$\%Ni \ (for \ 0\% \ \delta) = -4.71 + 0.92Cr - 0.088Mn + 0.007Mn^2 + 1.30Mo + 0.051Si$$
$$+ \ 0.17Nb - 14.6N - 16.7C - 0.42Cu.$$

His equation underlines the enormous effect slight variations of carbon and nitrogen contents can have on the occurrence of δ-ferrite.

Precipitating additions have varying effects on ductility, molybdenum and niobium reducing ductility less than aluminium, copper and titanium at similar strength levels. As the proportions of chromium and nickel are limited to avoid δ-ferrite formation it is usual for a high chromium content rather than nickel to be used, as nickel is more useful in increasing resistance to acidic conditions, situations in which these steels are not used to any great severity. Certain additional resistance to acids is conferred by the copper and molybdenum additions. The martensitic matrix makes the precipitation of chromium carbides on grain boundaries quite easy at temperatures above $400^\circ C$ and hence ageing and conditioning treatments will lead to intercrystalline corrosion when the free carbon level is above 0.05%.

2.4.2. Development of FV520B

This is a subject which has been excellently documented by Morley [134]. From considerations outlined in a previous section a basic composition of 16%Cr, 4.5-6.0%Ni, with additions of 2%Cu and 2%Mo appeared to be an alternative proposition. Such a steel, R.ex 520, was developed in 1954 as a martensitic steel with improved weldability and corrosion resistance, and after subsequent development renamed FV520B, the suffix indicating its suitability for bar and forgings. (Continuing growth of the aircraft industry called for a high tensile stainless steel available as thin sheet, but as the martensitic steel was unsuitable for complex forming an unstabilised version was developed which retained more austenite. Designated FV520S it was the first controlled transformation steel available commercially in this country). Until this time high tensile stainless steels

had suffered intercrystalline corrosion due to precipitation of chromium carbides in the 450°-600°C range such as would be encountered at some points during welding and brazing. Lowering the carbon content was an obvious answer but this led to δ-ferrite formation and lower hardenability. It would have been possible to overcome this with nickel additions but at that time the effects of retained austenite were unpredictable. The first experimental cast of R.ex 520 was titanium stabilised, showed no peak hardening after welding, and after forging to a billet showed a martensitic structure with δ-ferrite bands. The composition of R.ex 520 and the two derived steels are shown in Table I.

By reducing the chromium content from the R.ex 520 level the presence of δ-ferrite was practically eliminated leading to better fatigue properties and transverse ductility. Stringers of titanium oxides and nitrides were also found to reduce transverse properties in forgings and so niobium was used as the stabilising element in FV520B. An increase in molybdenum and copper contents helped to restore some of the corrosion resistance lost by the lower chromium content to a level which compares favourably with most similarly alloyed (but lower strength) stainless steels in all but strong acid environments. The lowered chromium content had the additional benefits of minimising the tendency to retained austenite and of not causing embrittlement after prolonged heating at 350°C. At slightly higher temperatures maximum precipitation occurs with corresponding higher strengths and lower ductilities. Overaging restores the ductility at the expense of strength. The copper addition helps in both corrosion resistance and as a slight precipitation hardener to compensate for the reduced strength otherwise obtained from a low carbon steel.

2.4.3. Heat treatment

A range of different treatments are available:

a) Normalised 950/1000°C, air cool

A recrystallisation treatment with low solution potential. Little used due to low fatigue resistance. Large components and forgings are solution treated at $1050^{\circ}C$, air cooled and then conditioned for two hours at $850/750^{\circ}C$ with air cooling before hardening. This raises the m_s by reducing the carbon in solution giving more complete transformation to martensite. At the solution temperature the matrix is austenitic with small amounts of δ-ferrite.

b) Precipitation hardened, (a) + $450^{\circ}C$ four hours.

Maximum hardness is obtained by this ageing temperature, so components are usually machined after the solution treatment.

c) Overaged, (a) + $550^{\circ}C$ two hours.

A slightly softer condition can be obtained in any section if the intermediate conditioning temperature after the $1050^{\circ}C$ solution is reduced to $750^{\circ}C$ for two hours and air-cooled. This takes the steel between Ac_1 and Ac_3 and so reduces the amount of martensite before ageing to 60%, the remainder being a fine aggregate of ferrite and carbides. In this condition the steel exhibits excellent ductility, fatigue strength and resistance to stress corrosion cracking.

d) Overaged, (a) + $620^{\circ}C$ two hours.

Again usually used in conjunction with the duplex $1050^{\circ}C$ + $850^{\circ}C$ (or $750^{\circ}C$) treatment to confer maximum ductility and stress corrosion resistance. Some stable austenite forms at $620^{\circ}C$ which slightly lowers the proof stress at room temperature.

Above $850^{\circ}C$ the alloy is almost entirely austenite; however on cooling to room temperature it reverts to martensite. (Cracked ammonia atmospheres for heat treatment must be avoided to prevent nitrogen pick-up).

2.4.4. Mechanical properties   Table II

The ductility and notch resistance is good at all strength levels but the fatigue strength falls as tensile strength increases, being

a maximum in the overaged 620°C condition. FV520B forgings show distinct advantages over other martensitic stainless steels at sub-zero temperatures, its transition being below -100°C when measured by the standard Izod test. High proof strengths are retained up to 450°C, dropping over this temperature as illustrated by creep and stress relaxation tests. This can be advantageous in that welded assemblies can be stress relieved at 550°C with minimum distortion risk.

2.5. WELD HEAT AFFECTED ZONES IN PRECIPITATION HARDENING STEELS

2.5.1. General observations.

This is an area of investigation in which very little information has been published. The only directly relevant work appears to be that by Kaae [34], which includes weld HAZ hardness surveys for a range of as welded conditions and post weld heat treatments. The great majority of work conducted to date concerns the nickel-based maraging steels, and it is from these studies that any general observations can be drawn, the similarity of metallurgical features making similar effects in FV520B likely. Non-uniformity in the HAZ (heat affected zone) of maraging steels has centred upon two main regions of deterioration, one of low toughness near the fusion line, and one of high toughness some way from the weld bead. Both Coleman [26] and Razikov [27] attribute the low toughness near the fusion line to constitutional liquation of inclusions. However the high toughness area is claimed by Coleman to be due to austenite reversion at 650°C, an explanation favoured by Kenyon [28], whereas Razikov attributes it to grain boundary composition effects and stress relaxation between 900°C-1300°C. At high heat inputs the width of the HAZ is increased with consequent broadening of the above mentioned zones [29]. Hence to prevent any large-scale non-uniformity it is advisable to keep heat inputs low. In contrast to this Strunck and Stout [30], working with a low carbon bainitic-

martensitic steel, advocated wide HAZs as a refining process in multi-pass welds. As the cooling rate is claimed to be substantially increased as penetration increases, the final run is recommended to be of medium heat input, allowing a shallow but broad HAZ profile. In addition to the refining effect of multi-pass welds Cina [31] has shown that the thermal stresses arising can affect the stability of austenite and help in its decomposition.

2.5.2. Welding of FV520B

Many of the high strength steels currently used suffer from their susceptibility to hydrogen induced cracking in the heat affected zone. This is particularly so in low-alloy steels, which gain their strength from the low temperature transformation products of austenite. This means that special precautions, such as low hydrogen electrodes (and ovens to keep them in), have to be taken. The advent of precipitation-hardened steels has brought a new class of high strength steels which show remarkably little hydrogen induced cracking. This is an important advantage in all but the simplest of structures.

The excellent weldability of FV520B is due to minimisation of the elements likely to cause trouble. This includes elimination of aluminium, very low carbon and residual nitrogen contents, and copper kept to within safe limits. Aluminium strongly promotes δ-ferrite formation; at the temperatures attained during welding the probability of this phase forming is greatl exaggerated. The low carbon content avoids retained austenite and eliminates severe hardening in the HAZ, so reducing the risk of cracking [32]. If full strength is not required in the weld bead an austenitic 18% Cr, 10% Ni, niobium stabilised electrode may be used without pre-heat or post-weld heat treatment. For full strength filler wire of the same composition as the parent plate should be used with the assembly in the 550°C overaged or intermediate 1050°C + 750°C condition. Either argon-arc or MIG welding is suitable. Generally steels of this type do not require preheat [33], but heavy section should be heated to 50°-150°C to minimise the risk of cracking (avoiding carburising flames). A post-welding treatment of at least six

hours at 550°C is recommended for full stress relief. Up to twenty four hours at this temperature will not cause any marked softening. Better notch toughness can be obtained by soaking for two hours at 750°C and then for a further two hours at 550°C after air cooling to room temperature, this also giving an excellent combination of strength and ductility (maximum strength is achieved by altering the second stage of the duplex heat treatment to two hours at 450°C). FV520B can be welded to other steels by MIG or TIG using similar composition filler wire, and in tensile tests failure usually occurs in the parent plate of the other material.

As is usual in all steels the welding process used creates a range of microstructures, the relative amount of each depending mainly on the specific heat input of the process, i.e. the higher the heat input the broader the microstructural bands become. With a precipitation hardened steel of the FV520 type it is to be expected that the material nearest to the fusion line will show a solution-treated type structure, with an over-aged region between that and the parent plate. The condition of the material before welding will be evident in the physical properties exhibited across the weld zone, the most marked changes showing in the fully hardened material. The tensile properties (excluding proof stress) of a joint will reflect the properties of the softest zone, and it is to be expected that the narrower the zones are kept the less effect any soft zone will have. In work carried out on this material by Kaae [34] using filler wire of the same composition, it was shown that post-weld heat treatment increased proof stress, tensile strength and ductility of welded specimens. To provide HAZs of differing widths several processes were used – multi-run TIG, three pass submerged arc and an electoslag weld – all on 32mm plate. The only time that tensile failure occurred in the HAZ during testing was in the case of the electroslag welded specimens aged at 450°C and 550°C, but even so the yield and proof stresses obtained were only slightly below those found for the

corresponding TIG welds. Generally the as-welded specimens failed in the weld metal with little reduction in area. The tensile strength of the weld metal increased as the number of passes increased, probably due to ageing of previously deposited weld metal. Usually increasing the temperature of ageing from 450°C to 550°C did not change the location of fracture. It was found that care had to be taken in specimen selection as specimens taken from near the start of welding where the joint depth-to-width ratio was large tended to form a continuous vein of delta-ferrite. In all welds the softest regions were the overaged areas, although the minimum hardness varied little with increased heat input. In no welds did ageing restore the value of hardness of the overaged region to that of the parent plate, whereas the solution treated regions were. In all cases ageing for twenty-four hours increased the hardness obtained after three hours at 450°C. As the post aged HAZ had the same minimum hardness whatever the process, the only advantage of a low heat input process appears to be the confining of the soft band to a narrow region. When the welds were carried out on over-aged (550°C) material the differences in hardness were reduced. The micro-structure in the solution treated region near the fusion boundary was found in all cases to be a mixture of austenite, martensite and high temperature ferrite. One anomaly which was noted by Kaae was a region of softness which did not respond to the post weld ageing treatment (fig.7). The location of this soft area varied according to the welding process, being further from the weld fusion line for higher heat input processes.

The susceptibility of high strength steels to hydrogen induced cracking led to a complete investigation of this aspect of FV520B by the same workers [34]. In low alloy steels this type of cracking occurs at hard-nesses above approximately $350H_v$ (and in high alloy steels at even lower hardnesses). The HAZ of FV520B shows a hardness of $340-380H_v$. The amount of martensite present is the critical factor, but generally the lower the

carbon content of the martensite the lower the susceptibility to hydrogen induced cracking. Specimens to be subjected to constant load rupture tests were heat treated at 1050°C or 1250°C in argon or hydrogen. The room temperature evolution of hydrogen measured over a week was exceedingly slow indicating a slow rate of hydrogen diffusion, and so the length of test was increased. The hydrogen charged specimens had only slightly reduced ductility compared to the hydrogen free, and the results showed that FV520B compared very favourably with other high strength steels in this respect. The coarser grained specimens did show increased susceptibility, the results being similar to those found by Ponizewski in 18% nickel maraging steel. In addition refrigeration to transform any retained austenite also increased the susceptibility to cracking. Only in the severest case, i.e. 1250°C treatment in hydrogen followed by sub-zero treatment is it thought that hydrogen induced cracking might occur.

High temperature cracking in stainless steel welding can be divided into three groups;

1) Super-solidus, in the weld metal whilst still molten;

2) Sub-solidus, below the bulk solidus in weld metal or HAZ, or crossing the fusion boundary to be in both;

3) Reheat cracking, also weld metal of multi-run deposits.

There is some indication that a small amount of δ-ferrite helps to prevent all three, and hence FV520B should show resistance to these types of cracking. In fact no cracks were found in the multi-run TIG, subarc or electroslag welds of the investigations described above and so to increase the severity the Varestraint test was employed, although this does not increase the possibility of reheat cracking. This test revealed some super-solidus cracks but considerably less than is encountered in some other stainless and low alloy steels. However a unique type of cracking did occur, consisting of numerous small weld metal cracks at the interdendritic two

phase boundaries between δ-ferrite and austenite. Furthermore sub-solidus cracks appeared when non-matching coated filler wire was used, these being due to the segregation of manganese sulphide films around δ-ferrite. Providing electrode coatings are carefully formulated it would appear that high temperature cracking is not a problem with FV520B.

2.6. WELD HEAT AFFECTED ZONE SIMULATION

2.6.1. Introduction

The weld heat affected zone may be defined as that part of the parent metal which is subjected to heat to the extent that its structure is altered without melting having taken place. The size of the HAZ varies according to several factors, i.e. welding process, heat input, type of joint, workpiece thickness and thermal properties of the parent metal. The thermal cycles experienced at various points in the HAZ include peak temperatures between the ambient of the surroundings and the melting point of the metal. Hence a continuous gradation of microstructures is formed, the amount of each depending on the overall HAZ width, being from 2mm in electron beam joints up to 25mm in electroslag welds. Even in the widest HAZs the microstructural gradient is too steep for proper mechanical testing of any particular structure to be satisfactorily performed. Saperstein et al [35] noted the difficulty experienced in endeavouring to propagate a crack through a single microstructural region of a real weld HAZ. To overcome these sorts of problems weld thermal simulators have been designed which allow bulk samples of microstructures to be obtained, subsequently permitting meaningful mechanical testing.

2.6.2. Simulator development

The first weld simulator was that at Rensselaer Polytechnic, USA, developed by Nippes and Savage [36] just after the war to investigate

notch toughness in the weld HAZ of a ship steel. Much of the initial equipment was manufactured under the name 'Gleeble', and this has been adopted as a generic name for this type of apparatus. The basic principle of this machine - resistance heating a metal sample by passing a heavy current - has been used almost exclusively in all other designs of simulator, although satisfactory results have been obtained by induction heating [37]. Problems associated with the 'skin' effect during induction heating have been overcome by a short holding time at the peak temperature to allow temperature equalisation throughout the cross-section of the specimen. Control of the heating cycle has been attempted in a number of ways. Initially the current-time relationship was pre-determined and controlled by a cam-operated potentiometer [36,38]. This was rather too sensitive to small differences in specimen size and resistance and so a closed loop feedback system was devised. This involves comparing specimen temperature (measured by a thermocouple) with the output of a reference generator, and the difference used to control the power applied. Methods of generating the reference voltage have included potentiometers [36], cam-controlled electrolytic rheostats [38], plug-in resistor networks [39] and potentiometer arrays [40]. Specimens have been square, rectangular or round cross-section, up to 25mm diameter. Obviously the larger the specimen the greater the current required to heat it. Heating rates up to 2000°C per second are possible [41] but some loss of consistency of the cycle results. Frequently the problem is with cooling rates, fast cooling being possible only by efficient grip design and short gauge lengths [42]. Problems in this area are exacerbated by low conductivity materials such as stainless steels.

Most modern weld simulators are equipped with a mechanical testing capability allowing actual testing during the thermal cycle, or alternatively the application of a small amount of strain typifying that experienced by a real weld subjected to thermal expansion and contraction stresses.

American methods for application of load are typically hydraulic or air/ hydraulic such as Nippes apparatus [43], while experimentation in Russia has favoured electromagnetic application [44]. A British simulator equipped with an electromagnetic clutch can control load applications within 0.2 seconds [45], such rates of response being vital to eliminate any variability of microstructure caused by thermal stresses.

2.6.3. Simulator problems

One of the most consuming topics in weld simulator research seems to be thermocouple attachment and associated temperature measurement [42,46-51]. Differences between the temperature at the specimen centre (as measured by a sheathed thermocouple in a blind hole) and the surface temperature of up to 100°C have been noted, depending on the maximum temperature simulated [50]. The cause of this has been variously attributed to thermocouple 'heat-sink' effects [42], cross-sectional temperature gradient [46], method of thermocouple attachment [48,50] and pickup of the heating current [51]. As the control thermocouple during simulation is usually surface attached careful examination of the situation is required to ensure that the specimen bulk receives the required cycle. The most exhaustive investigation of this problem to date is that conducted by Phillips [48]. He concluded that the most accurate method was to resistance spot weld separate wires onto the surface as close as possible without actually touching, a solution confirmed by Savage [41], who achieved the same end result by a different method. Temperature reproducibility of up to $\pm$ 7°C at 1200°C are quoted, but the dangers of offsetting separate wires along the specimen axis have been highlighted by Widgery [52]. He points out that a relative displacement of 0.1mm would be subject to a voltage drop of 9mV at the power required at 1400°C. A further source of errors caused by displacement is the induced emf produced in the wires [52], and hence careful attachment of the wires is essential. Phillips [48] finally

deduced that despite the surface temperature being 35°C lower than the centre at 1000°C and 60°C lower at 1400°C, these differences were consistent if thermocouple attachment was consistent, and hence due allowance could be made.

A second source of contention in thermal simulation appears to be the effect of strain. The microstructures derived are not formed with the same degree of restraint as in real weld HAZs, but no method exists for measuring the strain cycle occurring at each point in the HAZ [53]. Although various authors have noted the effect of strain on microstructures [54,55], Dolby [56] is of the opinion that in transformable steels, where the dislocation density is already high, a few extra percent of strain did not contribute greatly to embrittlement. This view is shared by Smith [49] and Watkins [57], but Hrivnak [58] found that in low dislocation density materials a superimposed strain cycle was essential.

2.6.4. Thermal cycles

For simulation to be carried out a thermal cycle must be used which is representative of a real weld thermal cycle. Two approaches may be made to the establishment of such a cycle, either by actual measurement during a real weld or by computational techniques.

2.6.4.1. Real weld cycles. This is the most accurate way to determine the precise thermal history of any point in the workpiece. Embedded thermocouples can be utilised to either measure the cycle under critical specified welding conditions [59] or to measure distribution during simple bead-on-plate runs which approximate closely to the required conditions [60]. The Welding Institute [61] has recently begun to compile a data bank of thermal cycles measured in a variety of welding processes, plate thicknesses, materials, number of runs and welding conditions. The data sheets give information of cycles at varying distances from the weld fusion line and are a valuable aid to saving time and money in defining

suitable programs for simulation.

2.6.4.2. Computational techniques. It is not always feasible to set up welding trials to obtain experimental values of temperature distribution, and so by use of heat flow equations it is possible to calculate thermal cycles for any point in a weld HAZ. A considerable number of theoretical approaches have been made; Rykalin [62] has made a study of heat flow equations applicable to welding, the differential equations obtained being applicable only to steady state conditions, but Rosenthal [63] converts this approach to a quasi-stationary state, obtained when the temperature distribution relative to the heat source is stationary. This does place some limitations on the assumed conditions, eg. it must be considered as a point heat source in an infinite plate, but useful results are obtained [63]. Westby [64] has extended the basic work of Rykalin to allow computer calculation based on the finite element analysis concept. This involves calculation beyond the scope of hand methods, and it is only recently, with the development of computers with large core-stores, that this technique has become feasible. Westby's program allows computation for two or three dimensional heat flow with material thermal 'constants' either fixed (TREDIM) or variable (VARIAB); Paley and Hibbert [65] have further extended the use of this program to allow for weld edge preparations and further refined the calculation mesh size to give better results in areas of high thermal gradient.

Whilst Savage [41] is sceptical of the applicability of calculated thermal cycles in HAZ simulation Myers et al [66] have shown that reasonable agreement is obtained between actual and calculated thermal cycles as long as areas very close to the fusion line are not considered. Both Myers [66] and Mueller et al [67] have shown that good estimates of HAZ width can be obtained, the latter extending the use of calculations to determine theoretical arc efficiencies of other processes prior to further thermal

cycle computation.

2.6.5. Validity of HAZ simulation

The object of thermal simulation is to obtain bulk samples of a certain microstructure. Clearly if the simulated structure does not closely resemble the real weld HAZ any conclusions based on the former will not necessarily apply to the latter. Much attention has been paid to this aspect and it is generally agreed that microstructures can be readily simulated to give acceptable resemblance to real HAZs [49,53,68]. Whilst agreeing that acceptable microstructures can be obtained no effort was made to correlate mechanical properties with real weld HAZs, the difficulty in obtaining the latter obviously prompting the simulation. However Dolby [69] has attempted to prove the validity of simulation from the mechanical testing aspect with work on HY80 steel. By correlating real and simulated microstructures (not peak temperatures) he was able to show similar results of fracture toughness, although the yield strengths of simulated specimens were somewhat higher. He found the severity of microstructural gradient to have little effect on fracture initiation. Nevertheless Dolby recommends that fracture toughness tests on simulated specimens should be used for optimising metallurgical variables rather than predicting failure risks in real structures [56]. This may result from the work conducted in conjunction with Widgery [46] where some uncertainty arose from grain size differences. It was found that a real weld HAZ grain size obtained at 1340°C could be obtained by simulating to 1210°C. Whilst some of the 130°C difference was ascribed to the temperature measurement difficulties mentioned previously, it was decided that generally simulation should be based on equivalent grain sizes rather than similar peak temperatures. However Coleman [42] has no hesitation in recommending the use of simulation in mechanical testing after exhaustive work on the fracture toughness of real and simulated heat affected zones in 18% Nickel maraging steels.

2.7. FRACTURE TOUGHNESS TESTING

2.7.1. Introduction

In the past when designing structures, due to uncertainties in the behaviour of a material containing notches, small defects etc. a safety factor has had to be applied. The greater the endangerment of human life involved by failure of a component the greater has been the safety factor applied. As the need for a greater working stress has arisen there have been two alternatives. The first is to use thicker sections, but this has drawbacks in such fields as transport engineering (especially aerospace) due to the undesirability of large deadweights. The second alternative is to use a material which is stronger, usually implying a greater uniaxial yield strength. However for most materials an increase in strength entails a decrease in ductility and also notch toughness as there is insufficient capacity for plasticity to blunt a crack growing from the tip of a notch. As most designs contain some sort of notch, whether it be keyway, web or other structural feature, it would be advantageous to use some method which actually measured the material notch toughness rather than rely on empirical safety factors. The first methods employed to this end were the Charpy and Izod impact tests. These are useful for showing a ductile-brittle transition with temperature and for empirically grading materials, but the high strain rates and moderate notch severity used do not have general applicability, measuring a parameter associated with combined initiation and propagation of cracks, the two components being inseparable. [70]

2.7.2. Plane strain fracture toughness.

Modern techniques of fracture toughness testing are based on the theory proposed by Griffiths [71] in 1920. He related the fracture strength of a material, σ_F, to the crack length (defect depth) 2c, in a large sheet by the equation

$$F = \sqrt{\frac{2E\gamma}{\pi c}}$$

where γ is the amount of energy required to form the new crack surface. This worked well for brittle materials such as glass when it was assumed that γ was equal to the surface free energy, but for metals the answers for σ_F were between one and two magnitudes too small. This led to a modification by Orowan [72] where γ was split into two components, γ_S, the surface free energy, and γ_p, the energy consumed in plastic deformation to the crack depth. Then $\gamma = \gamma_S + \gamma_p$; but as γ_p is approximately one thousand times greater than γ_S the latter was ignored and a simple substitution of γ_p for γ made. For crack initiation γ_S is still used as the plastic zone associated with microcracks is very small. Using Orowan's formula as a basis the Linear Elastic Fracture Mechanics approach was evolved for situations where the amount of plastic deformation before fracture was small compared to the elastic component. This utilises elastic stress analysis of a cracked part to define the conditions under which the flaw will extend. In isotropic materials brittle fracture occurs mainly due to crack surfaces moving directly apart (as opposed to the shear mode and the edge-sliding mode); this type of fracture is usually indicated by the subscript I. As a body is stressed the elastic stored energy of the body increases, but if a crack grows there is a relaxation of some of the stored energy which helps to provide the surface energy necessary for the formation of new crack surfaces. However if the released stored energy is greater than that required to form the new surfaces the crack extends more to take up the excess energy (fig.8 [73]). The increased crack length causes a greater gross stress on the section and a situation of unstable (accelerating) crack growth is set up. For any stress situation there is a critical crack length, beyond which the strain energy release rate, denoted by G, exceeds the energy required to form new surfaces. The critical value

of G where the two types of energy balance is called G_C, and if the fracture mode is type I, the value is known as G_{IC}. The fracture surface, being a free boundary, is stress free but there is a rapid build up in the intensity of the stress field at the crack tip, the stress intensity factor being denoted by K [74]. K is a function of the specimen dimensions and loading geometry, being greatest at the crack tip and falling off inversely with the square root of the distance from the tip. Crack growth occurs when K reaches a value of K_C, the minimum value of K_C being K_{IC}. K_{IC} can be regarded as a material property and is a convenient measure of 'fracture toughness'.

In thick sheets a hydrostatic stress situation will be set up (fig. 9) at the crack tip causing a mode I opening. At the surface there is no σ_Z force exerted due to lack of constraint and this causes a shear movement between the crack surfaces giving a 45° 'shear lip' as in fig.12. The depth to which the fracture is shear depends on the material, but as thickness increases, the influence of the shearing on the toughness is reduced until a steady value is obtained (figs.10 and 11). Materials are said to fracture in 'plane strain' if they are sufficiently thick for mode I fracture to predominate. In thin sheets the full effect of the σ_Z stress may not be realised (fig.12) and fracture is then said to be 'plane stress'. For plane strain

$$K^2 = \frac{EG}{1-\gamma^2}$$

and for plane stress

$$K^2 = EG$$

The stress needed to cause fracture is given by

$$F = \sqrt{\frac{EG_C}{\pi c}}$$

where 'c' is the crack depth.

The local stress, σ_L, generated at the tip of a crack of length c is

$$\sigma_L \propto (\frac{c}{\rho})^{\frac{1}{2}} \qquad [75]$$

where ρ is the root radius of the crack tip. Thus sharpening the crack (i.e. reducing the root radius) is equivalent to a substantial increase in crack length. The sharpest cracks are naturally grown fatigue cracks and the recommended technique for plane strain fracture toughness testing [76] lays down conditions for such growth. In very ductile materials some blunting of the crack occurs during initial loading, however Smith [77] and Terry [78] have found that for most purposes machined notches exceed the root radius of blunted fatigue cracks and hence affected results. It would therefore appear that fatigue cracks are essential to ensure conservative results.

With extremely ductile metals the very high stress intensification at the actual crack tip causes the plastic zone formed to be appreciable, and the estimate of K_C becomes more conservative, hence there is a built-in safety factor. Various workers [79,80] have attempted to correct for the effective change in crack length due to the added plastic zone, Irwin's [79] correction factor being a fairly simple geometrical deduction for small plasticity, whereas Dugdale's [80] is a more rigorous mathematical approach to larger scale yielding. These correction factors may be employed to allow the linear elastic fracture mechanics approach to be used up to stresses of 80% of the yield stress, but a more convenient approach is desirable for cases where fracture occurs after general yield, to enable conveniently small test pieces to be used.

2.7.3. General Yield Fracture Mechanics.

With very ductile materials the limitations on thickness placed by the standard procedure [76] mean that very large testpieces must be used.

This may not be representative of the section used in service and may also mean that very large capacity testing machines are required. A new parameter is required which will predict the resistance of ductile material to fracture and at the same time be compatible with the stress analyses of linear elastic fracture mechanics. Two different parameters have been postulated. The first is a measurement of the 'crack opening displacement' at fracture; the second is a measure of strain energy release rate under non-linear elastic conditions and is known as J.

2.7.3.1. Crack Opening Displacement (COD)

Crack opening displacement relies on the principle that the amount a sharp crack opens prior to fracture depends only on the local fracture ductility of the material, not whether fracture is before or after general yield, the only limit being that the constraint, i.e. 'hydrostatic' component, is the same in both cases. Hence COD is as fundamental a property as yield stress. Cottrell [81] and Wells [82] independently suggested the use of crack opening as a fracture toughness parameter; the conditions at the crack tip being examined mathematically by Bilby [83] who derived the relationship

$$\sigma = \left(\frac{\mu \sigma_y \delta}{\pi a}\right)^{\frac{1}{2}}$$

where μ is the shear modulus and a is the crack length. $\sigma_y \delta$ is equivalent to the amount of plastic work done in shearing a crack opening displacement δ. This can be compared directly with the original Griffith equation and is identical, except that $\sigma_y \delta$ replaces γ. Further work by Wells [84] also confirmed the relationship $\sigma_y \delta_C = G_C$ found by Bilby. Subsequently Wells [85] has suggested the modification

$$G_C = n \sigma_y \delta_C$$

with n tending to unity for plane stress and to two for plane strain, a relationship confirmed by Burdekin and Stone using stress functions [86].

Several techniques have been used to measure COD experimentally, but to be useful only reasonably accurate methods can be considered. Continuous measurement by means of an optical system and graticule [84] is possible but this involves accurate positioning of extra equipment and continuous observation. This technique then becomes impracticable when other observations have to be made (eg. detection of crack advancement) unless more than one observer is available. Some measure of COD is possible by considering the angle of bend of the specimen, but this method is rather inaccurate when measurements have to be made to a fraction of a millimetre. In an attempt to refine measurement a 'codmeter' was developed [86], which continuously monitored COD by the rotation of a small blade pushed into the tip of the notch. Due to the blade sticking or not being exactly at the notch tip considerable scatter of results occurred [87]. Further refinement of the codmeter [88] failed to provide sufficiently accurate results, although it did show that the COD at the specimen centre was the same as that at the surface. Knott [89] attempted to measure COD by testing double notched bars; when failure occurred at one notch the strain at the other could be measured. This technique suffered from having to grow similar sized fatigue cracks from each notch. Robinson [90] tackled the problem by infiltrating the crack with silicone rubber to obtain a three-dimensional replica of the crack tip. This allowed on or off-load values to be measured but suffered from any stress relaxation as the rubber set. Fearnehough and Watkins [91] decided that the most accurate method was by photographically recording the surface COD for a number of specimens and from these drawing up a calibration curve. The technique involves photographing a series of microhardness indentations at the crack tip during testing and correlating the displacement of these marks with the 'Offset

Plastic Displacement' of the specimen at that point (fig.13). This gives consistent results at, or very close to, the elastic-plastic boundary, where it should be measured. Elliot and May suggested using a clip gauge technique similar to that used for linear elastic fracture testing [92,93]. This enables the same simple basic equipment and test methods to be used as for K_{IC} testing, and has subsequently been put forward as a draft British Standard [94]. Certain basic assumptions have to be made about the development of a plastic 'hinge' below the notch tip without a crack extension to obtain a simple geometrical equation (fig.14). This involves a rotational constant which only gives an approximate fit due to a linear equation and a parabolic relationship between δ_{CG} (COD measured by the clip gauge) and δ_t (COD measured at the notch tip) for many materials. Only a reasonable estimate of δ_t can be expected due to the assumptions made, but the British Standard gives a modified equation which has been found to fit many situations. Archer [95], using a photographic technique, has further investigated a number of formulae and his experimental data shows the modified Wells equation [94] to give the best results at very small COD measurements.

It is claimed [96] that much of the discrepancy which arises is due to movement of the rotational point which the formulae assume to be fixed. The data of Archer [95] show that while this is indeed true, the initial movement of the rotational point is rapid and then remains effectively constant for most of the test.

Thornton [97] has shown that the equation linking linear elastic fracture mechanics and general yield fracture mechanics

$$G = \sigma_y \delta$$

is accurate providing precautions to ensure the correct measurements are taken. This has been substantiated for small values of COD using a finite element approach [98], but Levy et al

[99] found a factor of 2.14 to be necessary. Finite element theory does predict

$$G = 2 \sigma_y \delta$$

for plane strain but agreed experimental verification is lacking. Despite this several workers [100,101] have shown good agreement between the results of predicted COD values from small scale tests and actual values in field tests. Further, the use of the above equation to relate δ back to plane strain critical flaw sizes has been very successful [102,103]. Cottrell [104] does point out however that residual welding stresses due to lack of stress relief will reduce the critical defect size. Knott [105] shows that while COD is a material 'constant', if the specimen thickness is increased and fracture remains entirely fibrous the fracture toughness increases, due to overcoming the greater triaxial (constraint) stresses developed. Burdekin [106] has proposed limits of thickness over which the formulae of DD19 [94] should be considered valid.

2.7.3.2. The J Integral

The theory of the J contour integral was first suggested by Rice [107]. This considers the change in potential energy of a non-linear elastic body when a crack advances a small amount by defining a path independent contour. The two main methods of determining J are by compliance testing [108,109] or formulae [110.111]. The compliance technique involves estimating the change in potential energy caused by extending crack length from load-displacement curves. The formulae methods rely on techniques such as finite element analysis to deduce the relationships, but some variability in predicted results occurs when defining the amount of restraint [111]. However, Knott [112] has shown that for two geometries the critical J value, J_{IC}, is constant, the crack blunting occurring reducing plastic constraint effects. Further practical suggestions for

measuring J involve using the clip gauge technique, hence allowing δ and J to be calculated from the same load-displacement curve [113].

Little practical proof of the validity of the J approach exists. Begley and Landes [114] showed it to be independent of thickness, but lack of consideration of slow crack growth invalidated the results. Egan [115] shows J to be temperature dependent for several geometries. Harrison [116] showed K, δ and J to give compatible results but more attention should be given to their application. Little correlation exists so far to relate small scale J tests to large structures. It seems likely that J is proportional to COD for a given geometry. Much more work needs to be done to clarify the influence of temperature, stress rate etc., on the viability of J.

2.7.4. Critical Event.

Plane strain fracture toughness testing applies a geometric condition to the experimental curve, 5% offset being equivalent to 2% crack growth , to define the critical fracture toughness [76]. Due to the diversity of behaviour of ductile materials such an approach is not possible when testing for J or COD, and hence some definition of a critical event is required. Both Harrison [117] and Knott [118] have shown the large scatter of results which are obtained if this event is taken as occurring at maximum load. The event is now accepted as being the first advance of the crack front during testing and the method of defining this point has been the subject of much work.

Both ultrasonic [119] and acoustic emission [120] techniques have been attempted but are regarded as too insensitive. Knott [77] conducted tests on a number of specimens loaded to different values. The specimens were subsequently frozen in liquid nitrogen, the amount of fibrous 'thumb-nail' measured, and the results extrapolated back to zero crack growth. However the most recent technique [121] is to measure the change in

electrical potential which occurs across the crack during growth (fig.15). This gives extremely accurate and consistent results and is now widely accepted for measuring crack initiation.

2.7.5. Microstructure in fracture

Crack extension may be conveniently discussed as two separate processes, stretch zone formation and microvoid coalescence.

2.7.5.1. Stretch zone formation

Elliot at BISRA [122] has indicated that a region exists between the fatigue starter crack and main fracture area which is relatively smooth and at approximately 45° to the direction of crack propagation. The size of this 'stretch zone' increases with the test temperature and toughness as indicated by COD testing, and hence the possibility of measuring toughness by correlation with stretch zone width has been investigated. Green [123] has shown by simple geometry (fig.16) that stretch zone width (SZW) is related to COD by

$$\delta = \sqrt{2}. \text{ SZW}$$

assuming the plastic deformation to be at 45°. He then goes on to show good agreement applying this equation to the results of other workers. Elliot himself subsequently forwarded the relationship

$$\delta = 1.5. \text{ SZW} + 0.4 \text{ mm}$$

based on work with mild steel [124]. The difference in results of these workers emphasises the importance of standardising the technique of measurement, and this is an area which has been receiving some attention. It appears that stretch zone measurement could find use in diagnosing service failures [123].

2.7.5.2. Microvoid coalescence

Little definite work appears to have been conducted on

fracture initiation by microvoid coalescence. Generally voids form around second phase particles and by linking with other voids crack extension occurs. The ease with which the void forms depends on the amount of bonding between the particle and matrix. Manganese sulphide inclusions in steel have little bonding and hence voids nucleate easily at low plastic strains. The situation is exacerbated additionally in steels where the low final rolling temperature elongates the plastic sulphide inclusions [126] so that the void takes the form of an inbuilt crack. Some inclusions, while not chemically bonded, are tightly bound to the matrix due to thermal contraction [127]. Carbides and nitrides are strongly bonded in steel and void formation occurs due to dislocation pile-ups causing vacancies during plastic flow, although large strains are required [128]. Coherent particles do not produce the same effect as the dislocations can cut the particle. Similarly dislocations can cross-slip around very small incoherent particles. If the particles are widely spaced they must be drawn together during plastic deformation in order that the material between voids may neck down and rupture, the inter-inclusion spacing affecting ductility [129]. Several workers [130,131] have shown that the volume fraction of particles is of prime importance, rather than actual particle size; increased volume fractions dramatically reduce ductility and toughness. Turkalo et al [132] found a similar result and further classified the effect of the shape of inclusion, elongated particles predictably lowering ductility. If inclusions are closely spaced almost all the strain observed is due to necking between particles, but in very clean materials such as vacuum-melted steels, the amount of strain needed to bring inclusions together may be so great that fine microvoids form around matrix carbides and nitrides and a fine-scale microvoid surface forms between the large voids [133]. The ductility will only be limited by the extent of this fine microstructure.

The extent of microvoid coalescence is strongly influenced by the amount of strain. This in turn depends on both the yield strength of the material and its capacity to work harden. As the yield stress increases a smaller plastic zone is required below the notch to develop the tensile stresses which lead to cleavage fracture; a low yield stress allows the high strains necessary to bring inclusions together and produce fibrous necking. If in addition the work hardening rate is high the stresses can be redistributed more evenly increasing the size of the plastic zone and a high uniform strain results, again favouring fibrous fracture. Moderate increases in work hardening rate can result in dramatic increases in fracture strain under the conditions of high triaxiality experienced in front of a notch.

2. 7. 5. 3. Cleavage fracture

Whereas fibrous fracture is dependent on the extent of plastic strain, cleavage fracture is promoted by the development of tensile stresses. The theories of nucleation of cleavage cracks propose that slip bands or twins are blocked by obstructions such as grain boundaries or second phase particles. Krafft [125] assumed that a plane strain crack became unstable when the crack tip stress field caused a critical amount of strain a small distance in advance of the crack tip, the 'process zone'. He derived a relationship showing resistance to cleavage improved with increased process zone size and work hardening rate. If the process zone is large enough to encompass several grains difficulty is experienced in developing the tensile stresses ahead of the crack due to the obstruction of grain boundaries. Hence fine grained materials show improved resistance to cleavage; if cleavage does occur 'river patterns' are often visible on the fracture surface due to twisting of the crack. Grain boundary carbides can play a significant part in the initiation of cleavage cracks. The

tensile stresses developed are often enough to crack a brittle carbide, especially if it is coarse; it is then possible that the crack may propagate much more easily. Redistribution of carbides in these cases will usually improve fracture resistance.

2.8. SUMMARY

It is clear that being a relatively new class of materials low-carbon precipitation hardening martensitic stainless steels have not been the subject of widespread investigation. Little investigation into the precise hardening mechanisms of FV520B has been conducted to date and none at all into the effect of welding thermal cycle on mechanical properties of the weld HAZ. Thermal simulation is becoming better established as an aid to metallurgical investigation of welding now that causes of early discrepancies have been established and would appear a satisfactory experimental technique providing correlation is made with real HAZ results where these can be easily obtained. The fracture toughness testing of 'tough' or ductile materials is an area into which much effort has recently been put. The technique of testing, interpretation of results and subsequent application of the results are all fields in which there is much disagreement. With such wide interest it is probable that outside developments occurring during the period of this investigation will alter the course of work. At the present stage it seems advisable in basic studies of the type envisaged in the present work to include all the likely parameters in toughness assessment, i.e. COD, J, stretch zone width etc.

3. EXPERIMENTAL PROCEDURE AND RESULTS

Introduction

In order that a comprehensive study of the effects of weld heat on the mechanical properties of FV520B can be carried out it is necessary to examine in depth the characteristics, both metallurgical and mechanical, of this material. Accordingly initial samples of FV520B were examined microscopically and tested in the manufacturers recommended heat treatment conditions in order to relate the behaviour to the twin variables of time and temperature. With this information it was then feasible to ascertain any unexpected effects of welding heat by conducting a number of trial welds and subjecting them to microscopical and hardness surveys. Subsequently it was possible to attempt to reproduce a microstructure of interest in sufficient quantity to test mechanically by thermal simulation techniques. This could only be achieved by establishing the accuracy and reproducibility of the thermal simulation equipment to ensure confidence in the results obtained. At the same time it was necessary to standardise a fracture toughness testing technique which gave reproducible results, some difficulty being anticipated with the high toughness levels exhibited by FV520B.

3.1. ASSESSMENT OF PARENT PLATE

3.1.1. Structure

Three separate batches of material were used for the experimental investigation. The initial material consisted of 15mm diameter bar of FV520B, cast 37060 which was employed for metallographic investigation. Welding trials and airmelted stock for simulation utilised 6mm cross-rolled and 19mm rolled FV520B plate. For comparison of mechanical properties a quantity of vacuum-remelted 8mm FV520B plate was obtained from which specimens for thermal simulation could be machined. The chemical composition of all three types is shown in Table I.

The first work carried out endeavoured to identify particular morphologies revealed by etching and then to identify the various constituents by refined analytical techniques (eg. microprobe analysis, selected area diffraction electron metallography). Cut samples were polished down to 0.25μ diamond by conventional methods, the extreme hardness of this material making polishing a lengthy process. Samples were examined in a number of heat treated conditions; solution treated, conditioned, fully hardened and overaged. Many of the etchants tried had no effect on the structure at all, a tribute to the 'stainlessness' of the material. Etching in acidified ferric chloride revealed the prior austenitic grain size (fig. 17d. The grain size was extremely fine, being much finer than ASTM number 8, the smallest grain size obtainable by photographic charts. This etch also revealed a large number of extremely fine particles, having an average diameter of about 1 micron. Most of these particles occurred within the grains, although there are a small number of places where several particles run together along a grain boundary. Etching in alcoholic ferric chloride (fig.17b/e) revealed a very fine light brown dendritic type structure with a small number of white shiny particles which may be δ-ferrite.Pickering's

reagent revealed a massive martensite block structure (fig.17f) but had no effect on any particles present. Boiling in Murakami's reagent for thirty minutes is recommended for revealing carbides, especially chromium carbides. Two types of particle were revealed, the larger ones being black and the very fine ones green. The small green particles were also revealed by etching electrolytically in oxalic acid (fig.17c).

Electron microprobe analysis was attempted to identify some of the particles revealed by optical metallography, however the particle size was too small for identification even after artificially growing the particles by overaging. As an alternative thin film electron metallography was employed to try to identify the particles. Thin slices 0.3mm thick were spark planed in paraffin and from these slices 3mm discs were spark machined out using a brass tube. These discs were then mechanically polished on emery paper down to 0.1mm thickness. The thinned discs were then electropolished in a mixture of perchloric acid and butoxyethylene until a small hole appeared at which point polishing was stopped. As polishing takes place from both sides a large area of the disc was thinned sufficiently to be transparent to the electron beam at 80KV. The transmission electron micrographs (figs.18 a-d) show the martensitic lath morphology ending at grain boundaries, in some cases twinned. Precipitation has occurred on some of the martensite making it difficult to ascertain whether the structure in fig.18d is a different morphology ('massive' martensite) or due to the precipitation. A number of selected area diffraction patterns were obtained, but in no case were there sufficient to identify any particles. The spots enabled the lattice parameter of the matrix to be calculated at 2.878Å compared to the published value of 2.864Å for α-ferrite. This indicates that the low carbon content causes very little distortion of the lattice.

A final approach to identify the precipitating phase was the use of extraction replicas in the electron microscope. The replicas were obtained by standard procedures; after normal specimen preparation down to 0.25μ diamond compound the specimens were deeply etched in Marbles Reagent and placed in a coating unit. A thin film of carbon was then evaporated onto the specimen surface under vacuum; the films were subsequently floated off the specimen by immersing in 10% hydrochloric acid in alcohol and applying a potential of 30v for 5-10 seconds. The resulting sections of film were held in grids and placed in the specimen stage of a Jeol electron microscope operating at 100kv.

Various optical micrographs were taken, examples of which are shown in figs. 19a and 19b. These show the extremely fine grain size $(1.5-2.0\mu m)$ even in the fully overaged condition. Precipitates show as black particles and are quite fine and evenly dispersed. The particles are spherical and the majority are less than $0.1\mu m$ in diameter (fig.19a). Identification of these particles was achieved by taking diffraction patterns from selected particles as shown in figures 19b-d. Dark field imaging was used to ensure that the imaged particle was actually producing the diffraction pattern.

Standard methods were used to identify the planes giving rise to the diffraction pattern spots (i.e. measuring the distance between the transmitted beam and diffracted spot), and knowing the camera constant the 'd' (interplanar) spacing for each plane was calculated. A large number of 'd' spacings were obtained and the ASTM Powder File Index employed to identify the material. This was eventually shown to be Nb (C,N) but difficulty was experienced initially due to the absence in all cases of the strong (200) reflection; as the Powder File Index lists the four strongest spots in decreasing intensity the absence of the strongest spot leads to a search in the wrong area.

Appendix II shows that the precipitating particles are Niobium based. Many of the 'd' spacings for NbC and NbN are similar due to the close relationship of their atomic sizes; however certain values are characteristic of just one of these. The high degree of agreement (with the exception of the (200) reflection) over a large number of different characteristic reflections would appear to prove conclusively that both NbC and NbN are present, probably in conjunction as Nb (C,N), thus bearing a similarity to the Ti (C, N) precipitate in nickel maraging steels.

3.1.2. Ageing Response

As an alternative approach to identifying any precipitation phenomena the effect of ageing temperature on FV520B was studied (fig.20). The curves are all of the same general shape, but the simple solution treated material attains a higher peak hardness. This is probably due to the fact that the conditioning treatment at $750^\circ C$ for two hours tempers the martensite matrix at the same time that any retained austenite is converted into new martensite. This means that the difference in hardness between the two curves is entirely due to the different state of the martensite matrix. Up to an ageing temperature of approximately $350-400^\circ C$ the solution treated material shows a slightly lower hardness, the fine interspersion of retained austenite obviously being responsible. The precipitation hardening effect is much greater in the solution treated material; it would appear that the lattice strains associated with the untempered martensite provide preferential sites for precipitation. Although a small amount of carbon is removed from solution when precipitation occurs it is unlikely that this causes compositional shifts large enough to effect transformation of the retained austenite. Precipitation of ϵ-copper, which occurs in the $400-600^\circ C$ range, could have some influence, but why the effect is exaggerated in solution treated material is not known. An ordered precipitate seems unlikely due to the complete absence of superlattice spots on all of the diffraction patterns obtained. A third alternative is a Laves phase precipitate of the type Fe_2Nb or Fe_2Mo which have a weak hardening effect but provide the site for the growth of stronger precipitates at higher temperatures. The main precipitating phases which occur from $370^\circ C$ to $450^\circ C$ may be based on a number of compounds. Precipitates with a lattice parameter similar to the martensite matrix will preferentially appear and hence there are a large number of chromium-based intermetallic compounds which may occur with very little mismatch.

Similarly intermetallic phases based on molybdenum occur, these being especially fine in the presence of cobalt. A further possibility are nickel-niobium precipitates similar to the Ni-Ti series found in nickel maraging steels.

The ageing response curves at the recommended ageing temperatures show features typical of this class of material (fig.21). At 450°C the curve is sigmoidal, being the shape usually found at peak hardening temperatures; the hardness continues to increase marginally up to 1000 minutes, but never starts to overage. At 550°C ageing occurs rapidly, reaching a peak after fifteen minutes and then slowly overageing, mainly due to particle growth. At 620°C overageing is almost instantaneous, the combined effect of particle growth and formation of stable austenite resulting in a softer final structure than is obtained at 550°C. The peak obtained by the overageing treatments is indicative of the amount of particle coarsening which occurs; rapid conglomeration of the precipitate means that it is never fine enough to achieve the hardness obtained by ageing at 450°C. It may be concluded that the general structure of aged FV520B is very fine martensite interspersed with ferrite carbides resulting from tempering of martensite during heat treatment; strengthening precipitates are sub-microscopic. Generally the structure is clean, the only major inclusions being manganese sulphide. There is a tendency for the rolled airmelted stock to segregate at its mid-section as discussed later.

3.1.3. Tensile testing

Specimens for tensile testing were manufactured from sections of plate. Standard Hounsfield no.10 testpieces were turned and surface ground and subsequently tested on a Hounsfield Tensometer equipped with a motor drive. Elongation and reduction in area were also measured and the results shown in Table. III.

3.2 Thermal History, Metallography and Properties of the Weld Heat Affected Zone of FV520B.

Introduction.

In an investigation of the weld HAZ it is necessary to define clearly the regions of interest and the associated temperature conditions. This was achieved by parallel studies of the thermal history, hardness and microstructure of the weld HAZ in 6mm plate. After preliminary trials with mild steel plate of a similar thickness an initial weldment was made in FV520B to ensure satisfactory soundness. When this proved to be the case a series of welds were made with the following plate heat treatments and welding conditions;

a) 6mm plate, primary hardened;   29v,   295A,   4.8mm/sec

b) 6mm plate, solution heat treated;   "   "   " mm/sec

c) 18mm plate, primary hardened;   1st run 26v, 410A, 5mm/sec

2nd run 28v, 330A, 5mm/sec

3rd run 28v, 330A, 5mm/sec.

Solution heat treatment consisted of thirty minutes at 1050°C; primary hardening involved heating to 850°C for two hours subsequent to solution treatment.

3.2.1. Temperature conditions in the weld HAZ

In order to carry out an investigation on the metallographic and mechanical properties of the heat affected zone in FV520B welds, and to further delineate any areas of particular interest it was necessary to make a sound weldment. After preliminary trials a number of MIG welds were made, both parallel and perpendicular to the rolling direction, in 6mm FV520B plate using eighteen percent nickel maraging steel wire filler. The plate preparation and welding conditions are shown in fig.22, the shielding gas being commercial purity argon. A thick backing plate gave conditions approximating to three dimensional heat extraction. By inserting sheathed chromel-alumel thermocouples into 0.5mm holes drilled to the plate mid-section and connecting to a Honeywell multi-channel U.V. recorder it was possible to monitor the temperature distribution during welding. Four points were chosen which would give a reasonable picture of the thermal distribution, being 6, 11, 19 and 26mm from the fusion line after welding. The peak temperatures attained and the heating and cooling rates associated with each of the four points is shown in fig.23. By interpolation it is possible to obtain a reasonable estimate of the thermal cycle between 7mm and 30mm from the fusion line. The thermocouple at 6mm failed at some temperature above $1100^{o}C$, the recommended maximum temperature for use being $850^{o}C$, but before doing so a useful indication of the heating rate experienced was obtained. The slow cooling rate below $650^{o}C$ is most probably due to the high heat content of the backing plate after prolonged weld arcing. Assuming a melting point of $1560^{o}C$ it was possible to draw fig.24, showing the maximum temperature experienced at varying distances from the weld. Generally it is found that the peak temperature experienced at any point is one of the most important factors determining the structure after welding. Several plates were welded, all showing perfect profile,

and then sectioned perpendicular to the line of welding to enable metall-ographic examination and microhardness surveys in both as-welded and post-weld heat treated conditions.

Plates were welded in both primary hardened and re-solution treated conditions, and sections were examined in the following states;

a) as-welded;

b) as-welded + solution treated

c) as-welded + direct ageing

d) as-welded + solution treated + aged.

3.2.2. Hardness surveys of the weld HAZ   (Appendix III)

The ageing treatments employed to study the behaviour of the weldments. were either four hours at 450°C (fully hard) or two hours at 620°C (fully overaged). Figs. 25-28b show that the general level of hardness of each of the sections is that which would be expected from the final ageing heat treatment received, i.e. 390-420H_v for fully hardened and 310-330H_v for the overaged 620°C treatment. If material is to be used in the overaged condit-ion there appears to be little difference caused by the initial plate condition (figs.28 and 28b). In addition there is sufficient evidence that a resolution treatment does not confer any extra benefit of uniformity above that obtained by either a duplex or a direct ageing heat treatment (fig.26). Hence to avoid undue stress in fabrications a re-solution treat-ment is not recommended for overaged conditions. If plate is welded in either solution treated or primary hardened conditions little difference in hardness is obtained except for an increasing softness in the former material subjected to less than 1000°C (figs.28 and 28b). As the main initial differ-ence is grain size it would appear that the grain growth which occurs above 1000°C renders both structures similar.

The major part of the work was then conducted on primary hardened plate, as it is in this condition that material is usually supplied.*

* (solution treated + two hours 850°C).

Although the final overall hardness is characteristic of the final ageing treatment, the material within 4mm of the weld shows great variability (figs.25-28). In the 0.5mm of material closest to the weld fusion line the there is considerable coarsening of the microstructure. A further area of uncharacteristic softness occurs consistently throughout all surveys of the first 4mm; this reaches a minimum at 2.5mm and corresponds to the 1250°C isotherm according to fig. 24. As the maximum measured peak was 750°C some extrapolation was necessary up to the melting point, the possible envelope being shown by dotted lines. This envelope encompasses peak temperatures of 1180°C to 1310°C at 4mm. The exact peak temperature for thermal simulation was established by trial and error within this range.

As-welded the hardness only exceeds the solution treated level where the weld heat has exceeded 1000°C. From this it may be assumed that there is insufficient heat and time to maintain precipitation temperatures significantly, the precipitation phenomena being influenced by an inverse relationship between time and temperature. Once the temperature to initiate precipitation has been reached the hardness of solution treated plate rapidly rises to the precipitation hardened value.

Welds heat treated at 620°C without an intermediate heat treatment show a slight increase in hardness where the welding temperature had exceeded 1000°C (figs.28 and 28b), changes in particle distribution affecting the subsequent ageing response.

The second main area of varying hardness is that which occurs between 4mm and 14mm, corresponding to the 1000°C and 650°C isotherms respectively. Resolution gives a fairly uniform structure and hence a similarly homogeneous state after further ageing (fig.26). One exception is material cycled to just below 1000°C, welded primary hardened plate having the same hardness as the solution treated. This may be indicative of particle coarsening during welding to such an extent that complete resolution is not possible in the short time permissible for this treatment without grain growth. The major distinct

fall occurred in material 8.5mm to 11mm from the fusion line, corresponding to the $820^{o}C$ and $730^{o}C$ isotherms; the softness in this area was resistant to several heat treatments attempted to remove its effect. (figs.26-28).

Beyond approximately 14mm from the fusion line the structure is uniform at a hardness level in accord with the plate heat treatment. The 14mm line is equivalent to the $650^{o}C$ isotherm, all material further from the weld having experienced a lower peak temperature. Hence the time spent at temperature is insufficient to initiate precipitation below $650^{o}C$. Precipitation is time-temperature dependent, less time being needed at higher temperatures for the same particle growth, and earlier work has shown that at $620^{o}C$ approximately half a minute incubation time is required to produce any effect.

3.2.3. Metallography of the weld HAZ

The only obvious defect which occurred during the welding was that found in primary hardened plate directly aged at $450^{o}C$. This took the form of a series of extremely coarse carbides - up to 0.02mm diameter - along the fusion line (fig.29a), which would be a very easy path for crack propagation. However, as a non-matching filler wire was used it is possible that this has some influence and no firm conclusions can be drawn.

Examination of various sections showed that in all cases thin 'veins' of a light etching phase parallel to the plate rolling direction existed (fig.29b). These 'veins' become coarser until they merge into the coarse structure adjacent to the weld (fig.30). The semi-continuous morphology of this phase may be the reason for some variability of hardness, either as a softer or harder phase or due to matrix depletion of alloying elements absorbed into the veins. No segregation could be ascertained within the limits of resolution of electron micro-probe analysis; it is likely that these veins are (delta) ferritic in nature.

The two areas which consistently showed marked differences in hardness throughout the range of heat treatments are at 2.5-3.5mm and 9-12 mm, corresponding to the isotherms $1275^{o}-1225^{o}C$ and $820^{o}-730^{o}C$ respectively.

The region around 3mm cannot be correctly homogenised even by a re-solution treatment. Metallographically the area is difficult to distinguish, the proximity to the weld bead making the entire structure very diffuse. The confined but persistent nature of this material made it desirable to investigate larger samples in order to ascertain the mechanisms operating, and for this reason it was decided to make this one of the areas for study by simulation.

The material between nine and twelve millimetres exists in the weldment in larger bulk and some indication of the cause of the softness could be obtained by direct metallographic examination and further heat treatment. The temperature range experienced, 730-820°C, is that where transformation to austenite occurs, and so steps were taken to transform any of this non-ageing constituent which may have been present. This was achieved by refrigeration in solid carbon dioxide at -78°C for twenty hours before ageing and the results almost conclusively proved that the softness was caused by austenite, the hardness dip being removed by this treatment (fig.28a). No excess austenite appears to be retained in material subjected to temperatures in excess of 840°C. There is evidence that small amounts of austenite occur right back to the 675°C isotherm as refrigeration increases hardness in all material heated above this temperature. Refrigeration also increased the general hardness of material aged at 620°C, in this case the long ageing time enables austenite to occur at a lower temperature. A much greater variability of microstructure is found in material directly aged at 450°C compared to material which is re-solutioned before ageing, this being particularly exaggerated in material near to the weld. From this area the hardness gradually drops to a minimum at 9.5mm. At 1mm there is a lack of visible carbides, few very fine particles being intermingled with even fewer larger ones (fig.31), whereas at 8mm a large number of coarse carbides are visible. This indicates a matrix depletion

of alloying elements available to form the correct sub-microscopic precipitate necessary for optimum strength and toughness. This structure is consistent with high temperature particle growth at a temperature insufficient to dissolve the particle, i.e. below $1000^{\circ}C$.

3.3. Weld HAZ Simulation

Introduction.

Successful weld heat affected zone simulation demands a facility which accurately reproduces weld thermal cycles over the temperature ranges under investigation, in this case $730-820^{\circ}C$ and $1225-1275^{\circ}C$. The size of specimen simulated must be of sufficient size to allow a substantial region of uniformity which in turn permits determination of mechanical properties such as fracture toughness and tensile values. Accordingly it is necessary to thoroughly investigate the characteristics of any simulation apparatus to ensure that the foregoing requirements are met satisfactorily. This involves standardisation, calibration and correlation of attached thermocouples, determination of temperature distribution and cooling rates for specimens of varying sizes and finally optimisation of machine settings to ensure that the thermal cycle obtained is completely satisfactory.

This part of the practical work was carried out on a 'Mand' Servohydraulic closed loop testing machine of 50kN capacity (fig.32). The feedback element in the control loops may be the output from the load cell, position or strain transducer. The reference signals can be fed to control temperature and either load, position or strain by use of two R.I. 'Data-trak' programmers, FGE 5110 (fig.33). This is an electrostatic curve-following system which is both accurate and easily prepared. The program is drawn on a metallic coated plastics sheet with a hard stylus which conductively breaks the sheet into two. The sheet is loaded onto a drum which rotates at a speed selected by alteration of gears. A probe is driven by a servo-system to seek the zero-potential existing along program curve. Direct contact with the drum is not made as the probe follows the electro-static field. Movement of the probe along a horizontal axis generates the reference e.m.f. which programs the required temperature. Power is supplied to the specimen by a 50kVA transformer at 10V. A control thermocouple is attached to the specimen and the output during heating compared to the reference voltage. The rate of supply of power to the specimen avoiding lagging or overshoot is achieved by a 'Eurotherm' controller, which will be described in full later.

Initial problems with the simulator involved overheating of the hydraulic fluid in hot weather and electrical 'pick-up' causing the actuator ram to jump. These problems were eventually eliminated by modi-fication, and commissioning and calibration commenced. The original specimen jaws were circular in cross-section and allowed the facility of testing in

a controlled atmosphere (fig.34). These jaws gave a poor specimen cooling rate which necessitated a very short gauge length. Further problems were caused by the non-uniformity of temperature distribution (fig.35). This was attributed to the relative masses of copper in each jaw, the lower jaw increasing cooling due to its greater length as the moving jaw. A radical redesign of the jaws enabled more massive grips of equal size to be employed. The increased size of jaw coupled with silver plating also enabled much better cooling rates to be obtained, although this was at the expense of the controlled atmosphere box (fig.36). The present investigation anticipated that simulation in air would be satisfactory and hence the loss of use of the atmosphere box was not considered to be important.

Subsequent calibration for simulation was carried out in six stages:

1) Correlation of bulk specimen temperature with surface (signal) temperature. —Measurement of the bulk specimen temperature was achieved by inserting a 0.5mm sheathed chromel-alumel thermocouple into a blind hole drilled to the mid-section of the gauge length. The surface temperature was established by connecting a digital voltmeter across the platinum—platinum/13% rhodium wires attached to the surface; these wires transmit the specimen temperature to the control cabinet to enable the correct amount of power to be delivered. Using the technique of control thermocouple attachment recommended by Phillips [48] very close agreement between bulk and surface temperatures was obtained, there being very little thermocouple heat sink effect evident (fig.37). For temperatures above 950°C a 0.5mm sheathed platinum - platinum/rhodium thermocouple replaced the chromel-alumel equivalent.

2) Longitudinal temperature distribution; — In theory the grips should be at the same temperature as the cooling water fed to them and consequently the specimen will be at this temperature where it enters the

grip. When the specimen is heated a temperature gradient exists along its length, from the programmed maximum at the centre to the cold grips. The rapidity with which the temperature falls along the specimen determines how much material can be considered to have been subject to the correct thermal cycle. This temperature gradient was found by setting the controller to hold the specimen mid point at first $785^{o}C$ and then $1250^{o}C$ whilst measuring the temperature at various points along the specimen using a 0.5mm sheathed thermocouple in a blind drilled hole, the results being as shown in fig.38. At $785^{o}C$ using a 20mm gauge length, nearly 2mm of material reached $780^{o} \pm 5^{o}C$ and slightly over 1mm reached $783^{o} \pm 2^{o}C$. With a 25mm gauge length almost 5mm reached $780^{o} \pm 5^{o}C$ and over 3mm reached $783^{o} \pm 2^{o}C$. At $1250^{o}C$ a balance had to be achieved between obtaining a temperature plateau of reasonable length and a cooling rate fast enough to allow the thermal cycle to be followed (see later section). A gauge length of 17mm enabled the required cooling rate to be achieved with a small amount in reserve and at the same time gave 3mm of material at $1250^{o} \pm 6^{o}C$, this amount of error being well within the accuracy quoted for the thermocouples ($\pm 1\%$). Some difficulty was experienced at the higher temperature with thermocouple attachment. Satisfactory temperature reproducibility had been obtained at $785^{o}C$ using the method of thermocouple wire attachment indicated by Phillips, i.e. the platinum and platinum-rhodium wire on the same line, bisecting the grips, but the tips separated by about 0.5mm. At $1250^{o}C$ frequent separation of the platinum wire from the specimen occurred, either due to fracture of wire adjacent to the specimen or detachment of the wire and bead complete. It was found that the first type of failure was caused by excess welding current and the second type by insufficient current. The band of current which gave satisfactory attachment was found to be fairly narrow, and different to that which gave optimum durability for the platinum-rhodium wire. Hence the process of attachment had to be rigidly systemised, including a standard preparation of the specimen

surface immediately prior to welding.

3) Transverse temperature distribution — By inserting a sheathed thermocouple to various depths through the centre of the specimen in the 12mm direction it was possible to check the temperature distribution through the thickness. Accordingly a number of specimens had a 1.0mm blind hole drilled to varying depths to accomodate a sheathed platinum-platinum/rhodium thermocouple, and the output read whilst controlling the specimen at 785°C and 1250°C. The results, shown in fig.39, indicate no skin effects at the specimen surface, the slight temperature drop at the extremities being due to insufficient material surrounding the thermocouple tip.

4) Determination of specimen surface thermal efficiency. The re-designing of the simulator jaws meant that quite long specimens were required (100mm + gauge length) which in turn led to difficulties in specimen manufacture. It was decided that only the gauge length would be machined to the required thickness, (all tests being conducted in this region), the as-rolled finish and thickness being considered satisfactory for the remaining length (0.15-0.25mm oversize). The efficiency of this finish was then compared with other methods of obtaining a close contact with the heat extracting jaws and the results shown in Table IV. As expected a ground surface gave the best heat transfer but machining difficulties due to the nature of the material precluded such a finish on large quantities of specimens. The as-rolled surface is quite rough resulting in poor heat transfer. Two methods were used to overcome this problem, firstly aluminium foil was wrapped around the end of the specimen before loading in the grips. When the holding load is applied the foil is compressed into the surface imperfections to give a smoother effective surface, resulting in a 25% increase in the rate of heat transfer. To ensure that the foil was adequately filling the imperfections an extra layer of foil was added, but as the cooling rate fell it was decided that

practical problems in applying a double wrapping more than outweighed any improvement there may have been in refining this technique. The second method of improving the surface finish was to briefly linish the surface (i.e. with a rough polishing medium), and this reduced surface asperities to a level of uniformity which enabled fairly efficient heat extraction. No significant improvement was achieved surrounding the linished finish with aluminium foil and hence it was decided to standardise on linishing the specimens and loading straight into the grips. All cooling rates required for the investigation could be achieved with this surface finish.

5) Measurement of maximum cooling rate. — Depending on the plate thickness and welding process used cooling rates of up to 100°C per second can be experienced initially by heat affected zone material which reaches more than 1000°C. Although cooling rates of this magnitude can be easily programmed on the simulator, the actual rate of heat extraction from the specimen is limited by the capacity of the copper grips to remove heat. The cooling rate which may be achieved is governed by three factors;

a) specimen gauge length;

b) peak temperature;

and   c) specimen cross-section.

As this last factor is governed by the grips available only the first two were considered as variables. It is known that gauge length influences cooling rates to a much greater extent than cross-section [42], the fixed grip size was not therefore considered to be a great disadvantage. Previous metallographic studies had indicated peak temperatures of 785°C and 1250°C to be of interest, and hence it remained to vary the gauge length when cooling from these peak temperatures to determine the cooling rate versus gauge length curve. These were obtained by heating the specimen to the required peak and then switching off the heating current. The resulting natural specimen cooling rate due to the water-cooled jaws was

monitored by a 0.5mm sheathed thermocouple in a blind hole at the specimen centre and displayed on a pen recorder. The results are shown in fig.40, and indicate that gauge lengths of 17.5mm and 25.0mm are suitable for the respective peak temperatures of $1250^{o}C$ and $785^{o}C$ with a sufficient safety margin to allow controlled rather then natural cooling.

6) Eurotherm optimisation. — After ensuring confidence in the temperature readings being accurate and consistent it remained to ensure that the desired programs could be accurately followed. The accuracy with which the program on a Data-trak chart is followed depends on the settings on the 'Eurotherm' three-term control system. There are five control settings which briefly perform the following functions;

(i) Proportional control (X_p) – this controls the size of the bandwidth around the control temperature. If the temperature stays within the band the power is always on, the amount of power depending on how close to the lower end of the band the temperature is, i.e. at the lower end 100% power, at the mid-point 50% power etc. If the bandwidth is too narrow the power switches completely off and on frequently.

(ii) Derivative (D) – this considers the speed at which the temperature is changing and tries to anticipate in advance the power required if the temperature continues at that rate of change.

(iii) Integral (I) – this is capable of moving the entire bandwidth around the set point so that the power delivered according to the proportional setting will just compensate for any losses. Each point on the setting refers to an 'integral time' – if this is too short the band moves too rapidly and an on/off situation results, but if it is too long the band movement is sluggish and overshoot occurs.

(iv) Alarm control (L) — this controls the amount of deviation
(as a percentage of the total span) of the true temperature
from that desired before compensation occurs.

(v) Power control — this controls what percentage of the power
available can be used on maximum demand.

By trial and error it was found that the most suitable settings for each
peak temperature were:

	I	D	L	X_p	P
785°C	1	3	6	20%	100%
1250°C	3	3	4	5	100%

Examples of the simulated structures obtained are shown in figs.
41-49. The 785°C area could be distinguished in the real weld by dark
etching bands. This enabled highly accurate definition of the peak temp-
erature set, as when the peak is slightly too high the specimen etches
with two dark bands which have just separated (fig.50). The thermal cycle
of each specimen was monitored during simulation by means of a Rikadenki
chart recorder. This enabled the accuracy of heating and cooling rates to
be checked and the actual peak temperature measured; in general this was
within ± 4°C at 785°C and ± 7°C at 1250°C, these being within the quoted
accuracy for Pt-Pt/Rh thermocouples. A further guide that the correct
microstructure was being simulated was achieved by conducting microhardness
checks on the specimens. By comparing the hardness of simulated specimens
with the hardness of the area of interest in the real weld it was possible
to ensure both the required microstructure and consistency between speci-
mens. Specimens were simulated, commencing in either primary hardened or
overaged 550°C conditions as is normal welding practice, in sufficient
quantities to allow three fracture toughness tests and two tensile tests
to be carried out for each selected condition. A number of specimens were
also simulated to allow metallographic examination.

It is known that the major parameters in thermal simulation are the peak temperature attained and the heating and cooling rates experienced in cycling to that temperature. Accordingly a further number of specimens were simulated to the same peak temperature but at different heating and cooling rates; these thermal cycles were determined by use of a computer program specially designed to predict temperature distribution.

3.3.2. Computed Thermal Cycles.

Due to burn-off of the embedded thermocouples during welding no actual record of the thermal cycle to the 1250°C peak was obtained. To overcome this it was either necessary to obtain an approximation by use of the Welding Institute data [61], or use one of the many computer programs devised for this purpose. A copy of such a program by Westby [64] was obtained and work commenced to adapt it for use on the university ICL 1500 series computer. Due to the re-iterative nature of the program very long run-times result. A full description of the modified program and typical print-out are shown in the appendix. Comparison of the computed peak temperature with actual temperature at any cross-section during the MIG weld shows increasing variance as the distance from the fusion line increases (fig.24). This may be influenced by the backing plate acting as a heat-sink during welding, this consequently reducing the subsequent cooling rate. By comparing peak temperatures rather than cross-section it was possible with adjustment of the material thermal constants and welding process efficiency to obtain reasonable agreement with the 785°C cycle. The same print-out was then used to establish the thermal cycle which just reached 1250°C and this used for the second set of simulated specimens (fig.56).

Subsequent work to establish the effect of heating and cooling rates involved further use of this program. This was simply achieved by altering the welding speed whilst keeping the remaining conditions constant, increasing the speed reducing the heat input per unit length

resulting in faster heating and cooling rates at a cross-section much closer to the weld centre-line. It was not possible to simulate a cycle with increased heating and cooling rates to 1250°C, the original cycle being already very close to the limit of capabilities of the simulator.

3.4. Fracture Toughness and Tensile Properties of Weld Heat Affected Zones

Introduction

Earlier work on the hardness of the weld HAZ's indicated that the region where mechanical property variations could be expected were those corresponding to approximately 785°C and 1250°C. It was therefore decided that these areas would be rigorously investigated to measure the effect on properties (especially fracture toughness) by employing both real and simulated HAZ's. By reference to the microhardness surveys conducted it was possible to locate notches fairly accurately in areas of interest to enable fracture toughness tests to be carried out on the real MIG welds.

By combining actual measurements and computed cycles the thermal history of these areas could be determined, hence allowing simulation of an identical MIG cycle (fig.56). Due to material limitations actual welds were conducted on air-melted plate alone, but simulated specimens included vacuum remelted stock. The pre-weld treatments employed were those recomm-ended for plate to be welded, i.e. primary hardened (1050°C + 850°C) and overaged 550°C conditions. Specimens were simulated to 785°C and 1250°C peaks and then half of the former were sub-zero transformed at -78°C to quantify the effect of austenite in the microstructure. Specimens were

finally divided to allow testing of as-cycled conditions and the standard post-weld ageing treatments (at 450°C, 550°C and 620°C).

Conventional methods were used to determine tensile properties but the high toughnesses encountered meant that a great deal of time had to be devoted to the techniques of the three test methods tried, namely clip gauge testing, photographic calibration and stretch zone measurement.

3.4.1. Specimen configuration.

The size of specimen which could be employed for fracture toughness testing was to a great extent dictated by the physical capabilities of the thermal simulator. As the thickness of the specimen increases the heat flow during cooling becomes non-uniform and slow, especially in materials with poor thermal conductivity (such as stainless steels). This either results in non-uniform microstructures or non-programmed structures. Based on the experience of previous investigators the simulator jaws were designed for a specimen thickness of 6mm, which automatically determines a width of 12mm if the specimens are to conform to the dimensional ratios recommended for single edge notch bend (SENB) specimens in the British Standard for Fracture Toughness Testing (DD3). Specimens were cut from 6mm (nominal) FV520B plate in both longitudinal and transverse orientations (fig.57). The simulated specimens were notched on the line of peak temperature, this being visible by the remnants of the control thermocouple wires used during simulation. The notch was milled to a depth of 3mm, being 1.5mm wide, and of 60° included angle. To obtain approximate crack/width (i.e. a/w) ratios of 0.5 a further 3mm of crack depth was obtained by fatigue cracking. Using an Amsler Vibrophore fitted with a two ton dynamometer and a three point bend beam of 48mm span (fig.58) the specimens were cracked in four stages of reducing load (5, 4, 3 and 2kN amplitude). This was necessary due to the considerable time needed to re-initiate crack growth after lowering the load. For each specimen it was ensured that the last 1.2mm of crack growth occurred in at least 50,000 cycles.

The fracture toughness testing was carried out on an Instron Universal testing machine utilising a similar three point bend fixture and constant crosshead movement of 0.2mm per minute. A number of tests were conducted on a specially manufactured rig attached to the Mand simulator (fig.59). Whilst being satisfactory in all other respects this machine was only capable of crosshead movement in discrete steps and hence to avoid any inconsistencies testing was confined in later stages to the Instron. Support knife edges designed to roll apart in loading should be used to minimise friction effects but such a set-up would not allow mounting of a clip gauge and knife edges, essential for many of the tests. Frictional effects are difficult to quantify in three point bending, but as the specimens were small these effects would also be small and constant, hence the use of the Amsler beam was decided upon.

Fracture toughness could then be measured in a number of different ways, three separate techniques of COD measurement and calculation being employed (photographic calibration, clip gauge and stretch zone) and a further parameter, the J contour integral being measured.

3.4.2. Photographic calibration.

Specimens with nominal a/w ratios of 0.480, 0.500 and 0.530 were prepared in each orientation. These specimens were marked with a parallel series of microhardness indentations 0.05mm each side of the fatigued crack tip as shown in fig.60. Where the tip of the crack was not immediately obvious a short electrolytic etch in mixed acetic and perchloric acids was used to polish the area. While testing was in progress a record was made of load against time on the Instron chart recorder. A photographic record of each calibration specimen was made using a 35mm single lens reflex camera fitted with a microscope attachment instead of the normal lens (fig.61). The microscope was fitted with a x5 objective and a x10 eyepiece to give a total magnification of x50. This was found to

be the most satisfactory combination as higher magnifications resulted in a very shallow depth of field with the result that the slight specimen movement during the test was enough to require continual adjustments to the focus, a process made more difficult by the weight of the camera. In addition the smaller field of view at higher magnifications meant that the crack tip quickly moved out of view as the test arm descended. There would have been very little increase in accuracy at the greater magnifications as it was still possible to measure the crack opening displacement to 0.0025mm with the set-up used. Photographs were taken at approximately thirty second intervals during the test, using a cable release to avoid camera vibration, and marking the chart at each photograph. A dual source of illumination was used to provide light, consisting of an opthalmic spotlight to enable focussing to take place and a rapid recycling electronic flashgun for the actual photographic exposure. Trials were carried out with the flashgun at varying distances and angles to the specimen to determine the clearest image. The most suitable arrangement was found to be at 45° to the camera and specimen in the horizontal plane, and elevated by 30°. Using film with a speed of 125 ASA a flashgun with a guide number of 30 (at 25ASA) needed to be positioned 100mm from the specimen. After developing, the negatives were enlarged to give a total magnification of two hundred times normal, the projected image being measured directly on a white easel. With some specimens gross deformation occurred by means of a 'plastic hinge' which tended to obliterate the indentations at the actual tip (fig.62). In these cases extrapolation of the visible indentations was required to find the displacement at the extreme crack tip. As the specimen was invariably well beyond general yield when this occurred no inaccuracies were introduced, but the figures obtained did help to establish the general shape of the calibration curves. Each measurement gave the value of the crack opening displacement during the test and had

to be correlated to its offset plastic displacement by reference to the chart record. The offset plastic displacement was found by drawing a straight line along the initial portion of the chart record and then measuring the distance to each calibration point parallel to the time axis (fig.13). A calibration curve was then drawn for each of the two types of specimen (figs.63 & 64). Several curves were obtained for each specimen type each being for a different ^{a}/w ratio. The closeness of the curves indicates that crack length does not have a large effect within the normal range of experiment (approximately 0.48-0.52 ^{a}/w ratios). After calibration testing was conducted by simply breaking the specimens in three point bending without any form of instrumentation. A load-time trace was obtained from the built-in Instron chart recorder and the offset plastic displacement at crack initiation and maximum load measured. After determining the crack length before testing with a travelling microscope a COD value was obtained by reference to the calibration curves. (Table $\overline{V}$).

3.4.3. COD measurement.

The technique used was that recommended by the draft British Standard for COD testing (DD19) [94]. The clip gauge was manufactured to the specification within that standard, employing 'Welwyn' strain gauge type EA-05-125C-350. Detachable 'saddle-type' knife edges were made to the drawings contained in DD3 [76], these being employed to mount the clip gauge onto the bend specimens (fig.65). The specimens were loaded in three point bending on the Instron testing machine using the Amsler beam as described previously. The output from the clip gauge was fed through a Bryans C92 transducer amplifier unit to a Bryans X-Y plotter. The sensitivity controls of the plotter were adjusted to give a specimen trace with initial slope of 60° (the actual slope depends on the specimen compliance, which in turn is highly influenced by crack length). When the initial conditions were established calibration of the clip gauge could take place

to determine the range over which the output was reasonably linear (fig.66).
Any very slight non-linear behaviour was due to instrument amplification
effects, these being eliminated by consistently starting the trace from
the same point on the plotter X axis. Calibration was achieved by compres-
sing the arms of the clip gauge at the tip with a micrometer and then
noting the chart deflection for a given increase in clip gauge opening.
For actual specimen testing the detachable knife edges were mounted equi-
distant each side of the notch with a total separation approximately equal
to the value at the lower end of the linear portion of the calibration
curve. The calibration was checked at the beginning of each testing session
and every tenth specimen thereafter. From the curves obtained the output
at crack initiation and maximum load (ignoring stable crack growth)
was converted to clip gauge opening. This value was substituted into
the DD19 equation to calculate COD and the results shown in Table VI.

3.4.4. Stretch Zone Width.

Although it is possible to estimate stretch zones microscop-
ically on mounted and polished specimens measurement is far more accurate
if a reasonable portion of the zone can be examined in plan. This is due
to the intermittent nature of some stretch zones, where either an average
value is taken or short missing sections are ignored (figs.68-70). To
facilitate measurement and at the same time allow fractographic examination
of the fracture surface, broken specimens were viewed using a Cambridge
Stereoscan scanning electron microscope (figs.71-80). To ensure that the
full stretch zone width is measured it must be examined whilst normal to
the electron beam. This was achieved by eye judgement when loading the
specimen and final fine adjustment of the specimen stage whilst viewing
the electron image. At the same time deviations from the centreline
of the crack could be observed and these excluded from the experimental
determination. Any errors resulting from misalignment of the specimen
are related to the cosine of the angle of error and hence are extremely
small; a 10° error in alignment causes an error of only 1.5% in stretch

zone measurement. The amount of error is small in relation to the spread of results obtained (Table VII).

3.4.5. J Contour Integral

J values are an estimate of the work done in initiating fracture and hence can be measured from the area beneath the load—displacement curve obtained during testing. Convenience of testing is greatly improved if values can be obtained from the load-clip gauge opening traces obtained in plane strain fracture toughness testing and COD testing, thus facilitating comparisons on the same specimens between testing techniques. Sumpter [111] has shown that the relationship between clip gauge opening and load point displacement is essentially linear and suggests a J estimation procedure for load-clip gauge curves. Dawes [113] has simplified this procedure and this analysis was used to estimate J values in this investigation. Basically the curve is reduced to a straight sided trapezium by careful substitution of linear sections. The area of a trapezium is relatively easy to estimate. Of the various values necessary in Appendix 3 of reference [113] further simplification was employed where possible. Hence by substituting $^a/w$ values of 0.45, 0.475, 0.5, 0.525, and 0.55 a curve was drawn of values of q, and intermediate values of $^a/w$ interpolated. To eliminate the effect of varying yield point values introducing error into values of q_2, this value was obtained from the equation

$$q_2 = \frac{W(V-\delta)}{a+z}$$

where V and δ are clip gauge and crack tip openings respectively, these values being obtained in the simultaneous COD test. Providing that the linear relationship of load point displacement and clip gauge opening holds, actual values of displacement are not required. Values were calculated for the high temperature structure specimens and vacuum remelted parent plate, the results being shown in Tables VIII and IX.

3.4.6. Crack detection

Early attempts at detection of crack advancement, the critical value of COD, concentrated on the use of ultrasonics. A 60° transmitter-receiver probe was clamped to a specimen and the output read from the screen of a Solus-Schall ultrasonic detection unit. The probe was found to be highly sensitive to its position in relation to the specimen notch, even small misalignments resulting in the probe missing the reflected beam. To overcome this a simple cardboard jig was constructed which located in the specimen notch and accurately positioned the probe. A number of specimens were tested and when an indication of crack growth was obtained the load was immediately relaxed. The specimens were then etched while immersed in an ultrasonic cleaning bath, thus ensuring that the etchant reached the tip of the crack. After subsequent immersion in liquid nitrogen the specimens were quickly broken open. It was then possible to measure the extent of fibrous fracture propagation during testing by use of a travelling microscope, the relevant area being the etched portion between the fatigue crack and the unetched fibrous fracture. Results showed that it was not possible to detect crack advancement of less than 0.25mm, a disappointing figure when compared to values of less than 0.1mm obtained with electrical potential set-ups. [121].

In the light of this equipment was purchased which would allow crack detection by monitoring the change in potential which occurs across the crack when advancement occurs. The equipment is shown situated on a mobile trolley in fig.59 and illustrated schematically in fig.14. Current, supplied by a Farnell power pack was fed to the specimen by copper clamps as shown in fig.81. Fine platinum wires were micro-resistance spot welded to the top (notched) surface of the specimen, diagonally opposed each side of the notch. The output through these wires was backed off to a very low value using a Time Electronics D.C. Millivolt Calibrator and the remaining

output fed to a Tekman millivolt recorder-amplifier set to its most
sensitive scale (50 microvolt). During testing there was an initial rise
in the curve as the crack faces separate, followed by a reasonably linear
portion. The change in slope which occurs when crack propagation occurs
was fairly evident in most cases (fig.82); however in exceptionally tough
specimens it was very difficult to estimate this point, a gradual curve
being obtained. The definitive nature of the curves obtained decreased as
toughness increased, being of least value when needed most, i.e. when it
was impossible to estimate a critical event from the load-clip gauge trace.

3.4.7 Summary of results

The large number of results obtained during this investigation (shown
in Tables V-XII) are a consequence of having five variables to account for,
i.e. pre-weld heat treatment, plate type, peak temperature attained, post-
weld heat treatment, and testing method.

a) pre-weld heat treatment; parent plate and simulator specimens were
heat treated to one of the two conditions recommended by the manufact-
urer, i.e. primary hardened (solution treated + two hours at $850^{\circ}C$)
or overaged $550^{\circ}C$. This variable is shown in the results tables as
the main vertical subdivisions.

b) plate type; parent plate was obtained as either air-melted or vacuum
melted stock. The former was supplied in sheets large enough to
obtain test specimens both parallel and longitudinal to the rolling
direction. This effectively gave rise to three plate types, longitud-
inal airmelted, transverse airmelted and vacuum remelted; this variable
is shown in the results tables as the main horizontal divisions.

c) peak temperature attained; as previously discussed two regions were
deemed to be of interest, those experiencing peak temperatures of
either $785^{\circ}C$ or $1250^{\circ}C$. Both simulated specimens and the relevant
areas of weld runs were tested and separate results tables used for

each peak.

d) post weld heat treatment; the presence of austenite was important in specimens cycled to 785°C and hence half of these were sub-zero transformed at -78°C immediately after the welding thermal cycle. This variable is shown as the vertical subdivisions in the results tables. Specimens could then be tested without further heat treatment or after heating to one of the three standard ageing temperatures (450°C, 550°C and 620°C). These appear as the four horizontal sub-divisions in the results tables.

e) fracture toughness testing method; five different methods of determining the fracture toughness of simulated specimens were employed, being COD by photographic measurement (Table V), COD by clip gauge (Table VI), K (Table VI), COD by stretch zone measurement (Table VII) and J (Table VIII). The results of similar determinations on parent plate and welds are listed in Tables IX and X respectively. For comparison purposes selected values of these results are compounded in Tables XI and XII using clip gauge COD as a basis, this being the most commonly used test.

A similar layout scheme was used for the tensile testing results shown in Table III.

4. DISCUSSION

The findings of this investigation will now be discussed in more and the implications of these reviewed. Initially the findings in relation to FV520B parent plate are analysed in terms of microstructure and body of new data obtained relating to mechanical properties. The effect of welding heat on the metallurgy of FV520B is analysed in terms of the resulting microstructures and some areas of unexpected response delineated, with regard to their further investigation. The validity of the simulation technique is discussed from the aspect of microstructural similarity together with the assistance provided by this technique in ascertaining the micro-processes taking place during welding.

A further check on the validity is then provided by comparing the fracture toughness values obtained from real and simulated microstructures together with any changes in tensile properties which have occurred. The general levels of HAZ fracture toughness are subsequently discussed in relation to the values obtained from plate experiencing standard heat treatments, and the practical significance and implications of these results examined. Finally the success of the various fracture toughness parameters in denoting 'toughness' is considered together with practical difficulties which arise both in their measurement and in the correlation of parameters.

4.1 MICROSTRUCTURE, FRACTURE TOUGHNESS AND MECHANICAL

PROPERTIES OF FV520B PARENT PLATE

Whilst it is possible that the strength of FV520B is derived from a number of contributory precipitating phases, including possible Laves phases, two have been identified positively, Nb(C,N) and ϵ - copper. The very fine particle size precluded visual identification but fig. 17 shows that a carbide precipitation is present. Extraction replicas (fig. 19) show very fine carbide precipitation within grains with widely spaced coarser precipitates. Heavier precipitation occurs along the grain boundaries, and there is evidence of what may be fine columnar carbides growing for a short distance perpendicularly away from the grain boundary. The average grain size is approximately 0.002mm with the largest spherical precipitates being an order of magnitude smaller for the over-aged 620°C condition; in addition there are indications of a cell sub-structure forming. The diffraction pattern shown in fig. 19 is only one of a large number which provide correlation beyond coincidence with the 'd' spacings of NbC and NbN (Appendix II).

Fig. 42 shows two other types of precipitate which were found, being either block-like or acicular in morphology. The latter showed needles with aspect ratios of between 5:1 and 12:1. The diffraction patterns obtained from these areas were less distinct than those from the Nb(C,N) but there does seem reasonable proof that there is ϵ - copper (Appendix IIa). The angular block precipitates remain unidentified; it seems unlikely that they are another carbide as the ratio of Nb:C in FV520B is almost exactly stoichiometric, leaving little free carbon. This also leaves unanswered the question of what reduces the stacking fault energy to the extent that appreciable twinning occurs (fig. 18); both carbon and copper could be responsible but it appears that most of these elements are precipitated. The twins are distinct from the lath structure

which may be seen in fig. 18d; here the laths are beginning to break up into a sub-grain structure. Large indistinct areas appear in these transmission electron micrographs due to the very high density dislocation tangles. These tangles and the very fine grain size endow FV520B with both high strength and toughness by resisting dislocation movement and crack advance.

Parent plate fracture toughness values (COD, δ_i) range from 0.040 - 0.076mm for air melted plate and 0.069 - 0.081 for vacuum remelted plate. The improvement obtained by using vacuum remelted material is only marginal as tested but it is anticipated that test specimens in the transverse orientation would be very similar to longitudinal specimens and in this respect would be significantly superior to air melted stock. With fewer inclusions more strain must occur before ductile necking can occur between them; in transverse air melted material they are already bought into reasonable proximity by the rolling process. As was expected the general trend was for the fracture toughness to increase as the ageing temperature was raised; the higher ageing temperatures allow more recovery of the structure and the coarser precipitates allow easier dislocation movement. The lowered yield stress results in a larger plastic zone to spread the load and hence a larger COD. Comparison of these results with other workers is difficult. The only values of δ_i quoted are those by Baker [137] and these are considerably larger (0.2mm); the results are not comparable however due to differences in test temperature and specimen geometry.

The fracture toughness values obtained from parent plate are shown in Table IX. Comparison of air-melted and vacuum remelted specimens of the same orientation shows that the latter displays COD values at least 50% greater when considering new crack growth; the values obtained for COD at maximum load show that an improvement in excess of 100% is obtained. This would appear to emphasise the beneficial effect of removing

inclusions from the material to increase toughness. Comparison of scanning electron micrographs of fracture surfaces obtained for air melted material (figs.78,79) with those obtained for vacuum remelted plate (fig.80) illustrate clearly the difference in cleanliness. Elongated stringers of manganese sulphide are visible in large quantities in figs.78a, 79a, 79b and 79c. These give rise to enlarged areas of essentially flat fracture with little energy being absorbed. Equally large numbers of spherical inclusions of the same constituent can be seen in the same figures, these spheroids growing to quite large dimensions in places (fig.78b).

The way in which the manganese sulphide is extruded and broken up during rolling can be seen in figs.78a, 78b, 79b and 79c; hence a 'ladder' type of fracture surface is produced as a string of inclusions causes an enlarged void around each particle. The lack of ductility of thes inclusions points to a compound sulphide, possibly MnS with high Cr content. A third type of inclusion is also visible in fig.78c; these have the appearance of rod-like angular particles and are associated with a large area of flat fracture. Immediately adjacent to this flat area the crack shows a substantial change of direction; it is possible that the angular particles are associated with a grain boundary and the change in crack direction represents deviation along the boundary. Figs 78b and 79c also show areas of what is possibly a softer phase; the fracture surface is much smoother and of significantly different orientation.

Vacuum remelted specimens exhibit fracture surfaces which are radically different. Material aged at $450^{\circ}C$ (fig. 80a) is unique in this investigation in displaying cleavage. The yield strength has been raised to such a high level that only localised yielding occurs just below the notch before tensile stresses have built up to such a level that cleavage can occur. The lower yield strength after ageing at $550^{\circ}C$ (fig.80b) leads to a surface consists of fine dimpling with occasional inclusions leading to

larger cusps. The general void diameter for vacuum remelted specimens is much smaller than the average for air melted specimens; the greater amount of work done in the ductile necking which takes place during microvoid coalescence results in the superior toughness of the vacuum remelted material.

The fracture toughness values (Table IX) for the vacuum remelted plate show a difference of approximately 10% between specimen orientation when considering initial crack extension; an improvement of 50% is obtained when considering COD at maximum load comparing longitudinal to transverse specimens. The familiar relationship of decreasing toughness with increasing tensile strength is displayed, the toughness increasing with ageing temperature. Very little difference existed between the specimens aged at 550°C and 620°C in the longitudinal direction; all specimens in this orientation were particularly notable for the extremely high values of COD at maximum load, this fracture toughness criterion giving good consistency of results for the parent plate. Using the J contour integral, interestingly the 550°C specimens showed the best toughness; obviously on a work done to fracture basis the combination of high toughness with moderate strength gave the highest productive figure. The J values obtained also demonstrated a similar difference of approximately 10% between specimen orientations.

A wide range of heat treatment combinations were carried out on the air melted plate prior to COD testing (Table IX). From these results several conclusions may be drawn. With respect to the conditioning heat treatment at 850°C or 750°C better toughnesses (on an initiation basis) are obtained by employing the latter temperature; this is due to the m_s temperature being raised less at the lower temperature and so a less complete transformation to martensite results. The improvement obtained decreases as the ageing temperature increases although the actual value of toughness rises. Ageing at 620°C eradicates any effect of differing conditioning temperature.

From Table IXa it may be observed that the conditioning treatment at $750/850^{\circ}$C makes an important contribution to improved toughness. Direct

ageing of a martensitic matrix (treatments 4,5,11 and 12) results in lower values of δ_i in comparison to conditioned specimens. The effect is more exaggerated in the sub-zero treated testpieces. Sudden crack advance occurs with little ductility being exhibited; this is particularly marked after ageing at $450^{\circ}C$ where initiation and maximum load COD values coincide, although ageing at 620° does restore the latter to a more acceptable value. Although refrigeration raises initiation COD it exhibits the properties more usually associated with brittleness; on this basis the results are the opposite of those which may be intuitively deduced. The fine ferrite carbides which result from the conditioning treatment obviously play a significant part in increasing the toughness. This is probably the result of the initiation of very fine ductile dimpling allowing gradual crack advance whilst absorbing much of the work done.

The general toughness of the air melted material rises as the ageing temperature is increased; the increase obtained by raising from $450^{\circ}C$ to $620^{\circ}C$ is proportionally greater than in vacuum remelted material. This is more likely due to a lowered value after ageing at $450^{\circ}C$ due to the high inclusion content; after ageing at $620^{\circ}C$ the matrix is sufficiently ductile to minimise the effect of inclusions. The COD values of transverse specimens of air melted material are considerably lower than those obtained from vacuum remelted. Initiation COD's are approximately 65% of the vacuum remelted value while maximum load COD's average only 45%; the large difference in the latter case is no doubt due to the high uniform ductility exhibited by vacuum remelted material.

The values of tensile properties of air-melted parent plate are shown in Table III. These demonstrate the inverse relationship between tensile properties and ductility. Little difference exists between the $450^{\circ}C$ and $550^{\circ}C$ ageing treatments with respect to tensile strength, but a useful increase in ductility is obtained with the higher ageing temperature. Even so the ductility exhibited after

ageing at 450°C is quite remarkable in view of the high strength level. Strength shows a marked drop after ageing at 620°C but the best ductilities are obtained.

It may be concluded that the fracture toughness (COD, δ_i) of FV520B plate varied from 0.040 - 0.076mm for air melted plate and 0.069-0.081mm for vacuum remelted plate depending on heat treatment condition and orientation to the rolling direction. In general fracture toughness increased progressively as the ageing temperature increased from 450° to 620°C.

Aston University

Illustration removed for copyright restrictions

4.2 MICROSTRUCTURE AND HARDNESS OF THE WELD HEAT AFFECTED ZONE

During the course of hardness surveys of the HAZ of trial weld runs it became apparent that two areas showed persistent softness throughout a variety of heat treatments. These regions corresponded to peak temperatures of approximately 785°C and 1250°C and further efforts were directed towards establishing the cause of these effects.

4.1.1. Low Temperature Microstructures

Inspection of the weld hardness plots (figs.25-28) show that the as-welded plate has reasonable gradation of structures, the only notable deviation being found at 7-8mm from the fusion line (measured along the plate centre-line). This coincides with a band of carbide precipitation — (fig.31)-and hence may be assumed to be related. The temperatures experienced in this region are those where rapid carbide precipitation would be expected but below that at which the particles start to re-dissolve. The effect of subsequent ageing shows a much greater variability appearing, this being concentrated into two main regions, a high temperature region approximately 3mm from the fusion line, and a broader region experiencing a lower temperature between 9 and 12mm from the fusion line. This low temperature area is remarkably persistent, the 750° or 850°C conditioning treatments and ageing failing to remove the effect. Even resolution only has limited success. Due to similarity of this effect with that experienced in the nickel maraging steels a similar approach was tried, that of endeavouring to establish the presence of austenite. If local microalloy enrichment occurs the m_s temperature may be sufficiently depressed to be below room temperature. Kaae [34] has measured the 'normal' m_s temperature at 65°C, hence very little further alloying is required to depress this transformation a further 50°C locally. Sub-zero treatment at -78°C for twenty hours appeared to substantiate the belief that extra austenite was being formed. Kaae also measured the m_f temperature at -50°C, meaning that substantial amounts of austenite are dispersed throughout the microstructure. This would also be transformed by treatment at -78°C resulting in a substantially completely martensitic structure. The structures subsequently obtained would hence show a greater hardness and strength throughout all the regions where substantial amounts of austenite would be present. This is borne out by the microhardness surveys where the entire hardness beyond approximately 6mm from the fusion

line is increased (figs.25,28). This increase is maintained after subsequent ageing, the sub-zero and aged 620°C plot being a steady value above that found by direct 620°C ageing.

The effects of the heat treatments are visible macroscopically as shown in figures 51-54. The as-welded structure shows two broad dark etching bands separated by a light etching band. With subsequent ageing the band further from the weld bead contracts in size until at 620° only one band remains. This corresponds with the contraction of the austenite bearing band until it merges with the similar band formed at higher temperatures. Treatment at -78°C completely removes this second band (fig.53b), which would point to this etching effect being due to the austenite. The conditioning 750°C treatment shows that the worst effects of welding are removed but some evidence of their limited presence still remains (fig.54). A trial three-run weld conducted on 15mm plate is shown in fig.55. Here the dark etching bands formed in the first two runs are shown to be removed at the inner edge of the same zone of the third run. This roughly corresponds to the resolution temperature of 1050°-1100°C and shows that any effects of segregation are minimised by the refining effect of subsequent runs. Figs.51-54 also show the great amount of segregation which occurs on the centre line of the plate; this is also visible on a microscopic scale as a ferritic veining tending to follow prior austenite grain boundaries.

The microstructure of this region is very diffuse making features difficult to identify (fig.43). The general structure is of tempered martensite intimately diffused by a lighter etching phase. Efforts to identify this as discrete amounts of austenite by X-ray diffraction were unsuccessful in the limited time available due to the highly directional nature of the rolled plate. Nearly all of the small spherical particles visible are less than one micron in diameter making determination of the constituent elements impossible except by electron metallography.

Very little of note can be further distinguished in specimens simulated to 785°C (figs.41 a - d'). Patches of a light etching phase appear in substantial amounts (fig.41a) which become reduced in size after sub-zero treatment (fig.41b). This again leads to the conclusion that this phase is austenitic in nature. Further ageing at 620°C for two hours leads to an increase in this phase, consistent with the formation of fresh austenite which is known to form at this temperature, together with a diffusing of the general acicular martensitic structure. Little differentiation can be made between air-melted and vacuum remelted materials except that marginally more of the light etching phase occurs in the former and on a coarser scale (fig.41).

4.1.2   High Temperature Microstructures

Immediately adjacent to the weld bead the microstructure shows the features usually associated with temperatures close to the melting point. The 'veins' evident throughout the plate before welding appear to have liquated during the welding process (fig.30). These veins stretch a considerable distance into the parent plate on one plane, with very little branching between veins evident except very close to the weld bead. This feature does respond to the ageing process, the veins being considerably coarsened and more diffuse after ageing at 620°C compared to the same microstructure after ageing at 450°C, probably being due to diffusion away of segregated elements. This coarsening of the structure together with more normal grain coarsening slightly beyond this area mean that a very variable hardness curve is obtained, with a tendency to softening at a distance of approximately 3mm from the fusion line where the effects of grain coarsening are worst. A slight improvement in hardness is obtained by the sub-zero treatment (fig.28) indicating the presence of austenite in sufficient quantity to affect the general microstructure, rather than as isolated pools of reverted austenite. Figs.48b and 49b show the grain

coarsening which has occurred during welding. Precipitation has occurred on preferred planes within the grains, being very coarse in some areas. At a number of points there are what appear to be liquated inclusions, the morphology being akin to the similar effect found in the nickel maraging steels [42]. These tend to be associated with grain boundaries, having had a pinning effect during the period of grain growth (fig.49b).

The behaviour of the austenitic region when subjected to subsequent heat treatment can be seen in figs.51-53. As-welded (fig.51a) there is the appearance of a dark etching band close to the weld fusion line. On ageing at 450°C and 550°C (figs.51b and 52a) the width of this band decreases, presumably due to depletion of matrix alloying elements by precipitation, this in turn affecting the stability of any austenite present. Further raising of the ageing temperature to 620°C (fig.52b) is responsible for the re-appearance of fresh austenite throughout the structure, resulting in a generally darker-etching microstructure. Resolutioning at 1050°C (fig.53a) effectively re-establishes a uniform microstructure, this being reflected in a smoother hardness plot (fig.26); the fact that it is not completely smooth is indicative of the fact that austenite formation is only partly giving the structure variability, as previously indicated grain coarsening also plays a part. Treatment at -78°C for twenty hours (fig.53b) has the effect of concentrating the dark etching line and also moving it closer to the fusion line. A similar effect on hardness is obtained as by the resolution 1050°C treatment, i.e. a smoothing of the hardness·plot with a small amount of softening remaining (fig.28), this again being due to grain growth and non-ageing constituents.

In air-melted material there is much evidence of a light etching phase at grain boundaries and triple points. This phase exhibits an angular morphology and exists in far greater profusion in air melted material compared to vacuum remelted stock. Whilst it is possible that liquation of

inclusions may have occurred in a real weld it is improbable that a sufficiently high temperature was reached in the simulated specimens. In these circumstances it is most likely that this phase is delta ferrite. This demonstrates a double benefit of vacuum remelting; not only is the inclusion count reduced, but the compositional control reduces the incidence of the undesirable delta ferrite phase.. Evidence of a twinned structure is visible in the as-welded condition (fig.44b) followed by heavy precipitation during ageing (fig.44a), the light etching areas not responding to ageing. The grain boundaries become more easily defined during ageing (figs.44a and 45a) but precipitation is sufficiently fine to be unresolvable. Again ageing at 620°C leads to a more diffuse precipitated acicular structure and the formation of fresh austenite; the areas associated with the liquated inclusions remain unaffected at this ageing temperature (fig.45b). The prior grain boundary network is much more discernible in the vacuum remelted material, the general structure being 'cleaner' and easier to resolve (figs.46,47, and 49a). Grain boundary precipitation is much more intermittent in the as-welded condition, giving the appearance of resolvable particles of carbide (fig.49a). Precipitation within the grains is concentrated within the dark etching zones where the shear transformation to martensite has taken place, precipitation occurring on preferred planes within the grain (fig.49a). Ageing at 450°C coarsens the grain boundaries (fig.46b) and precipitates within the grain on selected planes (figs.46a and 46b). Again a small amount of light etching ferrite can be seen at triple points. Ageing at 620°C gives rise to easily resolvable precipitates up to 0.7 microns in diameter (fig.47). These predominate within the grains on the martensite habit planes and are part of a general coarsening of the entire precipitate structure.

Further investigation of the microstructure after cycling to 1250°C involved more use of the transmission electron microscope. A number of

thin foils were produced but the results obtained proved inconclusive. Extraction replicas were made by the process described in section 3.1.1. and examples of typical microstructures obtained are shown in fig. 42. These show the features which may have been anticipated from the influence of high temperatures, i.e. grain growth and coarse precipitation. The grain size is larger than the field of view, even for the lower magnification photograph , being measured at an average value of 20-30 μm. Fig. 42a shows that the average spherical precipitate has grown to about 0.25 μm and become more numerous compared to correctly aged material. The polygonal particles visible are unidentified. It is unlikely that they are chromium carbides as thermodynamically niobium carbide is favoured. However the addition of niobium does encourage the formation of a chromium-rich carbide of the type M_2X, where X can be carbon or nitrogen; in addition niobium will form Laves phases with iron or manganese.

These findings would appear to confirm the preliminary analysis of Kaae [34] with regard to the general microstructural effects and to further extend the knowledge of mechanisms operating. The main precipitate has been identified and the reactions of the precipitates to welding and subsequent heat treatment has been identified. In addition the weld surveys conducted have delineated areas worthy of further investigation.

Hence in conclusion it can be assumed that the two regions of reduced hardness in the weld HAZ of FV520B, corresponding to peak temperatures of approximately 1225-1275°C and 730-810°C, are due in the former case to structure coarsening and δ-ferrite formation and in the latter to austenite formation.

4.3 VALIDITY OF THERMAL SIMULATION

Before any conclusions can be drawn regarding microstructural and mechanical features of simulated specimens the validity of such an approach must be established. A certain amount of difficulty is naturally encountered as real weld heat affected zones have microstructures compressed into narrow bands making resolution difficult. However notwithstanding these limitations very good correlation appears to have been achieved. As discussed previously the zone which has experienced a peak temperature of 785°C is very fine and diffuse (figs. 43a/b). Within this the general martensitic grain size is unresolvable in either case, but the banding of the structure is more emphasised in the real weld microstructures. The general appearance of both structures is, however, similar and comparable mechanical properties should result from the features discernible.

The microstructure of the zone simulated to 1250°C is much easier to distinguish (figs.48 and 49). Dolby [46] advocates that the most accurate guide for comparison of simulated microstructures with real welds is the prior austenite grain size. Figure 49 shows good agreement in this respect, the simulated microstructure showing marginally greater grain size. Grain boundary precipitation is also slightly greater emphasised in the simulation case, whereas within the grains the relative amount of precipitation is similar. The martensitic microstructure shows a similar degree of coarseness in both cases (fig.48), and both structures show the presence of delta ferrite area up to 4μm in diameter. Again the banded structure is slightly more visible in the real weld although this depends on the specimen orientation. Again the general appearance is such that comparative mechanical results could be expected from both simulated and real microstructures based on discernible features.

Comparison of the results of mechanical testing of both the real and simulated weld HAZ's can be seen by reference to Tables V and X. It was decided that the most accurate way of ensuring that each specimen was of the required microstructure was to employ hardness testing. Once the simulation cycles had been determined specimens were produced and the microstructure compared optically with the real weld HAZ. Hardness tests were then conducted to ensure that they too were comparable, being approximately 350-370H$_v$ after cycling to 785°C, and 370-390H$_v$ after cycling to 1250°C (Appendix III). Such was the reproducibility of the simulator that all specimens did fall within these ranges unless an obvious fault occurred in the cycling programme.

Due to the extremely thin bands of any specific microstructure which occur in a real weld HAZ tensile tests are of a very limited value, showing only the weakest area of the HAZ. For this reason comparison of the tensile properties of real and simulated weld HAZ's is not possible.

Once again with fracture toughness testing, problems exist in confining the crack to the zones of interest. Even if a notch is accurately located there is always a tendency for the crack to run into adjacent areas, of different microstructure, particularly where isotherms are not plane and perpendicular, i.e. close to the weld bead. The broad soft band to material cycled between 730°C and 810°C allowed reasonably easy notch location and the COD results obtained (Table X) compare reasonably well with those of simulated specimens (Tables VIa and VIb). It is notable that where large differences do exist a wide variability in fracture toughness values was obtained, this being particularly so for as-welded specimens. Generally the results were within approximately 15% of each other . Whilst 15% may appear to be a substantial difference it should be viewed in perspective; absolute values of COD being measured were of the order of 0.04-0.10mm resulting in differences generally of less

than 0.01mm although greater variability exists when considering maximum load COD. An equally large difference can result from the equation chosen to measure COD; if both equations are considered to give acceptable results then the correlation between real and simulated HAZ fracture toughness is equally acceptable.

Correlation of real and simulated HAZ fracture toughness is not so good at a peak temperature of 1250°C (Tables.VId and X). Typical values for specimens aged at 620°C are $-\delta_i$, real HAZ 0.045mm, simulated HAZ 0.073mm. This is not entirely unexpected as the microstructure to be examined exists over a very small band, and it is for this reason that simulation was carried out.

Hence it can be said that thermal simulation is a valid method for studying the weld HAZ properties in this alloy; acceptable correlations of microstructure and properties have been obtained for the two peak temperatures of 1250°C and 785°C.

4.4. MECHANICAL PROPERTIES AND FRACTURE TOUGHNESS OF THE WELD HAZ

Comparison of parent plate tensile strengths (Table II) with those of simulated structures (Table III) reveals that in the case of air-melted material the response of HAZ microstructures to simple heat treatment is satisfactory. In all cases the post-weld heat treated structures show a greater strength than parent plate receiving a similar treatment. This effect is particularly emphasised for specimens oriented along the rolling direction. The general improvement due to this mechanical fibring is 5-10% when compared to specimens oriented at right angles to the rolling direction and slightly more compared to manufacturers values for parent plate.

The as-welded structures achieve a strength level intermediate between that achieved by 550°C and 620°C ageing treatments. This is partic-ularly true of low temperature microstructures (785°C) where the proof strength to ultimate tensile strength ratios are similar to those obtained from standard heat treatments on homogeneous parent plate. The 1250°C microstructures reveal radically different behaviour. Longitudinal specimens show lowered proof strengths and raised ultimate tensile strengths (UTS) resulting in a very low proof/UTS ratio. Transverse specimens on the other hand show greatly increased proof strengths with slightly increased UTS giving an overall proof/UTS ratio close to unity.

This latter case is more remarkable in view of the ductility figures obtained. Both the longitudinal and transverse specimens show broadly similar results for elongation and reduction in area, being inter-mediate in value between the results for 450°C and 550°C post-weld heat treatments. The difference in proof strengths may be explained by the mor-phology of any austenite present tending to be present along bands of seg-regation and giving rise to an early deviation from elastic behaviour in longitudinal specimens. However the transverse specimens showed just as

great a degree of elongation, which was not expected from consideration of the yield/UTS ratio. Part of this elongation figure resulted from the greater reduction in area which occurred in transverse specimens, this being the situation that would arise if austenite was present in thin transverse bands.

All air-melted specimens showed a fairly sudden yield to some extent. After yield a fairly long region of elongation at constant load took place. Despite this the ductility figures obtained for as-welded and aged 450°C conditions was much lower than expected. This is particularly so for the as-welded condition, normal elongation figures not being attained until ageing temperatures of approximately 550°C and above are employed. Specimens aged at 450°C showed ductilities reduced by up to 60% compared to comparative figures for homogeneous parent plate. Specimens cycled to 1250°C in both orientations had satisfactory ductility figures after ageing at 550°C whereas the effect of specimen orientation could not be removed from specimens cycled to 785°C. This would point to the fact that a certain amount of homogenisation takes place at this temperature, although it would not be expected that the dominating influence of inclusions would be significantly reduced.

The effect of sub-zero treatment cannot be confirmed as beneficial on the basis of the results obtained. Certainly no detrimental effects were apparent but no consistent virtues could be substantiated. The trends which were discernible were those that would be expected from austenite removal, i.e. increased strength and reduced ductility. The effect on strength and ductility was small for all except as-welded and aged 450°C conditions, and even in these cases the overlap of results reduced the significance. Hence, from a tensile property aspect, the expense of sub-zero treatment cannot be recommended.

Vacuum remelted plate showed HAZ results that were very little

different to those obtained from air melted plate. While the larger 'process zone' associated with widely spaced inclusions substantially improves fracture toughness, the plastic flow properties are not markedly altered. Thus the yield and tensile strengths remain similar to air-melted plate. Actual values obtained during testing gave elongations of up to 33% and reductions in area up to 74%. The area where vacuum remelted material was better was in the manner of elongation, being much more uniform. Air melted material tended to neck and fail suddenly. Differences in tensile behaviour may show using a 'harder' testing machine. The work hardening capacity and general cleanliness of vacuum remelted plate should give rise to good toughness and resistance to catastrophic failure. Stress-strain curves for this material showed a gradual deviation from elastic behaviour with no well-defined yield point; this leads to relatively low values of proof stress with consequent low proof/UTS ratios.

Fracture Toughness   (Tables V-VIII,XI and XII)

4.4.1.   Low Temperature Microstructures.

Significant differences were noted between the orientation of specimens, longitudinal specimens being on average twice as tough as transverse specimens. The longitudinal specimens also exhibited an interesting form of behaviour, as is shown in figs.67 and 72. This took the form of complete separation of the specimen over part of its midsection (figs.67 and 72a). On other occasions this behaviour manifested itself as small individual sites of separation spread over most of the central ('plane strain') area (figs.72a and 72b). This may be explained by considering the effect of the central band of segregation visible in many specimens. During loading a large hydrostatic force is formed at the centre of the specimen; the segregated band, being mainly manganese sulphide and other low strength constituents is relatively weak in comparison to the matrix. The forces set up tend to pull outwards towards the surface of specimen

and when they reach a sufficiently high value the segregated band separates, allowing what is effectively two new surfaces to form. The specimen now behaves as two smaller specimens of half the original width placed side by side. Hence a region of plane stress can form and miniature shear lips form along the new surface areas. These new shear lips are smaller than those at the outside surface as they begin to form later. During testing these specimens gave an audible 'click' accompanied by a sudden drop in load as the new surfaces formed. It is a matter for conjecture as to whether the crack front immediately grew to reach the tip of the new surfaces or whether surface formation was precipitated by stress build-up ahead of the advanced crack. The alternative behaviour of figs.72b and 72c may be explained by the morphology of the segregate; the deep holes parallel with the specimen length (and rolling direction) are consistent with manganese sulphide inclusions strung out during rolling. The large amount of pitting in fig.72b indicates that a large amount of this constituent is present; whether it is dispersed or segregated as a band depends on how it is distributed within the melt.

Examination of figure 71 shows that the general fracture surface is of flattish areas separated by regions of fine microvoid coalscence. This latter feature is a result of void formation around the fine ferrite carbides formed during the heat treatment (fig. 71d). This compares well with fractography of the weld HAZ experiencing the same peak temperature (fig.76). Figures 71a and 76a both show elongated flat areas, caused by stringers, in a parallel direction. Spherical inclusions still attached to cusps are visible in both photographs. Figures 71b, 71c, 76b and 76c all show the granulated surface found on the surface of the cusps. Figure 76c also shows a broken rod-like inclusion associated with the flat fracture area. In comparison the fractographs of vacuum remelted material simulated to the same temperature show a surface which is almost completely microvoid coalescence (fig.73). A slight tendency to intergranular fracture is

conveyed by fig. 73a; this actually is testimony to the extent which the crack has to twist to enable itself to advance, absorbing more energy with each twist. It is possible that the smooth areas in fig. 73b are associated with austenite, while the small number of cusps (e.g. fig. 73c) is a tribute to the cleanliness and low inclusion count of the vacuum remelted material.

Actual values of COD are shown in Tables VIa, VIb, XI and XII. Several conclusions may be drawn from an initial analysis. There would not appear to be any consistent effect due to sub-zero treatment, a similar state of affairs which exists in regard to tensile properties. Although only a small number of specimens of each treatment were tested all specimens, taken as one population, do not show a significant effect due to sub-zero treatment. For instance, transverse airmelted specimens aged 450°C show an increase (from 0.030 to 0.039mm.) while equivalent longitudinal specimens decreased (from 0.058 to 0.049mm.). This applied equally whether primary hardened or overaged, i.e. pre-weld heat treatment had no effect. Evidently austenite is not present in amounts significant enough to affect the fracture toughness greatly.

The general level of toughness was slightly higher for plate simulated in the overaged 550°C condition, although again the effect of this diminished when a 620°C ageing treatment was employed. Generally the as-welded fracture toughness approximated to the value obtained by ageing at 550°C, irrespective of the condition of the plate initially. This investigation shows that there is no significant difference between the fracture toughness of welded plate joined in either the primary hardened or overaged 550°C conditions. While the initial plate condition does not affect the results the final ageing treatment does; predictably in all cases the toughness increases with ageing temperature. This means that there is a drop in toughness from the as-welded condition to the fully hardened aged 450°C condition. This is due to fine precipitation onto the martensite making

dislocation movement difficult; the resulting low ductility leads to a drop in toughness which does not regain the as-welded value until the ageing temperature reaches 550°C. Generally the highest values of toughness were obtained at this ageing temperature, a drop being experienced on ageing at 620°C. Again the results were not entirely conclusive but there does seem to be a definite trend. This may be explained by the growth of precipitates to such a size that dislocations can climb past them very easily with little resistance or absorbtion of work. Additionally the void size will increase and the liklihood of sufficient strain to link voids leads to a drop in toughness.

To examine the effect of the austenite band on fracture toughness a further series of specimens were simulated to a temperature slightly beyond those experienced in the soft region (840°C), and the results shown in Table VIc. These show broadly the same trend of results with respect to initial plate conditions and effect of ageing temperature. However, the scatter of results in triplicate tests, similar to those shown in Tables VIa and VId, preclude any firm conclusions. The small differences, together with small numbers of each specimen treatment meant that this was a problem throughout the investigation.

The effect of varying the heat input was briefly examined and the results shown in Table X. These would indicate that the amount of stable austenite formation is related to heat input. A faster welding speed, and hence less heat per unit length, resulted in slight reduction in fracture toughness, i.e. less austenite formation. Conversely a slower welding speed (more heat per unit length) radically increased the toughness, presumably due to a much greater proportion of austenite. The actual relationship between heat input and fracture toughness is worthy of further investigation.

The crack paths shown in figs.41-43 illustrate the effect of the light etching constituent. This phase is present as large discrete units in the as-welded condition (figs.41a and 4 b). Sub-zero treatment reduces

the size of these particles (fig.41b) but subsequent ageing (figs.41c and 4 a) causes them to grow again. The effect of these areas on crack propagation is most readily shown in fig.4 b, where the crack can be seen to turn at right angles in several places to follow the edges of the light etching phase. This may either be a hard constituent deflecting the crack or a softer phase tearing around the edge. The effect of inclusions acting as stress raisers is exhibited in fig.43a where the crack has turned so that a large manganese sulphide lies in its direct path. Smaller inclusions may be seen along the length of the already existing crack.

Comparison of simulated HAZ values with those of parent plate (Table XII) show that general levels are similar with a slight tendency to be less in the HAZ. This is most marked in transverse airmelted specimens; COD values for these specimens remain fairly constant throughout the treatments. This is due to the dominating influence of the proximity of inclusions, the matrix condition having little chance to affect overall performance.

Generally it may be concluded that the region in the HAZ corresponding to a peak temperature of $785^{o}C$ shows a fracture toughness which is equal to or slightly less than that of the plate in the same post-weld aged condition.

4.4.2. High temperature microstructures

Many of the observations drawn from the low temperature region are equally valid in relation to those found in the higher zone. The fracture toughness values obtained by simulation to

1250°C are shown in Table VId. These again show that there is little sig-
nificant effect of the initial condition of the plate before ageing; the
differences that do exist mainly relate to longitudinal air melted specimens.
The increased strength and reduced ductility indicate that there may be a
reduction in toughness and this is indeed the case. All types of specimens
exhibit reducing toughness at the highest ageing temperatures, an optimum
being reached at 450° - 550°C. In all cases the lowest fracture toughness
value was obtained after ageing at 620°C.

Examination of the fracture surface of the welds (fig.77) reveals a struct-
ure of very broad parallel bands separated by extremely fine microvoid
coalescence. Whilst spherical inclusions and stringers are visible in all
three fractographs there also exist other features, such as the extremely
flat area in fig.77b which does not show cusps at the edge, found when this
feature is caused by inclusions.

Examination of fracture surfaces of simulated specimens (figs.74
and 75) reveals that in the case of the air melted material almost the
entire surface is covered by large voids, originated around inclusions.
The complete absence of fine microvoid coalescence indicates that the
presence of this feature on the real weld HAZ fractographs is due to crack
deviation from the required microstructure; if this is so it would
also explain the variance of fracture toughness values. The simulated HAZ
fracture surfaces also show the 'river bed' feature of parallel 'valleys'
due to the effects of rolled-out inclusions. The inclusion count is
obviously very high but it is significant that the number of large cusps
is reduced; evidently the structure consists of an even dispersion of
moderately sized inclusions, as is borne out by fig.49a. Smooth sided
outcrops of what appear to be a different phase can be seen in figs. 74b/c.

The fracture surfaces of vacuum remelted specimens indicates a much lower inclusion count (fig.75). The areas between inclusion sites comprises of very fine microvoid coalescence. All visible cusps indicate that only spherical inclusions are present; these cause much less stress concentration than angular particles and so reduce the toughness by a smaller amount.

A consequence of the reduced ductility found in these specimens is the greatly lowered values of maximum load COD, especially at the higher ageing temperature. The values follow the same trend as initiation COD's, i.e. reaching a maximum at ageing temperatures between 450°C and 550°C. Several factors contribute to the toughness value, these being the metallurgical features visible in figs.44-48. These take the form of grain boundary precipitation (figs. 46a, 47a and 49a), coarse precipitation within grains (figs. 47 and 49a), delta ferrite (figs. 44a, 45a, 48a and 49a) and grain growth (figs. 46 and 47), this latter factor influencing resistance to cleavage.. It can be seen from figs.45b and 47 that very coarse precipitation takes place at selected sites after ageing at 620°C, although there is no special tendency for these sites to be at grain boundaries. This is a consequence of the precipitation which takes place during welding, the fine carbides acting as nucleation sites during subsequent ageing. This would explain why, with air melted material, the fracture toughness drops with increasing ageing temperature, the coarse precipitates rapidly depleting the matrix of its strengthening alloying elements.

High heat input values (Table X) gave very poor values. Considerable grain coarsening had occurred with a heavy precipitation along the boundaries confirmed by microscopical examination.

Once again Table XII shows that pre- and post-weld heat treatments had marginal effects on COD. The transverse airmelted values were again dominated by the inclusions; the other two types of speci-

men did show some tendency to increase COD values over parent plate.

Hence, in general the region in the HAZ corresponding to a peak temperature of 1250°C shows some increase of fracture toughness over the parent plate in the same post-weld aged condition.

Also, the fracture toughness of the HAZ corresponding to peak temperatures of 785°C and 1250°C in all conditions is virtually identical with plate in primary hardened and 550°C overaged conditions.

4.5   PRACTICAL SIGNIFICANCE OF WELD HAZ STUDIES

The purpose of fracture toughness testing is to relate the results of small scale tests to the prediction of failure in full sized structures. One of the main criticisms of COD testing is the difficulty of applying the results reliably to real life situations; the situation in linear elastic fracture mechanics is much better with established methods of calculating maximum permissible flaw sizes from small scale tests. For this reason the J contour integral was received with enthusiasm; it is the natural extension of K, the plane strain fracture toughness, into the realms of general yielding fracture mechanics.

J is simply related to K by

$$J = \frac{K^2}{E} (1 - \nu^2) \qquad \text{for plane strain}$$

$$\text{and} \quad J = \frac{K^2}{E} \qquad \text{for plane stress}$$

where ν is Poissons Ratio. The relationship of maximum permissible flaw size, a_{crit}, to plane strain fracture toughness is given by

$$a_{crit} = \frac{Q}{\pi} \left(\frac{K_{IC}}{\sigma} \right)^2$$

where σ is the applied stress and Q is a non-dimensional factor expressing the shape of the flaw in terms of its length to width ratio (this being a

measure of the notch sharpness). For an embedded flaw a factor of approximately 1.5 is applicable, and substituting the lowest value of J found in this investigation (19.5 KN.m/m^2) a maximum flaw size of 4mm is indicated at working stresses of 80% of the yield stress. This is based upon the yield stress of the HAZ metal; if the working stress is limited to 80% of the yield stress quoted for the parent material (which would be the case in practice), then the critical flaw size is increased to 11mm. This is well within the capabilities of modern methods of non-destructive testing, such as radiography and ultrasonic testing. Hence it is feasible to use such a technique in a quality control mode, passing or failing fabrications according to the defect size.

This situation represents the worst possible case. While it is possible for a subcritical crack to grow to a size where it becomes critical, it is also possible that the crack grows into a tougher region. As this low toughness was obtained after simulating to 1250°C it is unlikely that a crack of 11mm could lie entirely within such a microstructure as it exists in a very thin band in the real weld. Hence it will be, at least in part, in a tougher region and the actual critical flaw size is much greater.

Using clip gauge COD as a criterion it would appear that this material is best welded in the overaged 550°C condition, the obvious exception being when full tensile strength is essential - welding in the primary hardened condition is then necessary. In no cases did the former pre-weld heat treatment give significantly worse results than the latter, frequently giving much better figures (Table VI).

It is also recommended that for most situations a 550°C post-weld ageing treatment is preferable to 450°C ageing as the reduction in tensile strength is so small (Table III). The average fracture toughness value considering all treatments is also favourable towards 550°C ageing (Table XII). Only in cases of fatigue stressing is it anticipated the 620°C ageing will be superior.

4.6. FRACTURE TOUGHNESS PARAMETERS

In the section which follows some attempt will be made to evaluate the effectiveness of various fracture toughness testing techniques and their ability to quantify toughness.

4.6.1. COD testing by clip gauge

This is the aspect of general yield fracture toughness testing which has received most attention in this country up until the present time. A large mass of data is being accumulated which at least allows comparisons to be drawn between various classes of material. Instrumentation is basically very simple, being the same as that required for plane strain fracture toughness testing, i.e. clip gauge, bridge amplifier and chart recorder. An extra testing step required is periodical calibration of the clip gauge. However the greatest difficulty practically is defining at what point crack growth has taken place (δ_i) and the equipment required to perform this task. In the case of FV520B it was frequently as simple to define δ_i from the load-clip gauge trace as from the electrical potential crack detection trace, the difficulty increasing with toughness. Utilising the results obtained from crack monitoring Table XIII was drawn, expressing the load at initiation (P_i) as a percentage of maximum load (P_m). This indicates that, notwithstanding differences in material and heat treatment, a remarkably constant ratio of P_i/P_m is obtained. Even greater consistency of results is obtained for specimens of any one material type. This would indicate that, for FV520B at least, little error would result from defining δ_i at that point where the load reached 93-94% of the maximum load.

During testing the centre of rotation of the plastic 'hinge' moves; while the Wells formula does not agree concisely with experiment it gives results which are compatible with other fracture toughness parameters. However, as indicated earlier, Archer has shown photographically that for most of the test the centre of rotation is fixed at the point concluded from Wells' analysis. Removing this objection two

alternative equations can be used to calculate COD, one deduced from analysis of experimental data, the other being Wells' equation. The latter is much more laborious to use unless computational facilities are available, and hence for large numbers of specimens the former, being simpler, has its attractions. The results of Tables VIa, VIb and IX are shown plotted graphically in fig.83. These indicate that a linear relationship exists between the two equations but the line does not pass through the origin. Using the initiation criterion the equations are equal at COD values of 0.050mm, a similar situation existing using the maximum load criterion. The divergence consequently becomes greater the further the COD values depart from 0.050mm.

Whilst extremely minute values of COD are generally experienced the consistency is good. Furthermore the order of results is similar to that which could be intuitively deduced from what is generally regarded as 'tough'. On this basis COD by clip gauge is a good assessment of toughness, but does suffer from difficulty in applying the results of small scale tests, as discussed earlier.

4.6.2. Photographic calibration

This technique of testing was applied at a very early stage of the investigation before other methods of testing had been established. The technique is very involved, required many specimens and a large amount of measuring to draw up the calibration curves. Subsequent testing is extremely simple, requiring only crack detection equipment. However an objection does arise in that to be strictly applicable the calibration curves should be drawn up for material experiencing the same thermal history as the testpiece. This is clearly not feasible for an investigation such as this, involving widely different thermal cycles and heat treatments. Hence the results of Tables Va and Vb ignore this aspect. The results are shown compared graphically with COD values in figure 84. These indicate a high consistency but poor correlation for values of δ_i. The situation is slightly

improved for the δ_m values in that the correlation is better; only a limited number of results were obtained for the higher values and more confirmation of the trend is required. This is interesting in view of the inconsistency generally observed in measuring δ_m due to varying W-a dimensions.

The results of direct photographic records are shown graphically in figure 85. Here the opposite situation arises in that the consistency is poor while the correlation is quite good, over a large range. It is a matter for conjecture as to whether this method or clip gauge measurement is the most accurate. Photographically the surface COD is measured, and as this is the most likely area for deformation errors may arise. On the other hand clip gauge measurement can suffer from mechanical discrepancies (bad seating etc) and the calculation is based on theoretical relationships.

4.6.3. Stretch zone width.   (figs.68-70).

By this technique all measurements are made after mechanical testing, hence no instrumentation is required which increases its attraction. The time taken to perform the measurement is limited by the Stereoscan facility and some errors may arise from specimen alignment. The results of Tables VIIa and VIIb are plotted against COD in figure 86. The fairly large mass of data utilised indicates that a parabolic relationship holds, albeit with a very wide bandspread. This relationship forecasts relative insensitivity at small values of COD but rapidly increasing sensitivity at higher values. This may relate to the relative proportions of the elastic and plastic components of COD. Stretch zone widths are a measure of plastic deformation occurring at the crack tip. At small COD values the elastic component is proportionally larger and plastic deformation small, hence the insensitivity of stretch zone width. At higher COD values the plastic component is large and stretch zone width becomes more sensitive.

If we take the criterion of toughness to be the ability of the material ahead of a crack to blunt it, stretch zone width is worthy of closer examination. In measuring the plastic deformation it is this very

ability which is being measured.

To examine the hypothesis that stretch zone width is directly related to COD a number of specimens were unloaded from maximum load and the permanent opening displacement measured photographically. This allowed determination of the elastic component within the limitations of the accuracy of the photographic method. The plastic component of COD was then replotted against stretch zone width and a substantially straight line plot obtained (fig. 91). Hence it appears to be possible to calculate COD with no test instrumentation other than load monitoring. For this material the relationship

$$El = \frac{25 \ (Pi)^{1.5}}{a(W-a)}$$

was found to hold, where El is the elastic component, Pi is the load at crack initiation (in KN) and a and W are measured in millimetres. By adding together the elastic component and the stretch zone component ($\sqrt{2}$ SZW) the total COD can be found. An underestimate may arise due to the coalescence of voids just in front of the crack tip and being lost from the measurement.

4.6.4. The J Contour Integral

The J values obtained in this investigation were derived from load-clip gauge traces. Calculation was based on Dawes [113] modification of Sumpter's analysis [111]; this is an extremely involved arithmetical method which also requires some estimation procedures which may introduce error. This lengthy technique needs validation before it can be considered seriously. The results of Tables VIIIa and IXb are plotted within the framework of Sumpter's finite element analysis in figure 87. Most of the results fall within the boundaries of plane strain and plane stress but are mainly grouped near to the latter. This is exactly what would be expected; using the plane strain criterion for minimum thickness of

$$B \geq 2.5 \left(\frac{K_c}{\sigma_y}\right)^2$$

the results would be expected to lie nearer to the plane stress limits, particularly at the high displacements encountered. The Sumpter model assumed a work hardening exponent which is not necessarily applicable to this steel; this may alter the distribution of experimental points. Nevertheless all the results lay within the predicted limits except for a small number at low clip gauge openings. These may be affected by experimental error at low displacements.

The J values obtained are plotted against COD in figs. 88 and 89. Direct plotting (fig.88) shows a straight line relationship with reasonable correlation. A non-dimensional plot (fig.89) again revealed essentially a straight line plot at approximately 45°, i.e. direct relationship. However in the latter case most of the results lie below the computed plane stress limits. This may be due to the value of yield stress employed in computation of J; 0.5% proof stress was used, use of 0.1% or 0.2% proof values would almost certainly bring the results within the limits. It is interesting that the two results which did fall within limits were transverse specimens aged $450^{\circ}C$ showing low ductility; these gave values of m=1.7 from the Rice relationship $J = m\sigma_y\delta$, i.e. close to the plane strain limit. Many of the results for J do fall very close to the limits proposed by Begley and Landes [114] and hence are of questionable validity.

Correlation of stress intensity factor with COD is also quite good, more so for K_{max} (fig.90); again a 1:1 relationship holds. Attempted corrections for plastic zone size were precluded by the proposed validity limit.

In conclusion it appears that a direct relationship does hold between the proposed elasto-plastic fracture toughness parameters.

5. CONCLUSIONS

The following conclusions may be drawn from the
work conducted;

1. The fracture toughness of FV520B plate (COD, δ_i) varied from
0.040-0.076mm for air melted plate and 0.069-0.081mm for
vacuum remelted plate depending on heat treatment condition
and orientation to the rolling direction. In general frac-
ture toughness increased progressively as the ageing temp-
erature increased from 450° to 620°C.

2. There are two regions of reduced hardness in the weld HAZ of
FV520B corresponding to peak temperatures of approximately 1225°-
1275°C and 730°-810°C, these being present over a wide range
of preweld and post-weld heat treatments. The higher temperature
softening is attributable to coarse precipitation and possible
δ-ferrite formation, while the lower temperature softening is
attributable to the presence of austenite.

3. Thermal simulation is a valid method for studying the weld
HAZ properties in this alloy; acceptable correlations of
microstructure and properties have been obtained for the two
peak temperatures of 1250°C and 785°C

4. In general the region in the weld HAZ corresponding to a peak
temperature of 1250°C shows a fracture toughness which is
equal to or slightly greater than the parent plate in the
same post-weld aged condition.

5. In general the region in the weld HAZ corresponding to a peak temperature of 785°C shows a fracture toughness which is equal to or less than that of parent plate in the same post-weld aged condition

6. The fracture toughness of the HAZ corresponding to peak temperatures of 1250°C and 785°C in all conditions is virtually identical with plate in primary hardened and 550°C overaged conditions.

7. For the specimen geometry considered there is reasonable linear agreement between the elasto-plastic fracture mechanics parameters COD, J and K; photographic measurements of surface displacements and stretch zone sizes were less conclusive and require refinement.

6. FURTHER WORK

It is considered that the following areas are worthy of further investigation;

1) a more detailed study of the mechanisms of hardening which operate; with modern advances in electron metallography this has become more feasible.

2) the relationship which exists between heat input and fracture toughness should be ascertained, in particular quantifying the effects of microstructural changes.

3) the field of fracture toughness testing is still in a state of flux; a convenient and accurate method of measuring a parameter which may be related to failure prediction in full size structures is required.

7. ACKNOWLEDGEMENTS

APPENDIX I

The computed thermal cycles employed in this investigation were generated from a modified program originally compiled by Westby [64]. A full description of the original program appears in this reference, but a brief description of the principles employed will follow.

Analytical temperature calculations make several assumptions, such as constant thermal properties and point heat sources, which result in very bad agreement with real conditions as the heat source is approached. Heat transfer to the surroundings and convection within the weld pool is ignored, most emphasis being on heat transfer by conduction based on

$$\frac{\partial T}{\partial t} = a \frac{\partial^2 T}{\partial x^2} + \frac{\partial^2 T}{\partial y^2} + \frac{\partial^2 T}{\partial z^2} + \frac{W}{c\gamma}$$

$\frac{\partial^2 T}{\partial x^2}$ referring to heat transfer in the x direction etc., and W being the heat exchange with the surroundings. Moving heat sources are represented by multiple sources of short duration and sufficient time allowed to elapse for a quasi-stationary heat state to be established; hence conditions cannot be predicted for short arcing times. Conditions such as water cooling mean that heat losses to the surroundings cannot be ignored and hence for finite plates 'fictive' heat sources are employed, these being imaginary heat sources placed in a mirror image position (outside the plate). This, together with errors introduced by considering the thermal properties to be constant despite temperature variation can lead to errors of up to 50% in comparison with experimental measurements.

The differential equations employed in analytical methods are frequently difficult to solve. There are several advantages in the use of numerical analyses, eg. the weld geometry can be ignored and the weld heat source can be of any shape. In addition, and most importantly, a quasi-stationary state of heat flow is not required in numerical methods and

hence temperature distributions can be obtained even for very short arcing times. The Fortran program TREDIM makes use of a modified form of the differential heat flow equation to enable a finite element analysis to be performed;

$$T = T_{ijk} + \frac{\dot{W} \cdot \Delta t}{c \cdot \gamma} + a \cdot \Delta t \left(\frac{T_{i+1,j,k} + T_{i-1,j,k} - 2T_{i,j,k}}{\Delta h^2} + \right.$$

$$\left. \frac{T_{i,j+1,k} + T_{i,j-1,k} - 2T_{i,j,k}}{\Delta b^2} + \frac{T_{i,j,k+1} + T_{i,j,k-1} - 2T_{i,j,k}}{\Delta l^2} \right)$$

where i,j,k are the three perpendicular plate axes and h,b and l are unit steps in each direction respectively. T and $T_{i,j,k}$ are the temperatures in a specified point (i,j,k) after and before a time step Δt. $\dot{W}$ denotes the heat exchange with the surroundings and is zero for all except surface units. The work piece is considered to be of infinite length and calculated temperature points are moved along the plate at the same speed as the welding heat source. In this way the origin of the heat source is always acting on the same unit of the plate (unit 2,2,12 for TREDIM) and hence a continual picture of the temperature distribution around the heat source is obtained.

The welding plate is considered to consist of a number of right angled volume elements, the temperature of each being that of the unit centre and the temperature distribution between units being of a straight line nature. Large temperature gradients exist near the heat source and hence it is desirable that a larger number of small units be specified in this region ('inner zone') compared to areas of the plate remote from the heat source ('outer zone'). As the heat distribution at points remote from the heat source results in the temperatures of the upper and lower surfaces being the same the outer zone is considered in terms of two-dimensional heat flow only. In addition the temperature distribution around the weld line is symmetrical, enabling calculations for just one half of the model

to be sufficient.

The heat is supplied to the plate for a time Δt and the temperature distribution of the inner zone is calculated. When complete the temperature points at the outer edge of the inner zone are transferred to the inner edge of the outer zone, the zones being designed to overlap at these points. Subsequently the temperature distribution in the outer zone is calculated. When both inner and outer zones are completed heat is supplied for a further time step Δt. To ensure that both upper and lower surfaces are at the same temperature throughout the outer zone trial runs should be made with very large inner zones (which are three dimensional). This gives very poor accuracy close to the heat source but enables a check on the validity of the assumption of uniform through thickness temperature to be made. For this investigation Δb was set at 6mm and Δl at 10mm (INITIALISATION, CHOSEN VALUES in program). The plate thickness is chosen by the data card. This gives an inner zone of unit size (3,8,18) the dimensions

$$6mm \times 8 \quad = \quad 48mm$$
$$10mm \times 18 \quad = \quad 180mm$$

and plate thickness.

Heat loss to the surroundings may be accounted for by changing the section 'BOUNDARY CONDITIONS FOR THE UPPER AND LOWER SURFACE OF THE PLATE'. Similarly the heat source, which acts at point (2,2,12) can be spread over several units to give a more diffuse source (such as a burner) by changing the section 'HEAT TRANSFER TO THE PLATE'.

Attached is a printout of the program using the welding parameters used experimentally for this investigation, i.e.

Plate thickness	6mm	(punch 0.6cm)
Welding current	370 amperes	
Arc voltage	33v	
Welding speed	10mm/sec.	(punch 1cm/sec)

Efficiency factor   75%

In addition an arcing time must be supplied; this should be suff-
icient to give steady state heat distribution but not so great that excess-
ively long run-times result. By trial and error a time of 15 seconds was
found to satisfy these criteria and the data card punched;

!!15.0!!!0.6!370.0!!33.0!1.00!0.75

the decimal points being in card columns 5,11,17,23,27,32. Hence the welding
conditions can be altered quickly and simply by changing a single data card.

```
0001              PROGRAM (TRE1)
0002              INPUT 5 = CR0
0003              OUTPUT 6 = LP0
0004              TRACE 2
0005              OUTPUT 7 = LP1
0006              COMPRESS INTEGER AND LOGICAL
0007              END

0008              MASTER TREDIM
0009       C
0010       C TREDIM
0011       C
0012       C TEMPERATURE CALCULATIONS WITH CONSTANT MATERIAL PROPERTIES
0013       C
0014              DIMENSION T( 8,10,18),VJ( 8),VK( 8,10),B(10),F(10,18),V4(10)
0015              REAL H(8)
0016              COMMON T,B,KM,DL,IMAX1,H
0017          1   FORMAT(21H REAL ARCING TIME(S)=,F6.1)
0018          3   FORMAT(/14F8.2)
0019          5   FORMAT(4F6.1,2F5.2)
0020          6   FORMAT(23H WANTED ARCING TIME(S)=,F6.1)
0021          7   FORMAT(21H PLATE THICKNESS(CM)=,F6.1)
0022          8   FORMAT(22H WELDING CURRENT(AMP)=,F6.1)
0023          9   FORMAT(19H ARC VOLTAGE(VOLT)=,F6.1)
0024         10   FORMAT(52H SPEED OF ELECTRODE ALONG THE LINE OF WELDING(CM/S)=,
0025             1F6.2)
0026         11   FORMAT(19H EFFICIENCY FACTOR=,F6.2)
0027         12   FORMAT(35H HEAT SUPPLIED TO THE PLATE(CAL/S)=,F8.1)
0028              READ(5,5)TSTART,TYKK,AMP,VOLT,FART,ETA
0029              WRITE(6,6)TSTART
0030              WRITE(6,7)TYKK
```

```
      WRITE(6,8)AMP
      WRITE(6,9)VOLT
      WRITE(6,10)FART
      WRITE(6,11)ETA
C
C INITIALISATION,CHOSEN VALUES
C
      DB=0.6
      DL=1.0
      IMAX=3
      JMAX=8
      KM=16
      KMAX=18
      TSLUTT=0.0
      C=1.0
      A=0.1
C
C INITIALIZATION,CALCULATED VALUES
C
      DI=FLOAT(IMAX)
      DH=TYKK/DI
      QPRIKK=0.24*ETA*AMP*VOLT
      ALFAMX=A
      DH2=DH**2
      DB2=DB**2
      DL2=DL**2
      DU=3.0*DB
      DV=3.0*DL
      DU2=DU**2
      DV2=DV**2
      M=(JMAX+1)/3+1
      KMAX2=KMAX
      N=2*KMAX2/3
      V=DH*DB*DL
      VINV=1.0/DH**2+1.0/DB**2+1.0/DL**2
      DTGO=DL/FART
```

```
0067        IMAX1=IMAX+1
0068        IMAX2=IMAX+2
0069        JMAX1=JMAX+1
0070        JMAX2=JMAX+2
0071        KMAX1=KMAX2-1
0072        WRITE(6,12)QPRIKK
0073     25 BMAX=(FLOAT(JMAX2)-1.5)*DB
0074        DO 26 J=1,JMAX2
0075     26 B(J)=(FLOAT(J)-1.5)*DB
0076        DO 27 I=1,IMAX2
0077     27 H(I)=(FLOAT(I)-1.5)*DH
0078  C
0079  C  INITIALIZATION,VALUES AT THE START OF WELDING
0080  C
0081        TIDINT=0.0
0082        SUMTID=0.0
0083     28 VI=0.0
0084        DO 29 J=1,JMAX2
0085        V4(J)=0.0
0086        DO 29 K=1,KMAX2
0087     29 F(J,K)=20.0
0088        DO 30 I=1,IMAX2
0089        VJ(I)=0.0
0090        DO 30 J=1,JMAX2
0091        VK(I,J)=0.0
0092        DO 30 K=1,KMAX2
0093     30 T(I,J,K)=20.0
0094  C
0095  C  RETURN TO THIS LABEL
0096  C
0097  C  CALCULATION OF THE MAXIMUM TIME STEP FOR ONE SINGLE LOOP
0098  C
0099    100 DTID=0.5/ALFAMX/VINV-1.0E-25
0100  C
0101  C  TIME CHECK CONCERNING SHIFT OF THE POSITIONS OF THE TEMPERATURE POINTS
0102  C
```

```
0067          IMAX1=IMAX+1
0068          IMAX2=IMAX+2
0069          JMAX1=JMAX+1
0070          JMAX2=JMAX+2
0071          KMAX1=KMAX2-1
0072          WRITE(6,12)QPRIKK
0073    25    BMAX=(FLOAT(JMAX2)-1.5)*DB
0074          DO 26 J=1,JMAX2
0075    26    R(J)=(FLOAT(J)-1.5)*DB
0076          DO 27 I=1,IMAX2
0077    27    H(I)=(FLOAT(I)-1.5)*DH
0078    C
0079    C     INITIALIZATION,VALUES AT THE START OF WELDING
0080    C
0081          TIDINT=0.0
0082          SUMTID=0.0
0083    28    VI=0.0
0084          DO 29 J=1,JMAX2
0085          V4(J)=0.0
0086          DO 29 K=1,KMAX2
0087    29    F(J,K)=20.0
0088          DO 30 I=1,IMAX2
0089          VJ(I)=0.0
0090          DO 30 J=1,JMAX2
0091          VK(I,J)=0.0
0092          DO 30 K=1,KMAX2
0093    30    T(I,J,K)=20.0
0094    C
0095    C     RETURN TO THIS LABEL
0096    C
0097    C     CALCULATION OF THE MAXIMUM TIME STEP FOR ONE SINGLE LOOP
0098    C
0099    100   DTID=0.5/ALFAMX/VINV-1.0E-25
0100    C
0101    C     TIME CHECK CONCERNING SHIFT OF THE POSITIONS OF THE TEMPERATURE POINTS
0102    C
```

```
0103        101 IF (DTGO.GT.(TIDINT+DTID)) GOTO 120
0104        102 IF(TIDINT.GT.DTGO)GOTO 104
0105        103 DTID=DTGO-TIDINT+1.0E-7
0106            GOTO 120
0107        104 SUMTID=SUMTID+TIDINT
0108            TIDINT=0.0
0109            WRITE(6,1)SUMTID
0110          C
0111          C SHIFT OF THE POSITIONS OF THE TEMPERATURE POINTS
0112          C
0113            DO 110 J=2,M
0114        110 F(J,N)=T(3,3*J-3,2)
0115            DO 112 K=2,KMAX2
0116            DO 112 J=1,JMAX2
0117            F(J,K-1)=(2.+F(J,K-1)+F(J,K))/3.
0118            DO112 I=1,IMAX2
0119        112 T(I,J,K-1)=T(I,J,K)
0120        120 TIDINT=TIDINT+DTID
0121          C
0122          C HEAT TRANSFER TO THE PLATE
0123          C
0124            DTP=QPRIKK*DTID/C/V/2.0
0125            T(2,2,KM)=T(2,2,KM)+DTP
0126          C
0127          C INNER ZONE
0128          C
0129          C BOUNDARY CONDITIONS BETWEEN OUTER AND INNER ZONE PARALLEL TO THE WELD
0130          C
0131            KS=KMAX2-N-1
0132            DO 140 K=0,KS,1
0133            DO 140 KK=1,3
0134            KE=KK+3*K
0135            DO 140 I=1,IMAX2
0136        140 T(I,JMAX2,KE)=(2.0*T(I,JMAX1,KE)+F(M+1,N+K))/3.0
0137          C
0138          C BOUNDARY CONDITIONS IN FRONT OF THE ARC
0139          C
```

```
0140         DO 141 I=1,IMAX2
0141         DO 141 J=1,JMAX2
0142  141    T(I,J,KMAX2)=20.0
0143  C
0144  C  BOUNDARY CONDITIONS IN THE VERTICAL PLANE OF SYMMETRY
0145  C
0146         DO 142 I=1,IMAX2
0147         DO 142 K=1,KMAX2
0148  142    T(I,1,K)=T(I,2,K)
0149  C
0150  C  BOUNDARY CONDITIONS BEHIND THE ARC
0151  C
0152         DO 402 J=2,M
0153         JJ=-5
0154  401    JJ=JJ+1
0155         JE=3*J+JJ
0156         DO 143 I=1,IMAX
0157  143    T(I,JE,1)=(2.0*T(I,JE,2)+T(I,JE,2)+F(J,N-1))/3.0
0158         IF (JJ.NE.-2) GOTO 401
0159  402    CONTINUE
0160  C
0161  C  BOUNDARY CONDITIONS FOR THE UPPER AND LOWER SURFACE OF THE PLATE
0162  C
0163         DO 145 J=1,JMAX2
0164         DO 145 K=1,KMAX2
0165         T(1,J,K)=T(2,J,K)
0166  145    T(IMAX2,J,K)=T(IMAX1,J,K)
0167  C
0168  C  TIME CHECK CONCERNING OUTPUT AND STOP
0169  C
0170  147    IF(SUMTID.LT.TSTART)GOTO 150
0171  148    DO 149 I=2,17
0172         CALL SKRFIR(I)
0173  149    CONTINUE
0174         TSTART=TSTART+20.0
0175         IF(TSLUTT.LT.SUMTID)GOTO 200
0176  C
```

```
C
C     CALCULATION OF THE TEMPERATURES IN THE INNER ZONE
C
  150 DO 151 K=1,KMAX1
      DO 151 J=1,JMAX1
      DO 151 I=1,IMAX1
      TP=T(I,J,K)
      VIU=A*(TP-T(I+1,J  ,K  ))/DH2
      VJU=A*(TP-T(I  ,J+1,K  ))/DB2
      VKU=A*(TP-T(I  ,J  ,K+1))/DL2
      T(I,J,K)=TP+DTID*(VI+VJ(I)+VK(I,J)-VIU-VJU-VKU)
      VI=VIU
      VJ(I)=VJU
  151 VK(I,J)=VKU
C
C     OUTER ZONE
C
C     BOUNDARY CONDITIONS BEHIND THE ARC
C
      DO 176 J=2,M
  176 F(J,N)=T(3,3+J-3,2)
C
C     BOUNDARY CONDITIONS BETWEEN OUTER AND INNER ZONE PARALLEL TO THE WELD
C
      I=KMAX2-N-1
      DO 178 K=1,I
  178 F(M,N+K)=T(3,JMAX1,2+3*K)
C
C     BOUNDARY CONDITIONS IN THE VERTICAL PLANE OF SYMMETRY
C
      DO 180 K=1,N
  180 F(1,K)=F(2,K)
C
C     CALCULATION OF THE TEMPERATURES IN THE OUTER ZONE
C
      DO 182 K=1,KMAX1
      DO 182 J=1,JMAX1
```

```
0213        V1=A*(F(J,K)-F(J+1,K))/DU2
0214        V2=A*(F(J,K)-F(J,K+1))/DV2
0215        F(J,K)=F(J,K)+DTID*(V3+V4(J)-V1-V2)
0216        V3=V1
0217    182 V4(J)=V2
0218  C
0219  C     BOUNDARY CONDITIONS BEHIND AND IN FRONT OF THE ARC
0220  C
0221        DO 186 J=1,JMAX2
0222        F(J,KMAX2)=20.0
0223    186 F(J,1)=F(J,2)
0224  C
0225  C     BOUNDARY CONDITIONS ALONG THE EDGE OF THE PLATE
0226  C
0227        DO 188 K=1,KMAX2
0228    188 F(JMAX2,K)=F(JMAX1,K)
0229        GOTO 100
0230    200 CONTINUE
0231        STOP
0232        END


END OF SEGMENT, LENGTH  1347, NAME  TREDIM


0233  C
0234  C     OUTPUT OF CALCULATED TEMPERATURES
0235  C
0236        SUBROUTINE SKRFIR(L  )
0237        DIMENSION T( 8,10,18),B(10)
0238        REAL H(8)
0239        COMMON T,B,KM,DL,IMAX1,H
0240      1 FORMAT(//41H TEMPERATURES(DEGR.C) IN A CROSS SECTION ,F6.1,
0241       113H CM BEHIND THE ARC)
0242      2 FORMAT(10H     B(CM)=,14F8.2)
0243      3 FORMAT(3H H=,F6.2,2HCM,14F8.1)
0244        RK=FLOAT(KM-L)
```

```
0245          AK=RK*DL
0246          WRITE(6,1)AK
0247          WRITE(6,2)(B(J),J=2,9)
0248          DO 10 I=2,IMAX1
0249       10 WRITE(6,3)H(I),(T(I,J,L),J=2,9)
0250          RETURN
0251          END
```

END OF SEGMENT, LENGTH 100, NAME SKRFIR

```
0252          FINISH
```

END OF COMPILATION - NO ERRORS

3/C SUBFILE: 28 BUCKETS USED

DOCUMENT   1

WANTED ARCING TIME(S) =   20.0
PLATE THICKNESS(CM) =   0.6
WELDING CURRENT(AMP) = 295.0
ARC VOLTAGE(VOLT) = 29.0
SPEED OF ELECTRODE ALONG THE LINE OF WELDING(CM/S) =   0.48
EFFICIENCY FACTOR= 0.75
HEAT SUPPLIED TO THE PLATE(CAL/S) =   1539.9
REAL ARCING TIME(S) =   2.1
REAL ARCING TIME(S) =   4.2
REAL ARCING TIME(S) =   6.3
REAL ARCING TIME(S) =   8.3
REAL ARCING TIME(S) =   10.4
REAL ARCING TIME(S) =   12.5
REAL ARCING TIME(S) =   14.6
REAL ARCING TIME(S) =   16.7
REAL ARCING TIME(S) =   18.8
REAL ARCING TIME(S) =   20.8

TEMPERATURES(DEGR.C) IN A CROSS SECTION 14.0 CM BEHIND THE ARC

B(CM)=	0.30	0.90	1.50	2.10	2.70	3.30	3.90	4.50
H= 0.10CM	56.9	53.5	47.7	40.8	34.3	29.1	25.4	23.3
H= 0.30CM	56.9	53.5	47.7	40.8	34.3	29.1	25.4	23.3
H= 0.50CM	56.9	53.5	47.7	40.8	34.3	29.1	25.4	23.3

TEMPERATURES(DEGR.C) IN A CROSS SECTION 13.0 CM BEHIND THE ARC

B(CM)=	0.30	0.90	1.50	2.10	2.70	3.30	3.90	4.50
H= 0.10CM	116.1	107.2	91.9	74.0	57.0	43.4	34.0	28.5
H= 0.30CM	116.1	107.2	91.9	74.0	57.0	43.4	34.0	28.5
H= 0.50CM	116.1	107.2	91.9	74.0	57.0	43.4	34.0	28.5

TEMPERATURES(DEGR.C) IN A CROSS SECTION 12.0 CM BEHIND THE ARC

B(CM)=	0.30	0.90	1.50	2.10	2.70	3.30	3.90	4.50
H= 0.10CM	232.9	212.9	178.5	138.5	100.9	70.9	50.1	38.0
H= 0.30CM	232.9	212.9	178.5	138.5	100.9	70.9	50.1	38.0
H= 0.50CM	232.9	212.9	178.5	138.5	100.9	70.9	50.1	38.0

TEMPERATURES(DEGR.C) IN A CROSS SECTION 11.0 CM BEHIND THE ARC

B(CM)=	0.30	0.90	1.50	2.10	2.70	3.30	3.90	4.50
H= 0.10CM	417.5	379.2	313.8	238.1	167.7	111.9	73.8	51.7
H= 0.30CM	417.5	379.2	313.8	238.1	167.7	111.9	73.8	51.7
H= 0.50CM	417.5	379.2	313.8	238.1	167.7	111.9	73.8	51.7

TEMPERATURES(DEGR.C) IN A CROSS SECTION 10.0 CM BEHIND THE ARC

B(CM)=	0.30	0.90	1.50	2.10	2.70	3.30	3.90	4.50
H= 0.10CM	647.7	584.7	478.0	356.1	244.3	157.4	99.0	65.9
H= 0.30CM	647.7	584.7	478.0	356.1	244.3	157.4	99.0	65.9
H= 0.50CM	647.7	584.7	478.0	356.1	244.3	157.4	99.0	65.9

TEMPERATURES(DEGR.C) IN A CROSS SECTION 9.0 CM BEHIND THE ARC

B(CM)=	0.30	0.90	1.50	2.10	2.70	3.30	3.90	4.50
H= 0.10CM	875.3	784.0	631.3	460.1	307.1	191.4	115.9	74.3
H= 0.30CM	875.3	784.0	631.3	460.1	307.1	191.4	115.9	74.3
H= 0.50CM	875.3	784.0	631.3	460.1	307.1	191.4	115.9	74.3

TEMPERATURES(DEGR.C) IN A CROSS SECTION 8.0 CM BEHIND THE ARC

B(CM)=	0.30	0.90	1.50	2.10	2.70	3.30	3.90	4.50
H= 0.10CM	1065.2	943.3	743.3	526.1	339.0	203.2	118.4	73.8
H= 0.30CM	1065.2	943.3	743.3	526.1	339.0	203.2	118.4	73.8
H= 0.50CM	1065.2	943.3	743.3	526.1	339.0	203.2	118.4	73.8

119

TEMPERATURES(DEGR.C) IN A CROSS SECTION 7.0 CM BEHIND THE ARC

B(CM)=	0.30	0.90	1.50	2.10	2.70	3.30	3.90	4.50
H= 0.10CM	1215.7	1058.8	809.0	549.5	337.6	192.8	107.6	65.4
H= 0.30CM	1215.7	1058.8	809.0	549.5	337.6	192.8	107.6	65.4
H= 0.50CM	1215.7	1058.8	809.0	549.5	337.6	192.8	107.6	65.4

TEMPERATURES(DEGR.C) IN A CROSS SECTION 6.0 CM BEHIND THE ARC

B(CM)=	0.30	0.90	1.50	2.10	2.70	3.30	3.90	4.50
H= 0.10CM	1348.3	1145.8	837.7	537.3	309.9	166.5	88.8	53.3
H= 0.30CM	1348.3	1145.8	837.7	537.3	309.9	166.5	88.8	53.3
H= 0.50CM	1348.3	1145.8	837.7	537.3	309.9	166.5	88.8	53.3

TEMPERATURES(DEGR.C) IN A CROSS SECTION 5.0 CM BEHIND THE ARC

B(CM)=	0.30	0.90	1.50	2.10	2.70	3.30	3.90	4.50
H= 0.10CM	1490.0	1220.5	837.3	496.2	263.3	131.5	67.3	40.9
H= 0.30CM	1490.0	1220.5	837.3	496.2	263.3	131.5	67.3	40.9
H= 0.50CM	1490.0	1220.5	837.3	496.2	263.3	131.5	67.3	40.9

TEMPERATURES(DEGR.C) IN A CROSS SECTION 4.0 CM BEHIND THE ARC

B(CM)=	0.30	0.90	1.50	2.10	2.70	3.30	3.90	4.50
H= 0.10CM	1668.9	1289.7	805.3	427.4	203.7	94.1	47.7	30.8
H= 0.30CM	1668.9	1289.6	805.2	427.4	203.7	94.1	47.7	30.8
H= 0.50CM	1668.8	1289.6	805.2	427.4	203.7	94.1	47.7	30.8

TEMPERATURES(DEGR.C) IN A CROSS SECTION 3.0 CM BEHIND THE ARC

B(CM)=	0.30	0.90	1.50	2.10	2.70	3.30	3.90	4.50
H= 0.10CM	1924.0	1343.9	724.6	328.8	137.3	60.1	32.8	24.4
H= 0.30CM	1922.6	1343.5	724.5	328.8	137.3	60.1	32.8	24.4
H= 0.50CM	1921.3	1343.2	724.4	328.8	137.3	60.1	32.8	24.4

TEMPERATURES(DEGR.C) IN A CROSS SECTION 2.0 CM BEHIND THE ARC

B(CM)=	0.30	0.90	1.50	2.10	2.70	3.30	3.90	4.50
H= 0.10CM	2349.4	1332.2	563.7	203.9	74.9	35.3	24.2	21.3
H= 0.30CM	2307.2	1325.7	562.9	203.8	74.9	35.3	24.2	21.3
H= 0.50CM	2275.0	1319.8	562.1	203.7	74.8	35.3	24.2	21.3

TEMPERATURES(DEGR.C) IN A CROSS SECTION 1.0 CM BEHIND THE ARC

B(CM)=	0.30	0.90	1.50	2.10	2.70	3.30	3.90	4.50
H= 0.10CM	3884.1	1144.0	277.7	79.2	33.9	23.4	20.8	20.2
H= 0.30CM	3497.9	1037.1	269.1	78.5	33.9	23.4	20.8	20.2
H= 0.50CM	2816.6	956.7	261.5	77.8	33.8	23.4	20.8	20.2

TEMPERATURES(DEGR.C) IN A CROSS SECTION 0.0 CM BEHIND THE ARC

B(CM)=	0.30	0.90	1.50	2.10	2.70	3.30	3.90	4.50
H= 0.10CM	1543.3	154.4	53.1	27.4	21.7	20.4	20.1	20.0
H= 0.30CM	386.6	148.0	52.3	27.3	21.7	20.4	20.1	20.0
H= 0.50CM	354.6	142.2	51.5	27.2	21.7	20.4	20.1	20.0

TEMPERATURES(DEGR.C) IN A CROSS SECTION -1.0 CM BEHIND THE ARC

B(CM)=	0.30	0.90	1.50	2.10	2.70	3.30	3.90	4.50
H= 0.10CM	20.0	20.0	20.0	20.0	20.0	20.0	20.0	20.0
H= 0.30CM	20.0	20.0	20.0	20.0	20.0	20.0	20.0	20.0
H= 0.50CM	20.0	20.0	20.0	20.0	20.0	20.0	20.0	20.0

NbC ASTM 16-856	NbN ASTM 14-547	Experimental measurements
	2.74	
2.68		
	2.55	
2.47		
2.35	2.31	2.32
1.82	1.87	1.90
1.55		1.54
	1.49	1.50
	1.47	1.47
1.41		1.42
	1.37	1.37
1.34		1.33
1.31	1.30	1.31
1.29		1.29
	1.27	1.27
1.24	1.24	1.25
	1.21	1.22
1.18		1.18
	1.16	1.15
1.12		1.11
1.04	1.05	1.03
1.01	1.01	
0.99		0.98
0.97	0.97	0.97
	0.95	
0.94	0.94	
0.93		
0.91	0.91	
0.89	0.87	
0.86	0.85	0.86
0.84	0.84	
0.83	0.82	
0.80		
0.79	0.79	
0.78	0.78	0.78

Appendix II. 'd' spacings for NbC and NbN

Cu ASTM 4-0836	Experimental measurements
2.088	2.085
1.808	1.801
1.278	1.305
1.090	1.105
1.044	1.039
0.904	0.904
0.829	0.829
0.808	0.805

Appendix IIa.   'd' spacings for Copper

Figure	25 (i)	25 (ii)	25 (iii)	26 (i)	26 (iii)	27 (i)	27 (iii)
Post-weld Heat Treat.	-78°C	As-welded	1050°C	1050/ 850/ 450°C	1050/ 850/ 620°C	750/ 450°C	750/ 620°C
fusion line	374	374	324	389	299	400	327
0.5mm	404	407	333	416	296	407	323
1.0	396	398	349	412	267	423	312
1.5	399	391	351	419	291	411	314
2.0	388	385	346	435	301	381	330
2.5	409	386	341	428	303	382	316
3.0	407	388	343	414	299	395	305
3.5	391	405	354	432	305	391	326
4.0	383	412	342	429	319	394	323
4.5	369	394	337	414	310	394	318
5.0	361	380	335	412	297	387	323
5.5	376	371	333	423	312	394	319
6.0	358	367	340	427	312	394	320
6.5	363	353	345	427	323	395	313
7.0	354	345	346	438	320	399	319
7.5	361	349	340	436	317	404	312
8.0	370	353	343	421	318	404	319
8.5	386	360	347	420	306	402	310
9.0	410	369	353	412	298	380	324
9.5	412	377	358	423	306	388	314
10.0	415	383	361	415	317	394	315
10.5	410	383	365	414	313	399	320
11.0	400	381	368	404	323	391	308
11.5	388	378	370	412	318	382	320
12.0	392	379	370	415	318	385	317
13.0	388	386	372	420	320	387	315

Appendix III.   Microhardness surveys, H_v (continued over)

Figure	28(a) (i)	28(a) (ii)	28(a) (iii)	28(a) (iv)	28(b) (i)	28(b) (ii)	28(b) (iii)
Post-weld Heat Treat.	450°C	As-welded	-78/620°C	620°C	450°C	As-welded	620°C
fusion line	415	374	351	357	420	377	362
0.5mm	460	407	358	362	448	404	359
1.0	430	398	346	332	454	399	362
1.5	455	391	354	355	458	393	367
2.0	435	385	315	348	462	386	366
2.5	453	386	343	332	456	377	349
3.0	463	388	330	337	388	359	333
3.5	460	405	336	341	459	410	344
4.0	460	412	342	345	450	396	345
4.5	444	394	343	336	436	378	339
5.0	440	380	318	330	431	369	332
5.5	431	371	336	323	422	344	316
6.0	416	367	336	326	409	342	323
6.5	398	353	310	322	404	348	331
7.0	394	345	326	325	399	348	327
7.5	388	349	323	326	394	347	324
8.0	373	353	331	325	382	348	326
8.5	363	360	330	321	367	348	326
9.0	364	369	329	315	351	347	322
10.0	385	383	316	312	332	346	313
10.5	391	383	328	322	332	347	313
11.0	394	381	327	317	338	349	317
11.5	395	378	328	328	348	352	321
12.0	393	379	328	323	357	353	322
15.0	398	368	324	317	384	348	323

Appendix III. Microhardness surveys, H_v (continued)

E — Young's Modulus

G — Strain energy release rate

H_v — Vickers hardness number

J — Non-elastic strain energy release rate

J_C — Non-elastic strain energy release rate at fracture

K — Stress intensification factor

K_{IC} — Critical stress intensification factor, mode I.

a — Length of a surface crack

c — Length of an embedded crack

m_s — Start of martensite transformation

ν — Poisson's Ratio

μ — Shear Modulus

σ_y — Yield stress

σ_F — Fracture stress

ρ — Crack tip root radius

γ_s — Surface free energy

γ_p — Surface energy effect due to plastic deformation

δ — Crack opening displacement (COD).

δ_c — COD at fracture

δ_i — COD at initiation of crack growth

δ_m — COD at maximum load.

$\alpha', \gamma, \delta, \sigma$ — phases of iron

Appendix IV — List of Symbols

REFERENCES

1.A Guinier,G.D.Preston
          Nature, 1938, 142, (3595), 569-570

2.R.E.Read-Hill
          Physical Metallurgy Principles, Van Nostrand, 1964

3.R.E.Smallman
          Modern Physical Metallurgy, Butterworths, 1963

4.E.Orowan
          Dislocations in Metals, 69, AIME, 1954.

5.A.L.Schaeffler
          Metal Progress, 1949, 56, 680

6.E.R.Petty
          Physical Metallurgy of Engineering Materials, 100,
                George Allen and Unwin 1968.

7.G.Krapf et al
          JISI, 1973, 211, (5), 353-356.

8.N.Lambert et al
          Mem.Sci.Rev.Met. 1970, 67, (7/8), 459-469.

9.I.Kirman & D.H.Warrington
          Met.Trans. 1970, 1, (10), 2667-2675.

10.A.Shlyamneva et al.
          Metal Science and Heat Treatment, 1975,17,(1-2),157-159.

11.G.Baldi et al.
          Met.Ital. 1974, 66, (12), 667-676 ·

12.M.D.J.Vowles & D.R.F.West.
          JISI   1973, 211, (2), 147-160

13.T.Kimoshita et al.
          Nippon Kinzoku Gakkai-Si. 1969, 33, (2), 254-259.

14.H.Goudo
          'Proceedings on the Symposium on High Strength Steel
          and Its Joint' 53-58, Japan Society for the Promotion
          of Science, Tokyo, 1966

15.H.J.Rack & D.Kalish
          Met.Trans. 1974, 5, (7), 1595-1605

16.J.P.Adamson & J.W.Martin
          Acta Met. 1971, 19, (10), 1015-1018

17.H.R.Smith & D.R.F.West
          Metals Technology 1974, 1, (6), 295-299

18.D.Webster
          Trans. ASM Quarterly 1968, 61, (4), 807-815

19. G.A.Beresnev et al.
Sbornik. Nauchn. Trudov. Permsk. Politekhn. Inst.
1974, (148), 22-27

20. A.J.Sedriks & J.V.Craig
JISI 1966, 204, 360-365

21. Yu.N.Goikenberg et al.
Sbornik. Nauchn. Trudov. Chelyab. Politekhn. Inst.
1973, 118, 126-132.

22. H.R.Smith & D.R.F.West.
Metals Technology 1974, 1, (6), 295-299

23. M.M.Shteinberg et al.
Metal Science and Heat Treatment 1972, 14, (7), 586-589

24. J.E.Truman
'Metallurgical Developments in High Alloy Steels',
84-91, ISI Special Report no. 86

25. F.C.Hull
Welding Journal 1973, 80, (5), 193s-203s.

26. M.C.Coleman & M.F.Jordan
Metals Technology 1974, 1, (1), 24-30

27. M.I.Razikov et al.
Welding Production 1975, 22, (4), 33-37

28. N.Kenyon
Welding Journal 1968, 47, 193s-198s

29. M.M.Shorshovov et al.
Metal Science and Heat Treatment 1973, 15, 11-12

30. S.S.Strunck & R.D.Stout
Welding Journal 1972, 51, (10), 508s-520s

31. B.Cina
JISI 1954, 177, (8), 406-422

32. J.E.Truman & B.Crawshaw
'Stainless Steels' ISI Publication 117, 1969, 195-204

33. T.G.Gooch
'Stainless Steels' ISI P117, 1969, 77-84

34. J.L.Kaae
Brit.Weld.Journal. 1968, 15, (7), 333-334

35. Z.P.Zaperstein et al.
AIME Met.Soc.Conf. 1966, 31, 163-225

36. E.F.Nippes & W.F.Savage
Welding J. 1949, 28, (11), 534s-546s

37. J.M.Lowes et al.
'Weld Thermal Simulators for Research' 9-13,
Welding Institute Seminar, London, 1972

38. M.Kh.Shorshovov
Svar.Proiz. 1956, 3, (9), 1-4

39. C.S.Williams
Welding Journal 1963, 42, (1), 1s-8s

40. N.C.Balchin
BWRA Bulletin 1968, 9, (3), 66-67

41. W.F.Savage
'Weld Thermal Simulators for Research' Discussion 1,
Welding Institute Seminar, London, 1972

42. M.C.Coleman
Ph.D.Thesis, University of Aston, 1971

43. E.F.Nippes
Welding Journal 1959, 38, (1), 1s-18s

44. M.Kh.Shorshovov
Brit.Weld.Journal 1957, 4, (5), 239-243

45. D.F.Adams & A.J.Mombrun
Metallurgia 1969, 80, (480), 131-134

46. R.E.Dolby & D.J.Widgery
Welding Research Int. 1971, 1, (3)

47. A.Vinckier
Metal Construction, 1969, 1, (6), 276-277

48. R.H.Phillips & M.F.Jordan
Welding Research Int. 1973, 3, (3), 59-68

49. E.Smith et al.
Welding and Metal Fab. 1970, 38, 242-251

50. D.M.Keane et al.
'Weld Thermal Simulators for Research' 44-49,
Welding Institute Seminar. London, 1972

51. W.F.Savage
J.Appl.Polymer Sci. 1962, 6, (21), 303-315

52. D.Widgery
'Weld Thermal Simulators for Research' 14-20,
Welding Institute Seminar. London, 1972

53. E.Smith et al.
Welding and Metal Fab. 1970, 38, (12), 496-504

54. M.G.Dawes
Brit.Weld.Journal 1968, 15, (11), 563-570

55. J.Cargill

Strain   1970, 6,   6-13

56. R.E.Dolby

'Weld Thermal Simulators for Research' Discussion II,
Welding Institute Seminar. London, 1972

57. B.Watkins et al.

Brit.Weld.Journal.   1966, 13, (6),   350-356

58. I.Hrivnak

Theory of mild and microalloy steels weldability,
Bratislava, Alfa, 1969

59. J.Myers

'Weld Thermal Simulators for Research' 38-43,
Welding Institute Seminar, London, 1972

60. J.Kilpatrick et al.

ibid   25-37.

61. Welding Institute

Weld Thermal Cycle Data

62. N.N.Rykalin

'The Calculation of Thermal Processes in Welding' 1963

63. D.Rosenthal

Trans.ASME   1946, 68, 849-866

64. O.Westby

'Temperature Distribution in the Workpiece by Welding'.
Technical University of Norway. 1968

65. Z.Paley & P.D.Hibbert

Welding Journal   1975, 54, (11), 385s-392s

66. P.S.Myers et al

Welding Research Council Bulletin,   1968

67. R.A.Mueller et al.

Welding Journal   1973, 52, (9), 411s-416s

68. J.J.Pepe & W.F.Savage

ibid   1970, 49, (12), 545s-553s

69. R.E.Dolby

Metal Construction 1972, 4, (2), 59-63

70. J.F.Knott

Metallurgia   1968, 77, (461), 93-99

71. A.A.Griffith

Phil.Trans.R.Soc. 1920, 221, 163-198

72. E.Orowan

Trans.Instn.Engrs.Shipbuilders Scotl. 1945, 89, 165-215

73. J.F.Knott
    'Fundamentals of Fracture Mechanics' Butterworths, 1973

74. G.R.Irwin
    Trans.ASME, J.Appl.Mech. 1957, $\underline{24}$, 361.

75. J.T.Barnby
    Welding and Metal Fab. 1969, $\underline{37}$, (2), 71-75

76. ASTM E399 'Method of test for plane strain fracture toughness of
    metallic materials.
  Also British Standards Draft for Development DD3

77. R.F.Smith & J.F.Knott
    Conf.'Practical Application of Fracture Mechanics to
    Pressure Vessel Technology'. Inst.Mech.Eng. 1971, 65

78. P.Terry
    Ph.D.Thesis, University of Aston. 1972

79. G.R.Irwin.
    Appl.Mater.Research. 1964, $\underline{3}$, 65

80. D.S.Dugdale
    J.Mech.Phys.Solids. 1960, $\underline{8}$, 100

81. A.H.Cottrell
    ISI Spec.Report 69, 1961, 281

82. A.A.Wells
    Crack Propagation Symposium Proc. Cranfield. 1961, $\underline{1}$, 210

83. B.A.Bilby et al
    Proc.Roy.Soc.A. 1963, $\underline{272}$, 304

84. A.A.Wells
    Brit.Weld.Journal 1963, $\underline{10}$, (11), 563-570

85. A.A.Wells
    Eng.Frac.Mech. 1969, $\underline{1}$, (3), 399-410

86. F.M.Burdekin & D.E.W.Stone
    J.Strain Analysis 1966, $\underline{1}$, (3), 399-410

87. R.W.Nicholls et al.
    'Practical Fracture Mechanics for Structural Steels'
    FI-FI3 U.K.A.E.A. 1969

88. R.Pilkington
    COD measurements at elevated temperatures'
    GEGB Report RD/L/N75/70

89. J.F.Knott
    JISI 1966, $\underline{204}$, 1014

90. J.N.Robinson & A.S.Tetelman
    'The measurement of K_{IC} on small specimens using critical
    COD'. ASTM STP 559

91. G.D.Fearnehough & B.Watkins
    Int.J.Fract.Mech. 1968, 4, (3), 233-243

92. D.Elliot & M.J.May
    COD Inferred from Plasticity Phenomena
      BISRA Report MG/C/86/68

93. D.Elliot & M.J.May
    The effect of Position on Measurement of COD
      BISRA report MG/C/47/69

94. British Standards Draft for Development DD19. 1972
    'Methods for Crack Opening Displacement Testing'.

95. G.L.Archer
    Welding Institute Report E/63/75. 1975

96. J.E.Srawley
    Int.J.Frac.Mech.   1970, 6, 441-444

97. D.V.Thornton
    Eng.Fract.Mech.   1970, 2, 125-143

98. D.J.Hayes & C.E.Turner
    Int.J.Frac.Mech.   1974, 10, (1), 17-32

99. N.Levy et al
    Int.J.Fracture   1971, 7, 143-156

100. F.M.Burdekin & T.E.Taylor
    J.Mech.Eng.Sci.   1969, 11, (5), 486

101. J.N.Robinson & A.S.Tetelmen
    Third International Congress on Fracture. Munich, 1973

102. C.F.Tiffany & J.N.Masters
    'Fracture Toughness Testing and Its Applications'.
    ASTM STP 381 249-277

103. J.F.Kiefner et al.
    'Progress in Flaw Growth and Fracture Toughness Testing'.
    ASTM STP 536 1973

104. C.L.M.Cottrell
    Brit.Weld.Journal   1968, 15, 262-267

105. J.F.Knott
    Proc.Roy.Soc. A285 1965, 150

106. F.M.Burdekin & M.G.Dawes
    The Practical Application of Fracture Mechanics to
    Pressure Vessel Technology. London, 1971

107. J.R.Rice
    Trans. ASME, J.Appl. Mech. 1968, 379

108. R.J.Bucci et al.
    ASTM STP 514 1972, 40.

109. J.A.Begley & J.D.Landes
ibid   1-20

110. J.R.Rice et al.
ASTM   STP   536.   1972

111. J.D.G.Sumpter
Third International Post-experience Course on Fracture
Mechanics,   London,   1974

112. G.Green et al.
'Mechanics & Mechanisms of Crack Growth'. Cambridge 1973

113. M.G.Dawes
Welding Institute Report   E/65/75   1975

114. J.D.Landes & J.A.Begley
Westinghouse Research Report,   1973

115. G.R.Egan
Eng.Frac.Mech.   1973, 5, (1), 167

116. J.D.Harrison
Welding Institute Report   E/64/75   1975

117. T.C.Harrison & G.D.Fearnehough
Int.J.Frac.Mech.   1969, 5, (3), 348-349

118. J.F.Knott
JISI   1967, 205, (3), 288-291

119. W.J.Clarke & L.J.Ceschini
Materials Evaluation   1969, 27, 180-184

120. M.H.Jones & W.F.Brown
Materials, Research and Standards, 1964, 4, (3), 120-129

121. D.M.Gilbey & S.Pearson
Royal Aircraft Establishment Technical Report 66402, 1966

122. D.Elliot
Effect of second phase particles on the mechanical
properties of steel. ISI 1971, 66

123. G.Green
The Practical Implications of Fracture Mechanisms.
Institution of Metallurgists, Newcastle, 1971, 159-160.

124. D.Elliot
ibid   21-27

125. J.M.Krafft
Applied Materials Research, 1964, 3, 88-101.

126. P.J.H.Maunder & J.A.Charles
JISI, 1968, 206, 705

127. D.Brooksbank & K.W.Andrews
ibid   595

128. M.F.Ashby

        Phil.Mag.   1966, <u>14</u>, 1157

129. T.J.Baker & J.A.Charles

        ISI/BISRA Conference, Scarborough, 1971

130. B.I.Edelson & W.M.Baldwin

        Trans ASM   1962, <u>55</u>, 230.

131. A.C.Steel

        Welding Institute Report   M/64/71   1971

132. A.M.Turkalo & J.R.Low

        Trans AIMMPE   1958, <u>212</u>, 750

133. C.G.Chipperfield et al

        Third International Congress on Fracture. Munich, 1973

134. J.I.Morley

        'Metallurgical Developments in High Alloy Steels'
        ISI Special Report 86,   92-100

135. British Aircraft Corporation

        Reports ATN   382/420/440/480, Warton   1966

136. Brown-Firth Laboratories.

        Firth Vickers   Data Sheet 65/1

137. R.Johnson et al.

        Fulmer Research Association Report K43A/55/CB43A2
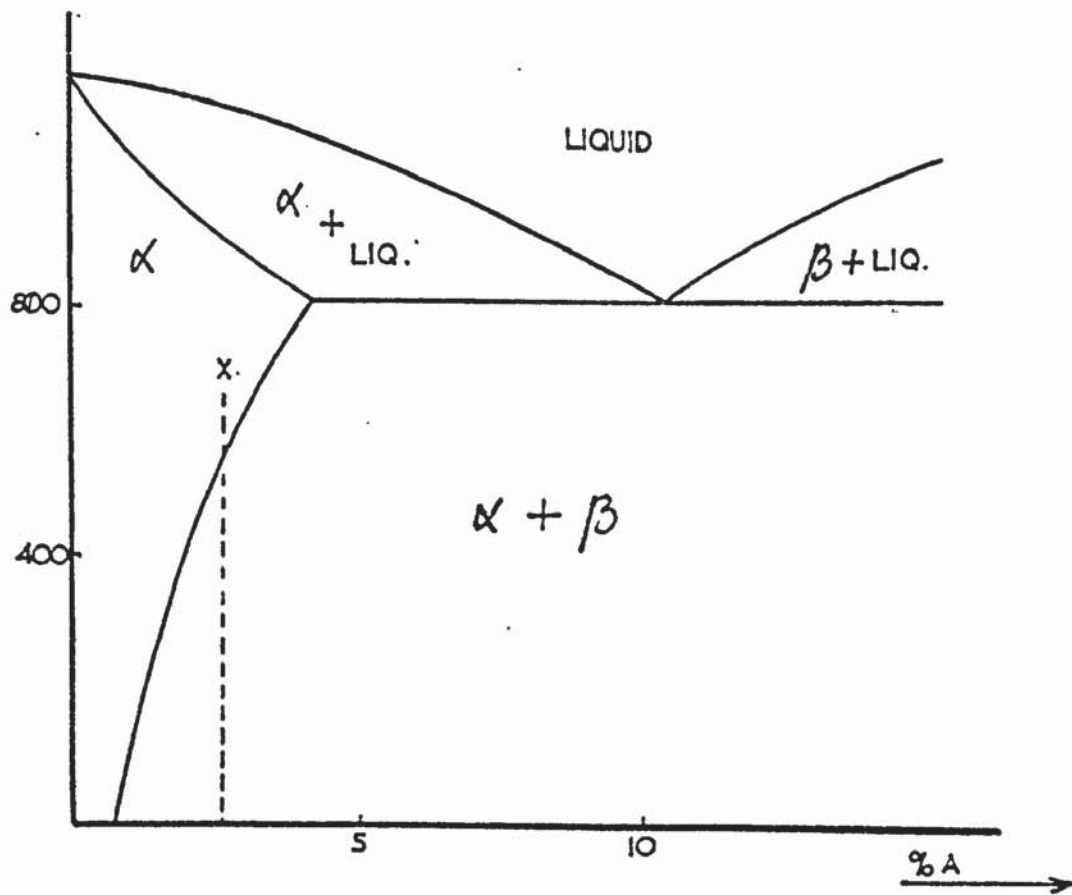
Fig. 1. Diagram of decreasing solid solubility.
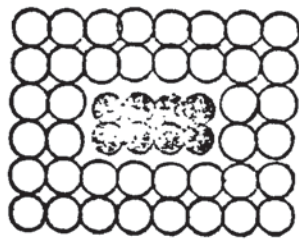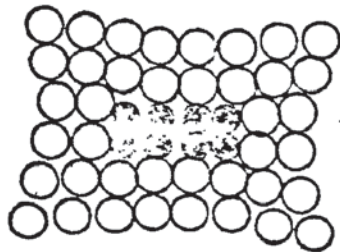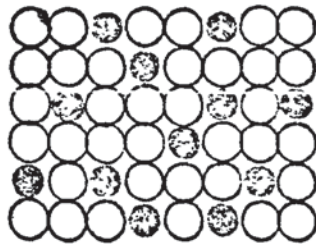
Fig. 2. Effect of precipitate coherency.
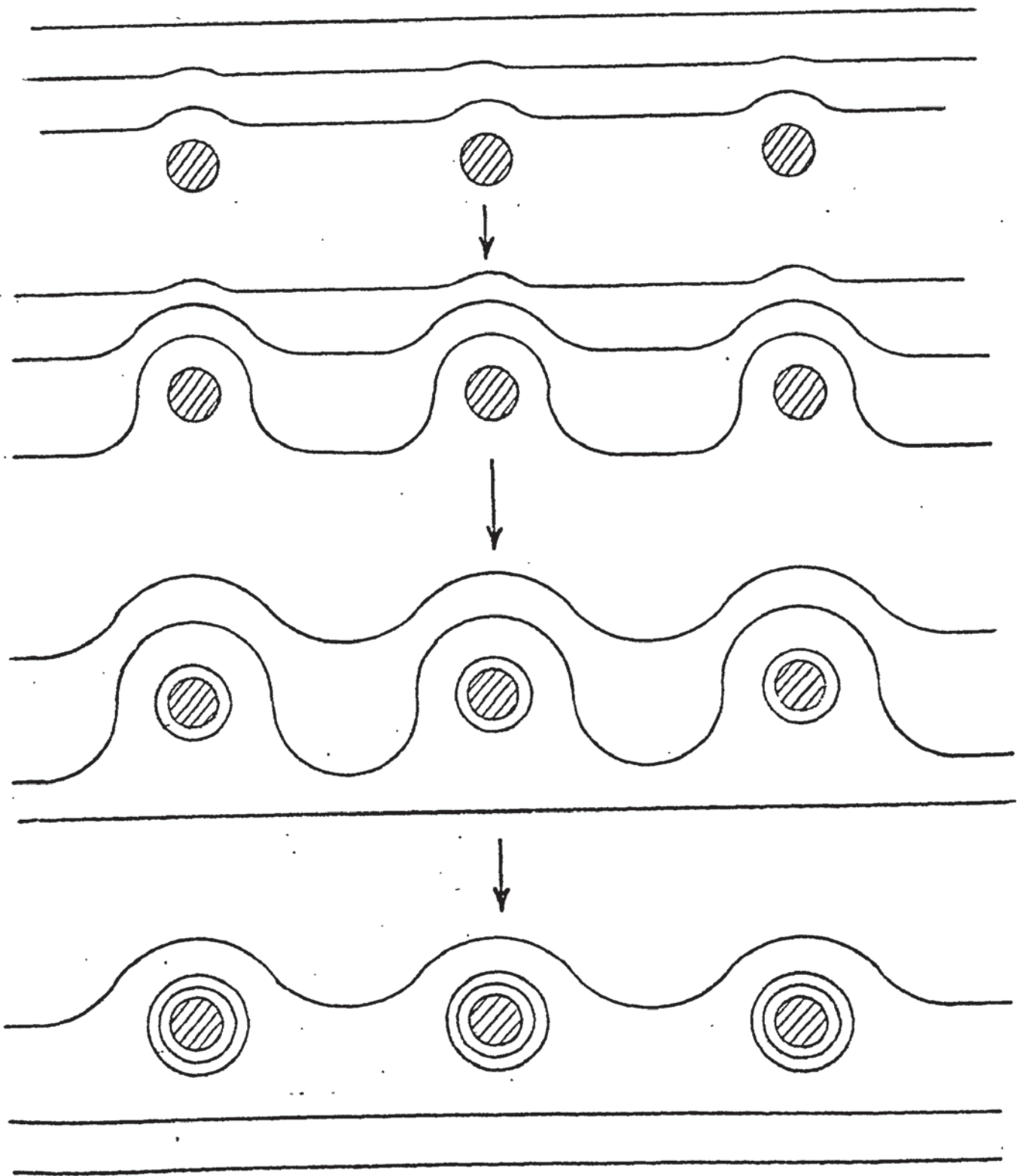
Fig. 3. Orowan model of dislocation bowing.
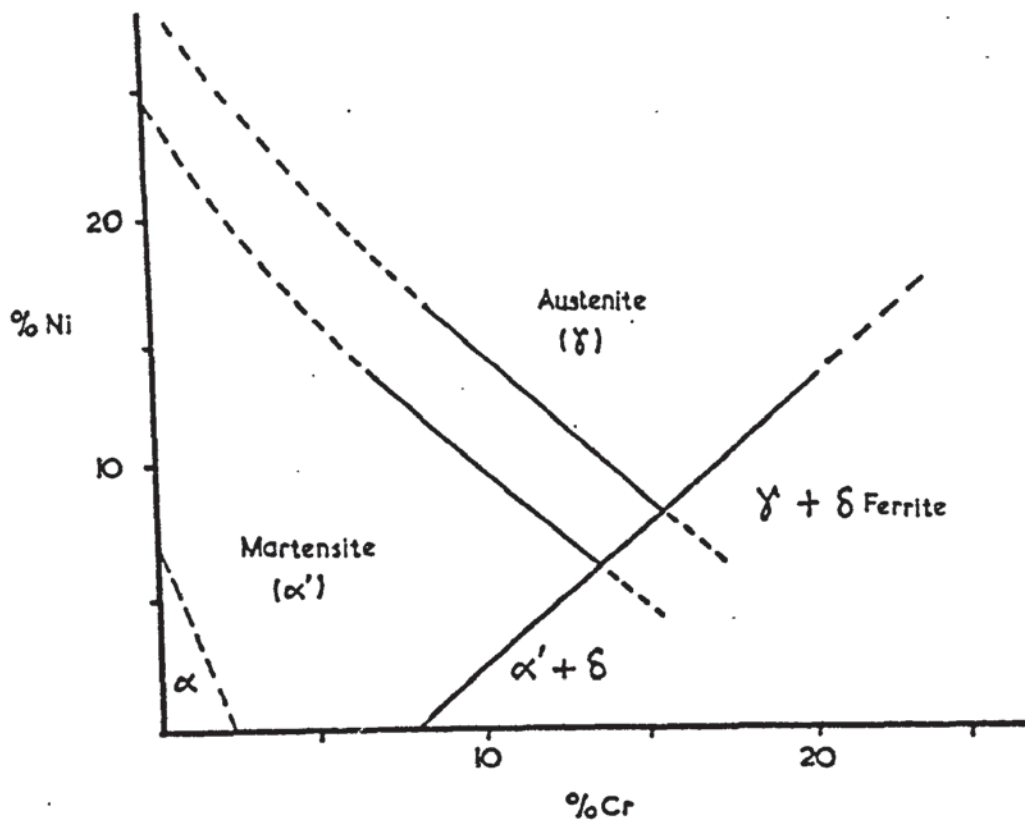
Fig. 4. Schaeffler diagram of nickel-chromium system.
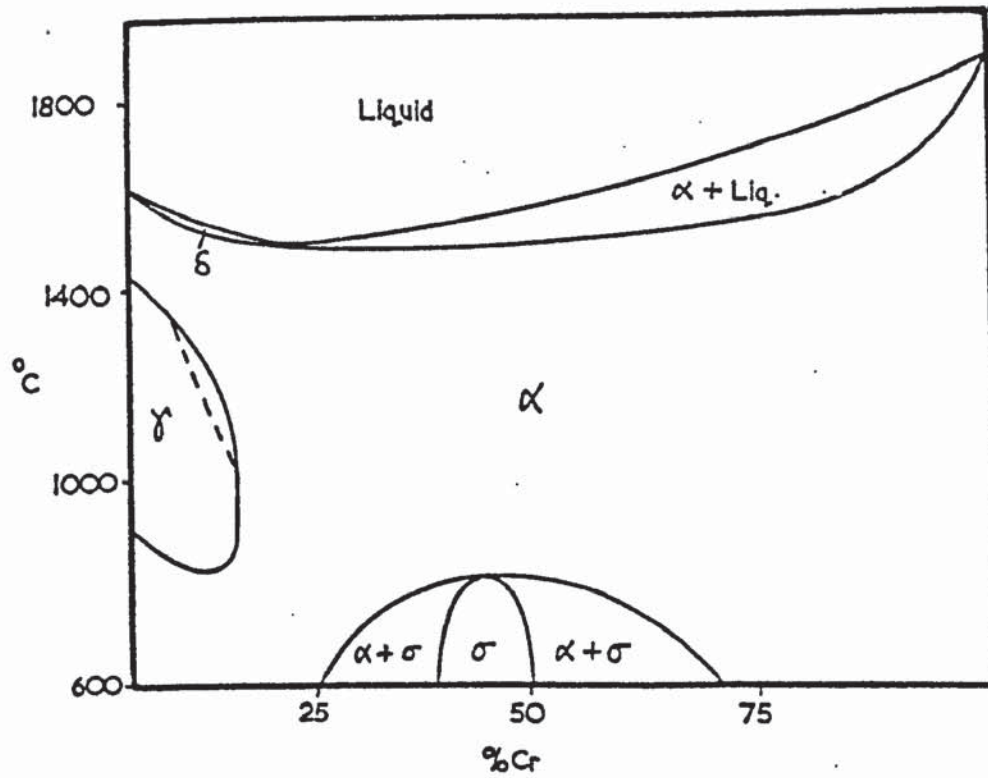
Fig. 5. The iron-chromium equilibrium diagram.
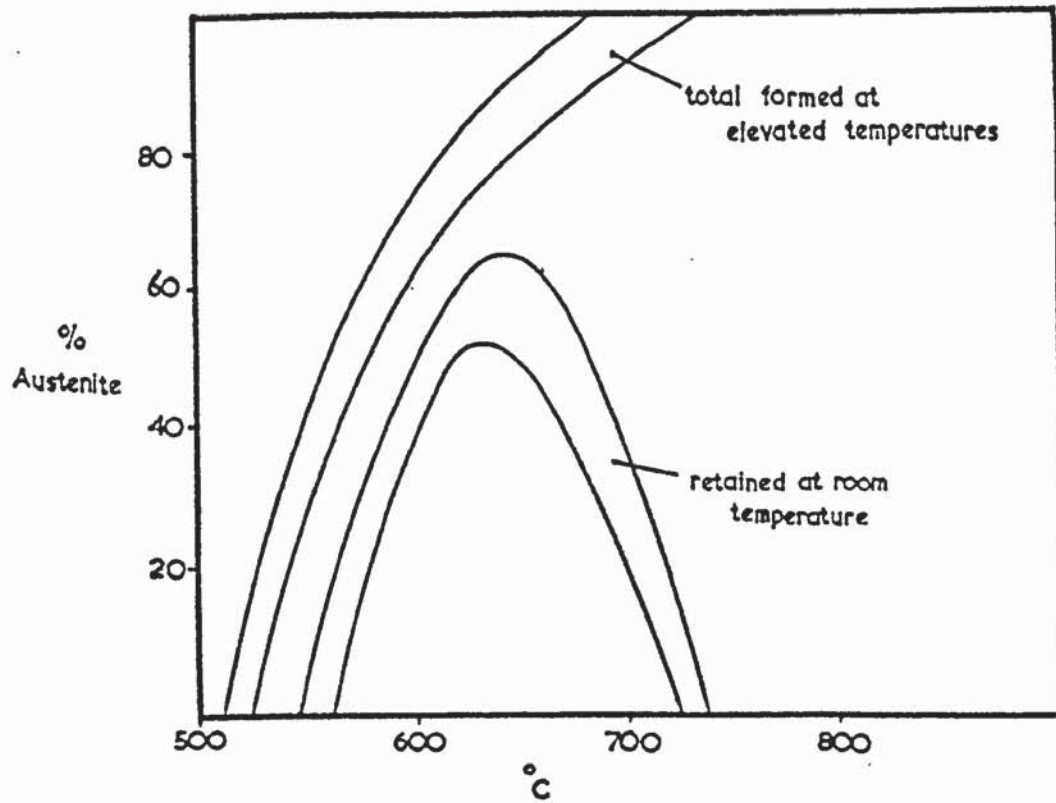
Fig. 6. Austenite formation in maraging steel.
(double lines indicate experimental scatter)
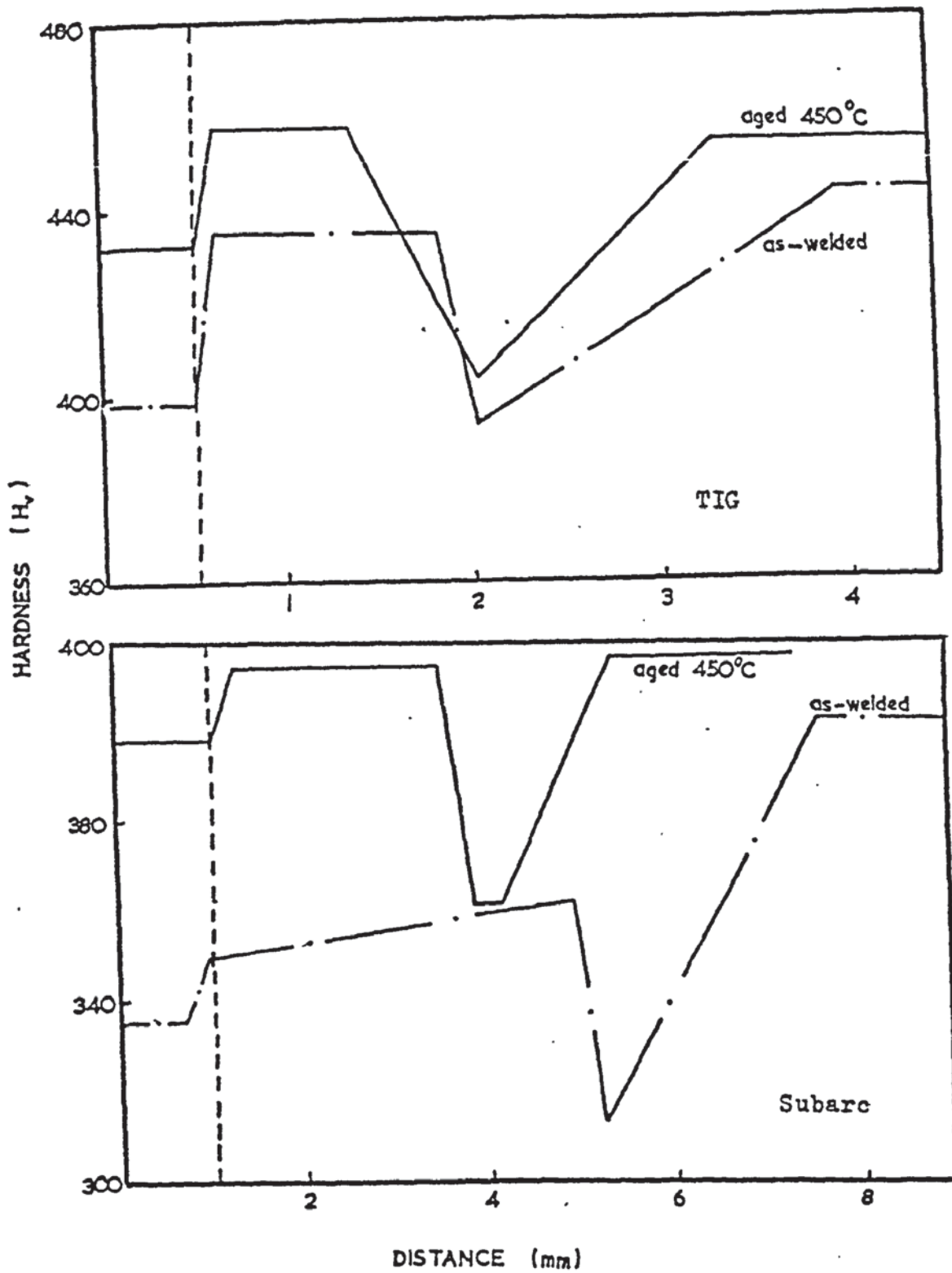
Fig. 7. Hardness traverse of FV520B weld beads [34]
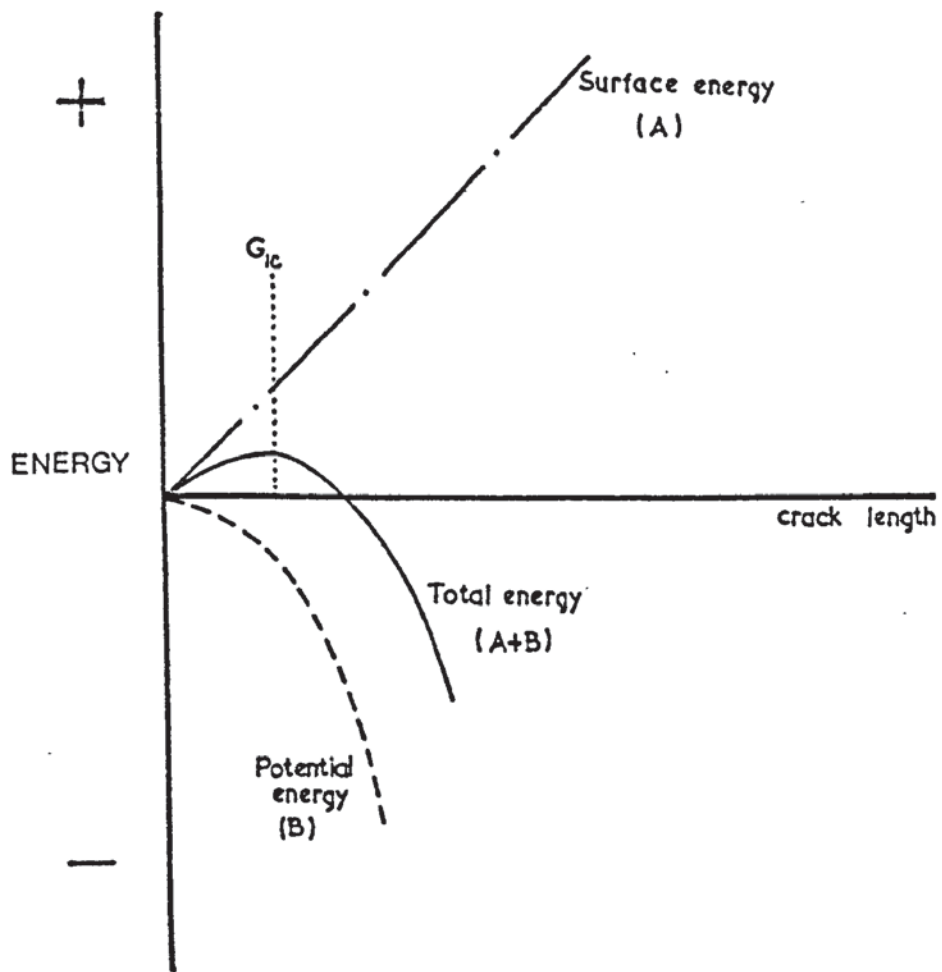
Fig. 8. Variation of energy content with crack length.
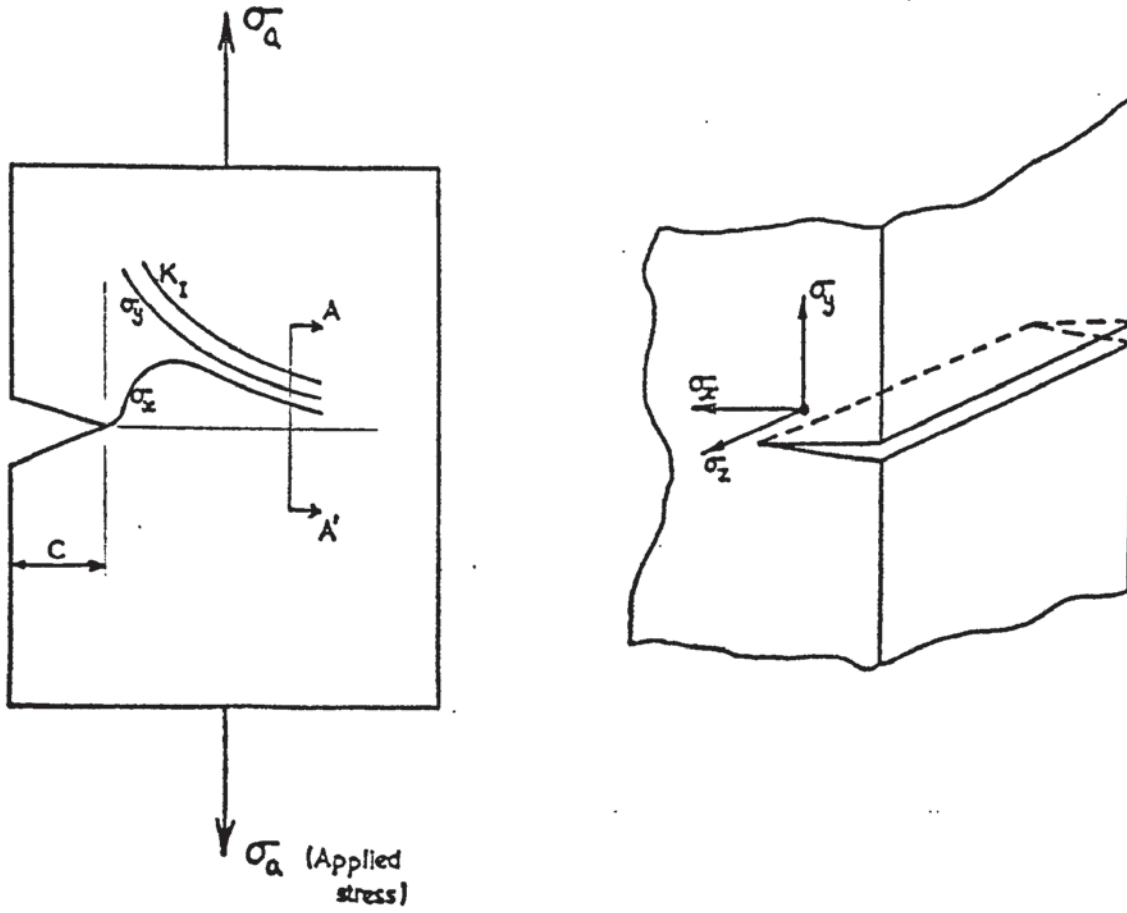
Fig. 9.   Stresses at the root of a notch.
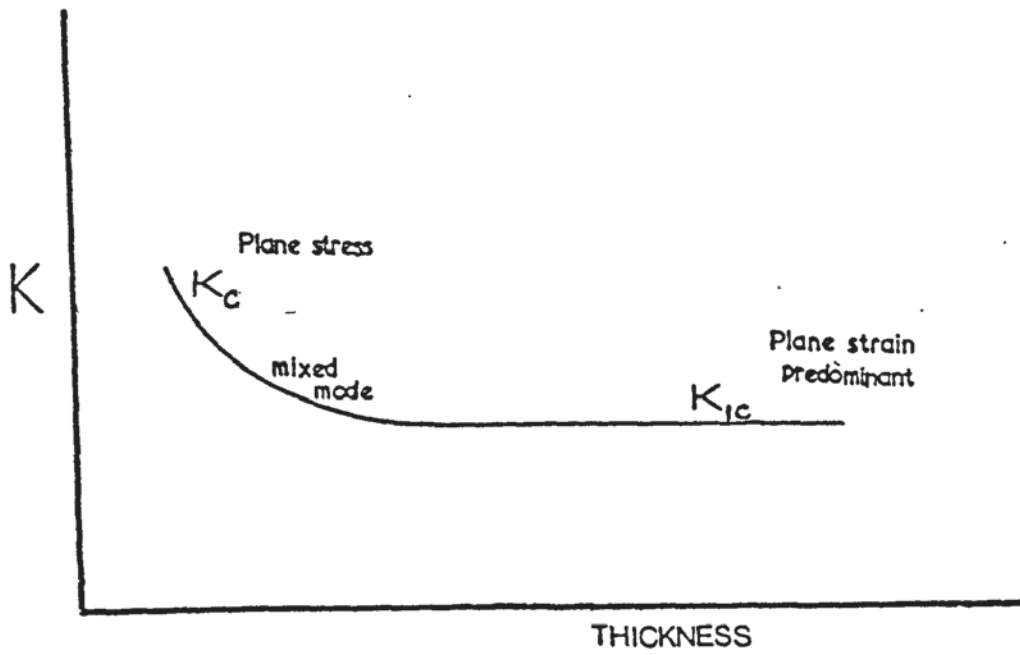
Fig. 10. Variation of fracture toughness with thickness.
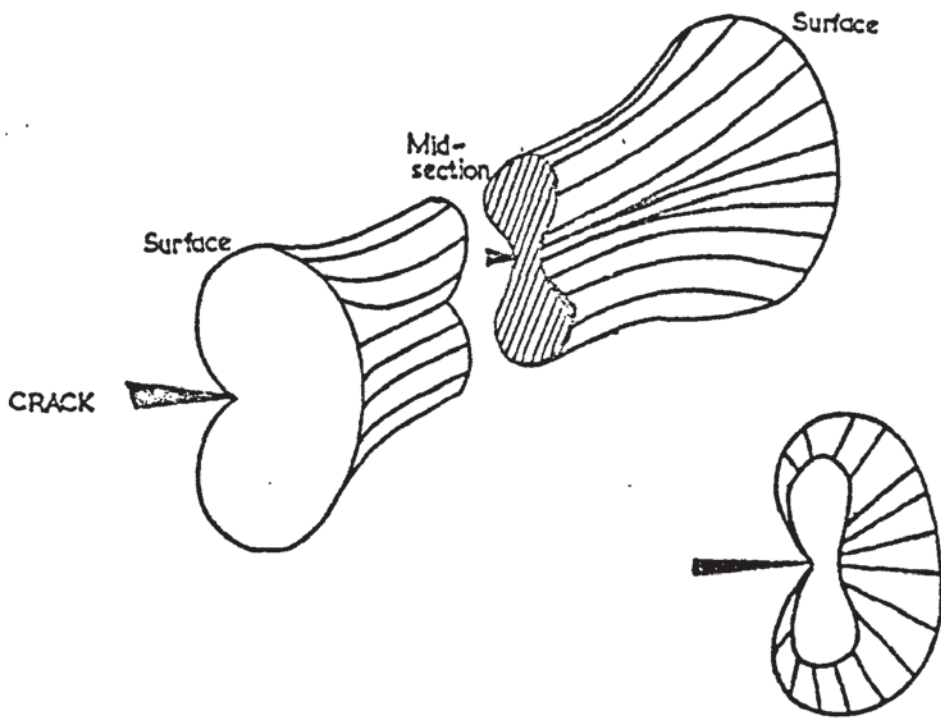
Fig. 11. Zones of plane strain and plane stress.
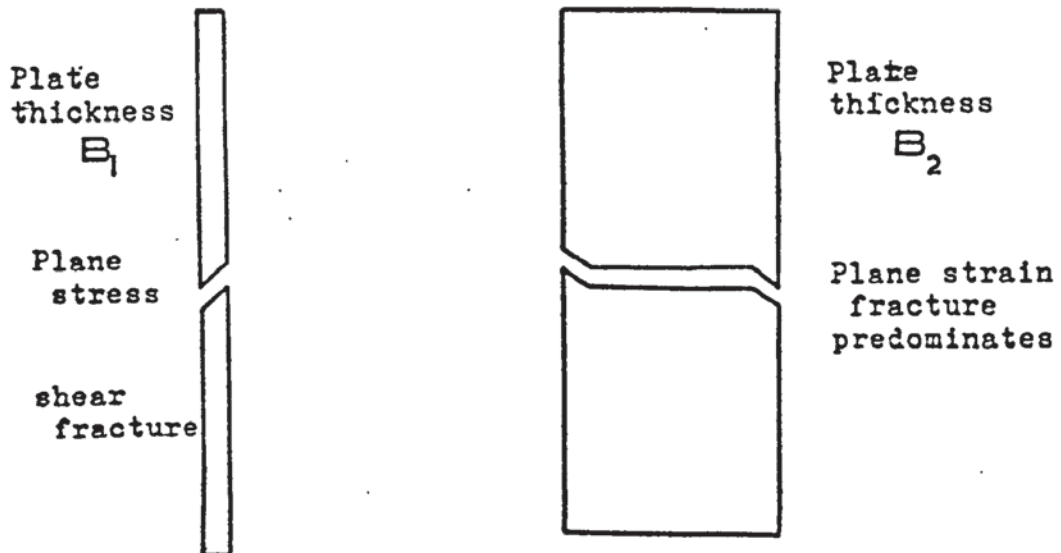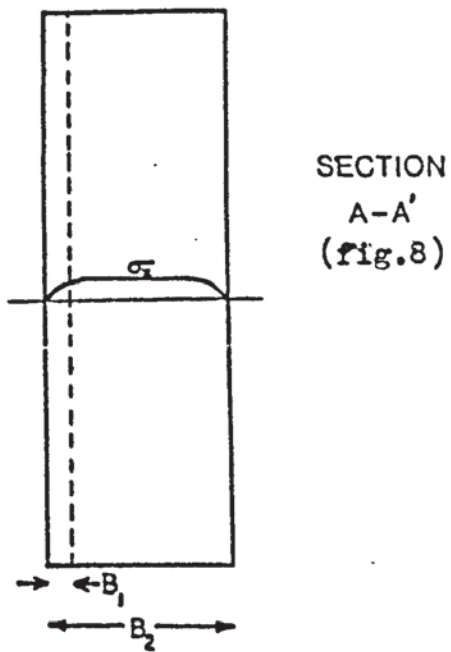
Fig. 12. Influence of through-thickness (σ_z) stress on fracture surface topography.
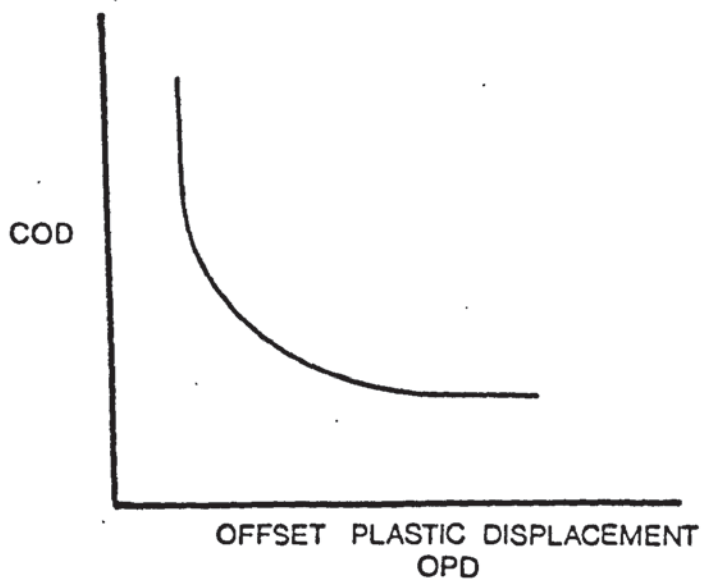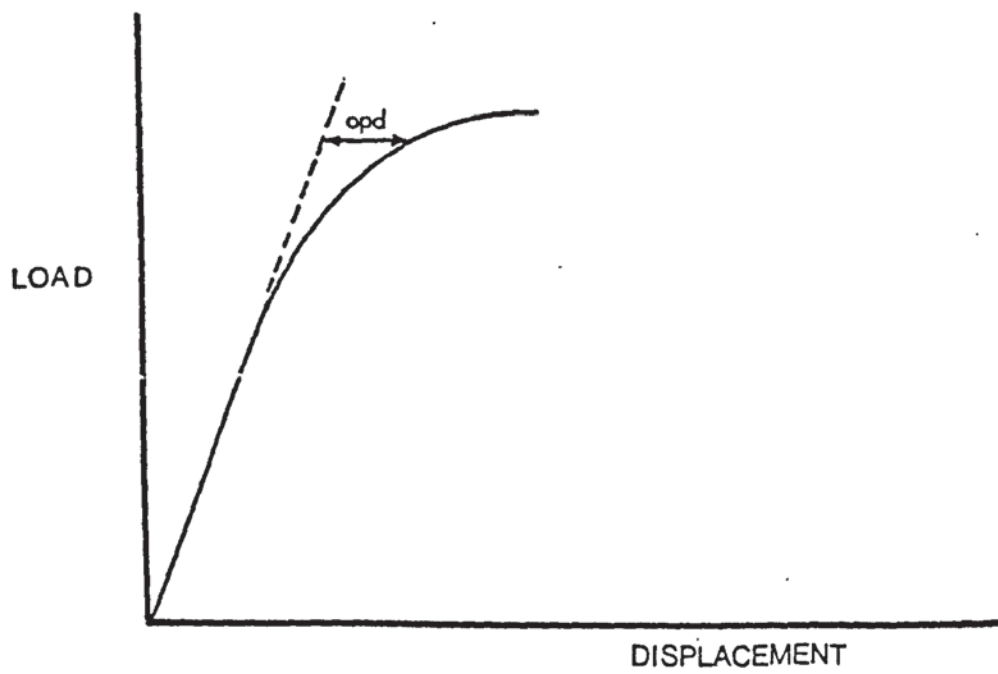
Fig. 13. Method of deriving Offset Plastic Displacement
calibration curves.

$$\delta = \frac{(W-a)\,V_g}{W+2a+3z}$$
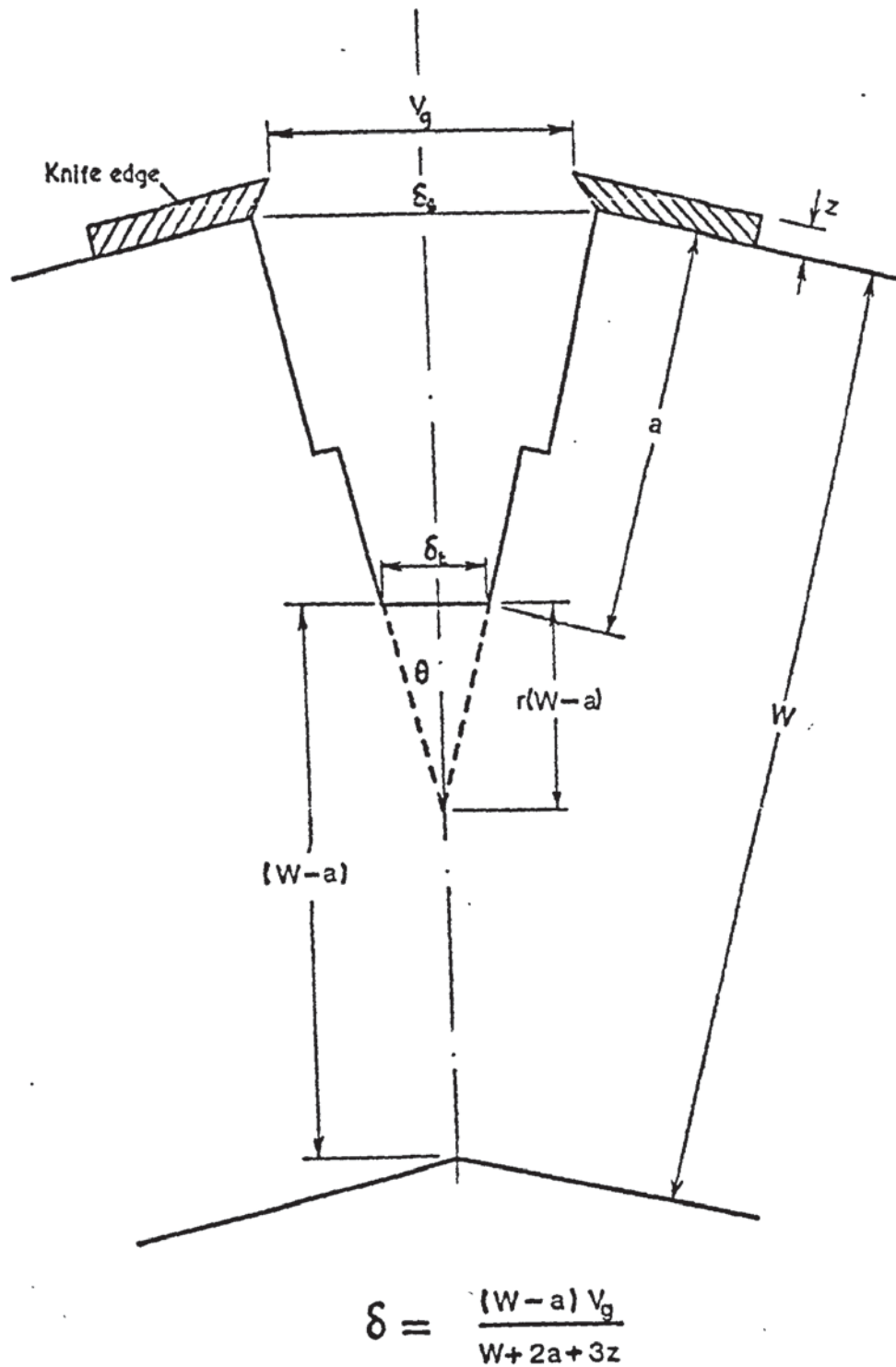
Fig. 14. Geometric assumptions in calculation of COD.
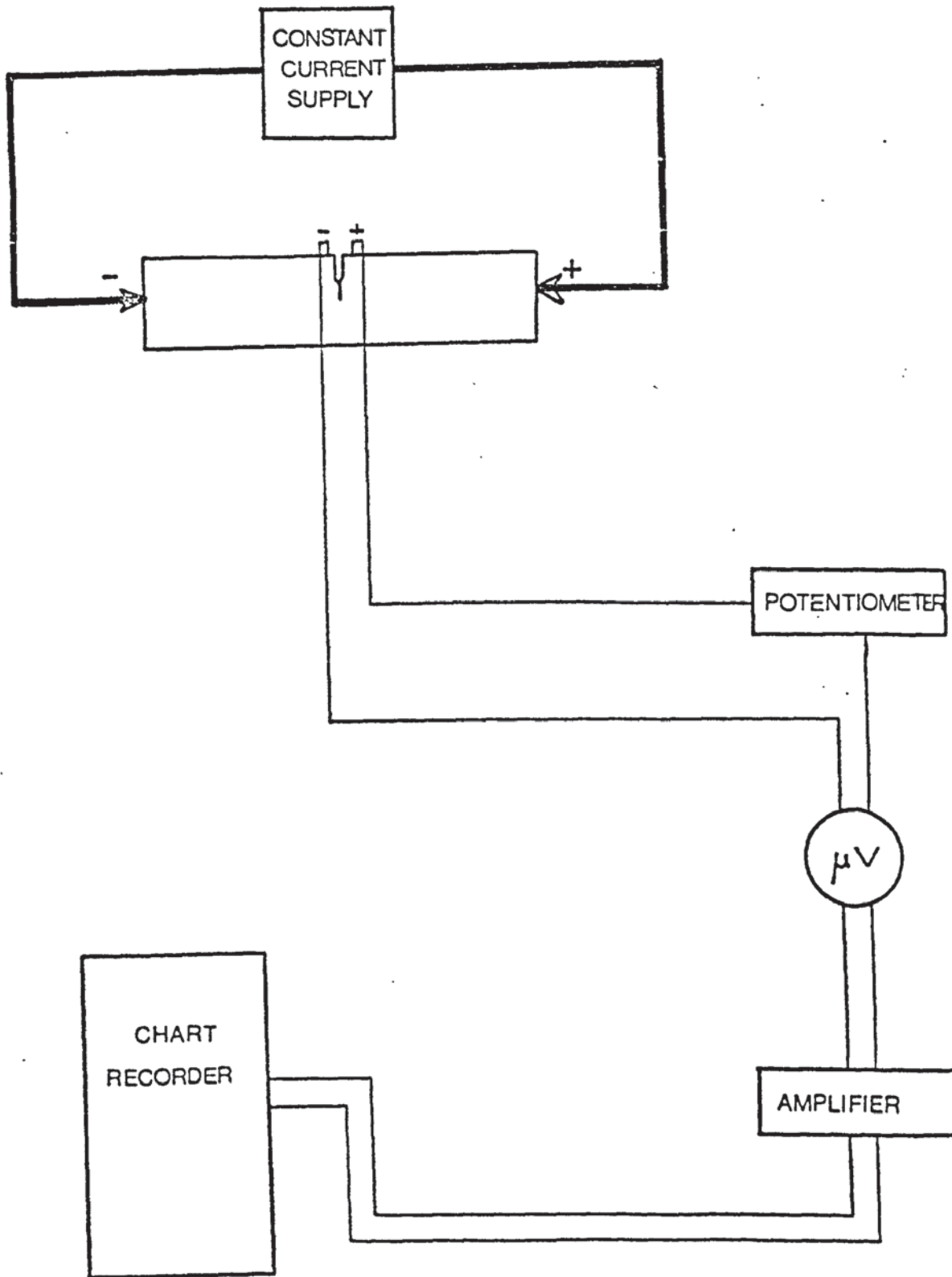
Fig. 15. Schematic diagram of potential drop crack monitoring system.
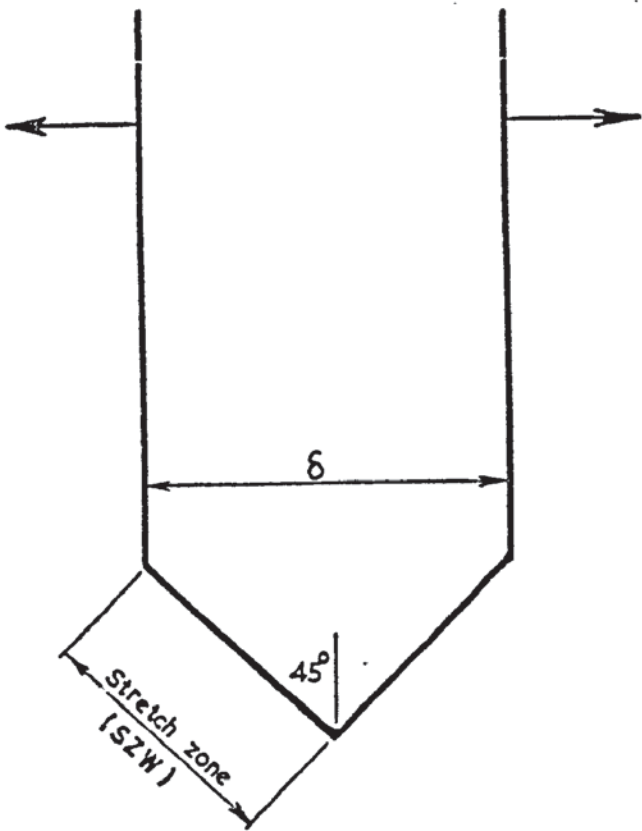
By Pythagoras

$$(SZW)^2 + (SZW)^2 = \delta^2$$
$$2(SZW)^2 = \delta^2$$
$$\delta = \sqrt{2} \cdot SZW$$

Fig. 16. Relationship of stretch zone width to COD.
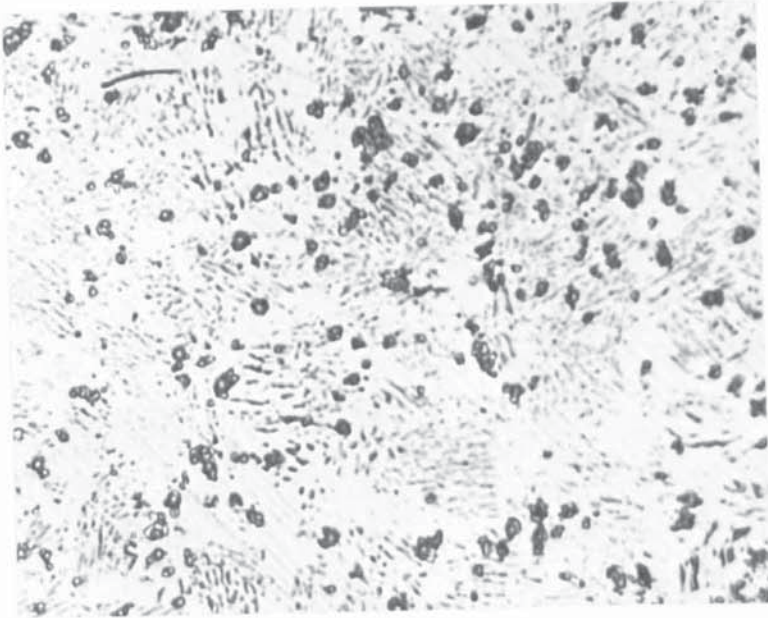
Etch; Murikami's
    X 1000
    aged 620°C
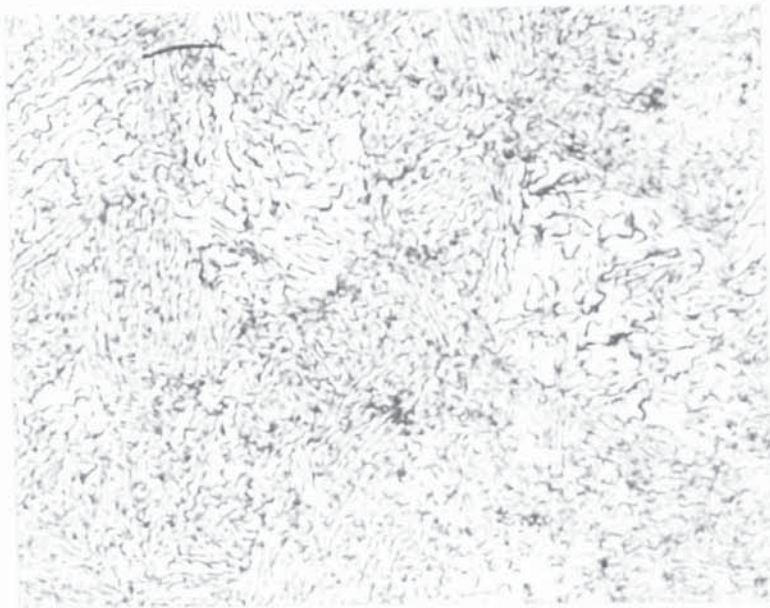
Carbide distribution

Etch;   Alcoholic
        Ferric Chloride
    X 1000
    aged 620°C

Martensitic matrix
 with pools of
 retained austenite
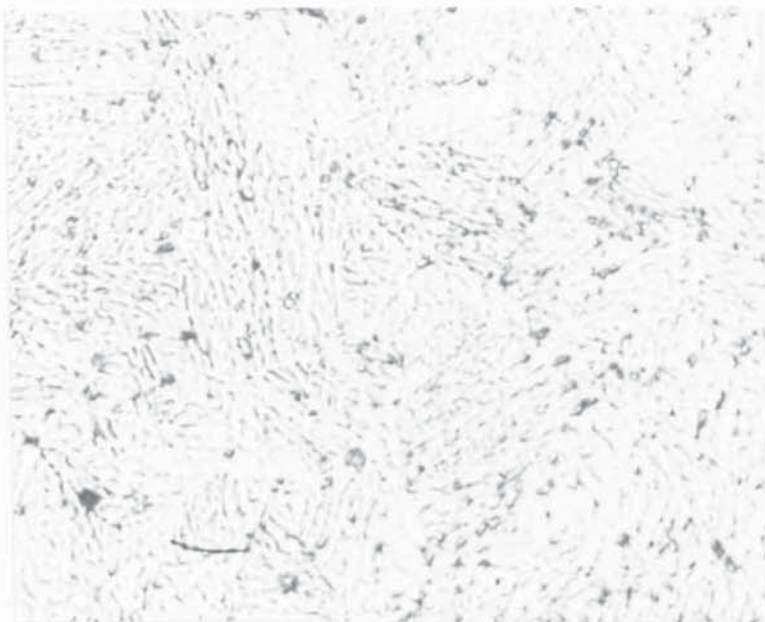
Etch;   Electrolytic
        Oxalic Acid
    X 1000
    aged 620°C

Axial distribution
 of carbides

Fig. 17.   Microstructure of FV520B

(a)
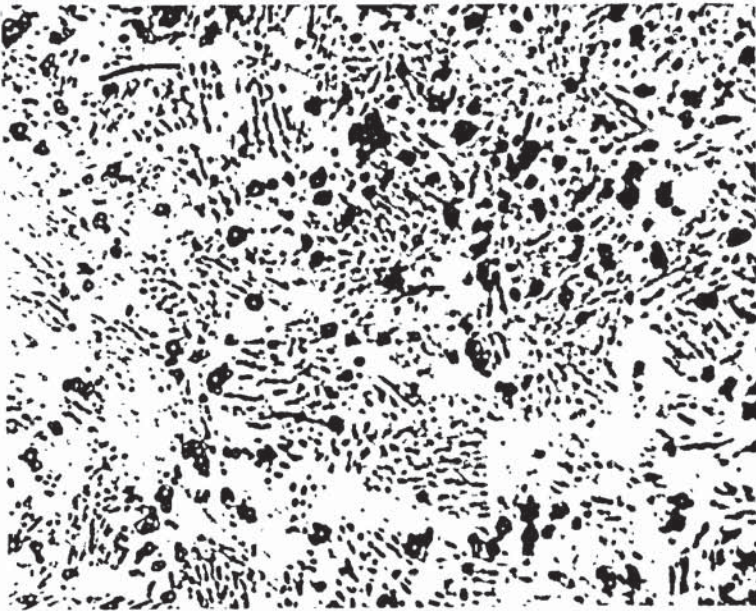
Etch; Murikami's
    X 1000
    aged 620°C

Carbide distribution

(b)
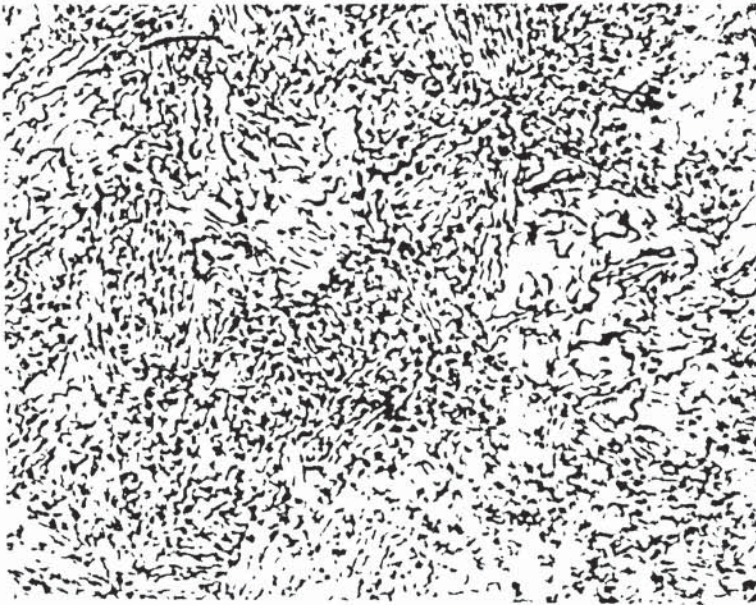
Etch; Alcoholic
       Ferric Chloride
    X 1000
    aged 620°C

Martensitic matrix
with pools of
retained austenite

(c)

Etch; Electrolytic
       Oxalic Acid
    X 1000
    aged 620°C

Axial distribution
of carbides

Fig. 17.   Microstructure of FV520B

(d)

Etch; Acidified
        Ferric Chloride

X 1000

aged 620°C

Grain size

(e)
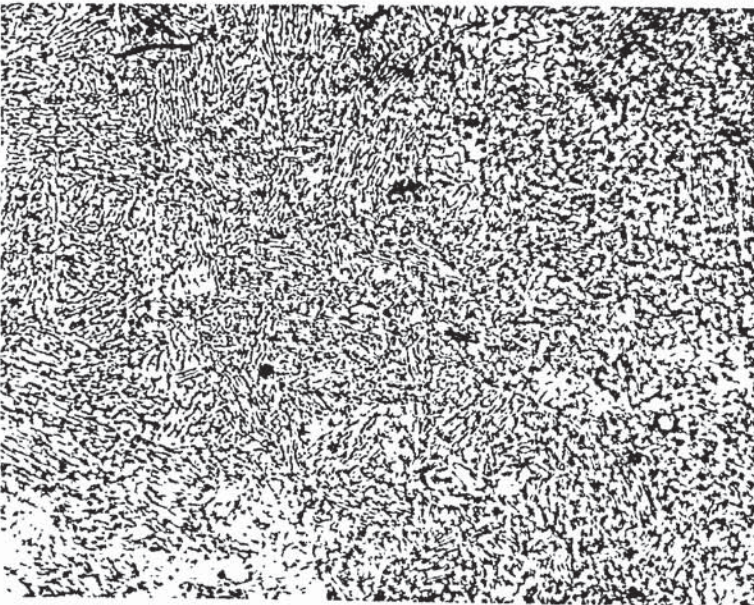
Etch; Alcoholic
        Ferric Chloride

X 500

aged 450°C

Martensitic matrix

(f)
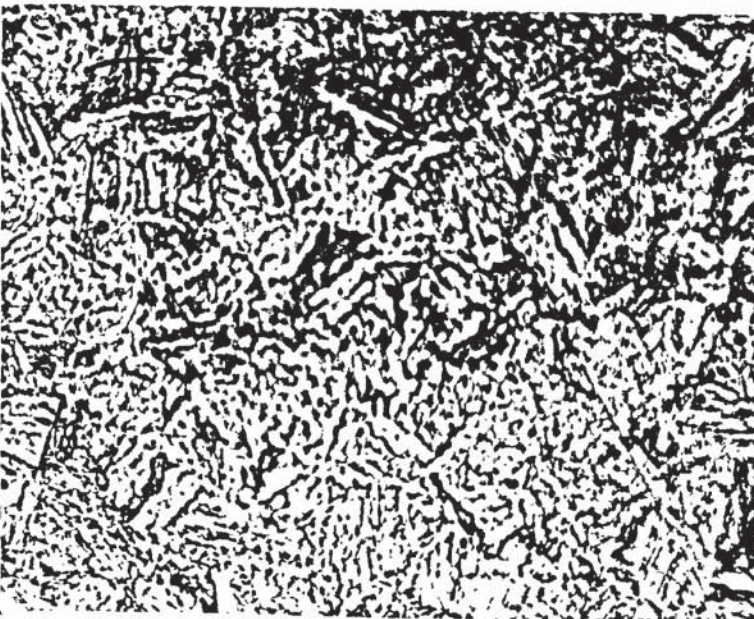
Etch; Pickering's
        Reagent

X 500

aged 450°C

Martensitic block
structure

Fig. 17. (cont.)   Microstructure of FV520B
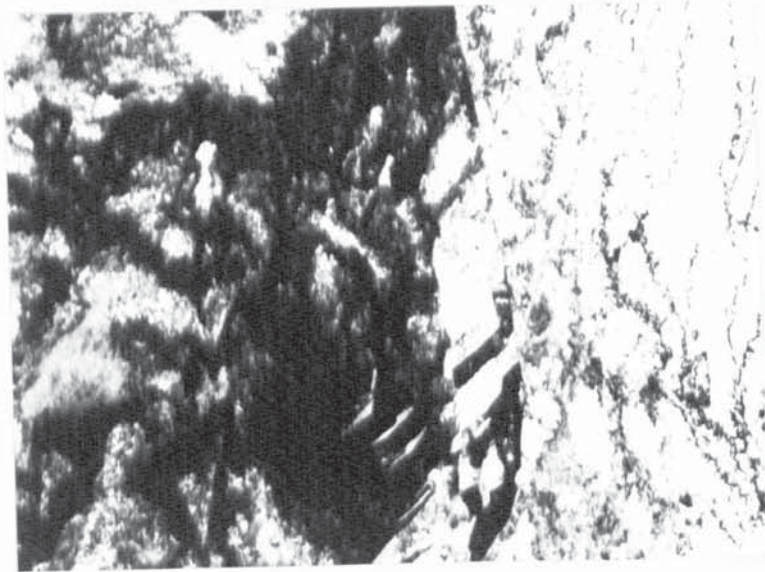
grain
boundary

diffuse
areas of
high
dislocation
density

(a) Aged 620°C, X 12,000

triple
point

(b) Aged 620°C, X 50,000

Fig. 18. Transmission Electron Micrographs of FV520B
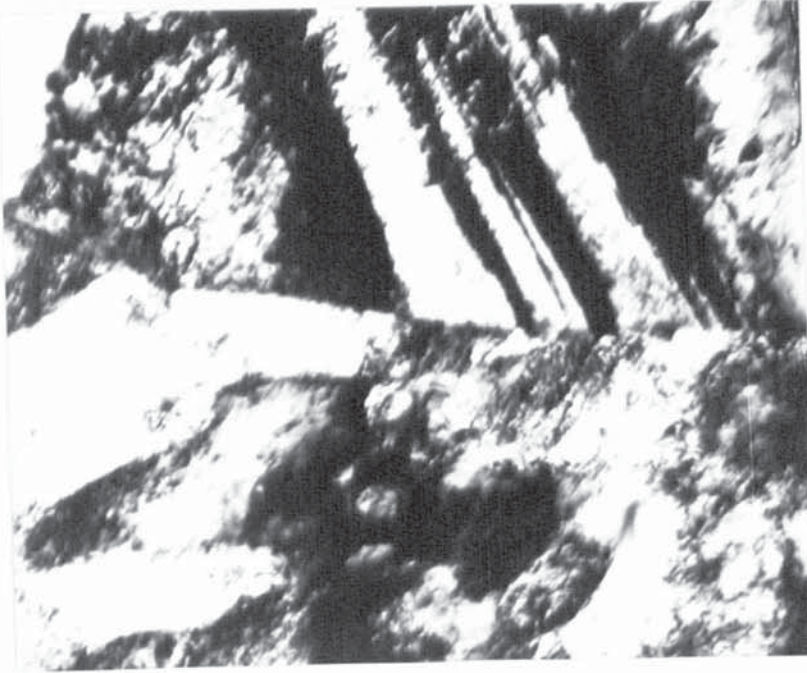
twinning

(c)   Aged 620°C,   X 40,000
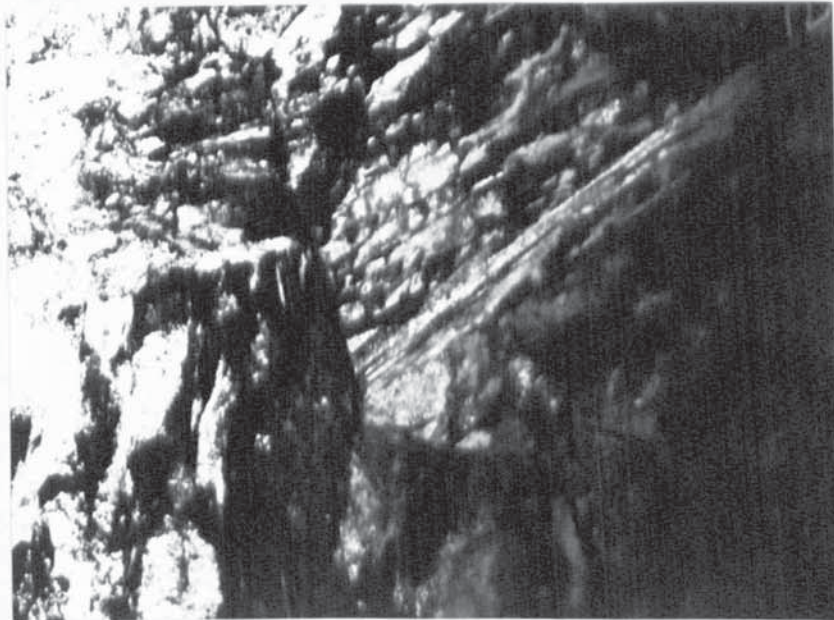
martensite
laths
breaking
down into
sub-cells

(d)   Aged 620°C,   X 7,000

Fig. 18.(cont.)   Transmission Electron Micrographs of FV520B
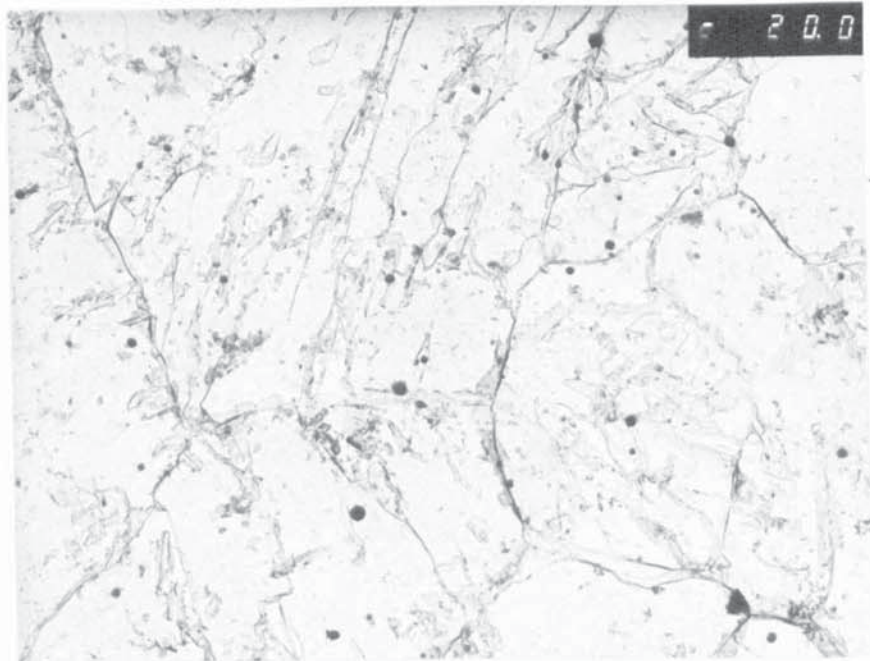
(a) showing grain size; fine precipitation
    within grains; fine columnar precipitate
    along grain boundaries; formation of cell
    sub-structure.   X 20,000
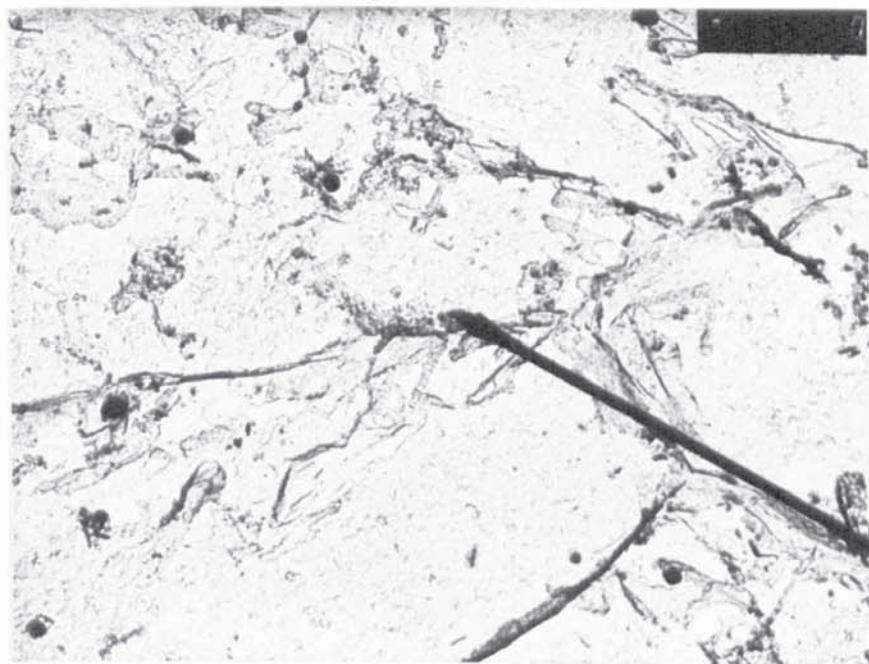
(b) arrowed particle indicates source of diffraction
    patterns in figs. 19c and 19d.   X 50,000

Fig. 19.   Extraction replicas of FV520B
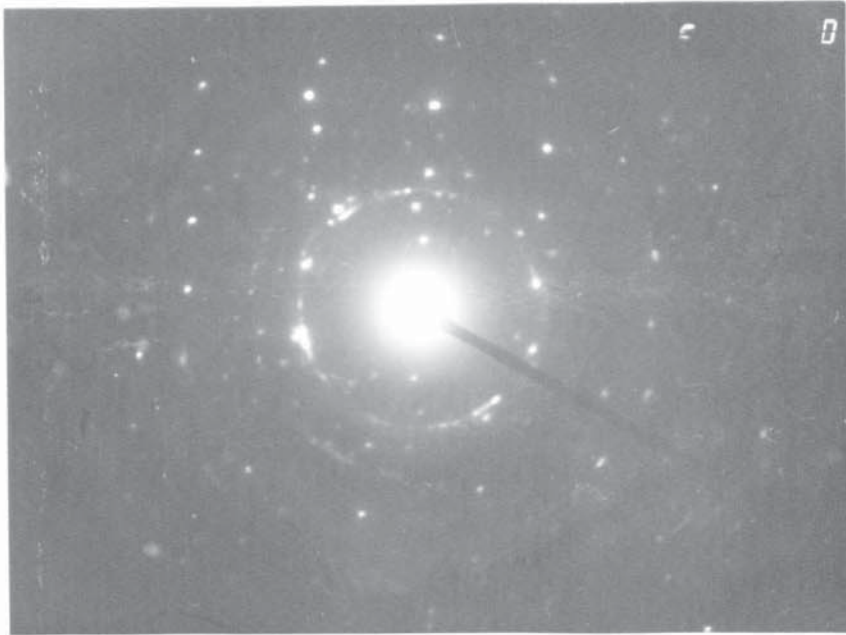
(c) diffraction pattern obtained from fig.19b

(110)

(310)

(211)

A
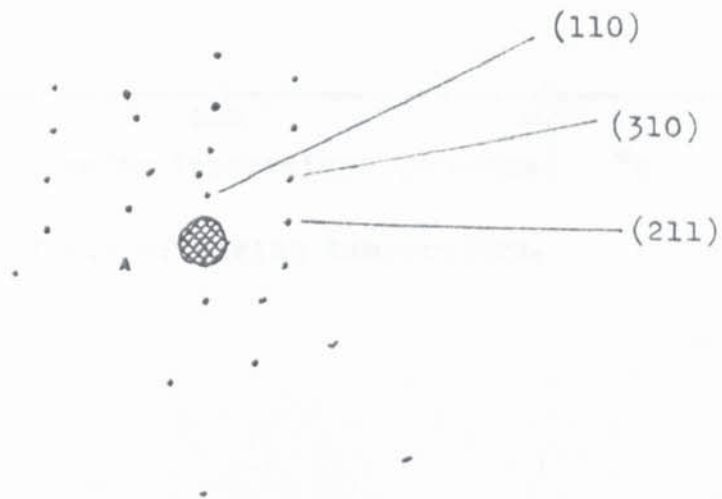
(d) indexing of diffraction pattern

Fig. 19.(cont.)   Extraction replicas of FV520B
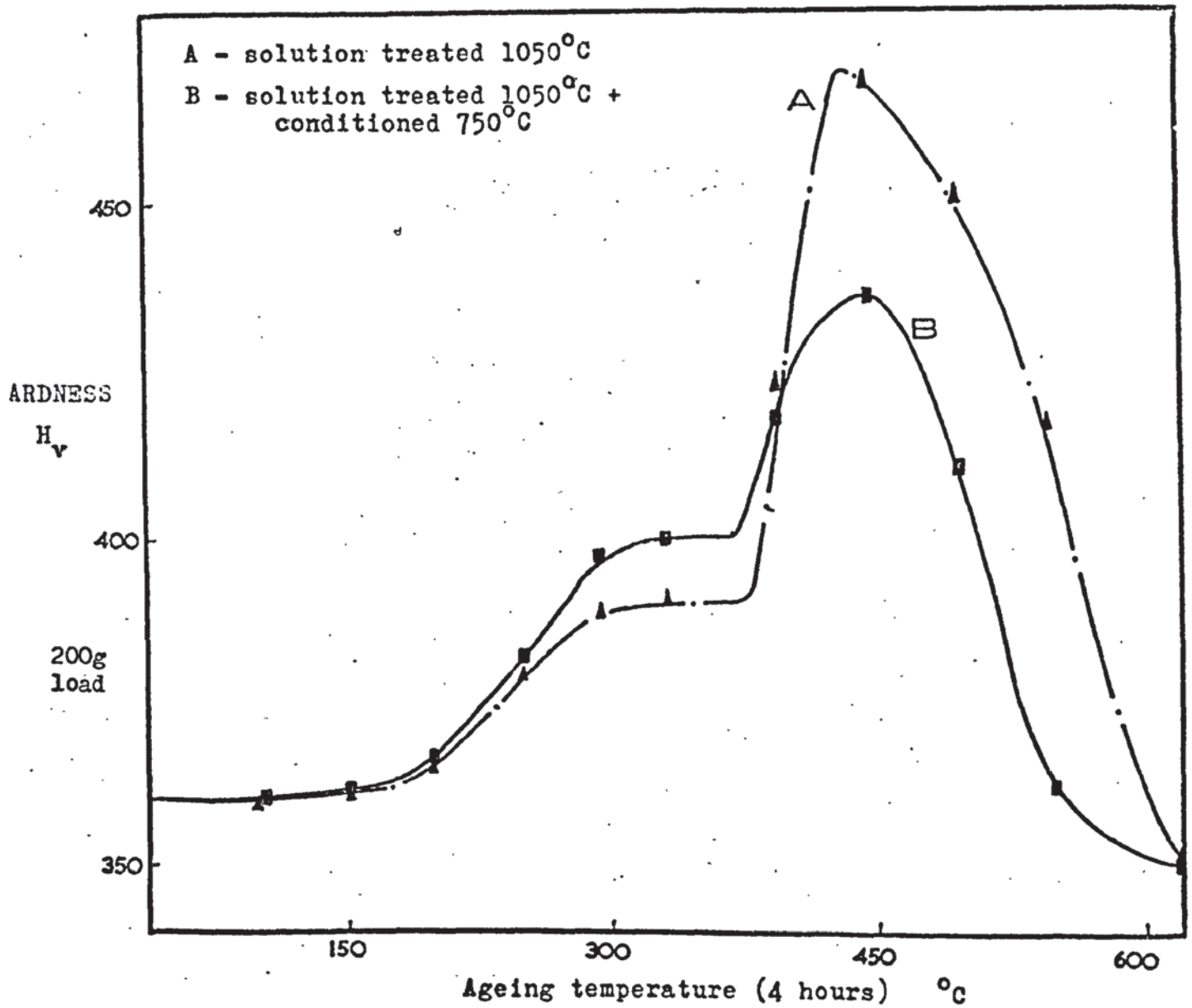
Fig. 20. Effect of ageing temperature.
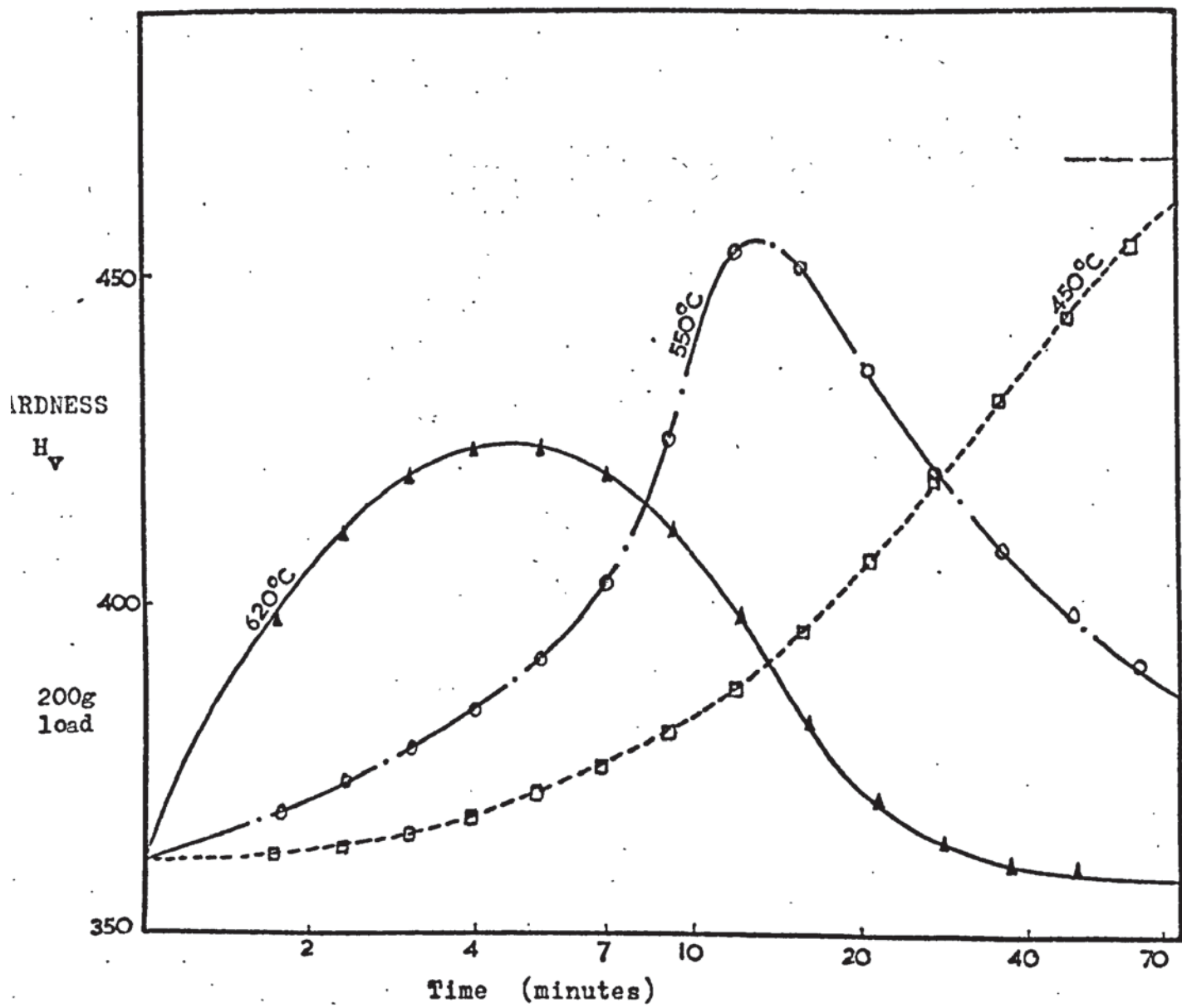
Fig. 21. Speed of ageing response.

ELECTRODE POSITIVE

HIGH PURITY ARGON SHIELDING GAS - 14 litres/hour

ARC VOLTAGE	29 V
WELDING CURRENT	295 A
WELDING SPEED	4.8 mm/sec
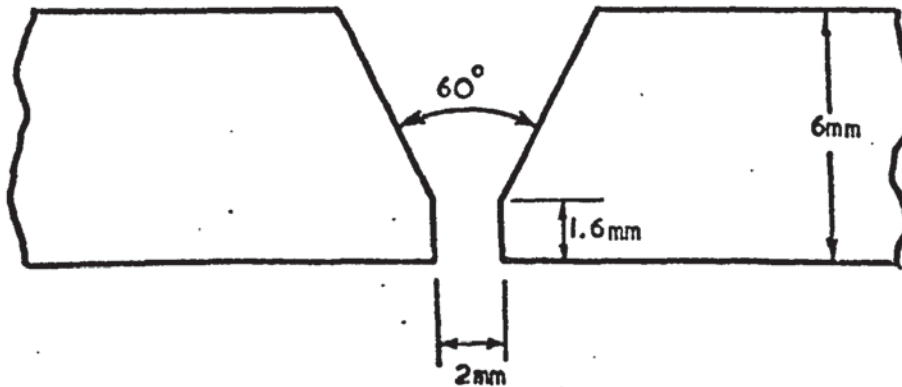
Fig. 22. Plate preparation and welding conditions employed
for welding trials.
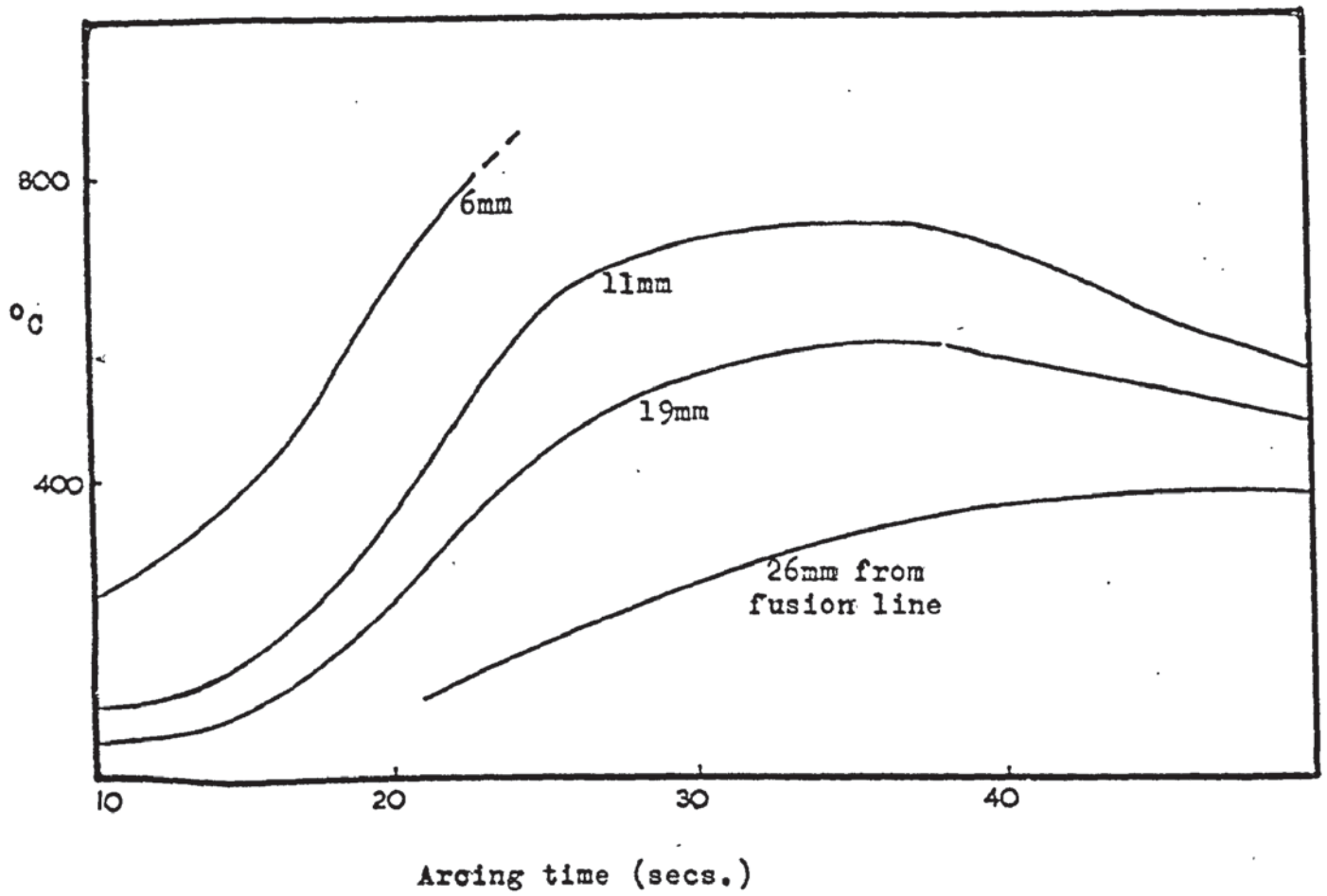
Fig. 23. Temperature distribution in the plate during welding.
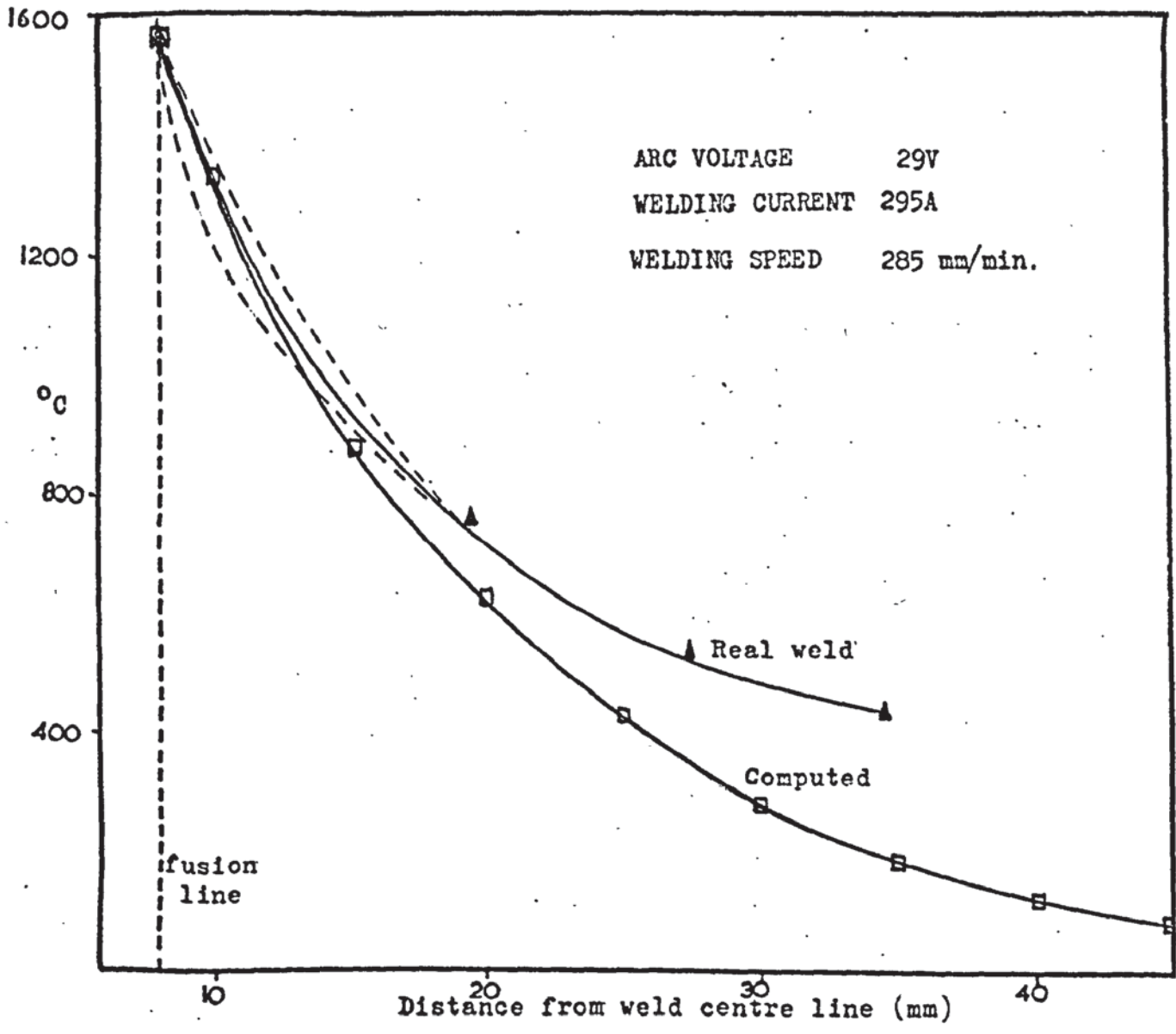
Fig. 24. Comparison of real and simulated weld temperature
distribution.
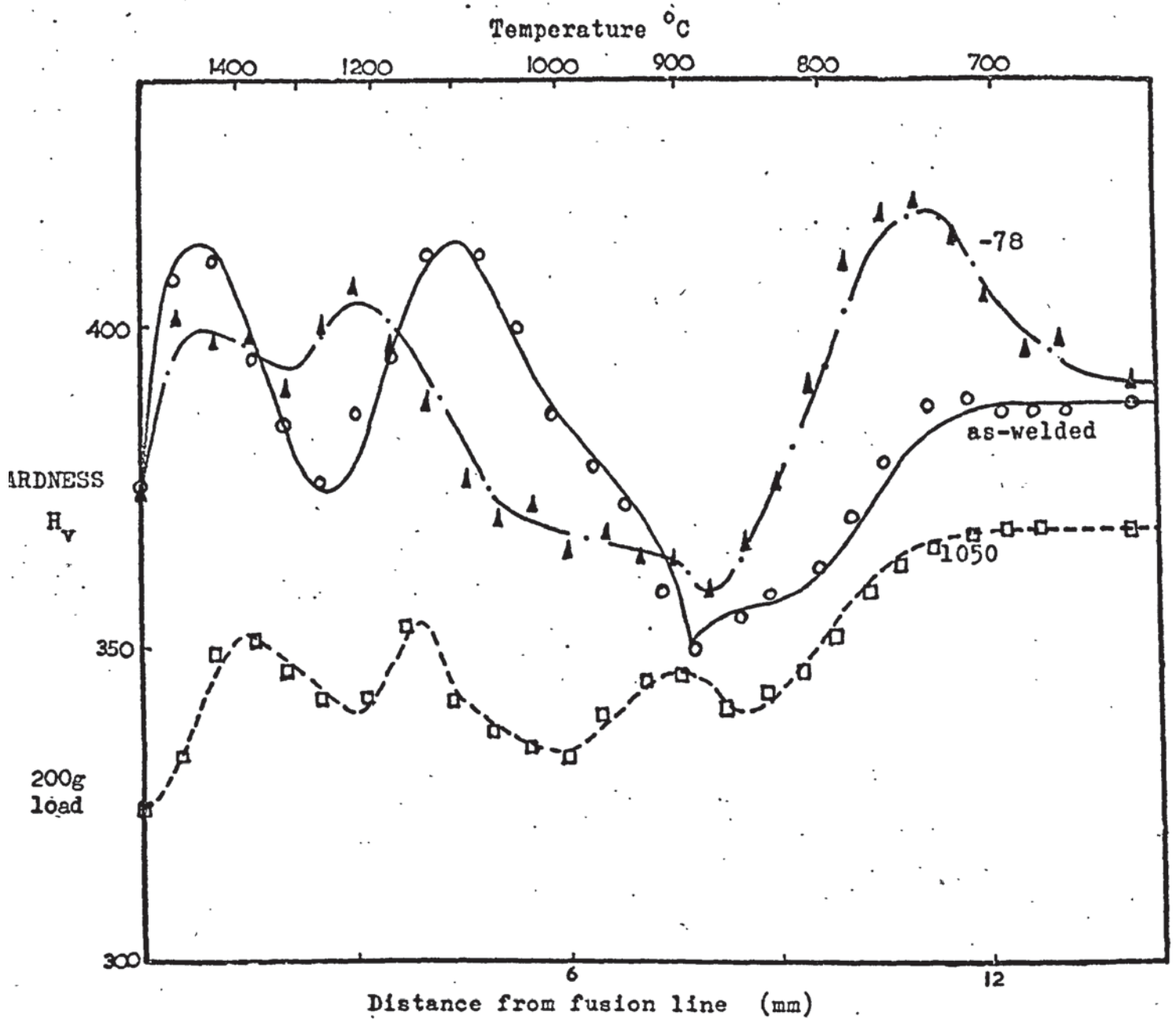
Fig. 25. Hardness surveys -- resolutioned and sub-zero
treated welds.

    (i)   Weld sub-zero treated; - 78°C for twenty hours.

    (ii) As-welded.

    (iii) Weld resolutioned; 1050°C for thirty minutes.
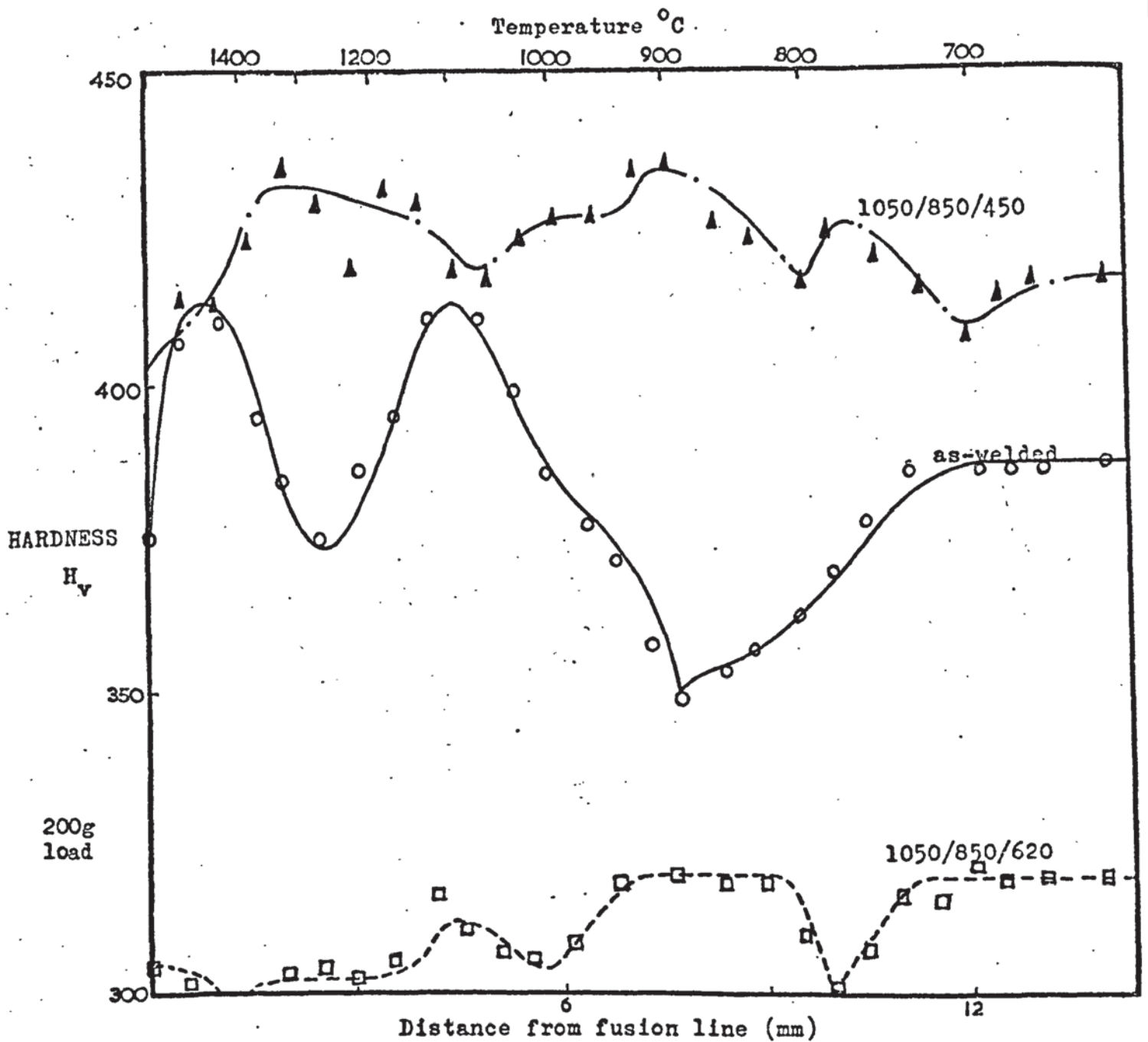
Fig. 26. Hardness surveys -- fully heat treated welds.

(i)   Weld fully hardened; 1050°C for thirty minutes,
      air cool, conditioned 850°C for two hours,
      air cool, aged 450°C for four hours.

(ii) As-welded

(iii) Weld overaged; 1050°C for thirty minutes,
      air cool, conditioned 850°C for two hours,
      air cool, aged 620°C for two hours.
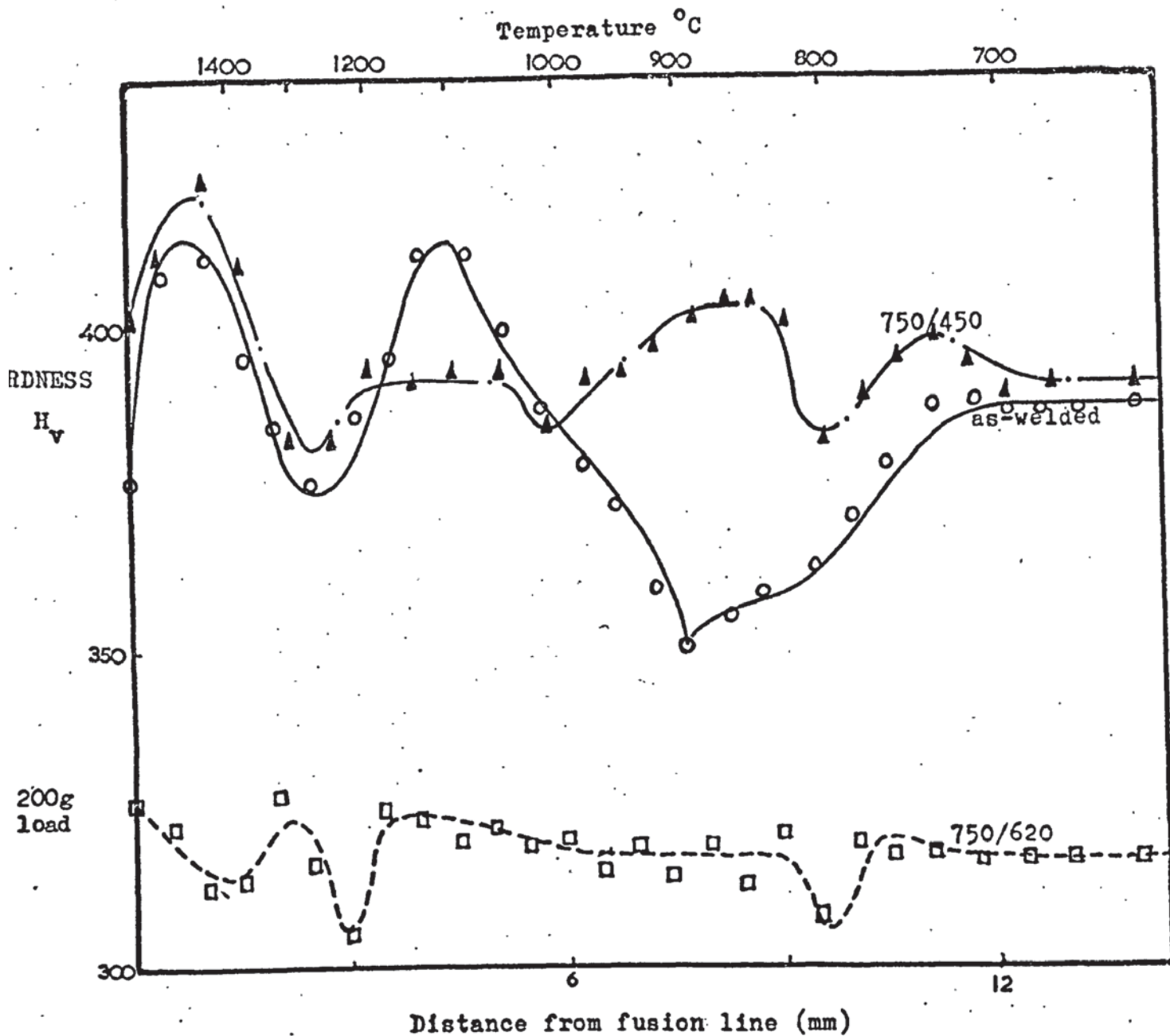
Fig. 27. Hardness surveys -- conditioned and aged welds.

(i) Weld fully hardened; conditioned 750°C for two hours, air cool, aged 450°C for four hours

(ii) As welded

(iii) Weld overaged; conditioned 750°C for two hours, air cool, aged 620°C for two hours.
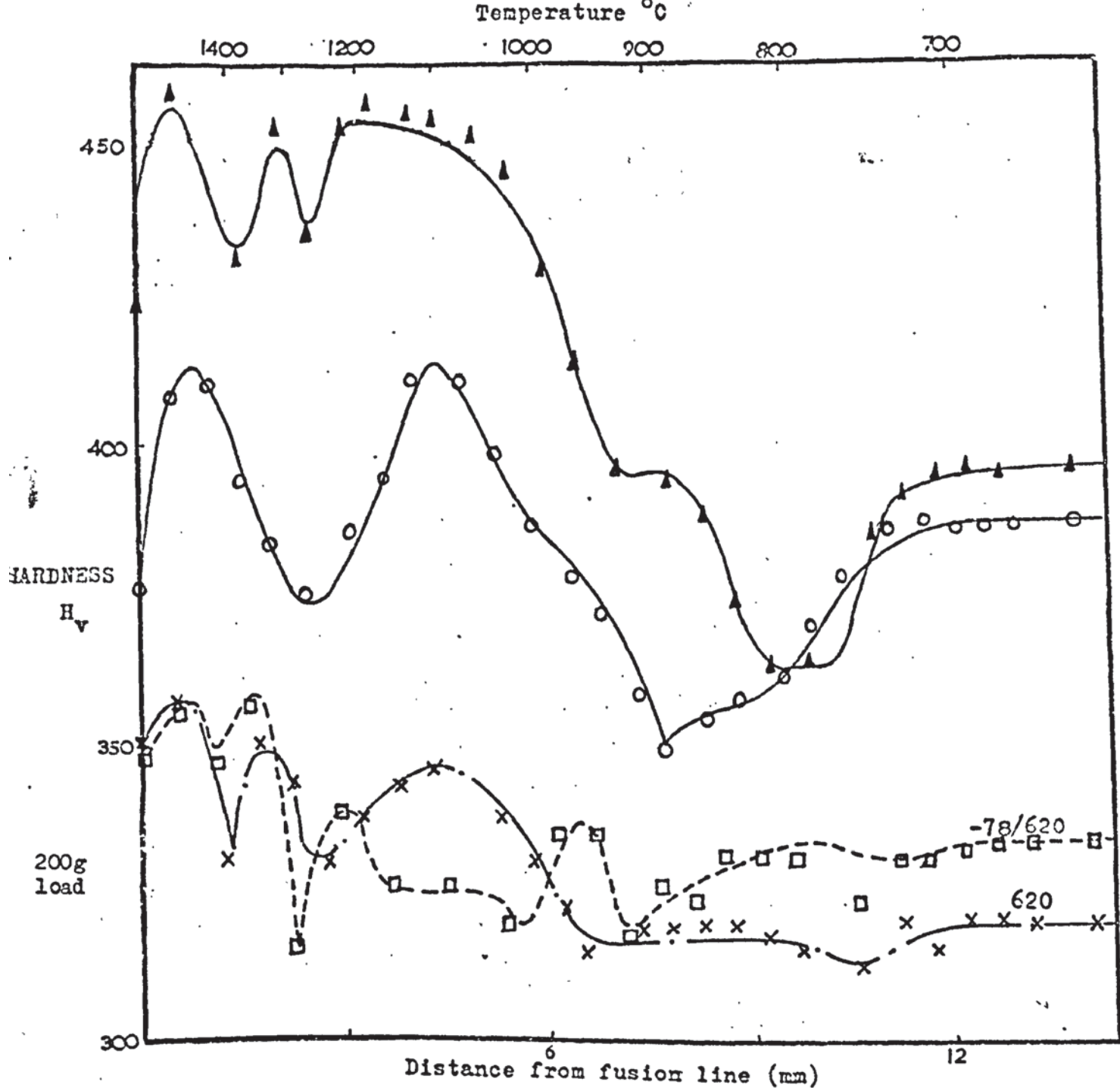
Fig. 28. Hardness surveys -- directly aged welds.

(i) Weld fully hardened; directly aged 450°C for four hours.

(ii) As-welded.

(iii) Weld overaged; sub-zero transformed – 78°C for twenty hours, aged 620°C for two hours

(iv) Weld overaged; directly aged 620°C for two hours.
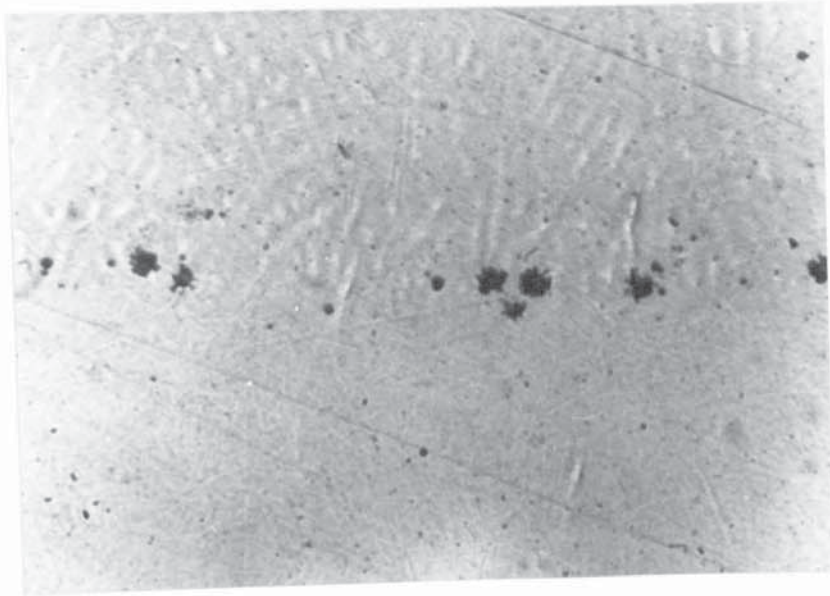
(a)   Inclusions along fusion line;   aged 450°C.
       Etch; Ammonium persulphate/hydrochloric acid, X 175
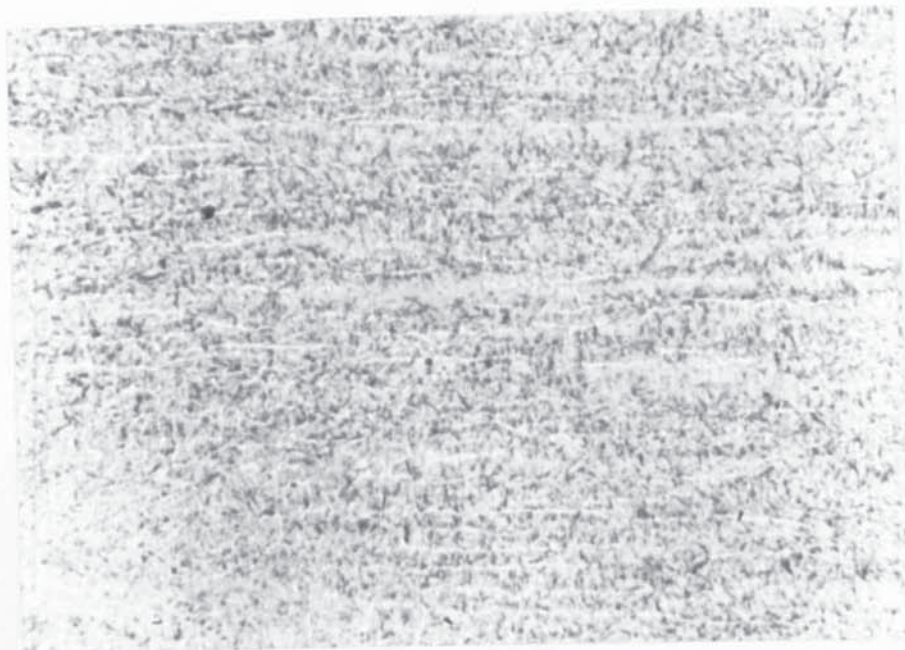
(b)   Light etching 'veins';   aged 550°C.
       Etch; Acidified ferric chloride,   X 200

Fig. 29.   Heat affected zone microstructures.

(a)   Aged 450°C.   Marble's Reagent etch,   X450
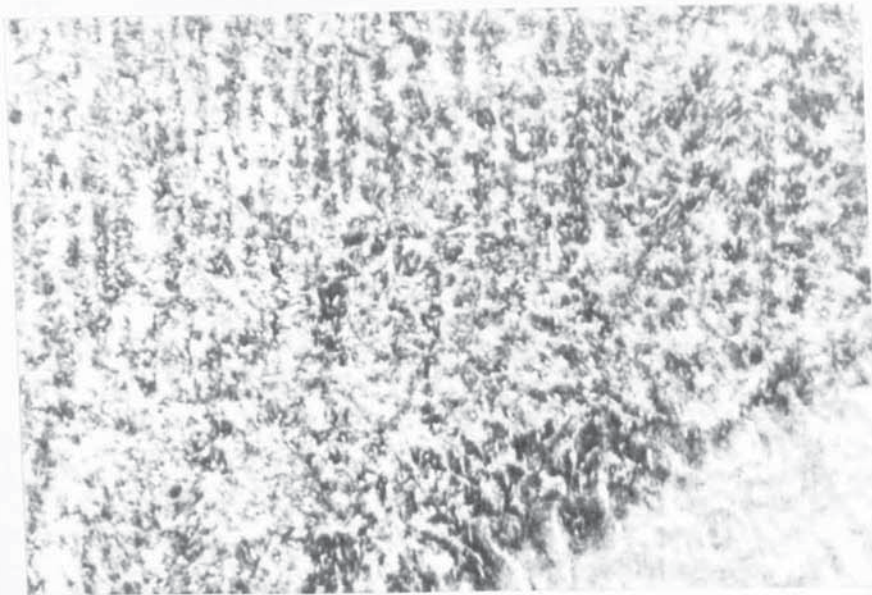
(b)   Aged 620°C.   Marble's Reagent etch,   X450

Fig. 30.   Banded microstructure adjacent to weld bead,
coarsening of 'veins'.

(a)   2mm. from fusion line.

(b)   8mm. from fusion line.

Fig. 31.   Carbide distribution in HAZ.

Aged 450°C,   Murikami's etch,   X 250
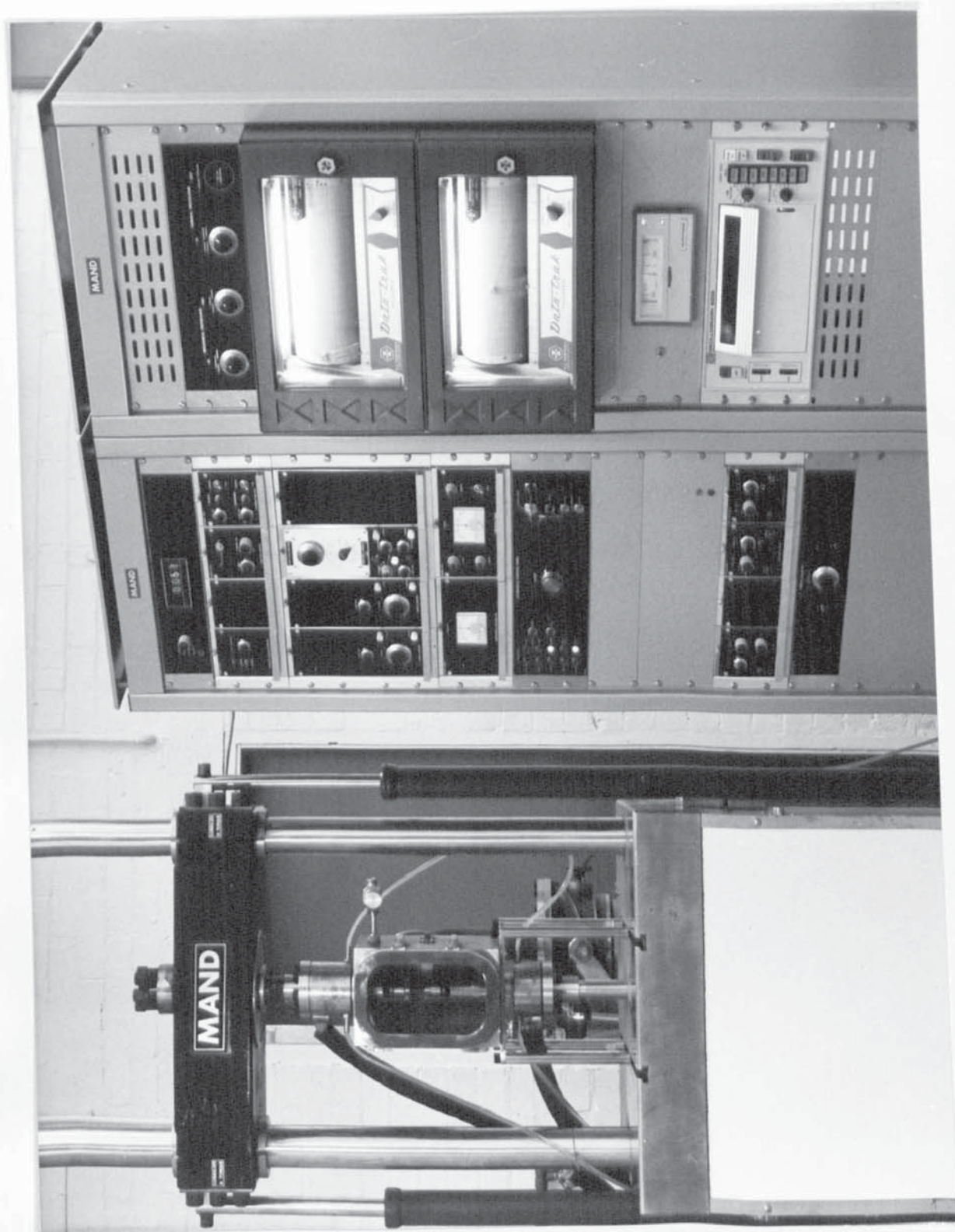
Fig. 32.   'Mand' weld thermal simulator, a servo-hydraulic
           closed loop mechanical testing machine coupled
           to a progammable resistance heating unit.

Fig. 33. - 'Datatrak' cycle programmer and 'Eurotherm' temperature optimisation controller.
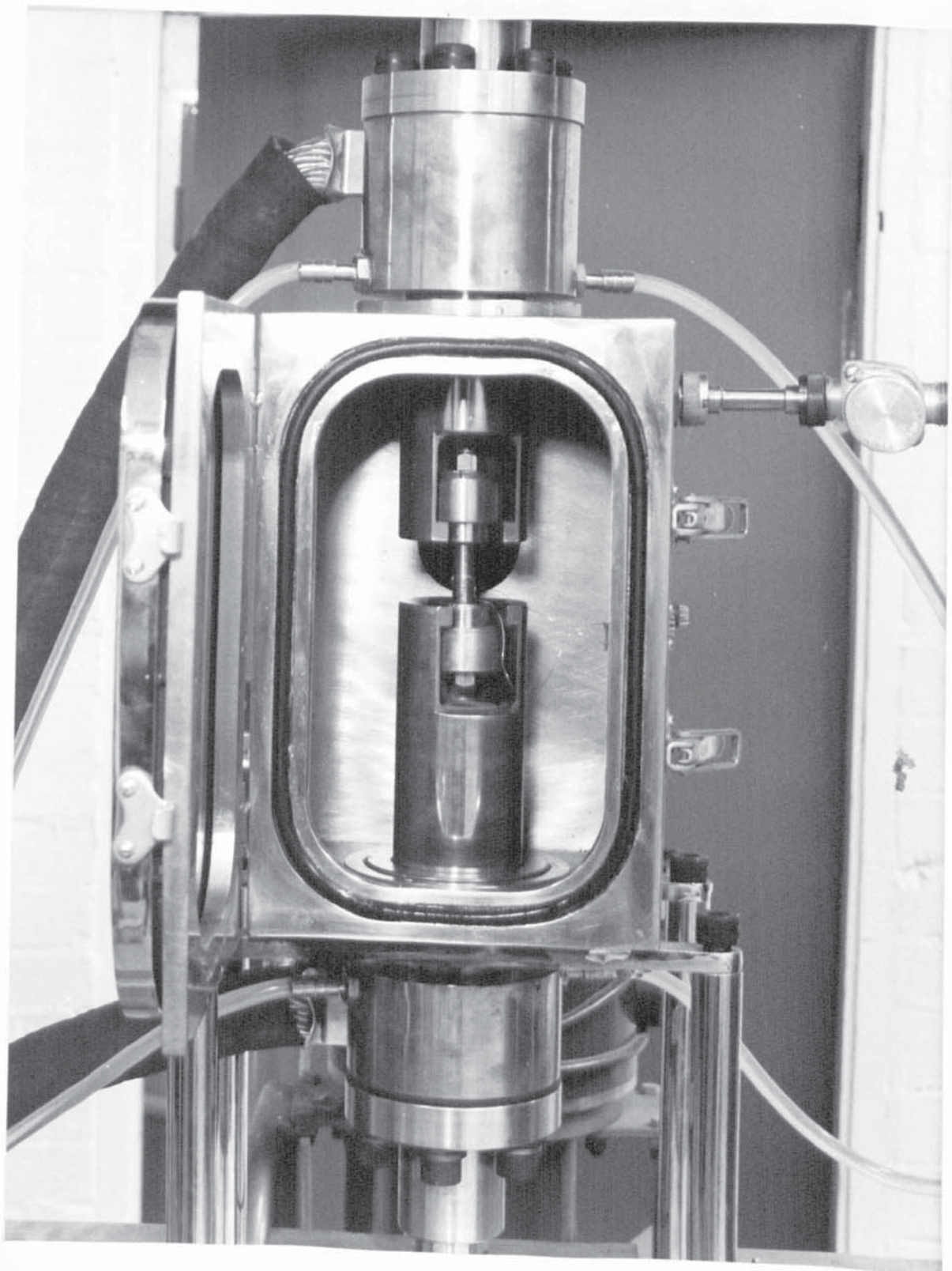
Fig. 34.   Original specimen jaws and controlled
atmosphere box.
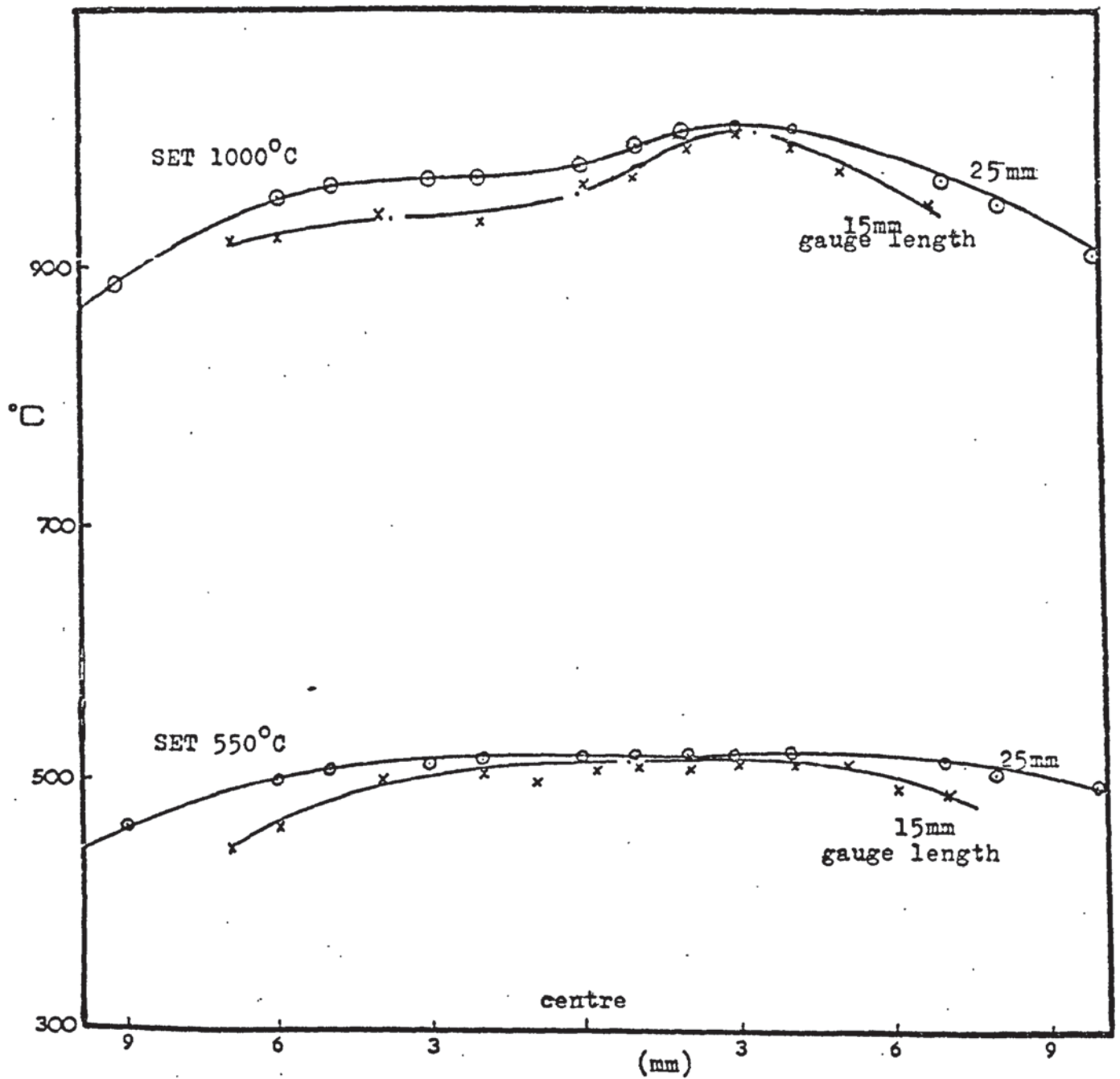
Fig. 35. Specimen temperature distribution -- original jaws.
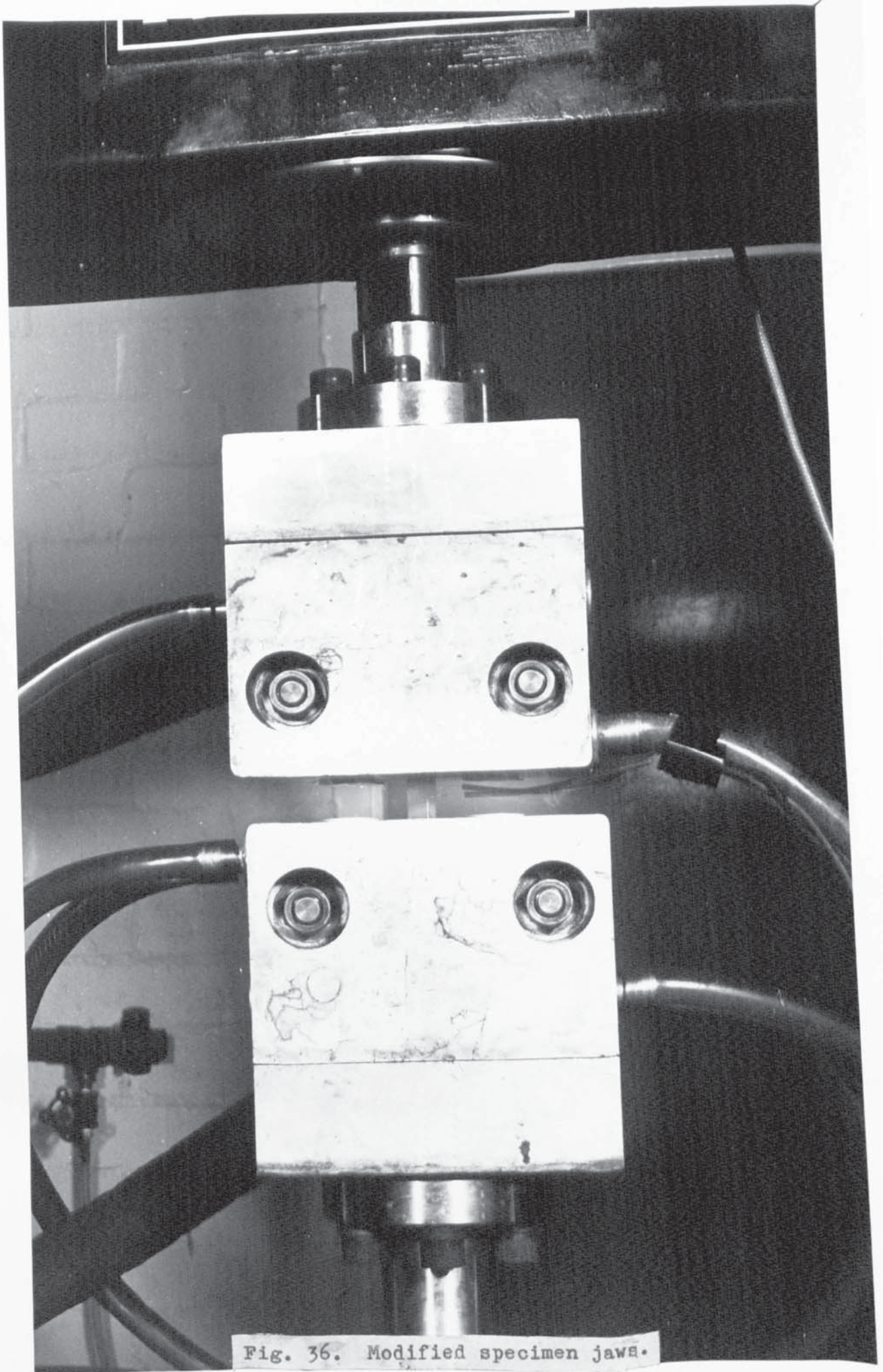
Fig. 36.   Modified specimen jaws.
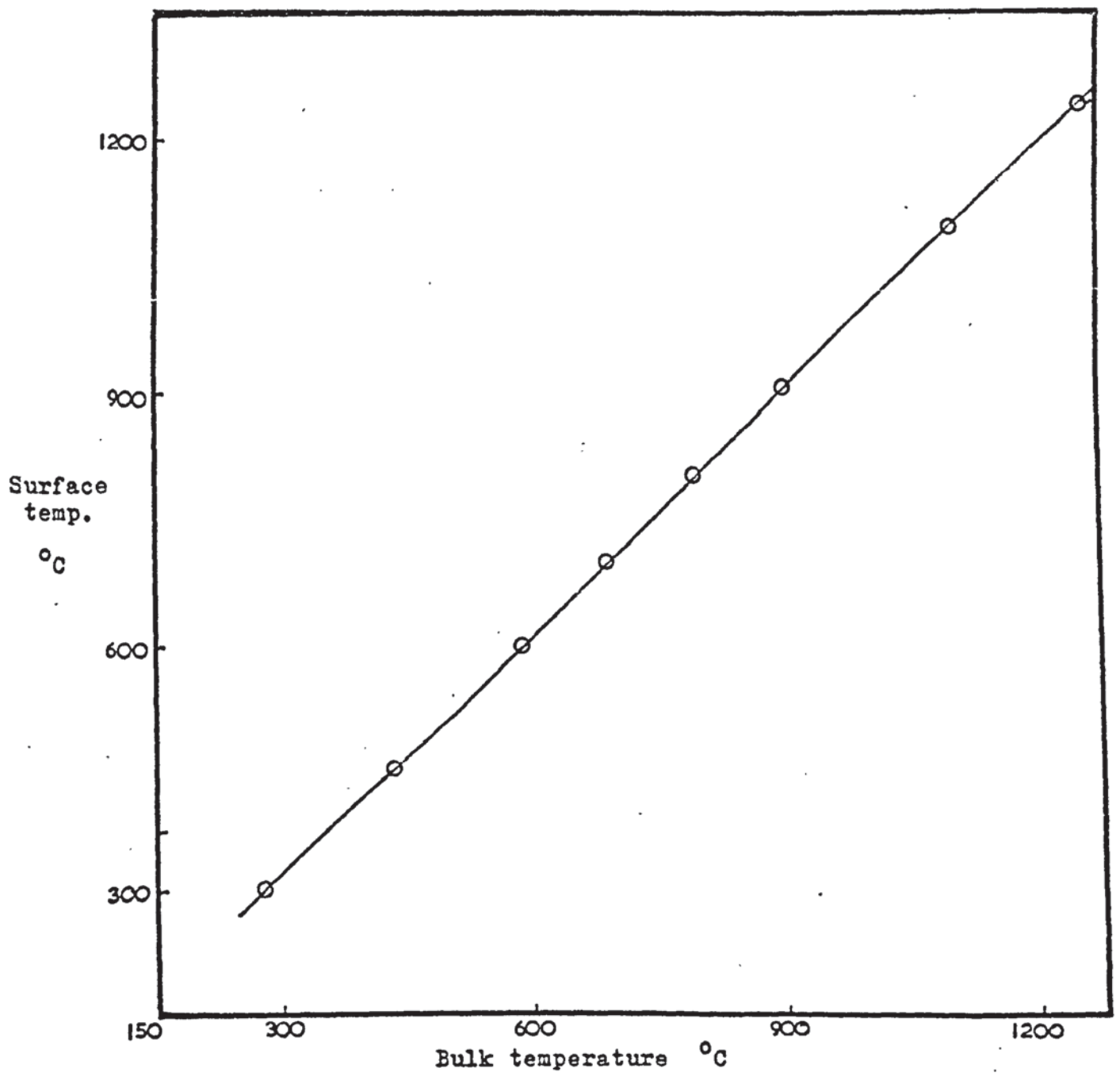
Fig. 37. Correlation of specimen surface and bulk temperatures.
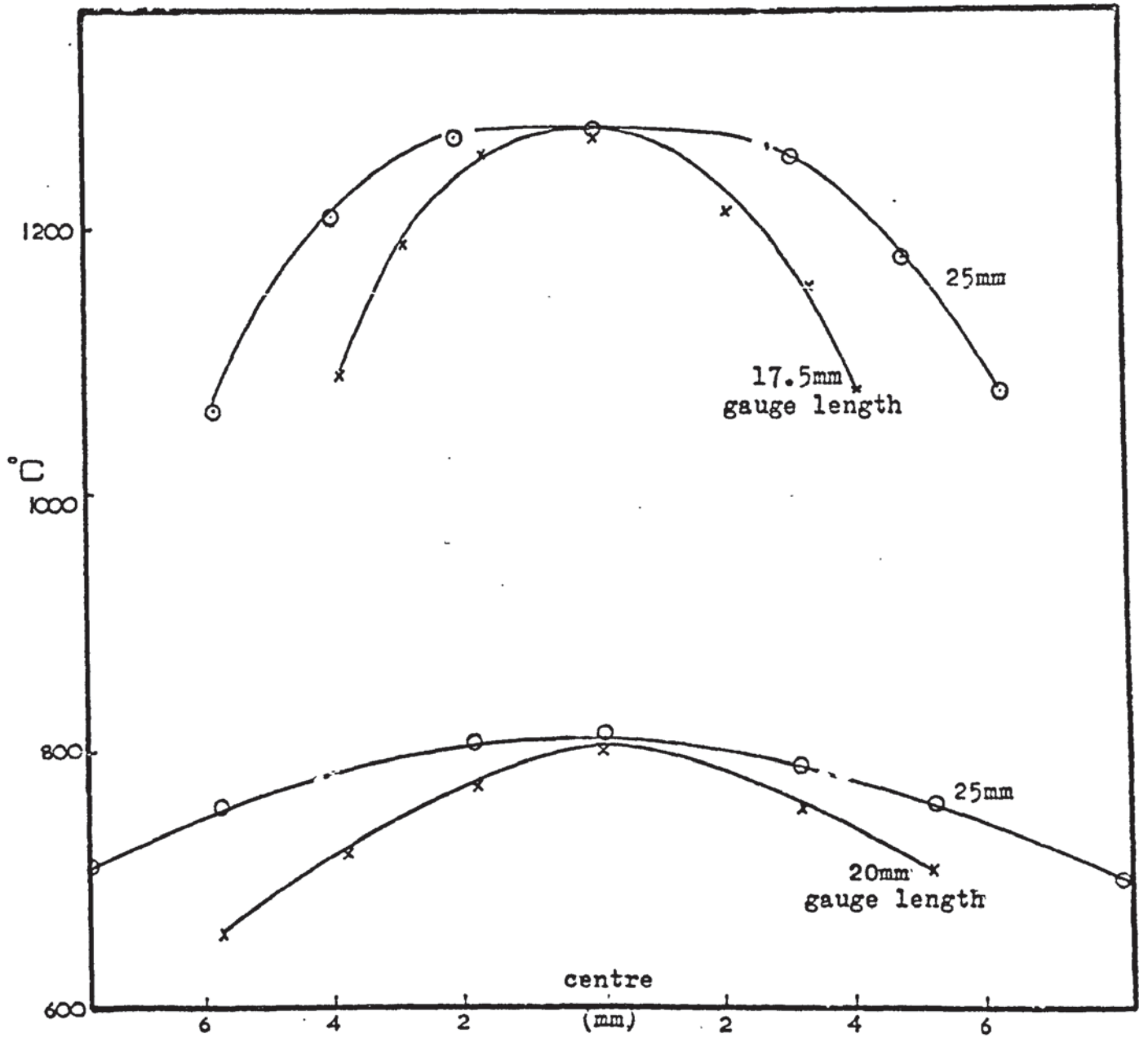
Fig. 38. Specimen longitudinal temperature distribution.
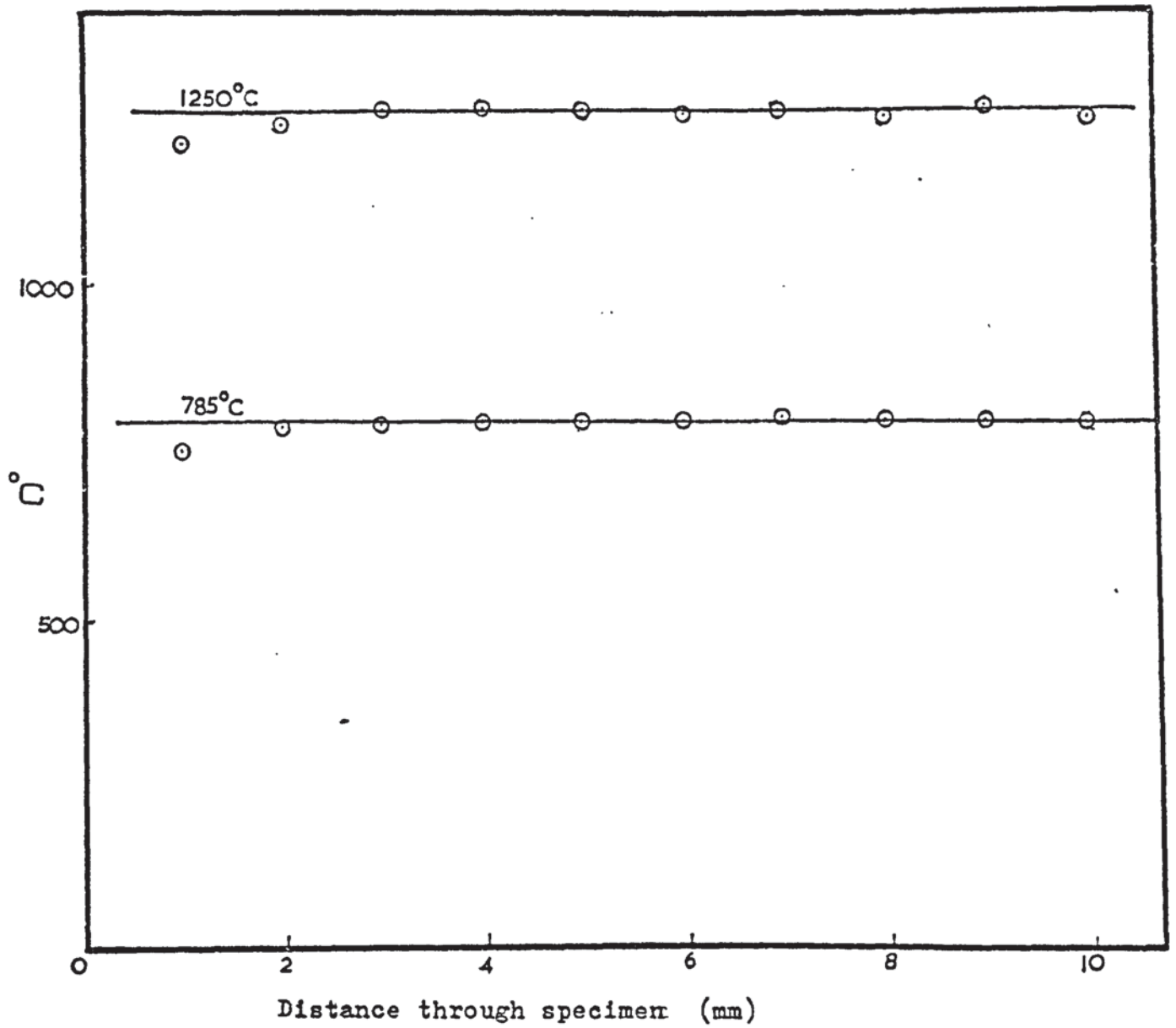
Fig. 39. Specimen transverse temperature distribution.
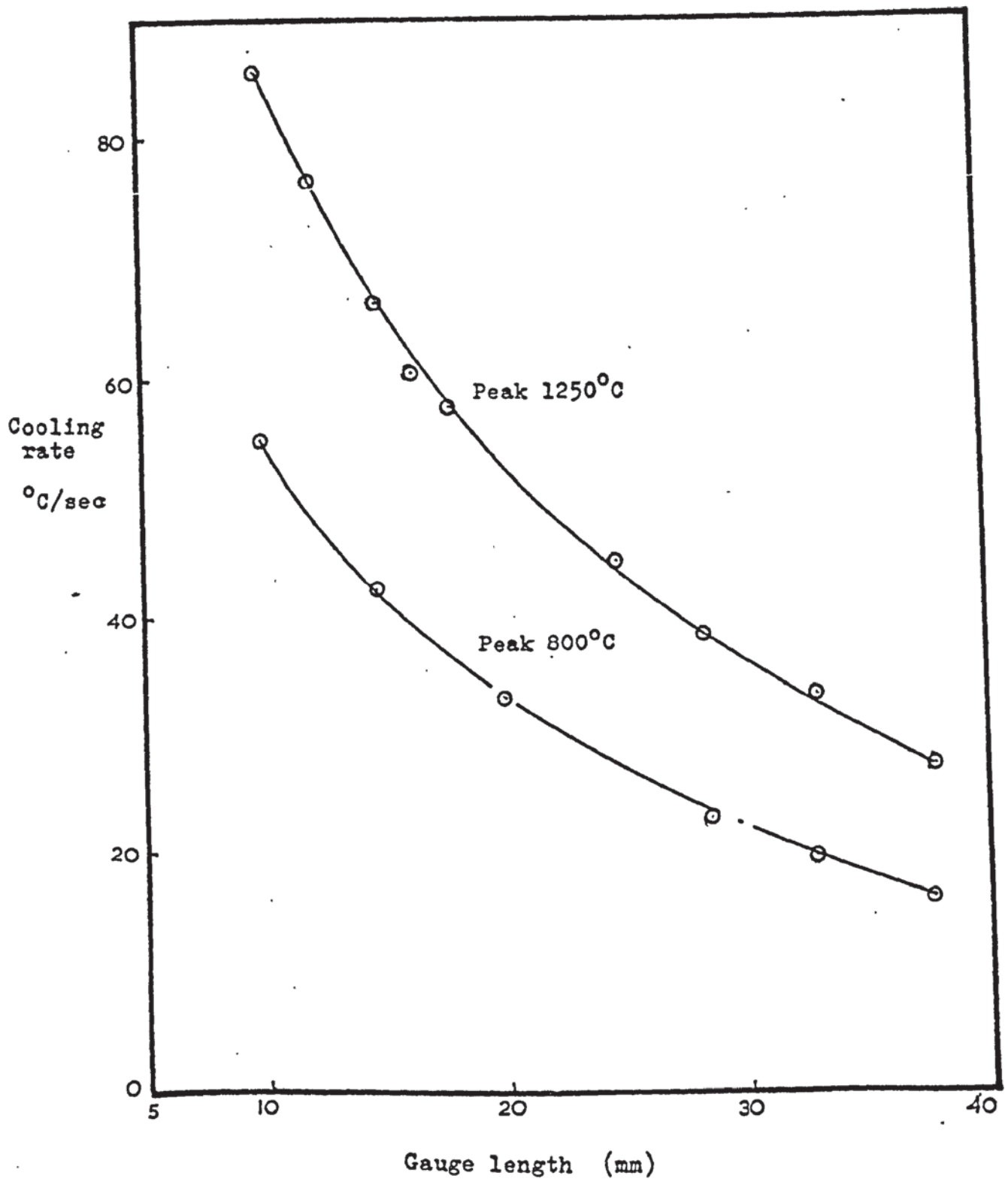
Fig. 40. Specimen cooling rates.
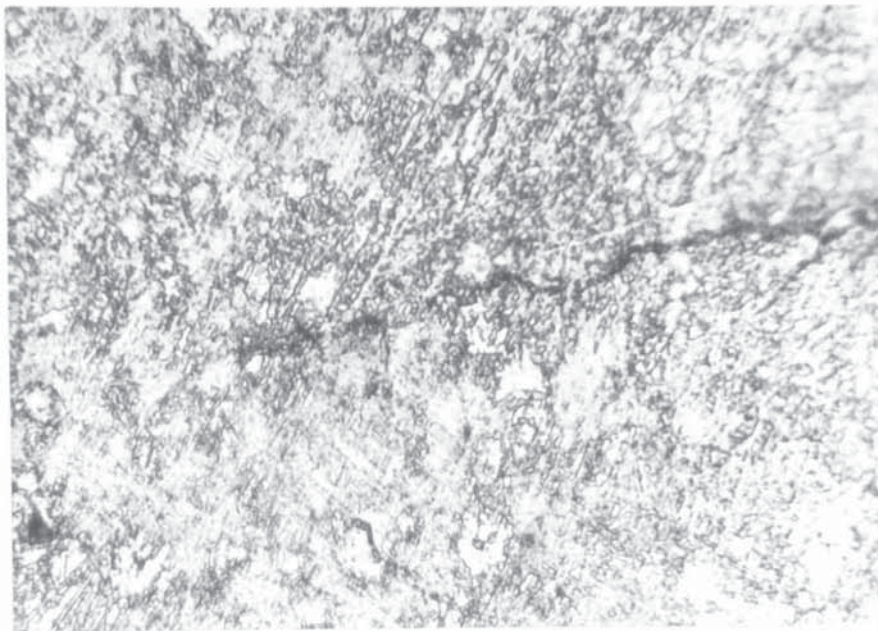
(a)   As-welded.   X 1200
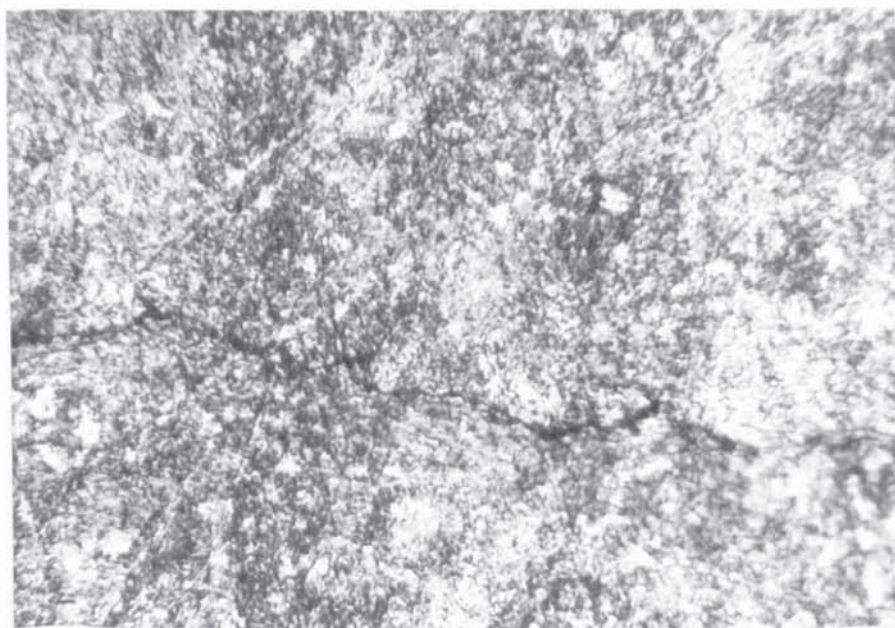
(b)   As-welded, transformed at -78°C for 20 hours.
          X 1250

Fig. 41.   Simulated HAZ microstructures, 785°C peak-- vacuum
              remelted plate.
          Compare light-etching phase with figs. 41c/d.
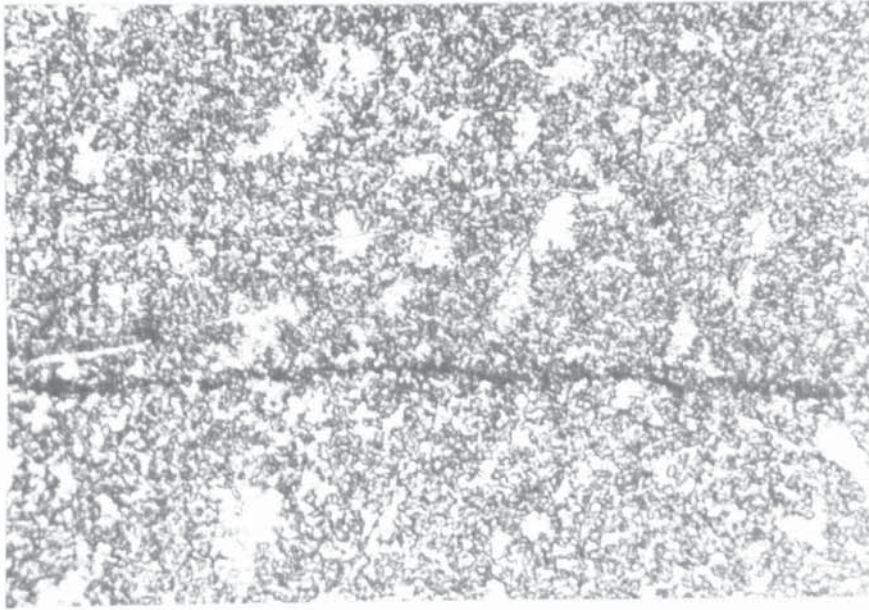
(c)   Aged   X 450
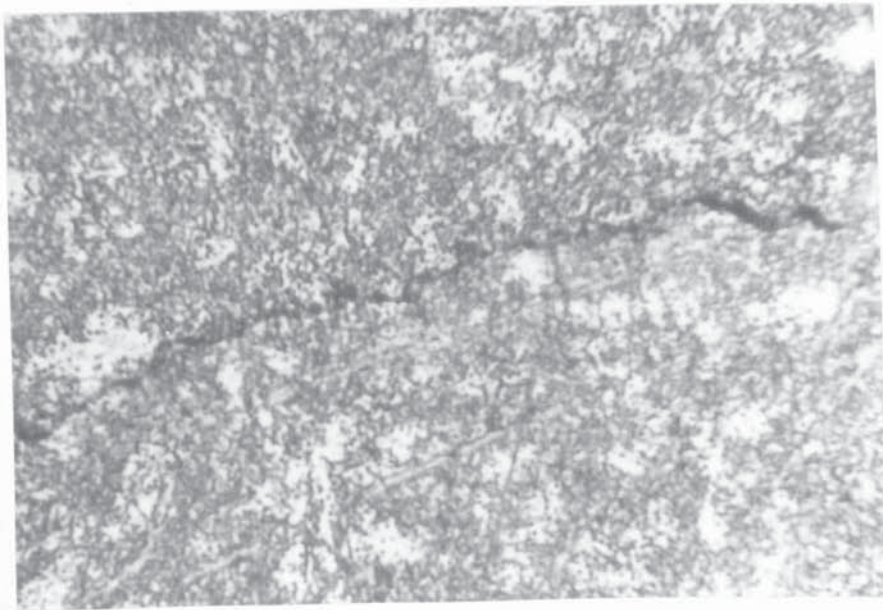
(d)   Aged   X 450

Fig. 41. Simulated HAZ microstructures, 785°C peak-- air
(cont)   melted plate.
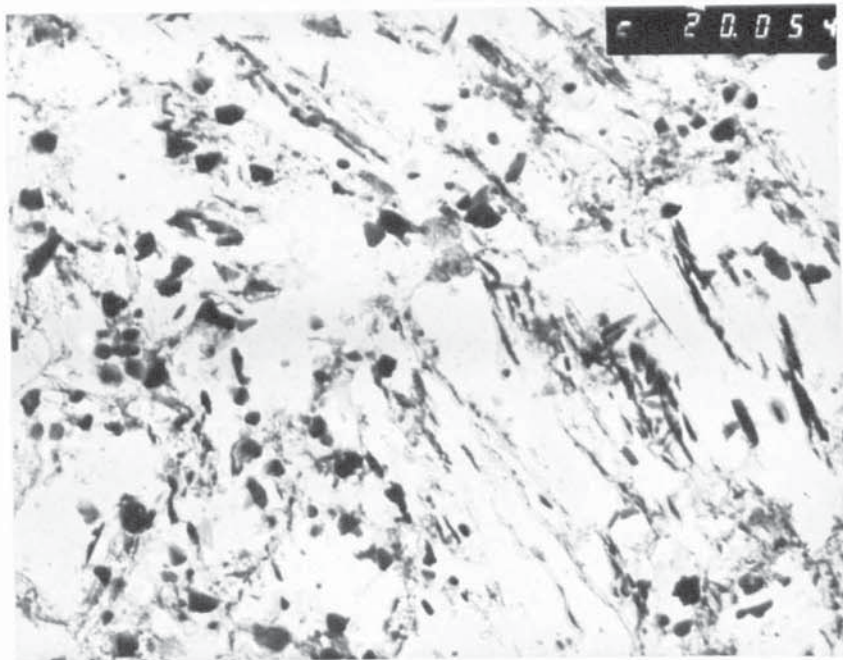
(a) showing coarse precipitation; elongated
     showing preferred orientation, together
     with polygonal blocks in clusters (poss-
     ibly chromium-rich M_2X); fine precipit-
     ation along sub-structure.   X 20,000
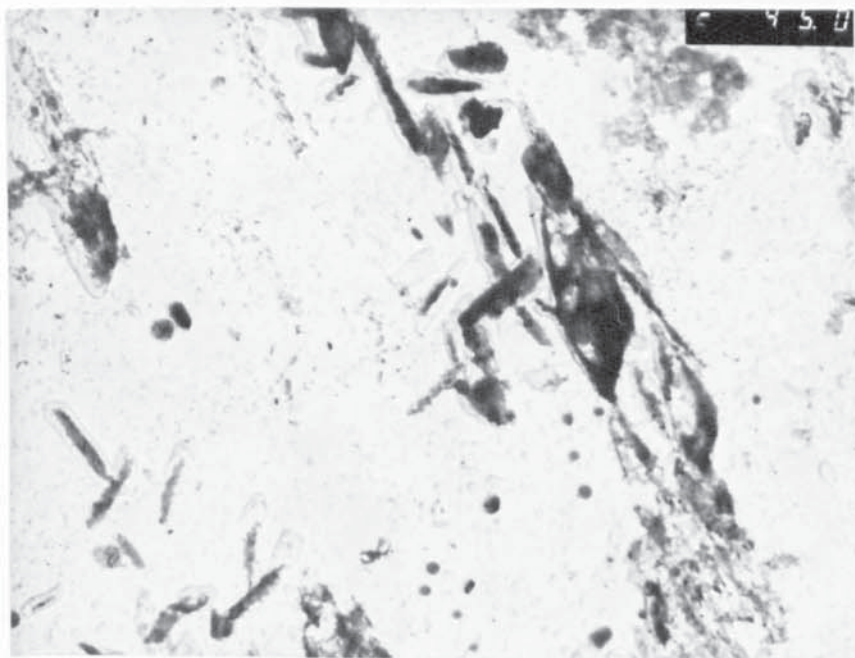
(b) showing elongated particle precipitation
     (probably ϵ-copper) on preferred planes.
                  X 45,000

Fig. 42. Extraction replicas of simulated HAZ microstructures;
          1250°C peak.
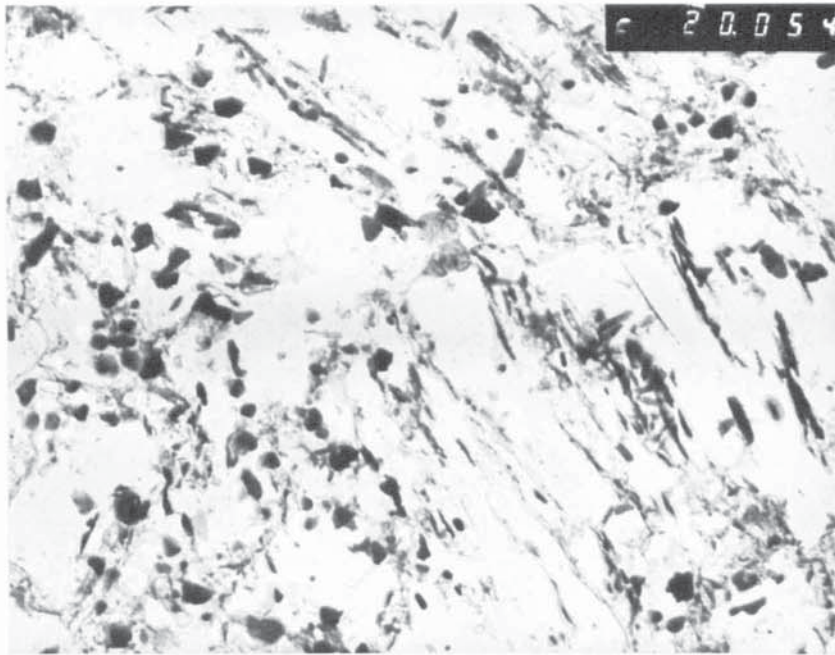
(a) showing coarse precipitation; elongated
     showing preferred orientation, together
     with polygonal blocks in clusters (poss-
     ibly chromium-rich M_2X); fine precipit-
     ation along sub-structure.   X 20,000
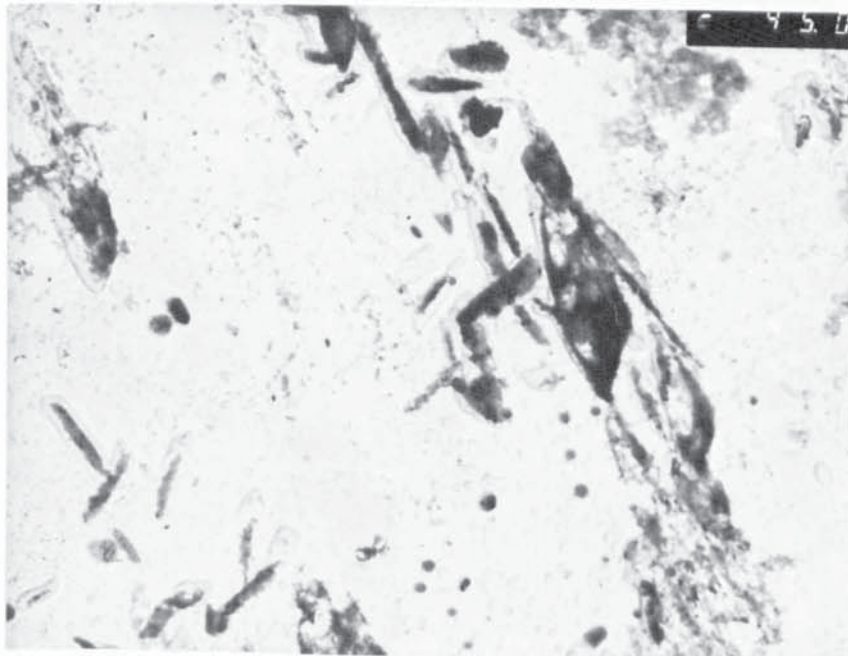
(b)   showing elongated particle precipitation
       (probably ϵ-copper) on preferred planes.
                    X 45,000

Fig. 42.   Extraction replicas of simulated HAZ microstructures;
            1250°C peak.
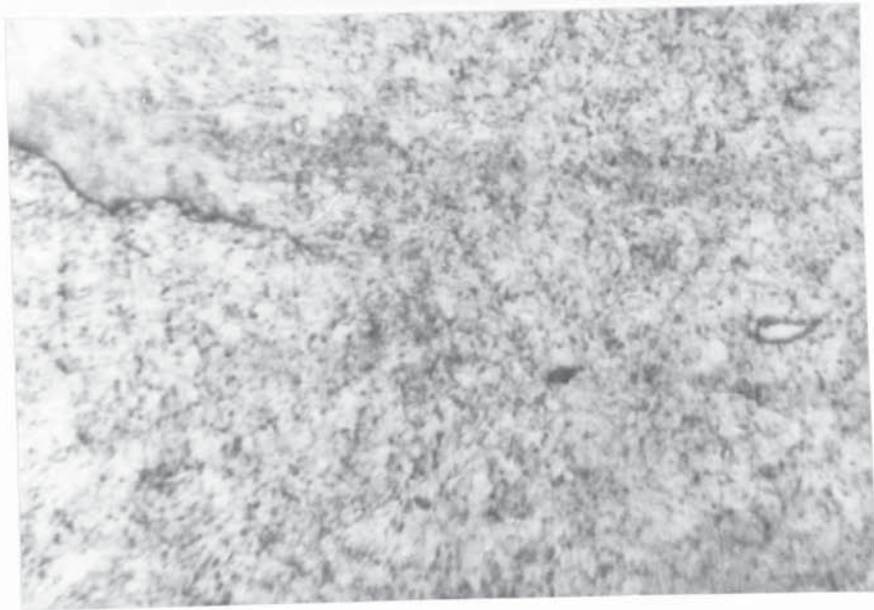
(i)   Simulated.   X 1250
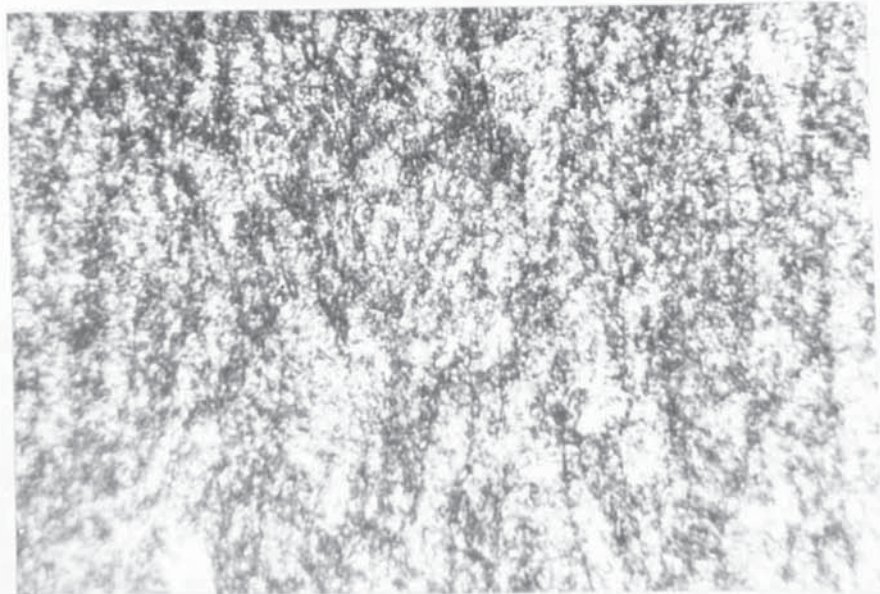
(ii)   Welded.   X 1250

Fig. 43(a). Comparison of real and simulated weld HAZ
microstructures, 785°C peak. Aged.
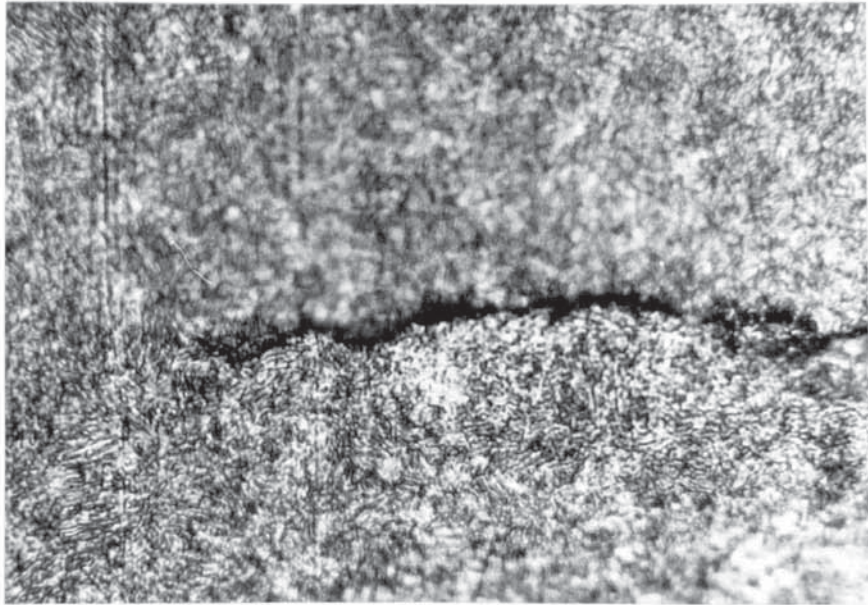
(i)   Simulated.   X 1250

(ii)   Welded.   X 1250

Fig. 43(b).   Comparison of real and simulated weld HAZ
microstructures, 785°C peak. As-welded.

(a)   Showing delta-ferrite formation.
        Aged 450°C.   X 1250
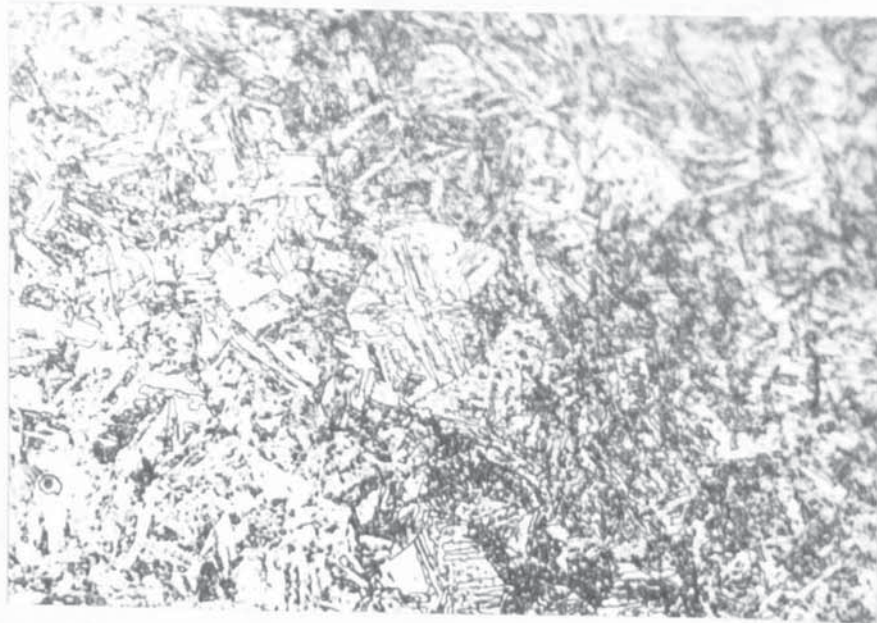
(b)   Showing twinning. As-welded.   X 450

Fig. 44. Simulated HAZ microstructures, 1250°C peak--
          air-melted plate.
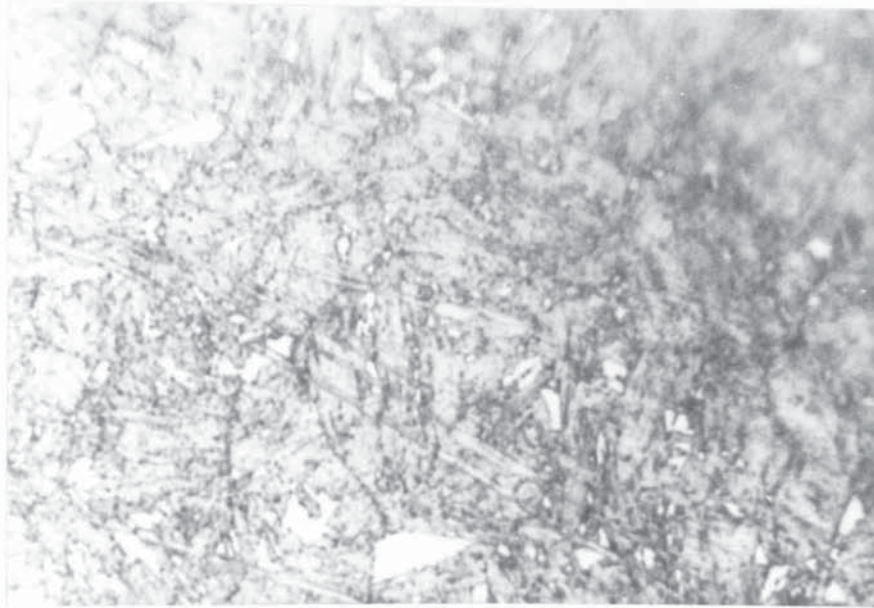
(a)   Showing dispersed delta-ferrite; also
        pinning of grain boundaries by small
        precipitates.   Aged 450°C.   X 2,000
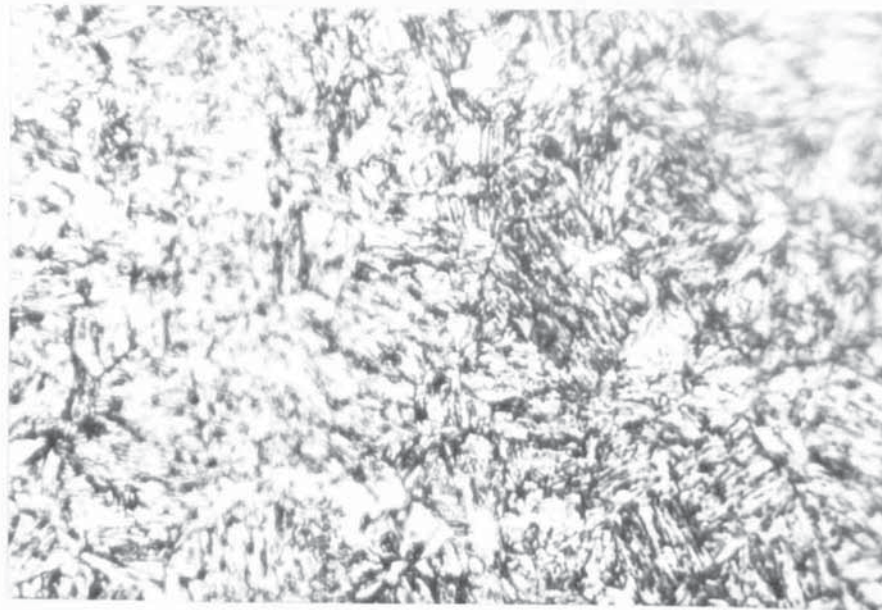
(b)   Resistance of inclusions to ageing.
        Aged 620°C.   X 1250

Fig. 45.   Simulated HAZ microstructures, 1250°C peak--
           air melted plate.

(a) Grain boundaries and preferred precipitation.
     Aged 450°C. Electrolytic perchloric/acetic
     acids etch.   X 1900
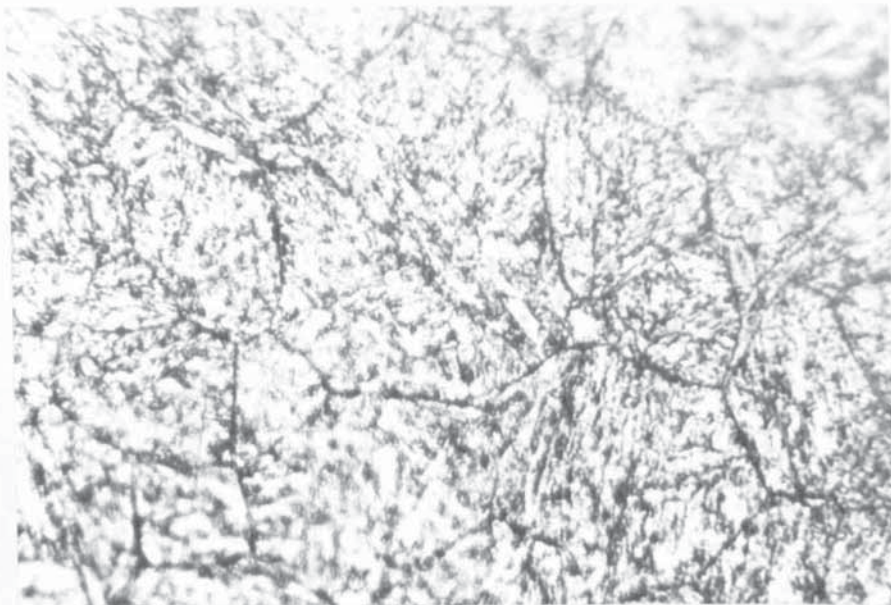
(b) Grain boundaries and martensitic matrix;
     possible delta ferrite at triple points.
     Aged 450°C. Marble's Reagent etch.   X 1900

Fig. 46. Simulated HAZ microstructures, 1250°C peak--
          vacuum remelted plate.
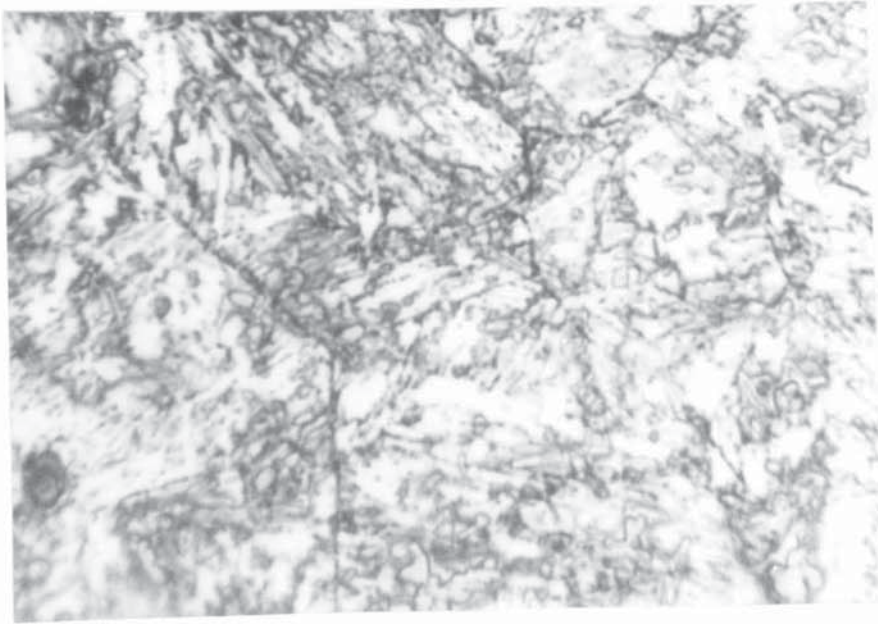
(a)   Marble's Reagent etch.   X 2,000
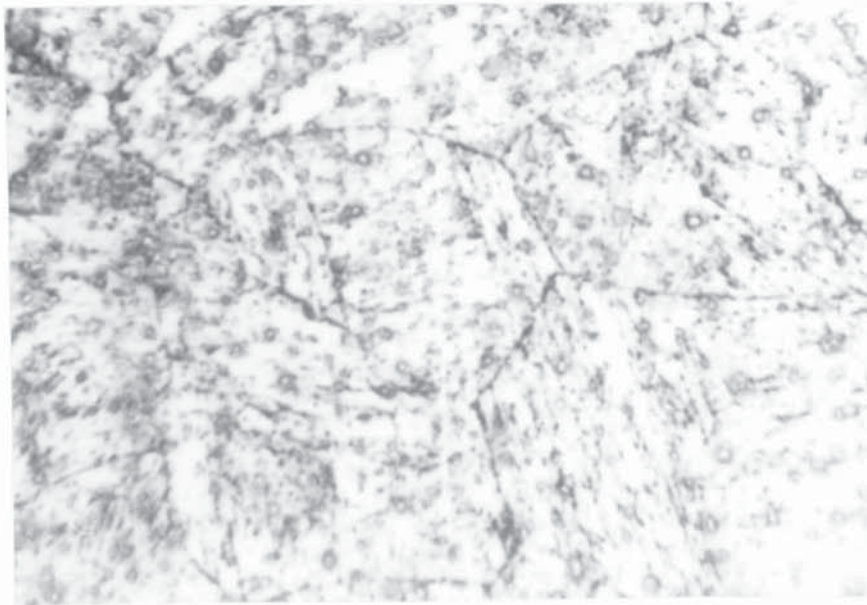
(b)   Electrolytic perchloric/acetic acids etch.
      X 2,000

Fig. 47.   Simulated HAZ microstructure, 1250°C peak--
           vacuum remelted plate. Aged 620°C.

           Note coarse precipitates compared to fig. 46.
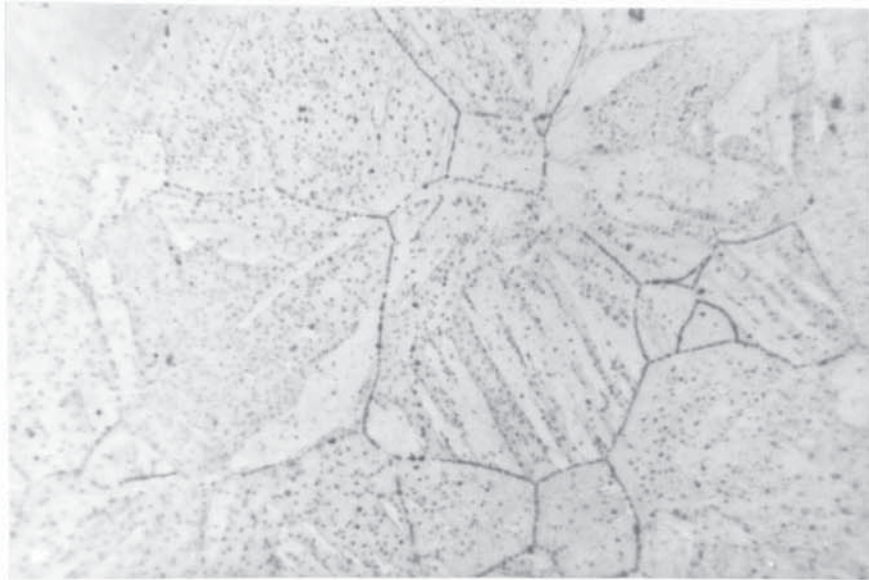
(a)   Simulated. Electrolytic polish/etch.   X 1400

(b)   Welded. Electrolytic polish/etch.   X 1400

Fig. 49.   Comparison of real and simulated weld HAZ
grain size, 1250°C peak.
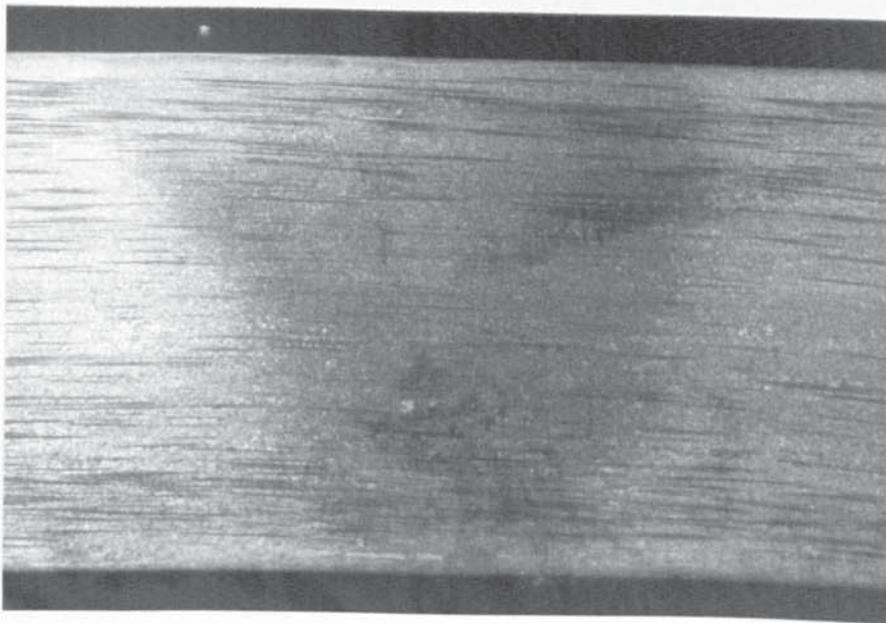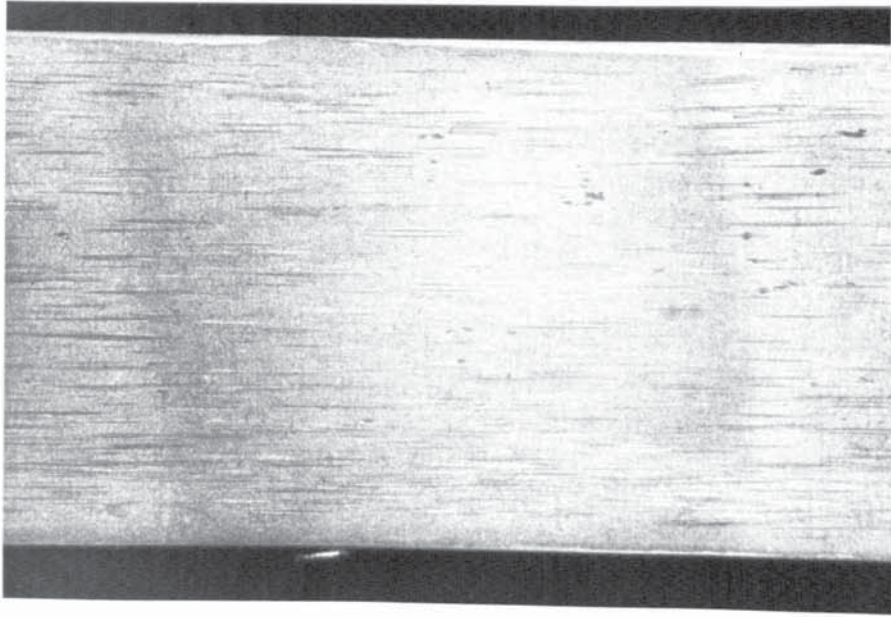
Fig. 50. Divergence of dark-etching bands when simulated
at too high peak temperature.
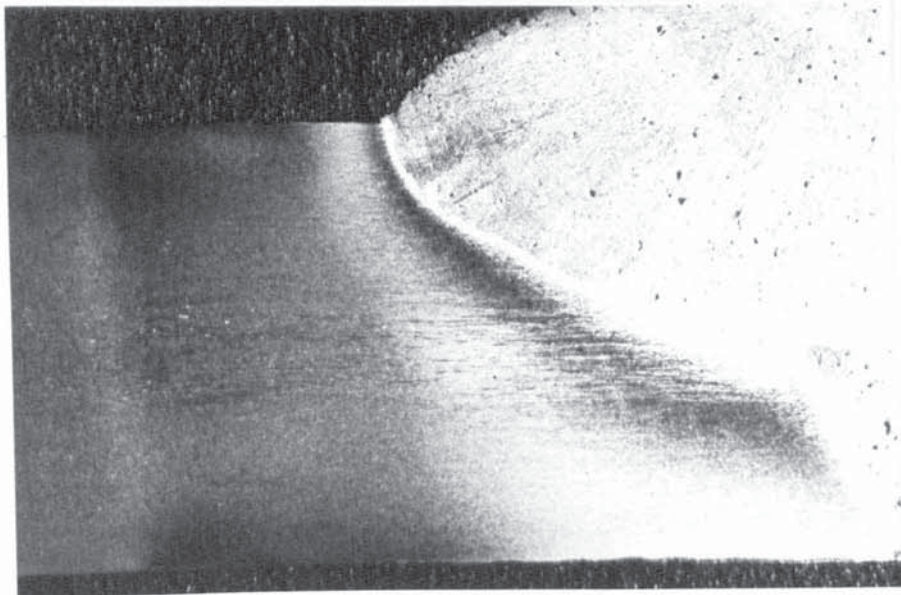
(a)   As-welded.
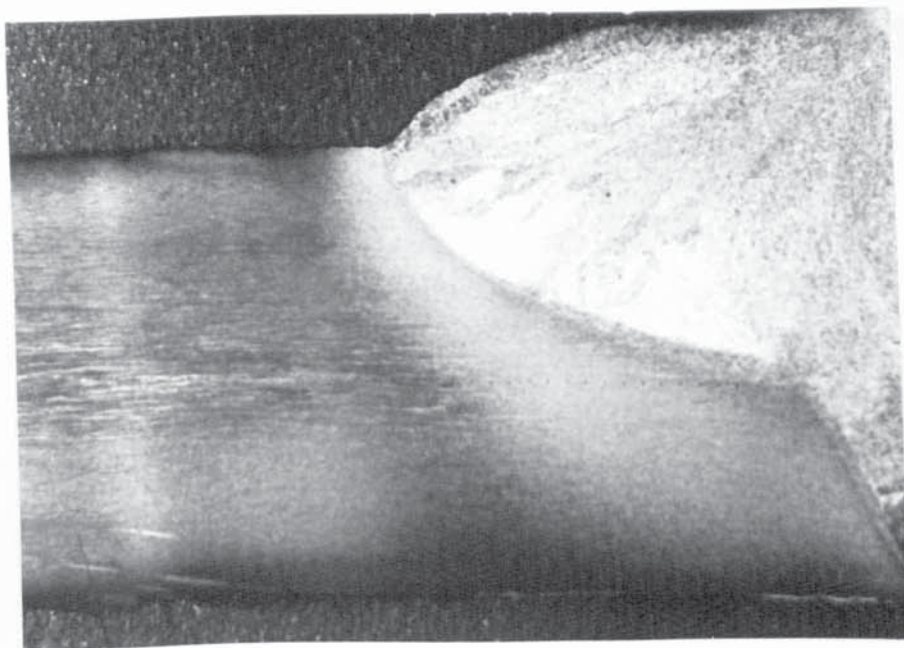
(b)   Aged 450°C.

Fig. 51.   Macrostructure of weld joint.
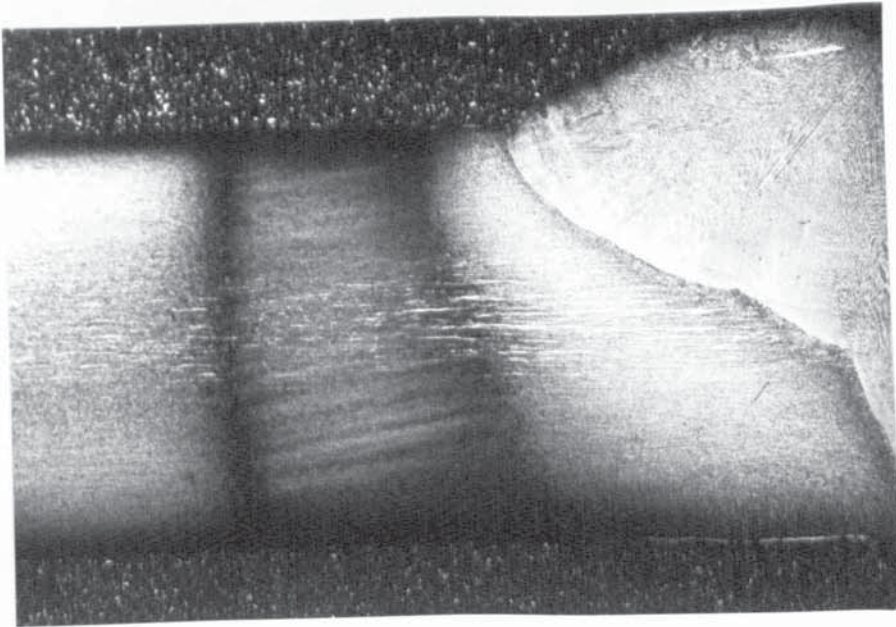
(a)   Aged 550°C.
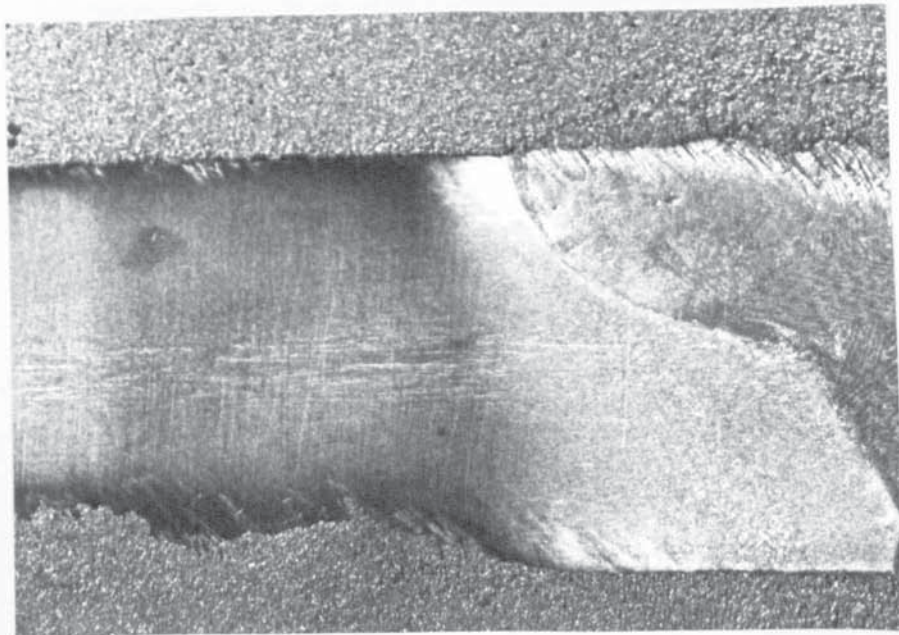
(b)   Aged 620°C.

Fig. 52.   Macrostructure of weld joint.
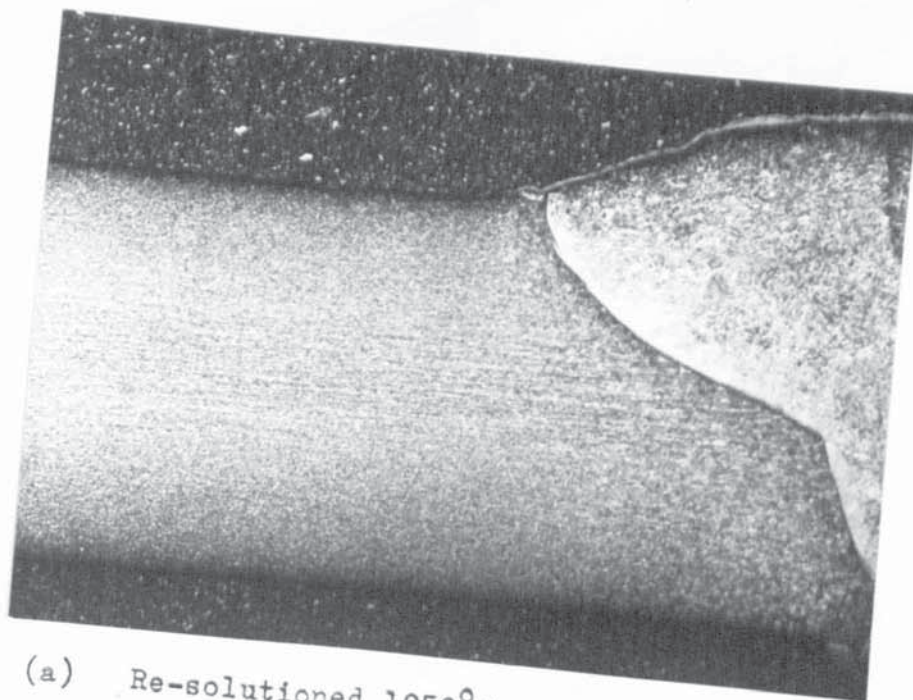
(a) Re-solutioned 1050°C.
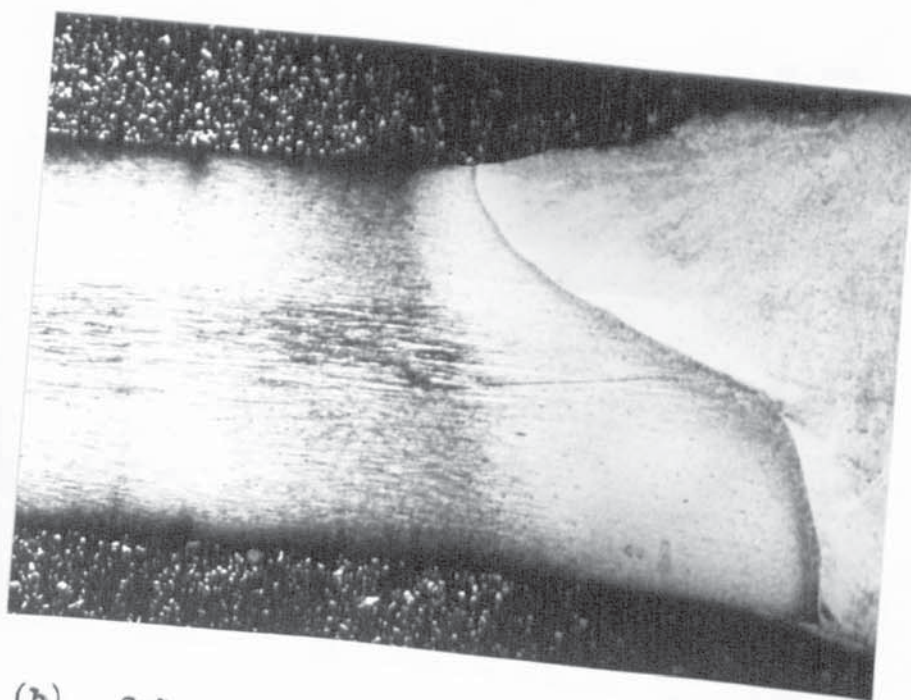
(b) Sub-zero treated at -78°C.

Fig. 53. Macrostructure of weld joint.
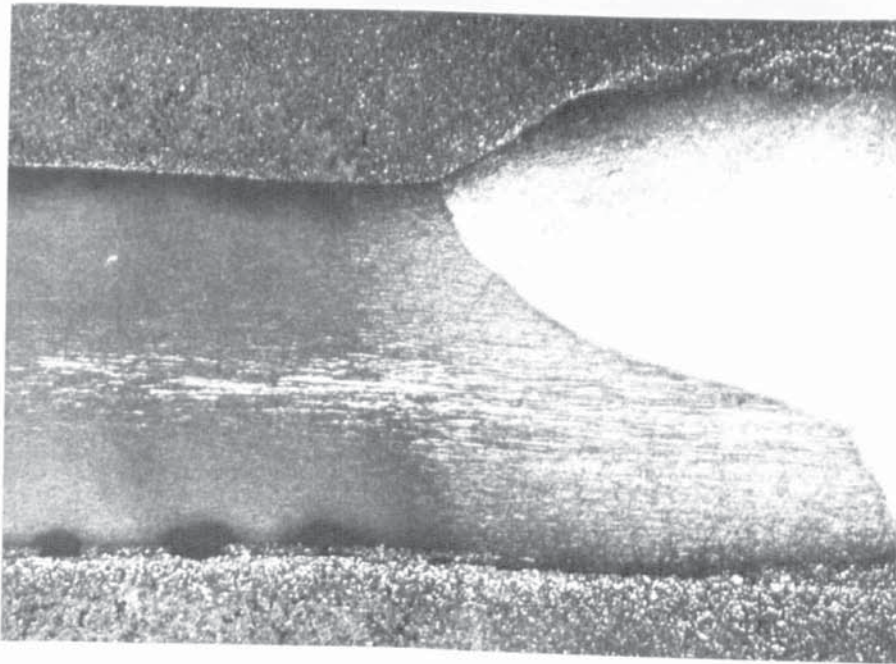
(a)   Conditioned 750°C and aged 450°C.
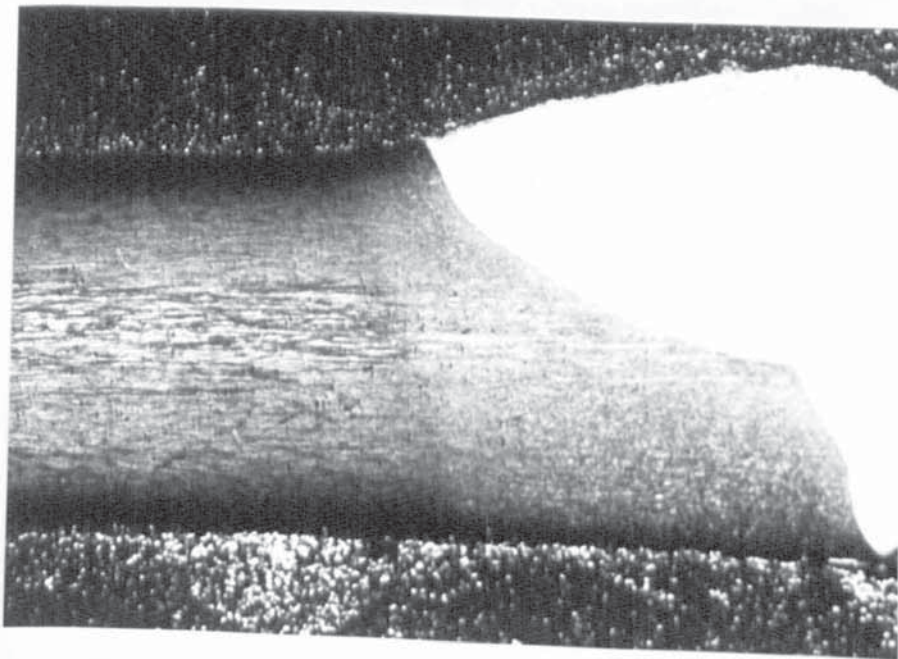
(b)   Conditioned 750°C and aged 620°C.

Fig. 54.   Macrostructure of weld joint.

Fig. 55. Macrostructure of three-run weld joint. x5.
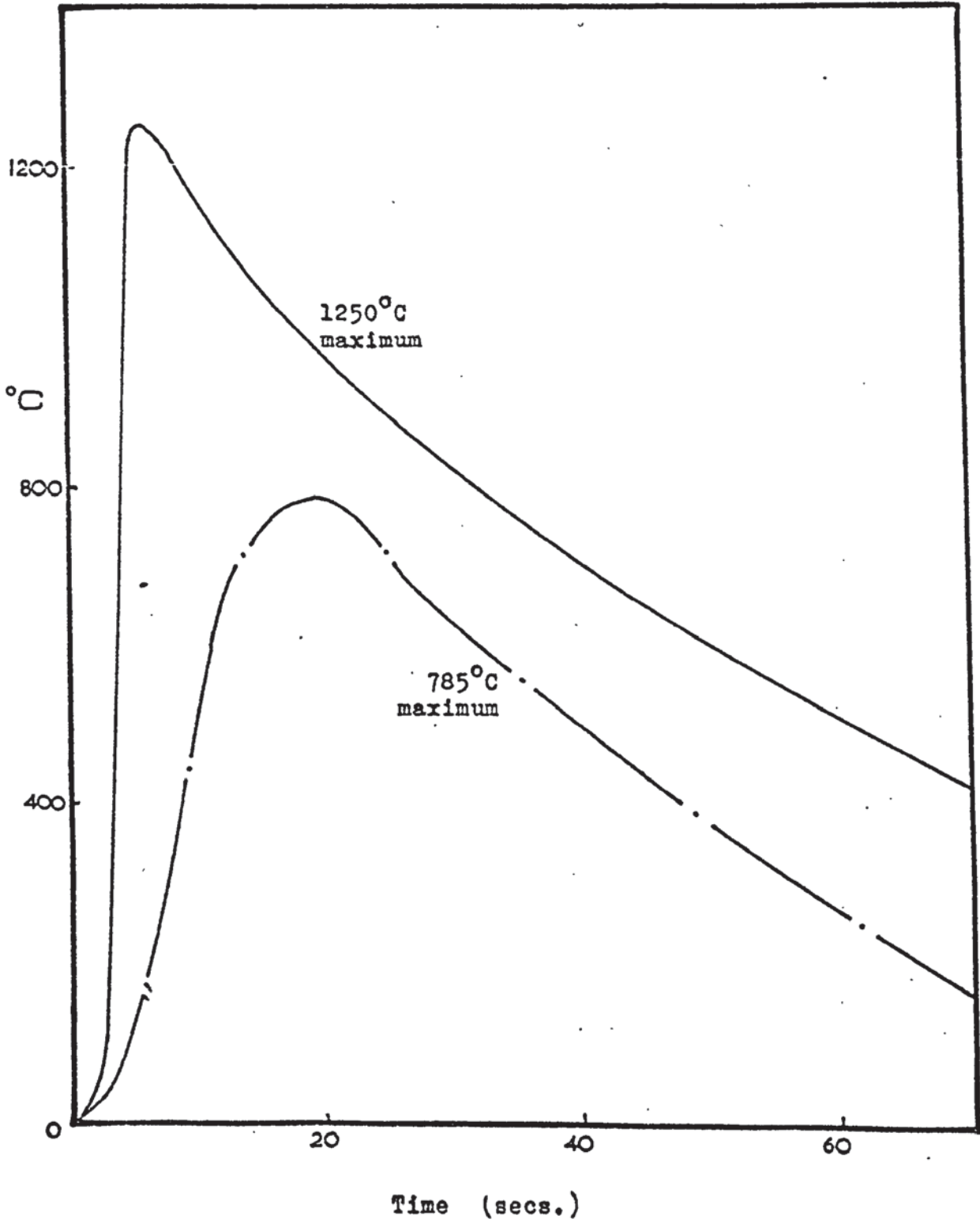
Fig. 56. Thermal cycles employed for simulation.
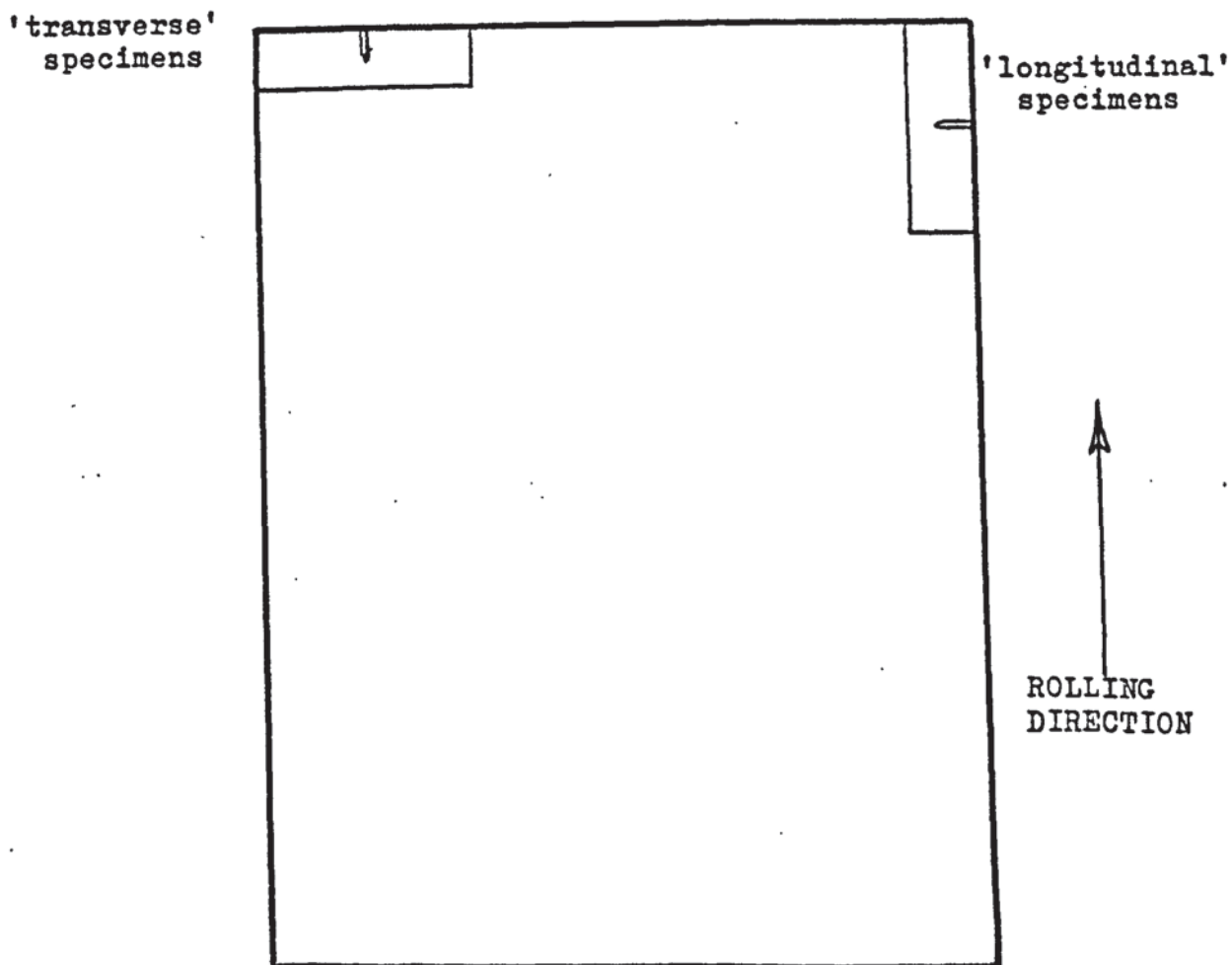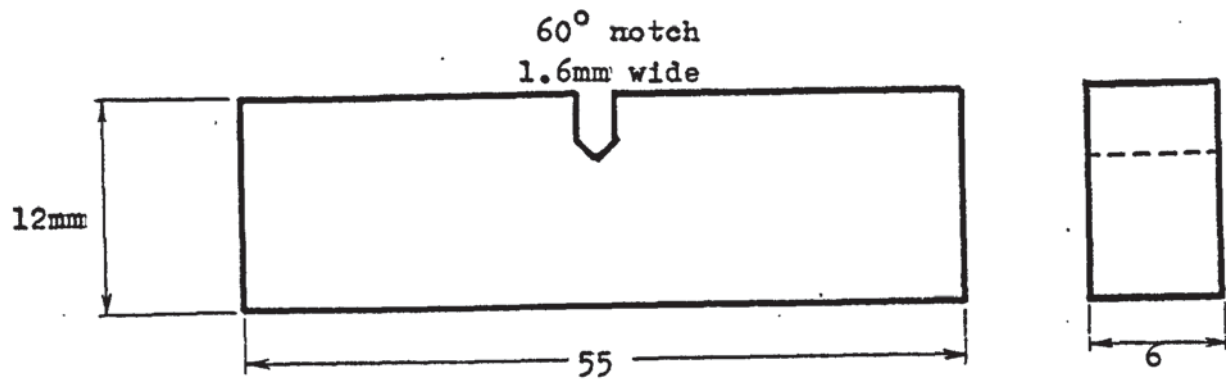
Fig. 57. Fracture toughness specimen configuration and plate orientation.
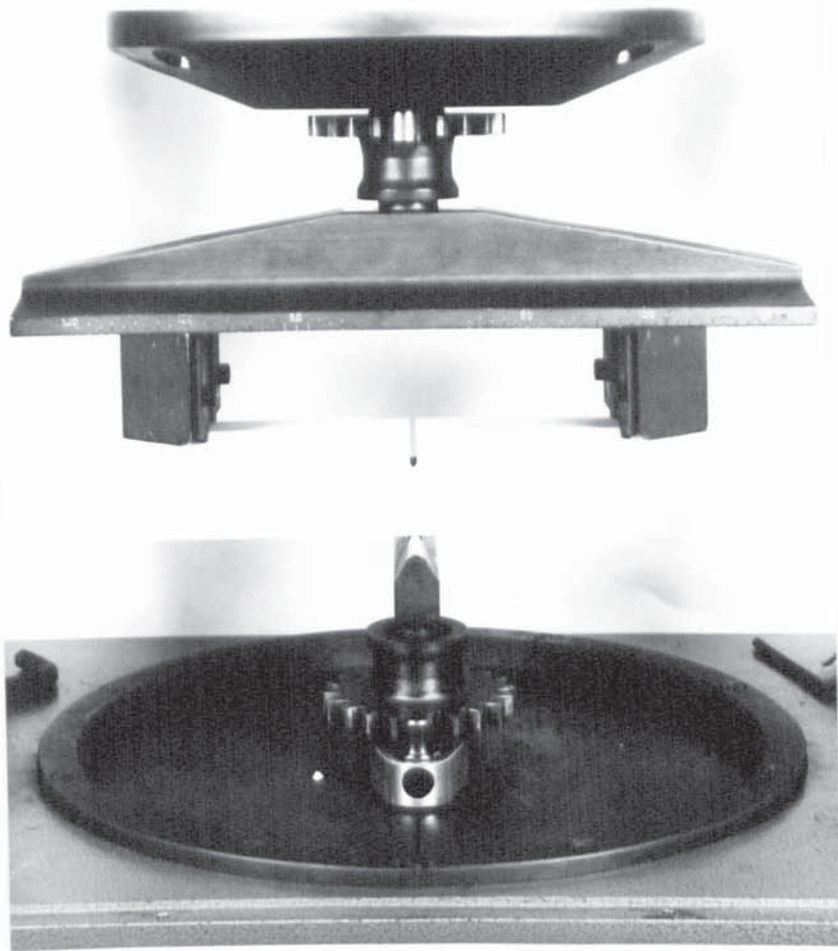
Fig. 58.   Amsler Vibrophore Fatigue cracking arrangement.
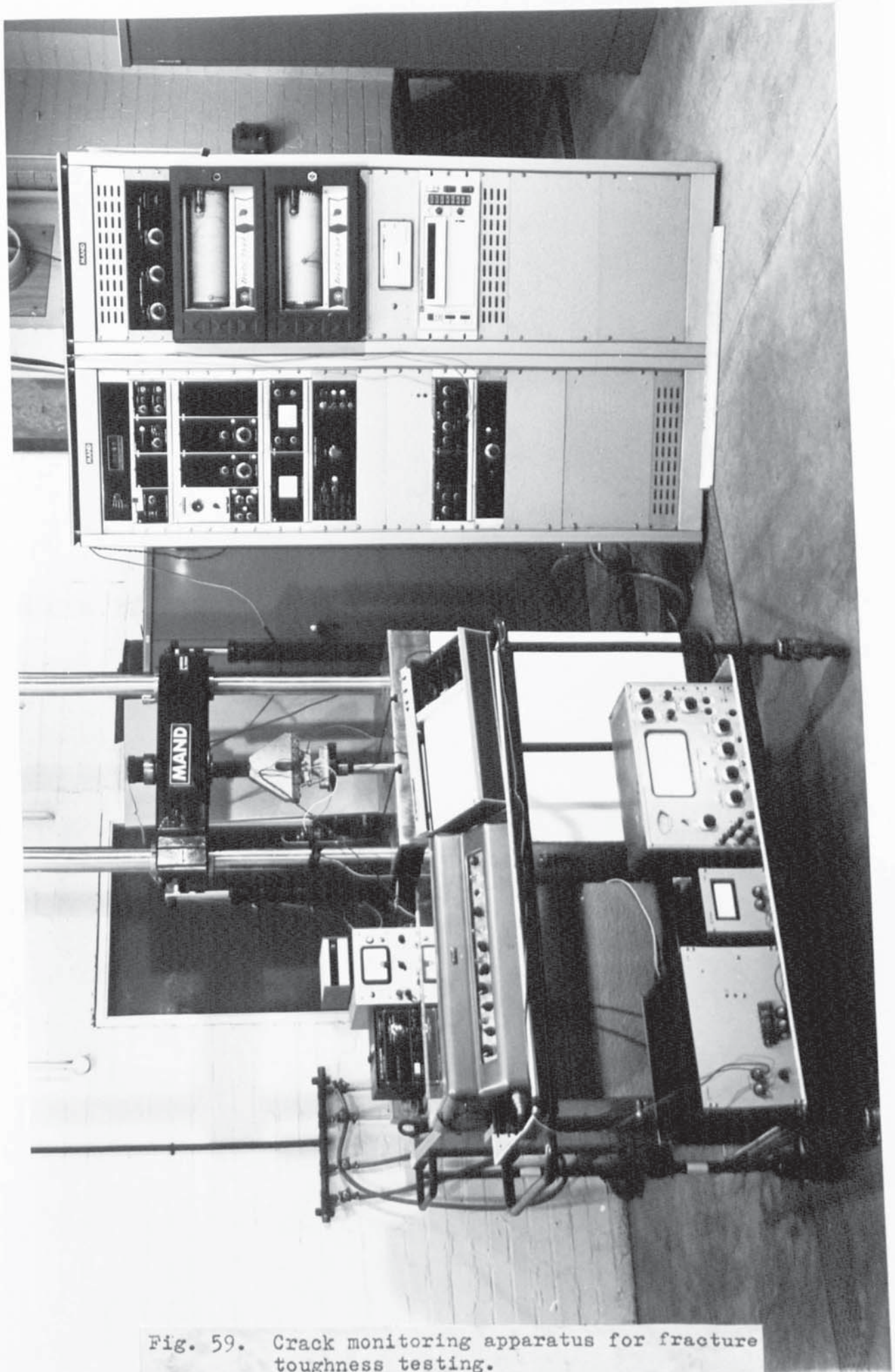
Fig. 59. Crack monitoring apparatus for fracture
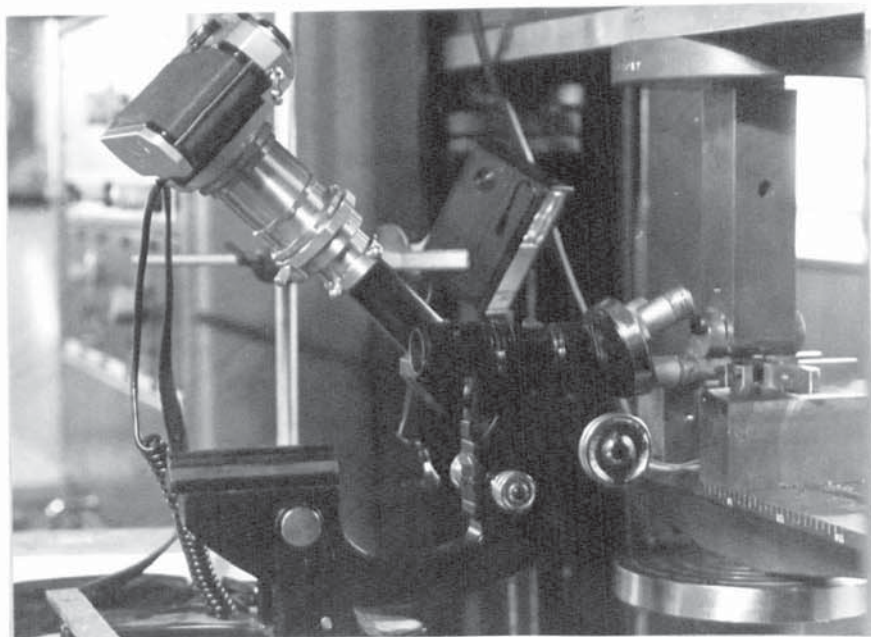toughness testing.
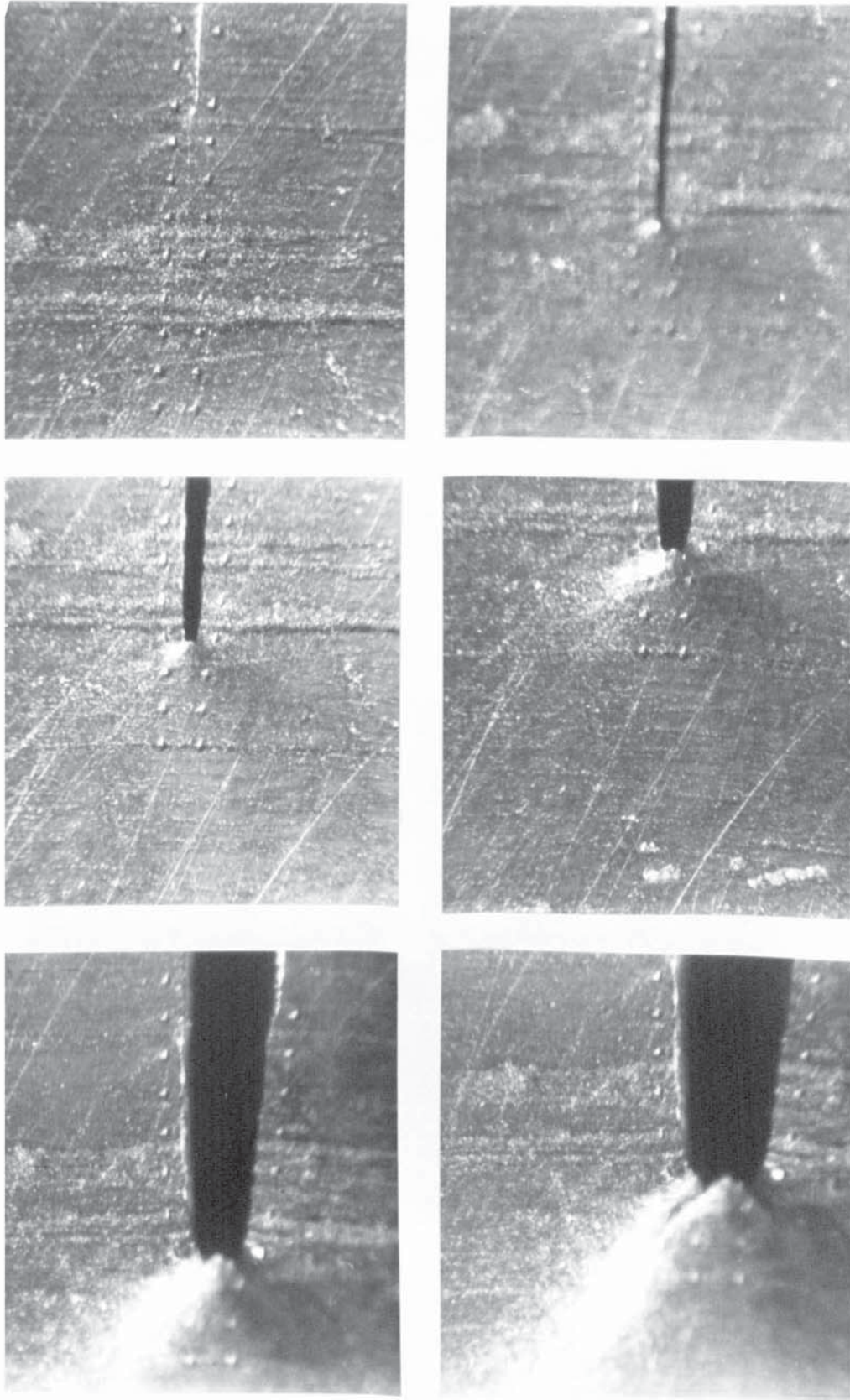
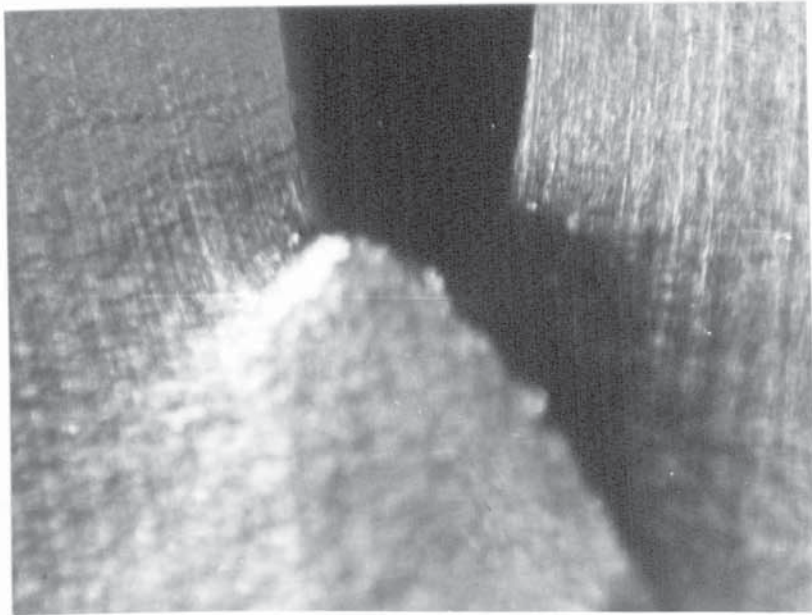Fig. 60. Photographic record of fracture toughness test.
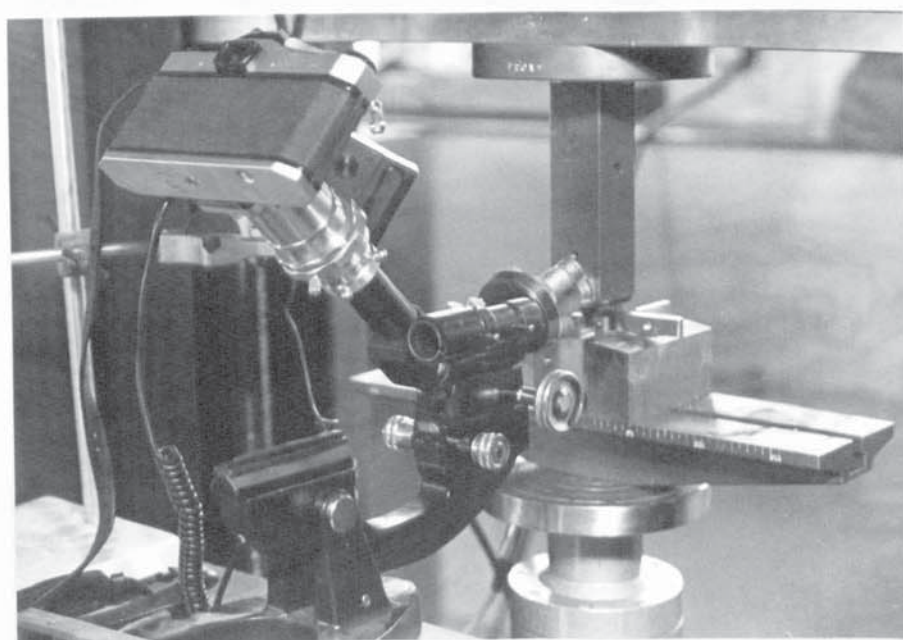
Fig. 61. Photographic recording apparatus.

Fig. 62. Obliteration of microhardness marks by growth
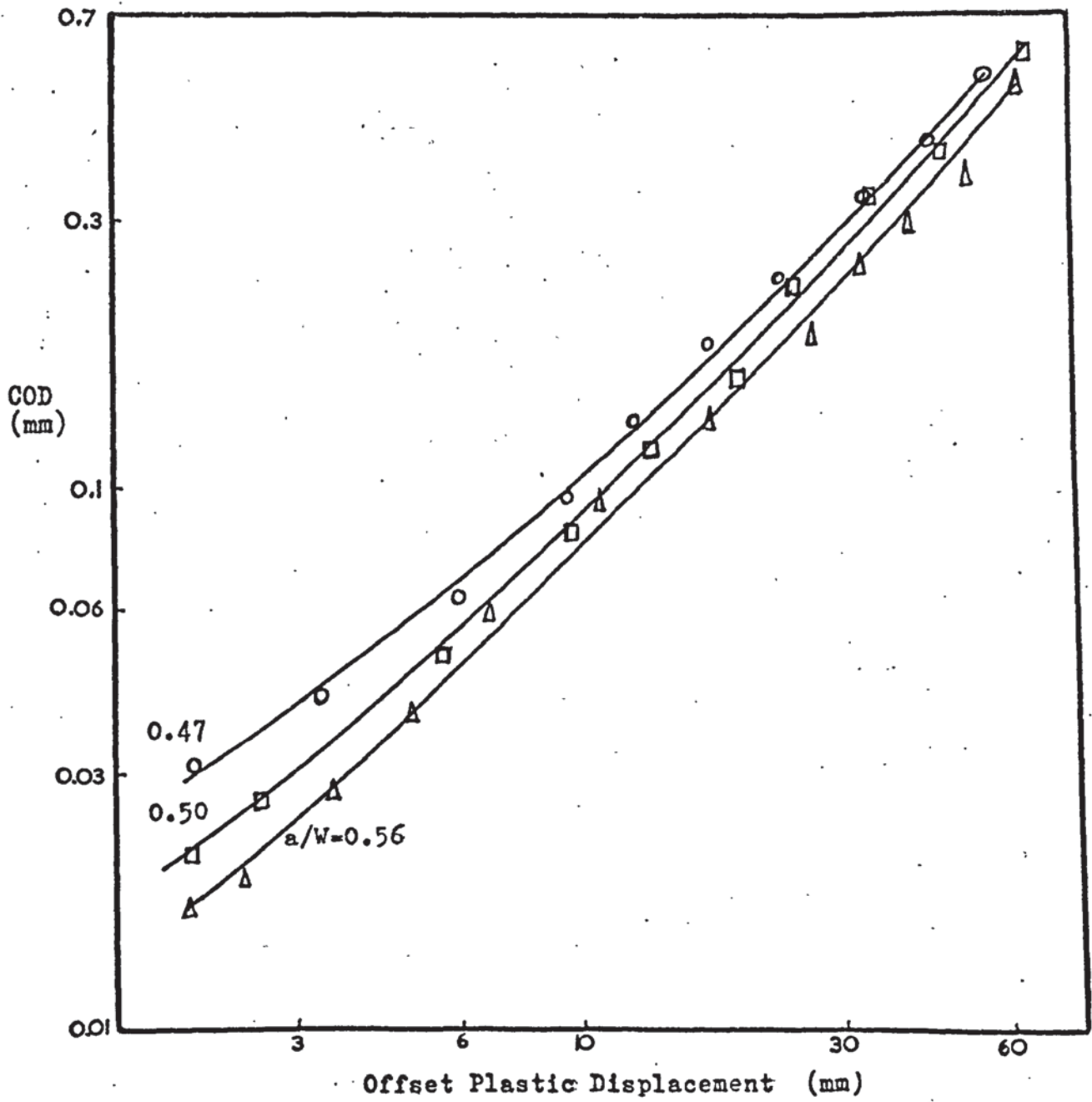of plastic zone.

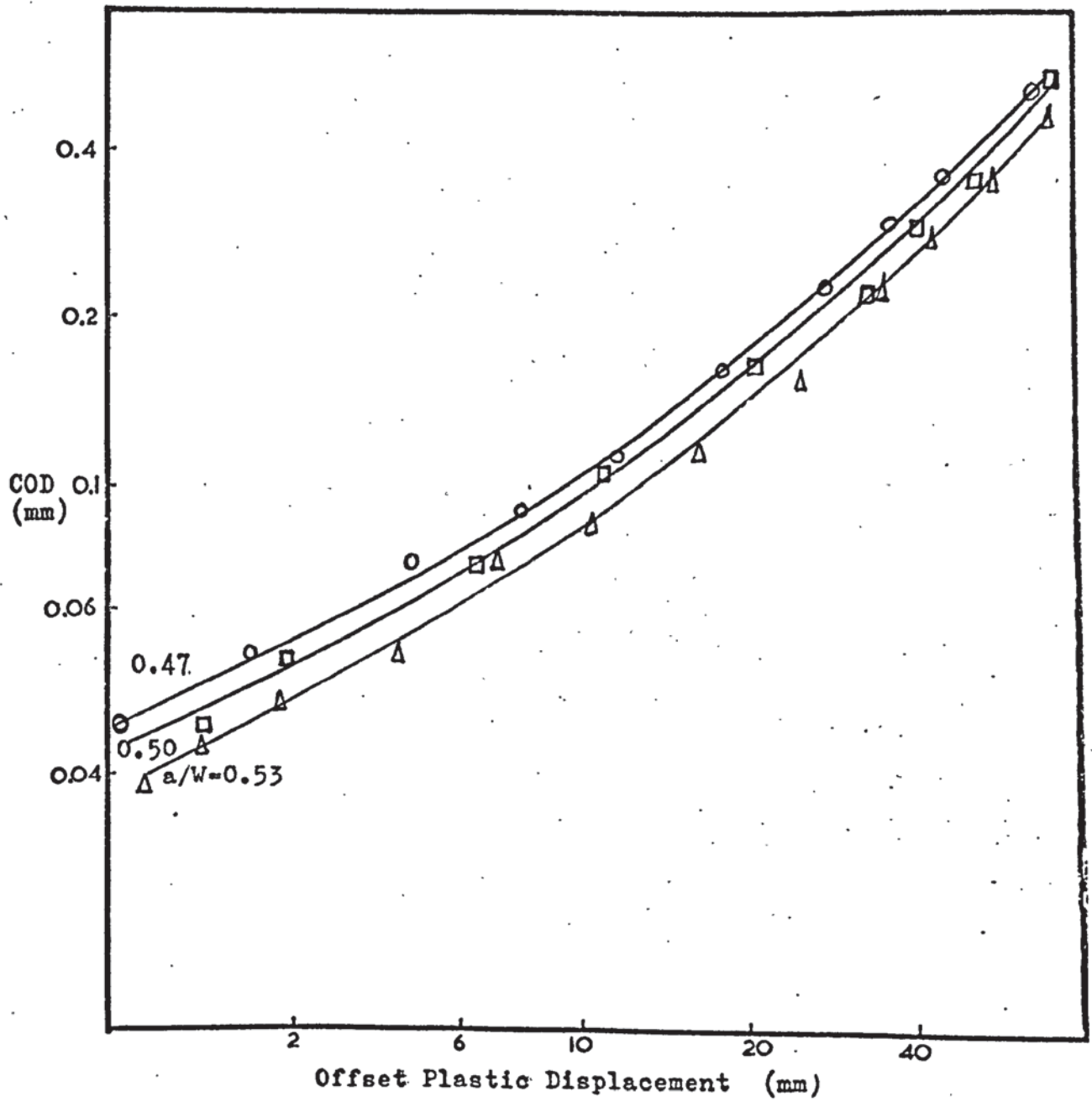Fig. 63. Photographic COD calibration curves -- transverse specimens.

Fig. 64. Photographic COD calibration curves --
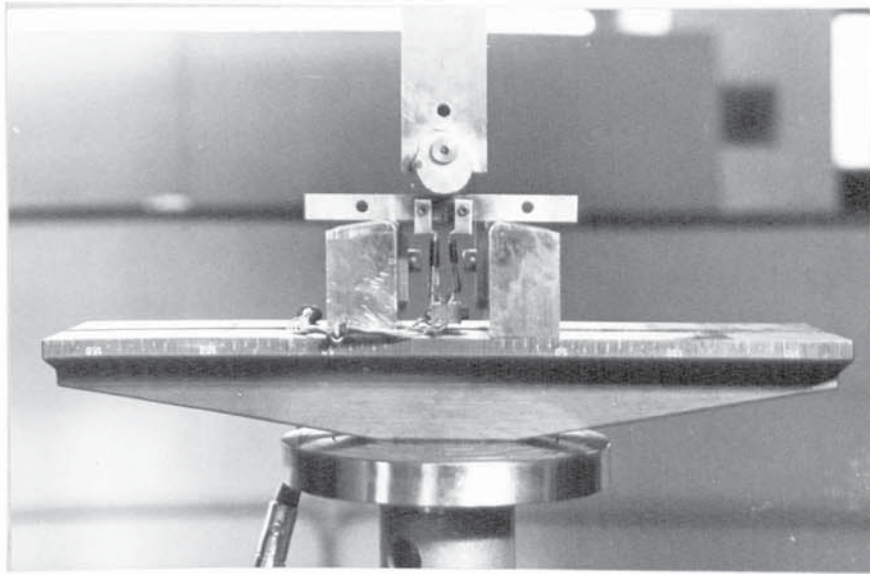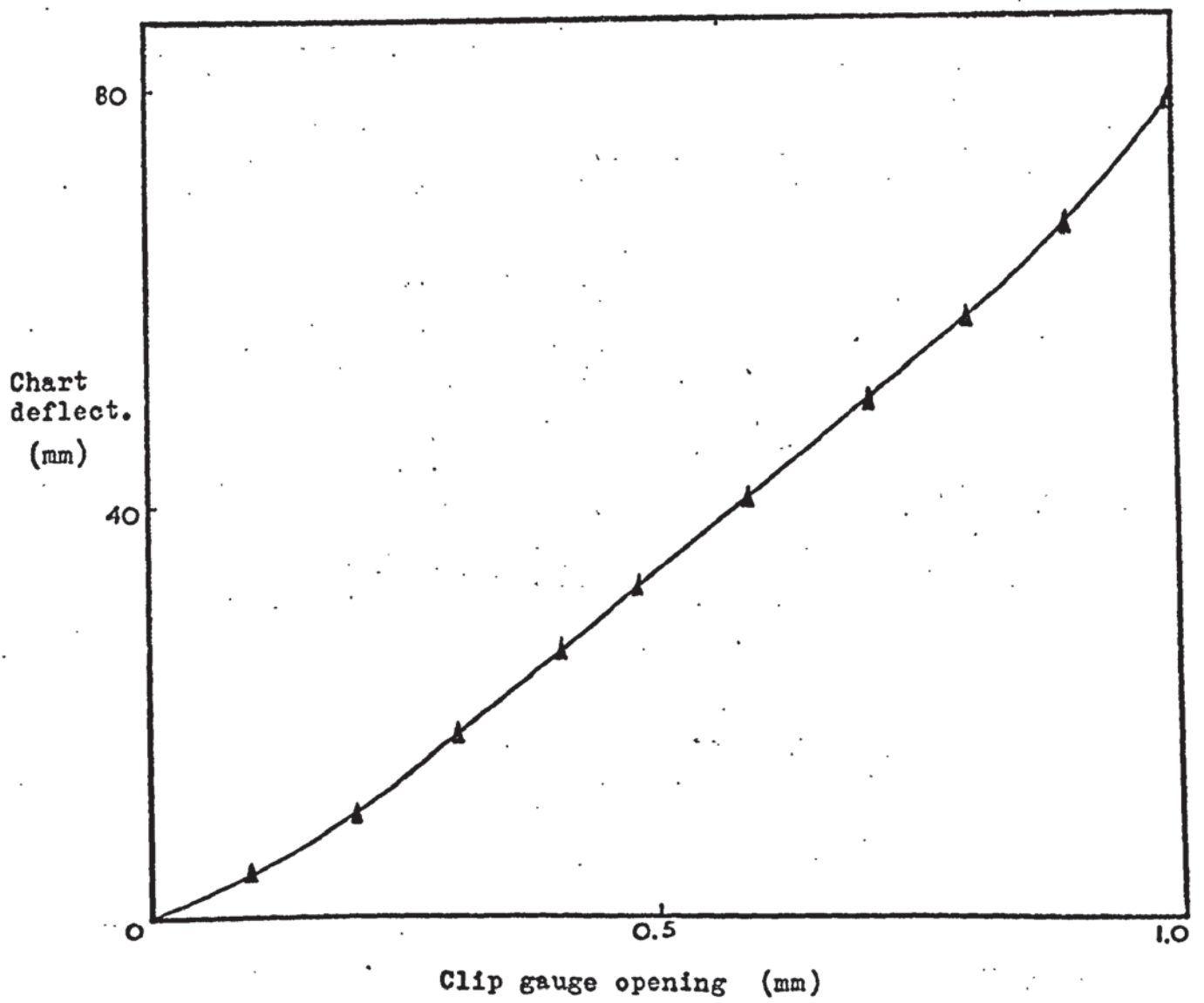longitudinal specimens.

Fig. 65. Fracture toughness testing with clip gauge.

Fig. 66. Clip gauge calibration curve.

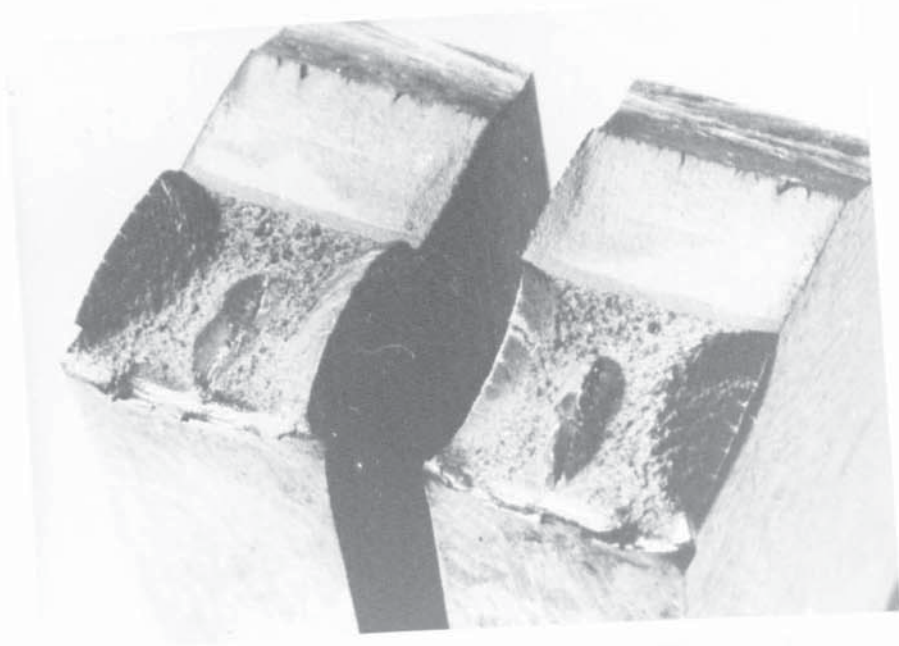Fig. 67.   Formation of shear lips.
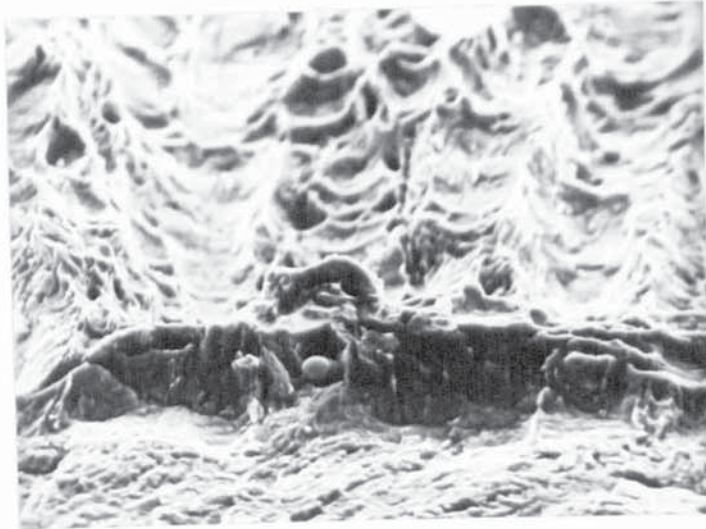
X 1200
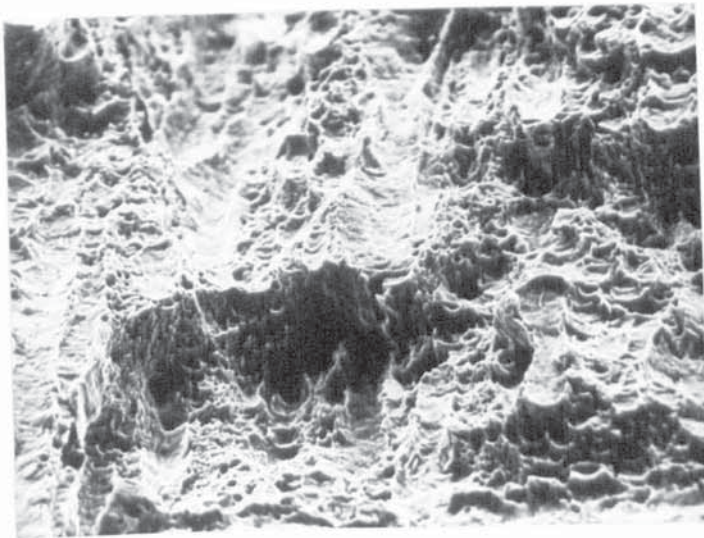
X 580
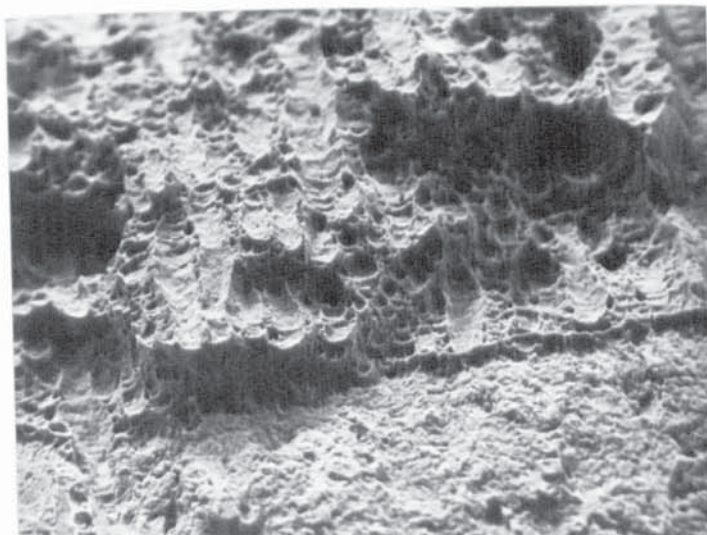
X 580

Fig. 68. Stretch zones -- air melted plate, transverse specimens.
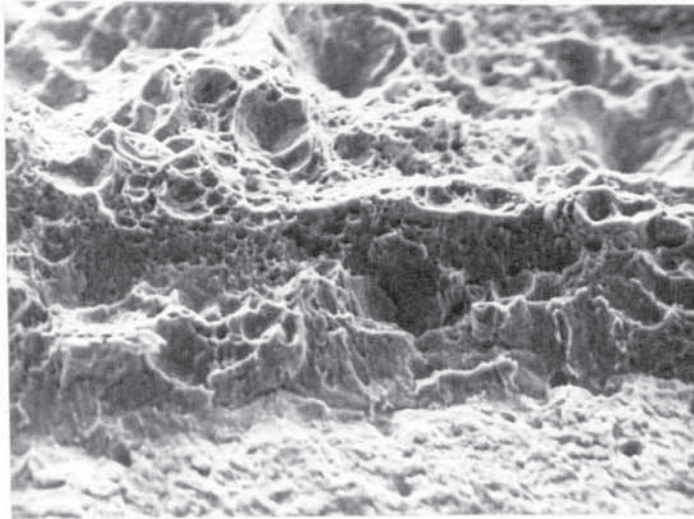
X 730
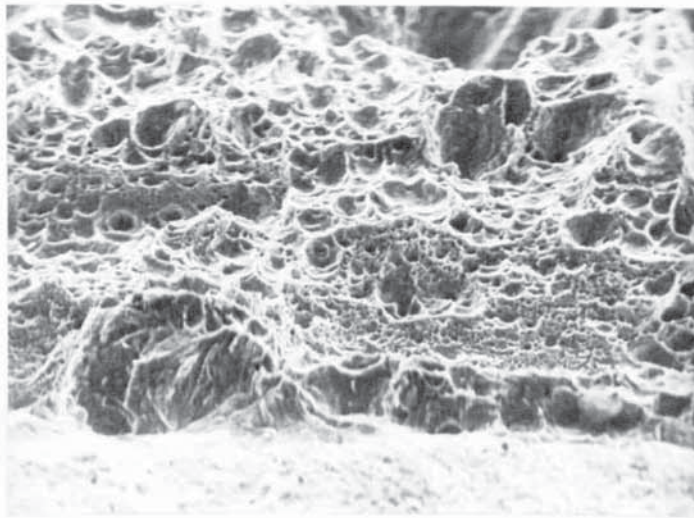
X 530
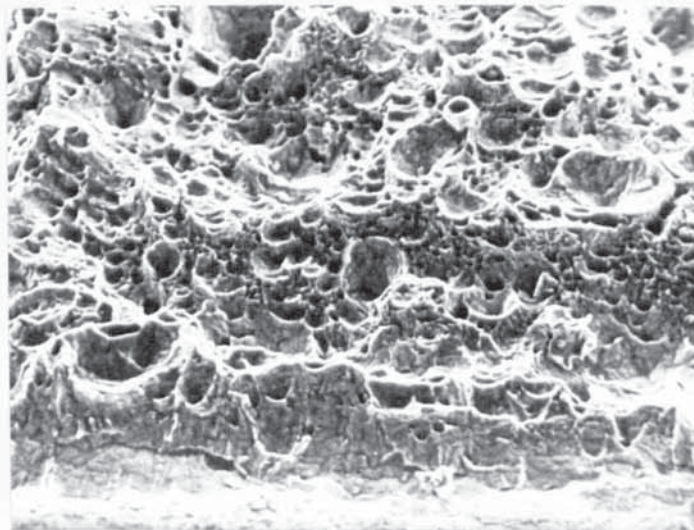
X 540

Fig. 69. Stretch zones -- air melted plate, longitudinal
specimens.
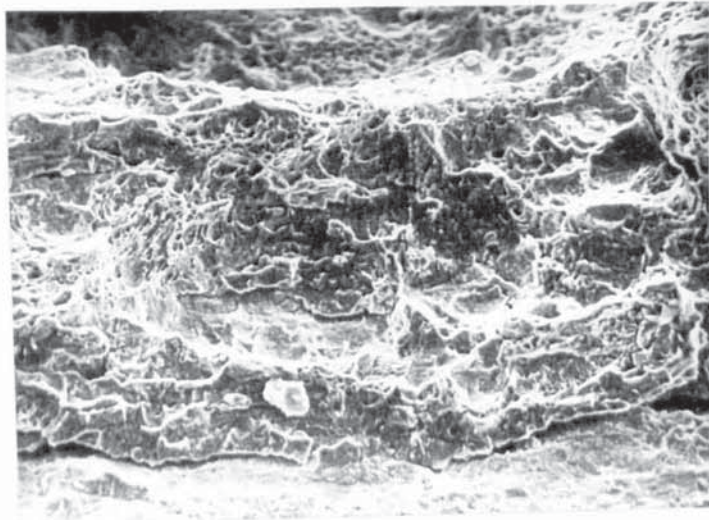
X 560
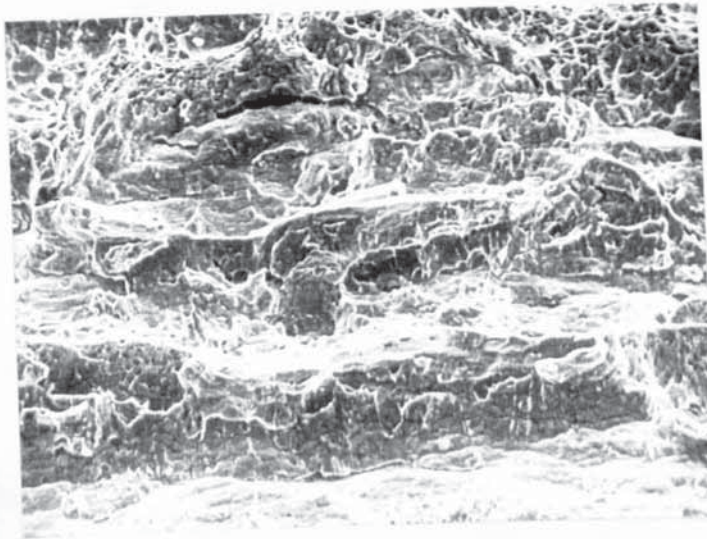
X 540
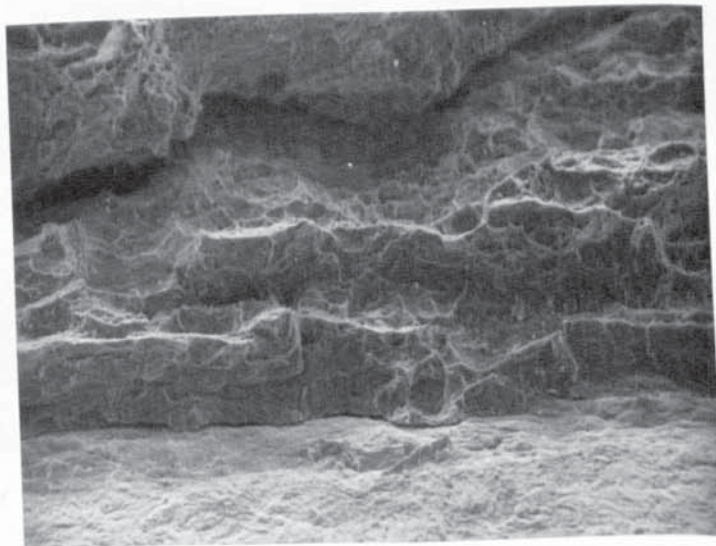
X 290

Fig. 70. Stretch zones -- vacuum remelted plate.
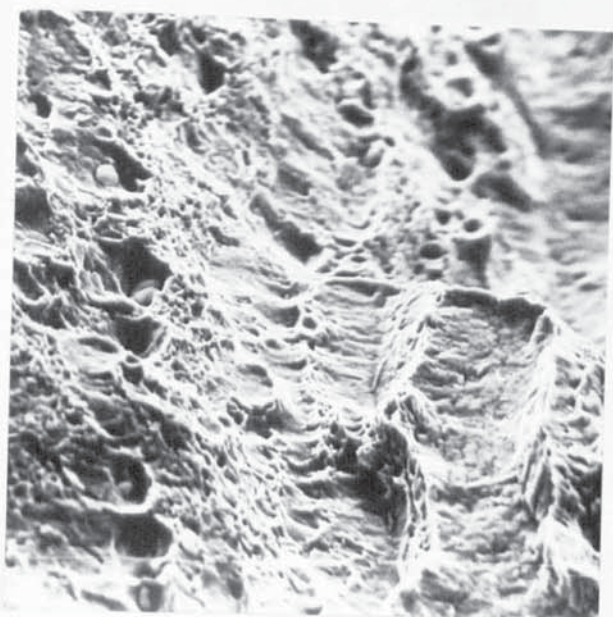
X 1200
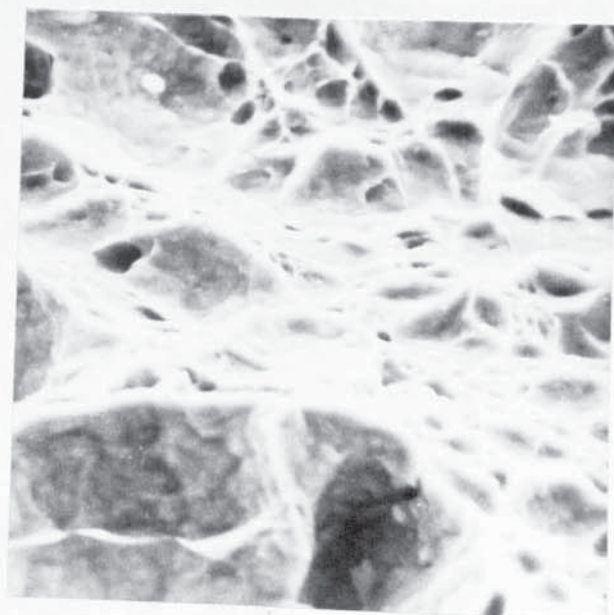
X 2800
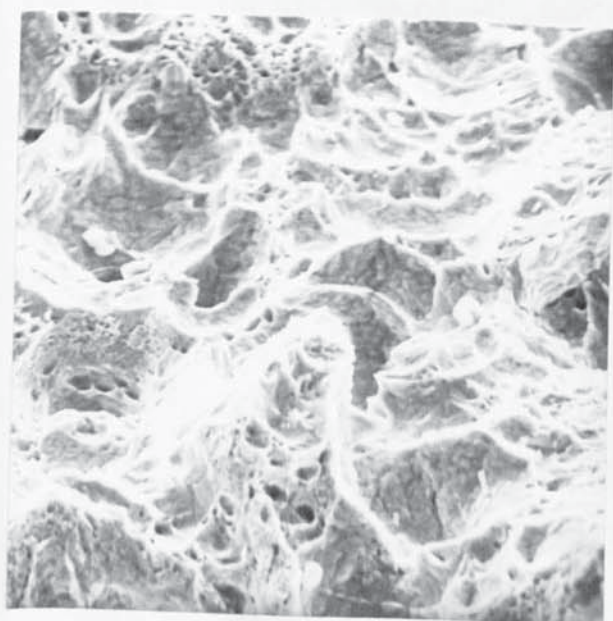
X 1100
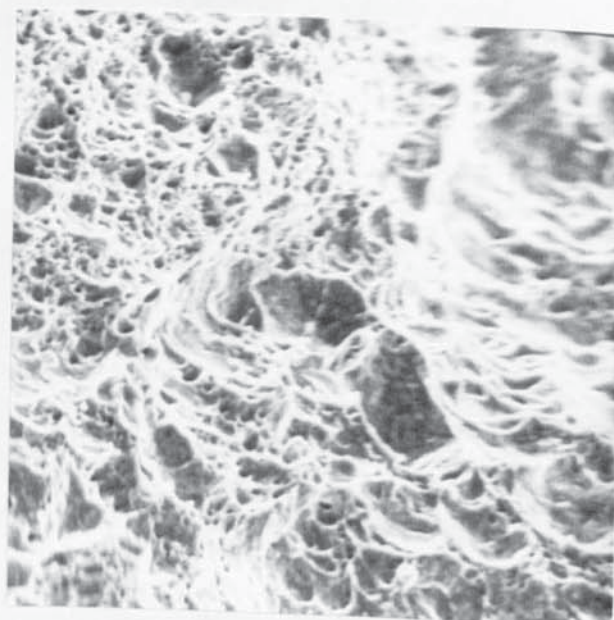
X 1100

Fig. 71. Fracture surfaces -- simulated HAZ specimens, 785°C peak, air melted plate.

X 52
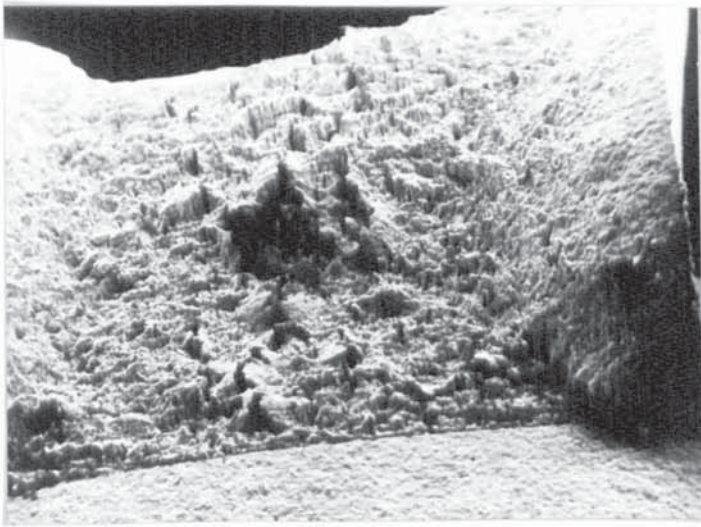
X 22

X 750

Fig. 72. Fracture surfaces -- simulated HAZ specimens, longitudinal orientation.
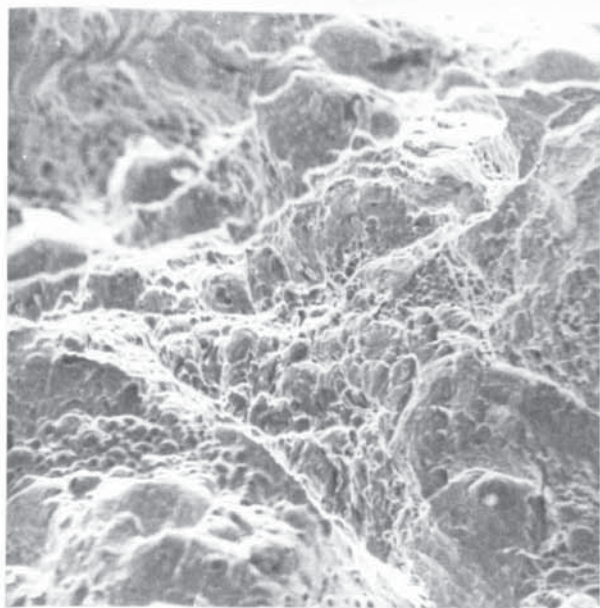
X 650
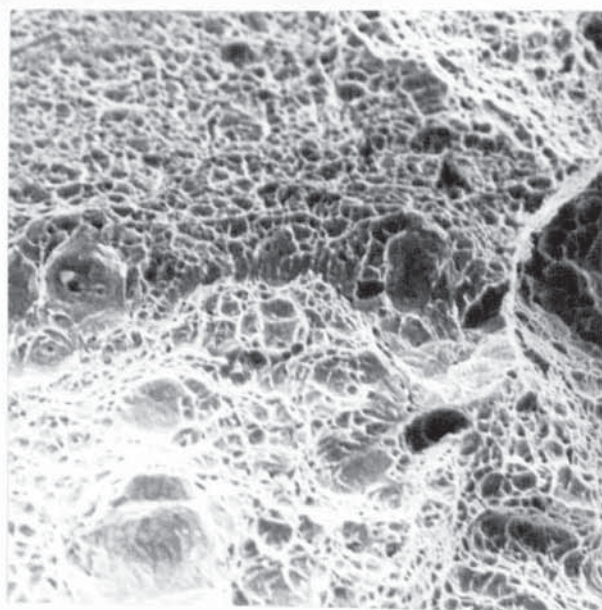
X 710
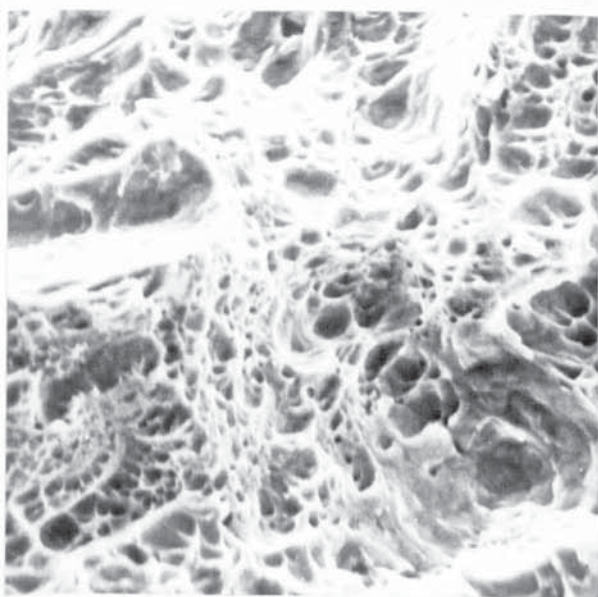
X 2200
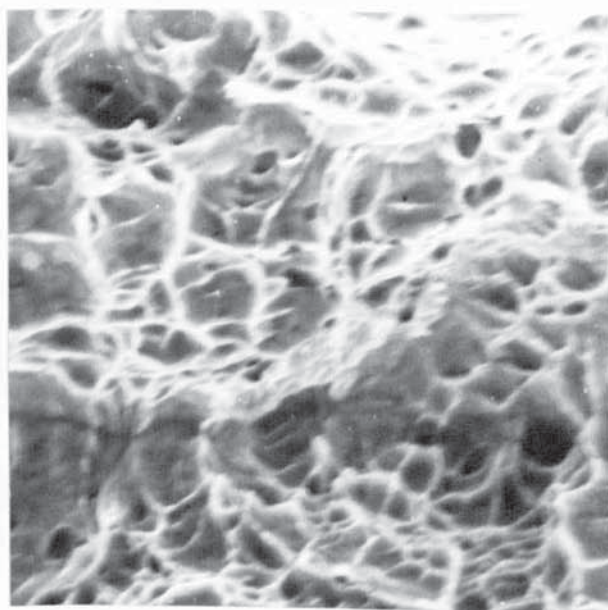
X 2600

Fig. 73. Fracture surfaces -- simulated HAZ specimens, 785°C peak, vacuum remelted plate.
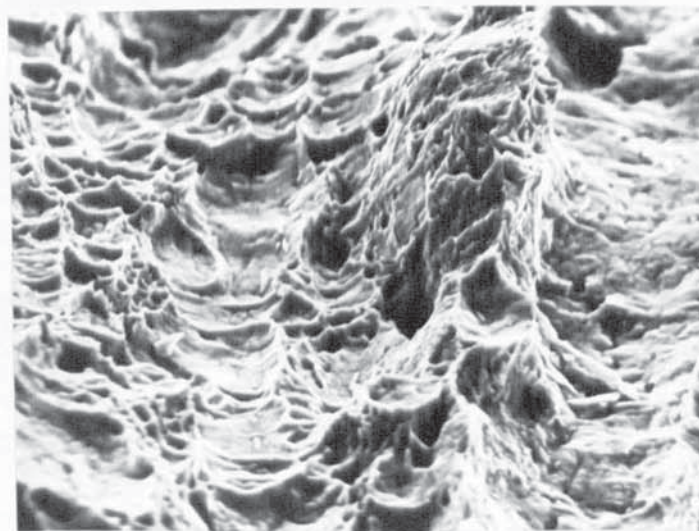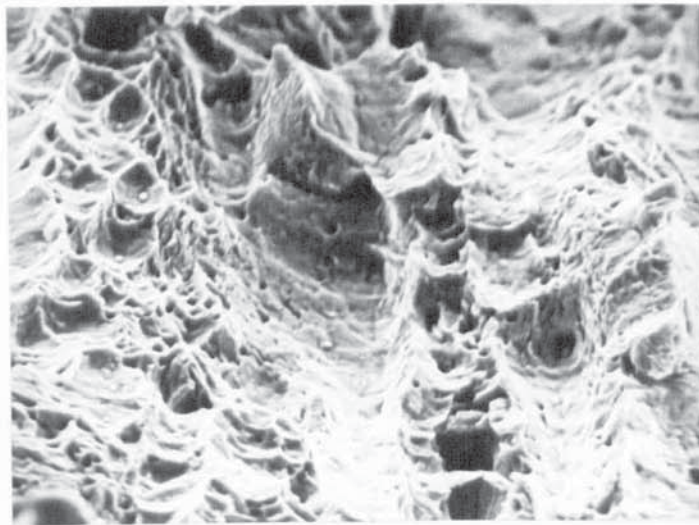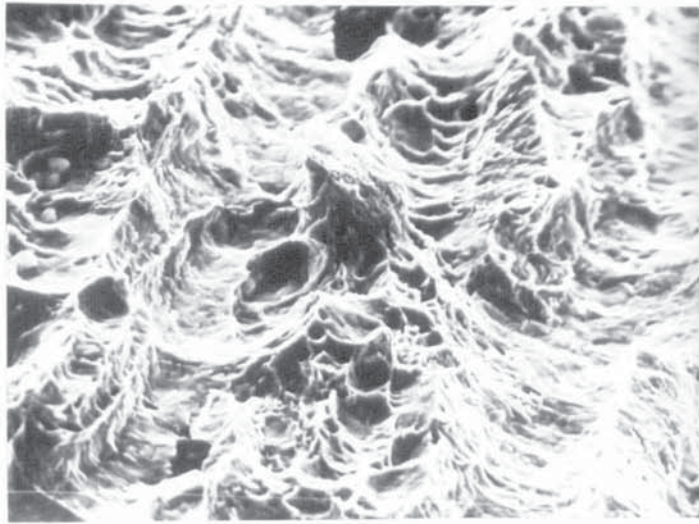
Fig. 74. Fracture surfaces -- simulated HAZ specimens,
1250°C peak, air melted plate.
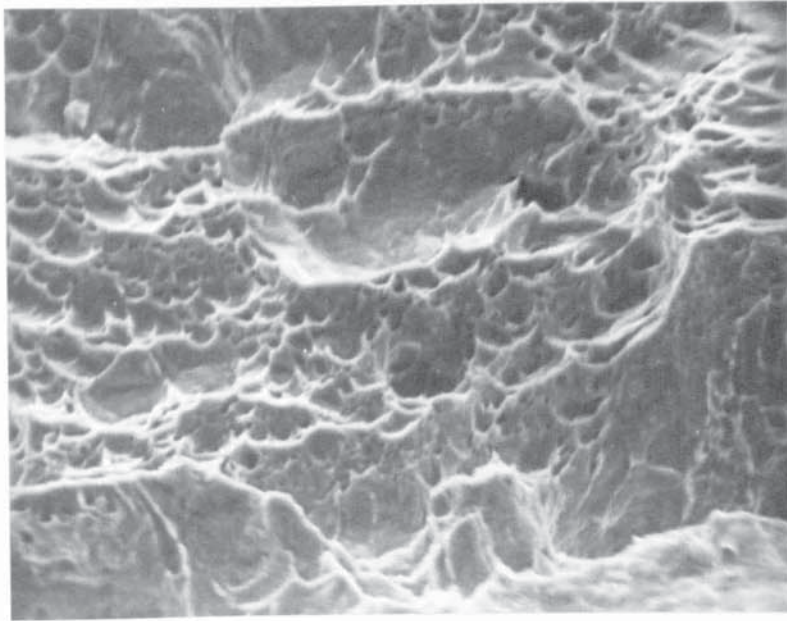
X 1300
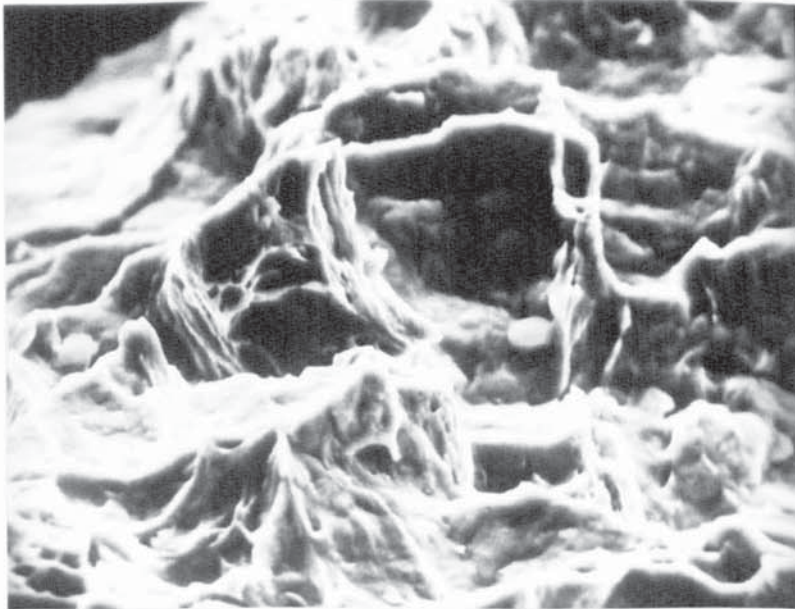
X 2300

Fig. 75. Fracture surfaces -- simulated HAZ specimens, 1250°C peak, vacuum remelted plate.
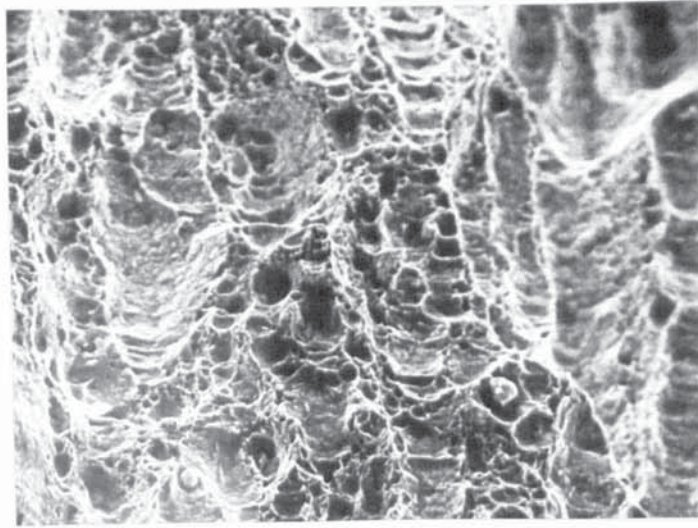
X 580

X 2900
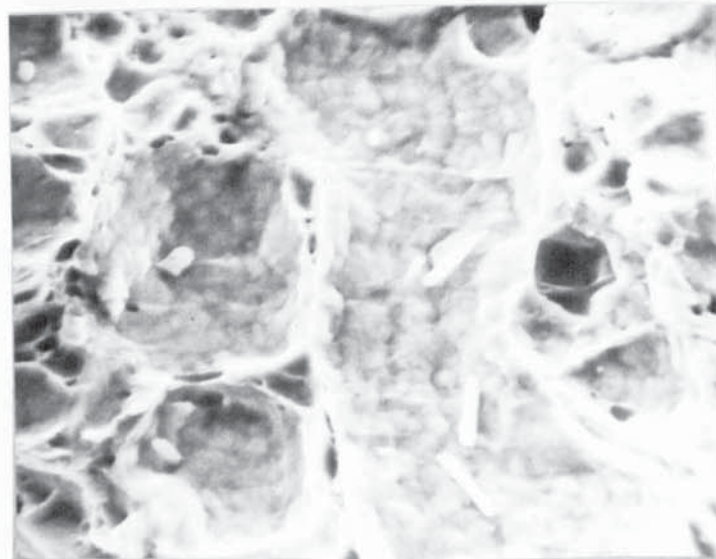
X 2900

Fig. 76. Fracture surfaces -- welded specimens, 785°C peak.
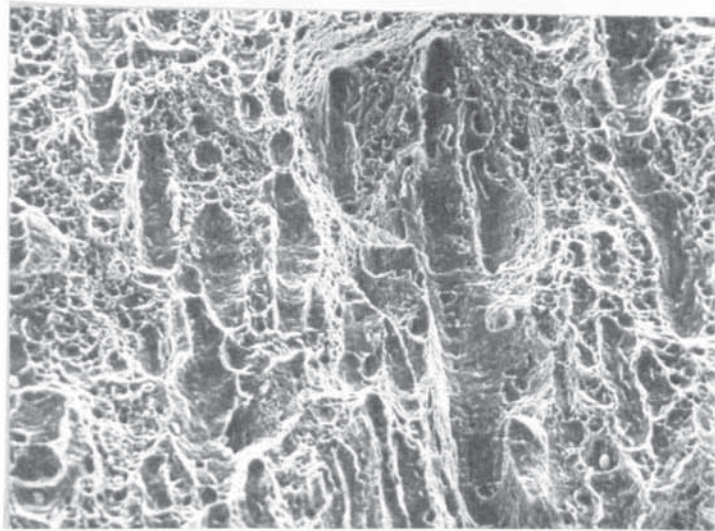
X 570

X 1100
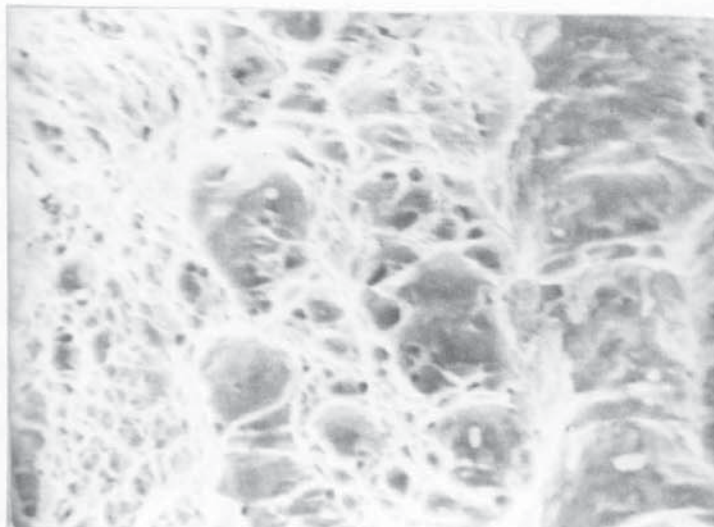
X 2200

Fig. 77. Fracture surfaces -- welded specimens, 1250°C peak.
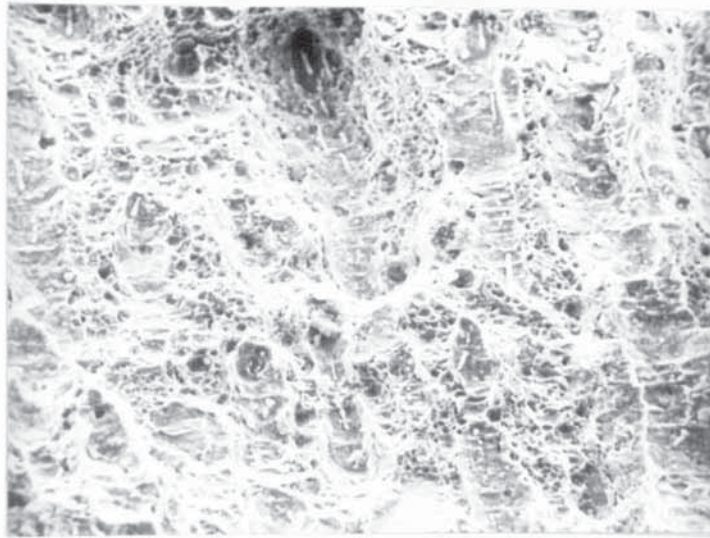
X 700
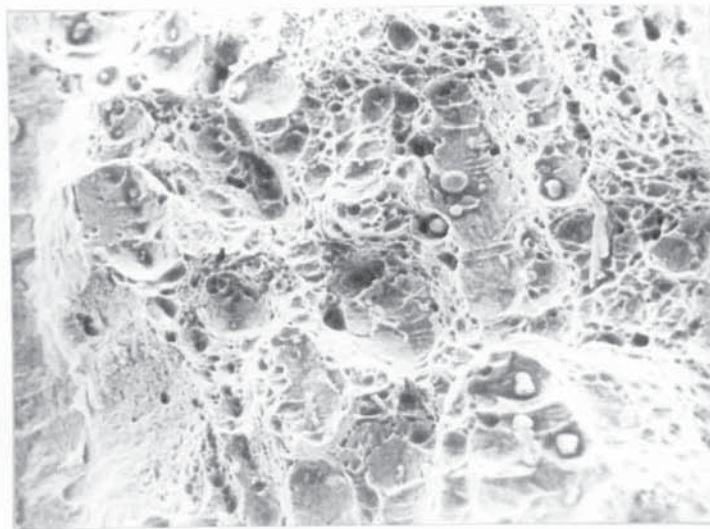
X 700
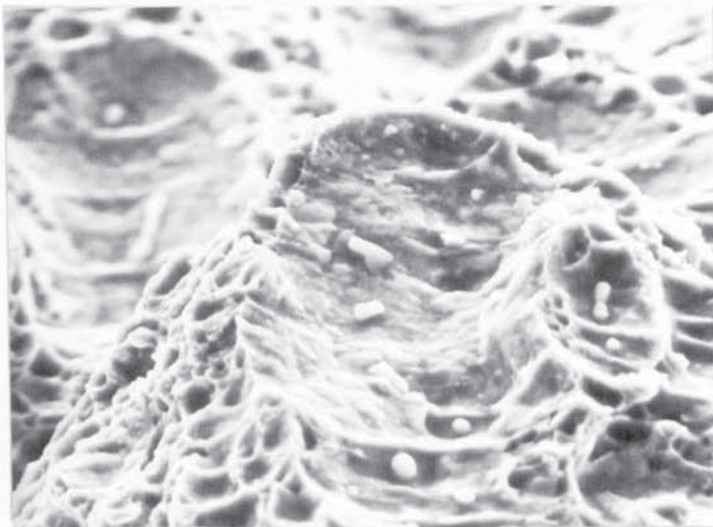
X 2200

Fig. 78. Fracture surfaces -- air melted parent plate.
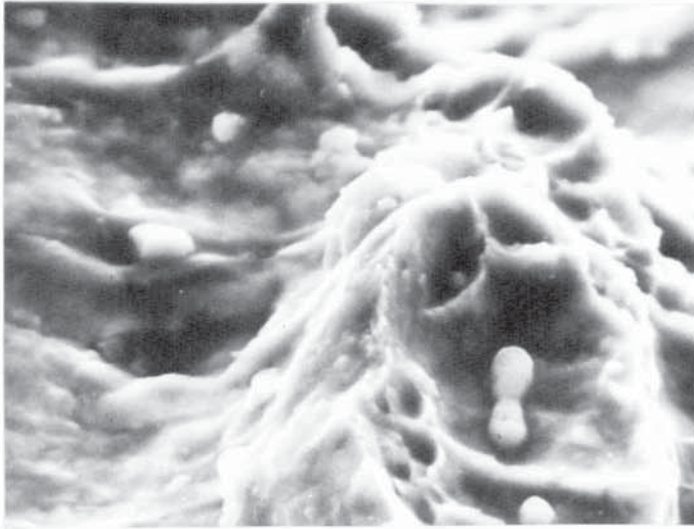
X 2900
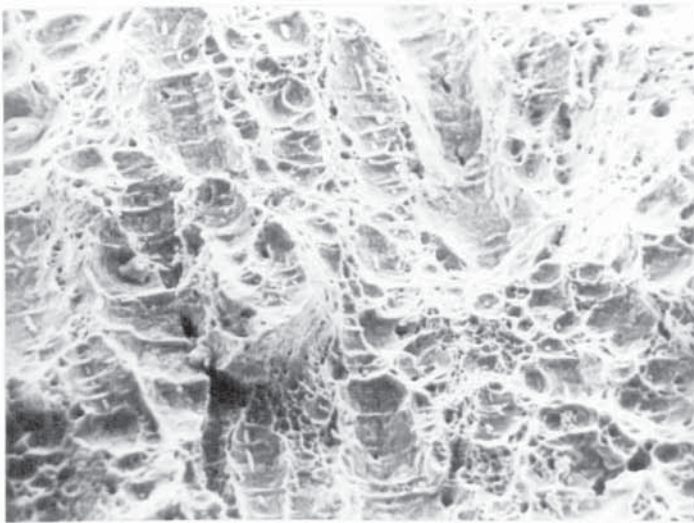
X 700
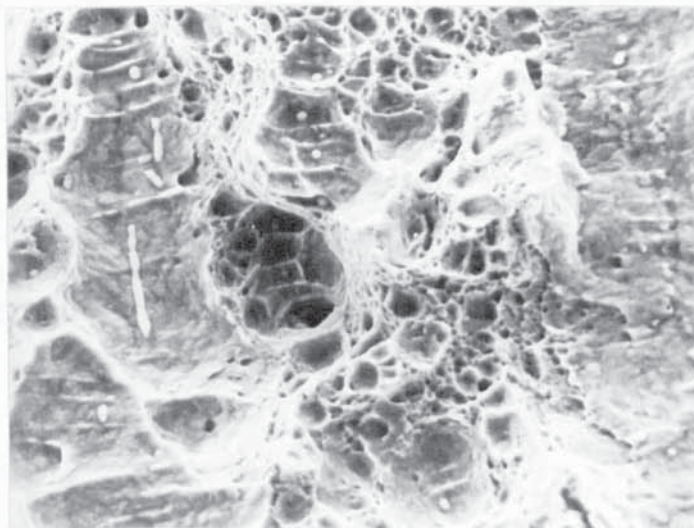
X 1450

Fig. 79. Fracture surfaces -- air melted parent plate.
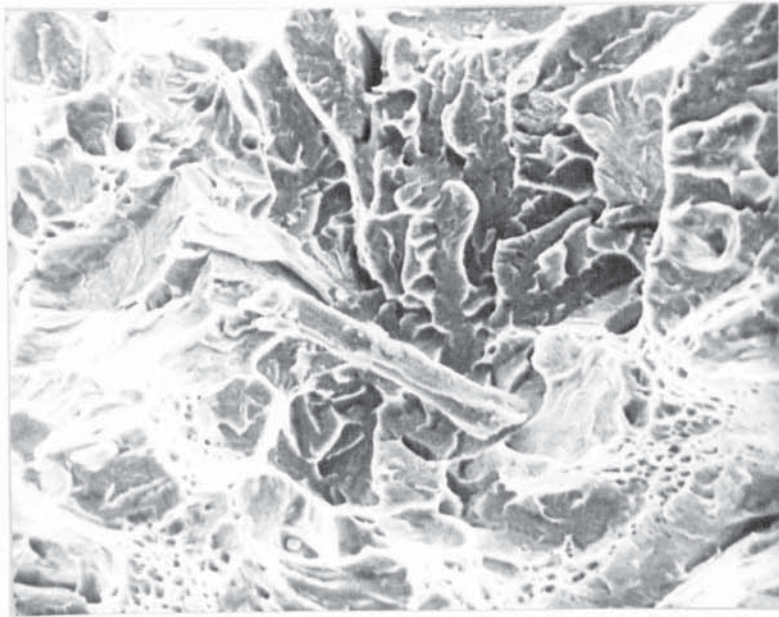
X 1150
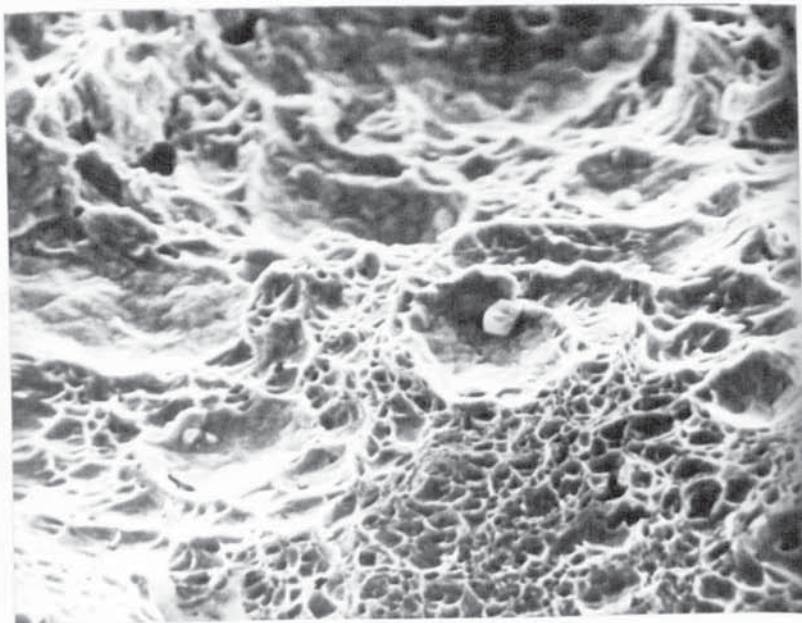
X 1150

Fig. 80. Fracture surfaces -- vacuum remelted parent plate.
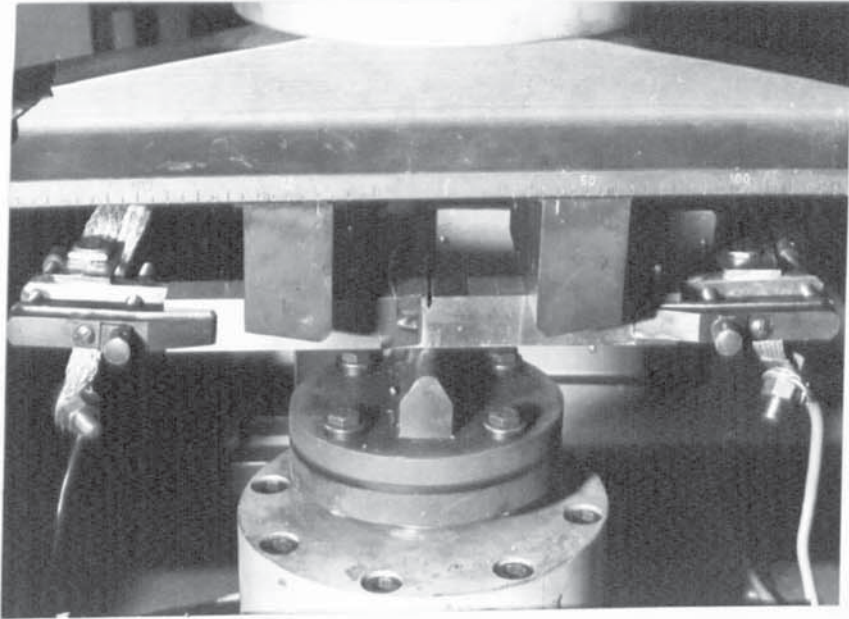
Fig. 81. Clamping arrangement, crack monitoring apparatus.
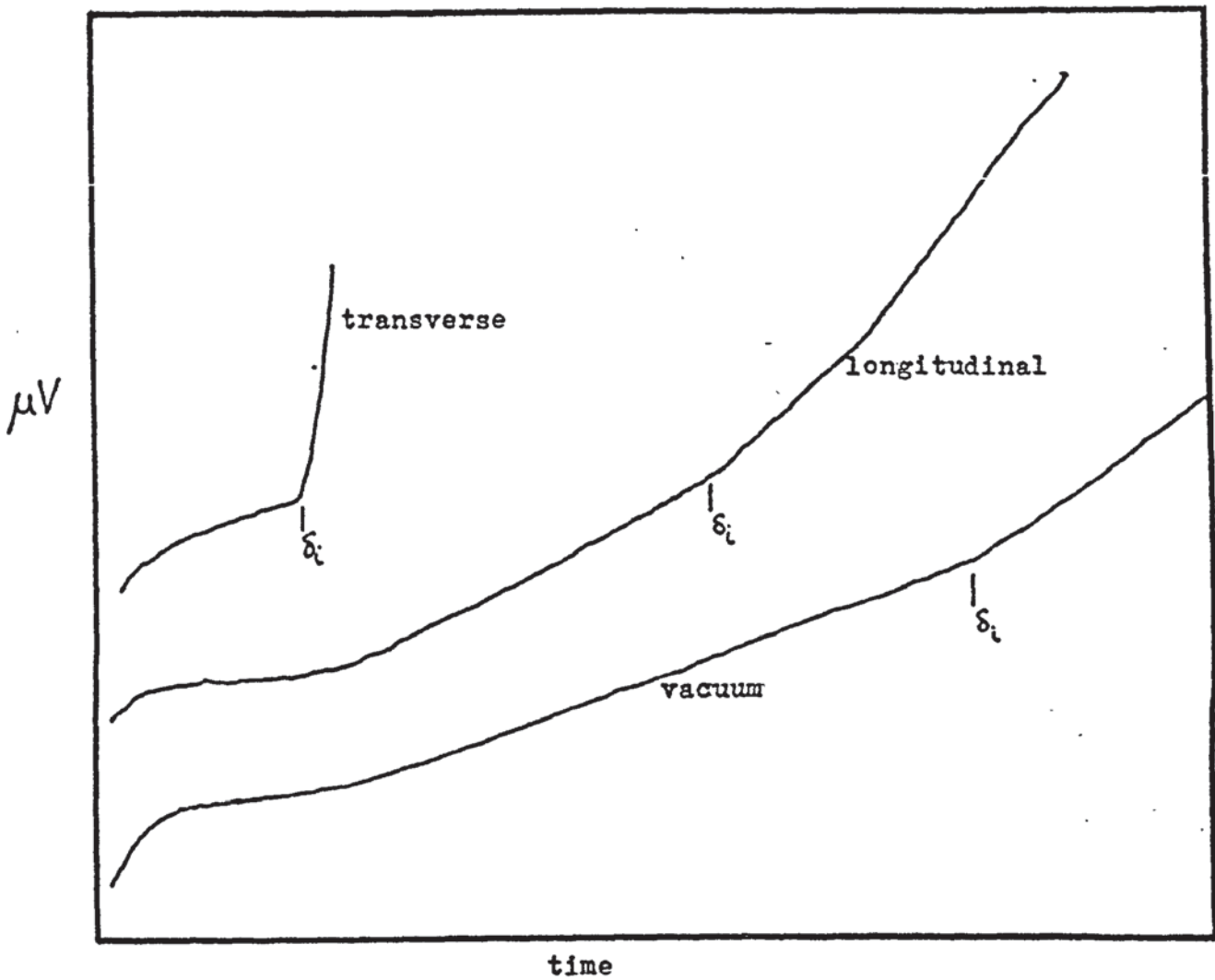
Fig. 82. Typical crack monitoring traces.
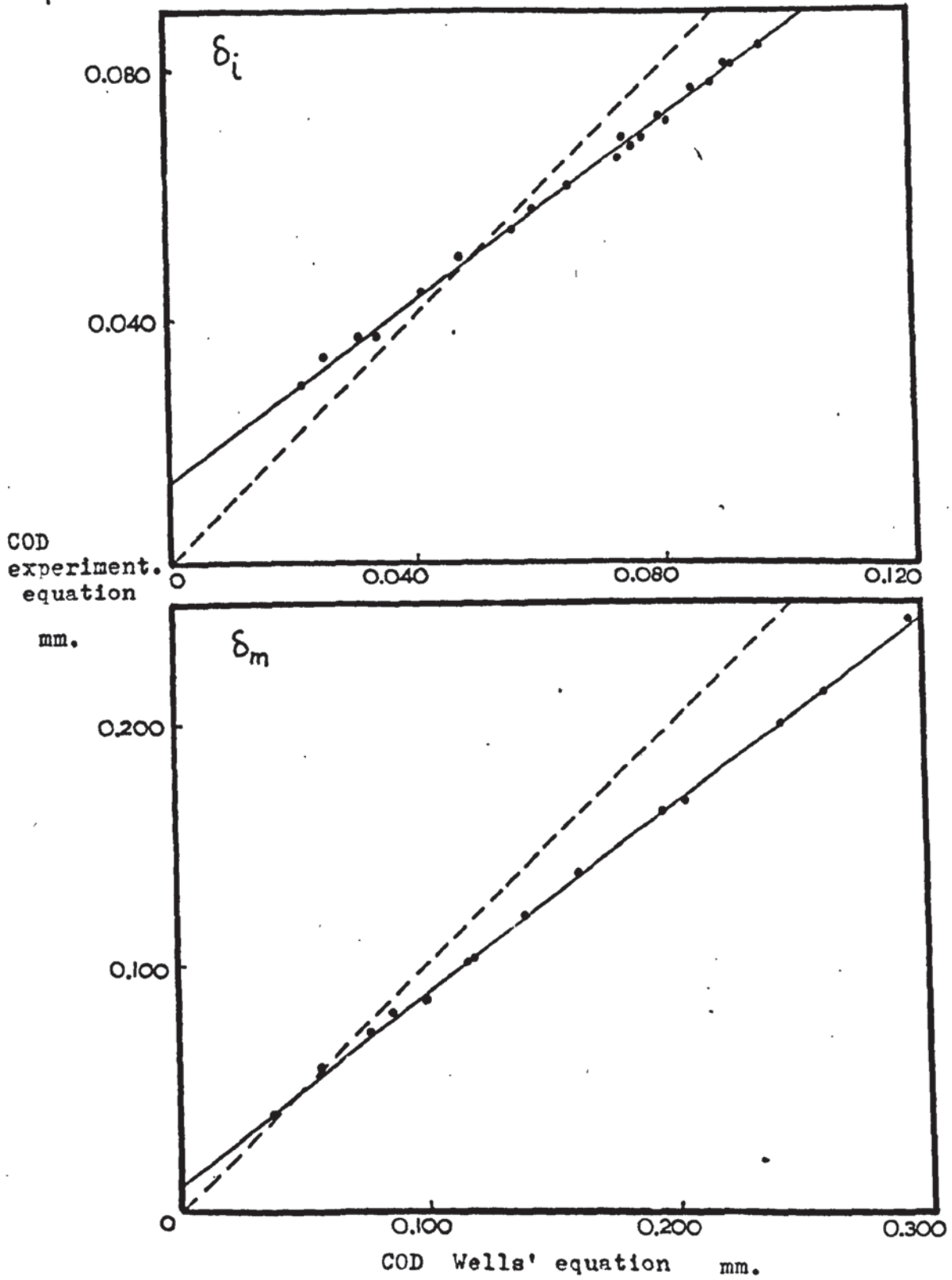
Fig. 83. Correlation of methods of calculating COD from clip gauge output.
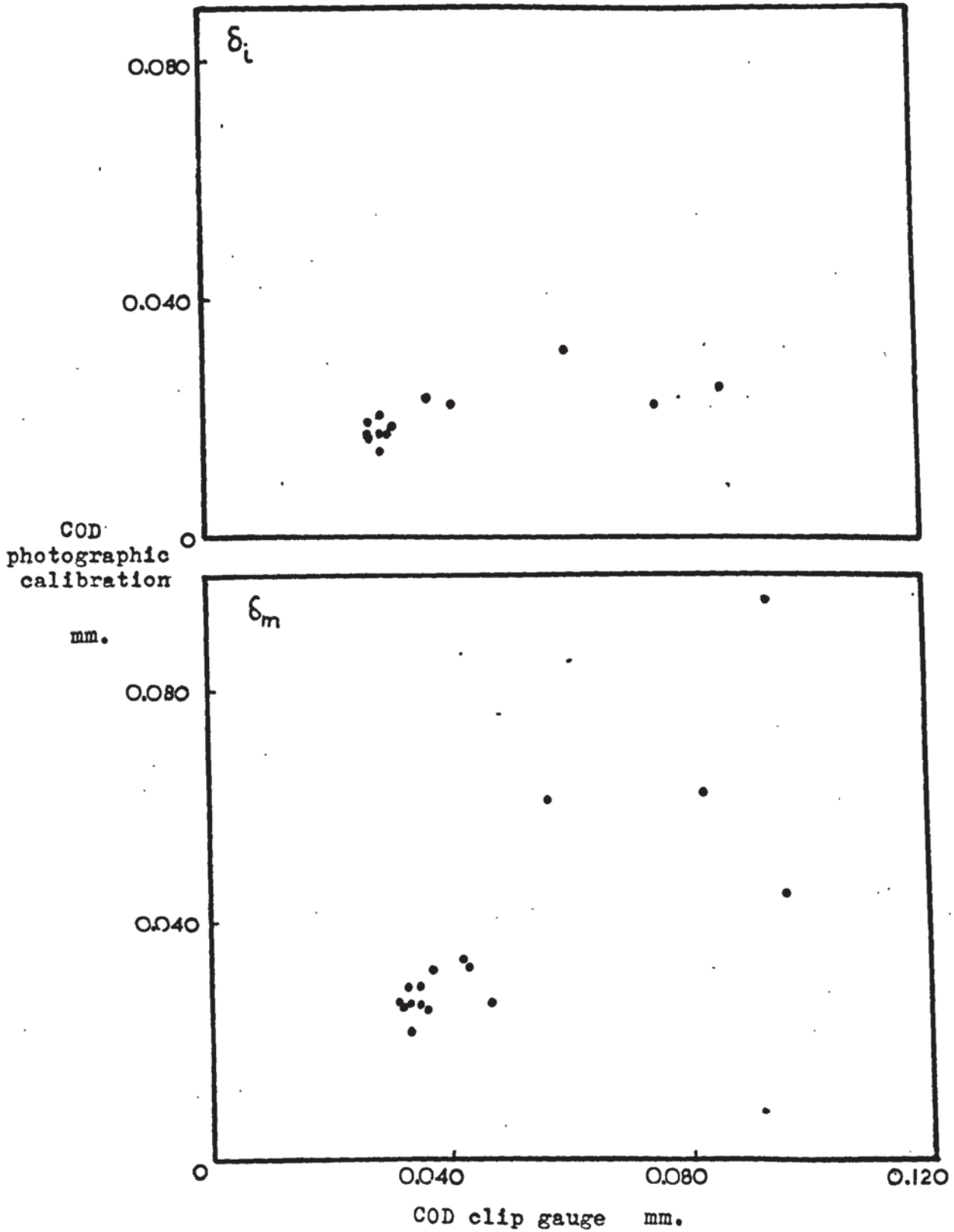
Fig. 84. Correlation of photographic calibration with
clip gauge COD.
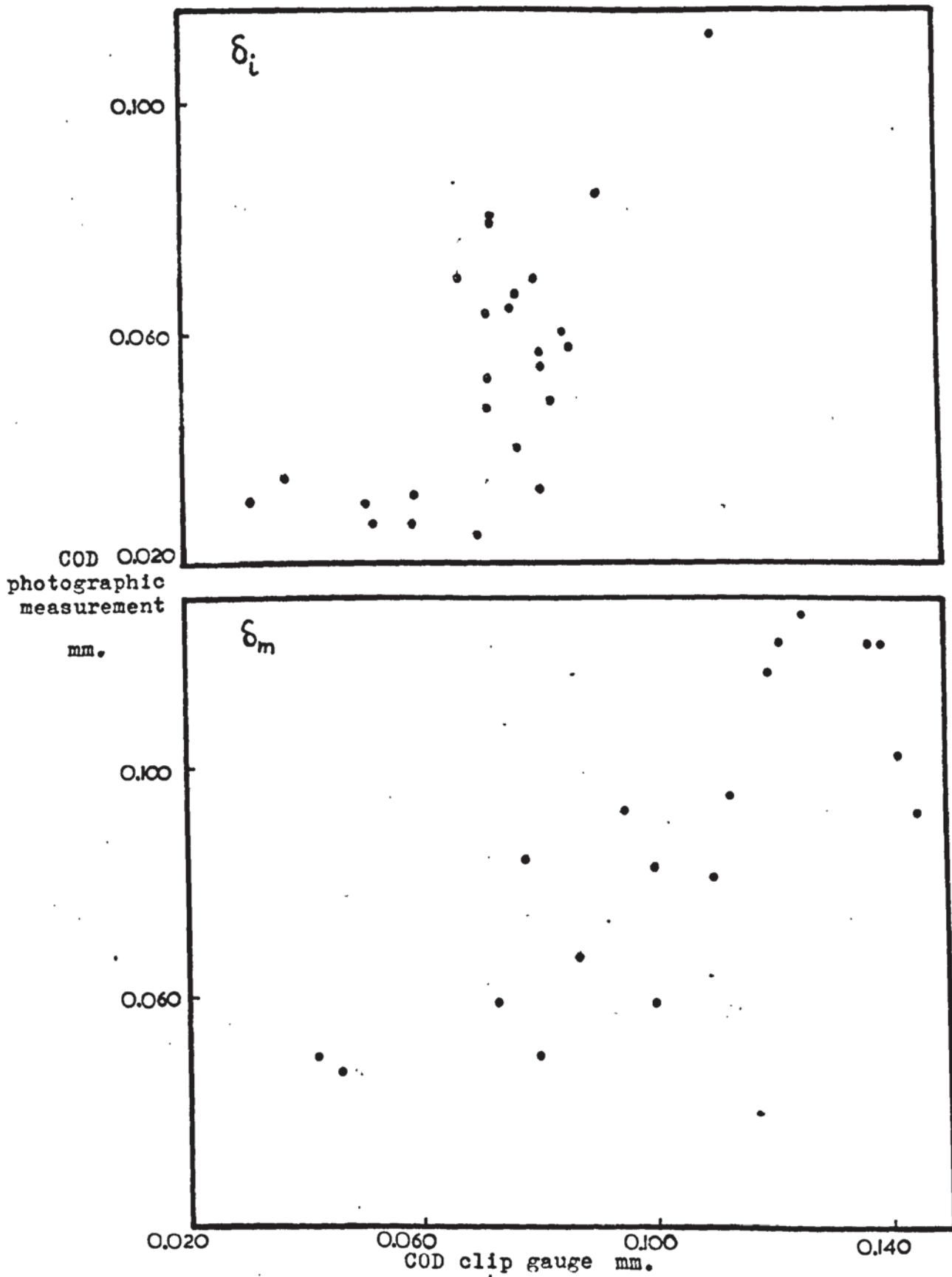
Fig. 85. Correlation of direct photographic measurement
with clip gauge COD.
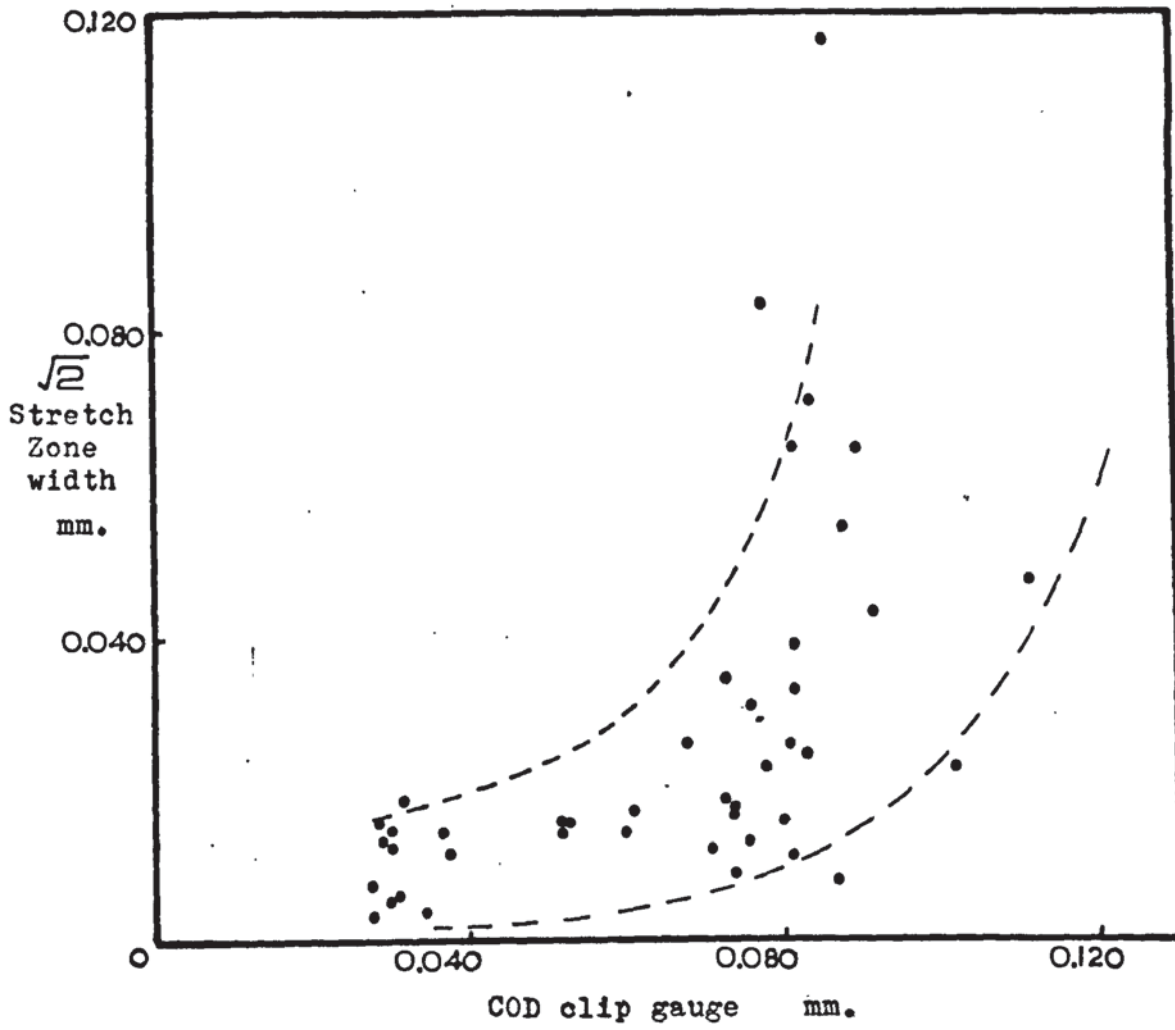
Fig. 86. Correlation of stretch zone width with clip gauge COD.

Axis labels:

$\dfrac{P}{BW\,\sigma_y}$ (vertical axis)

$\dfrac{V_g\,E}{W\,\sigma_y}$ (horizontal axis)

Legend:
- ● vac. remelted – longitudinsl
- ○ vac. remelted – transverse
- ▲ air melted
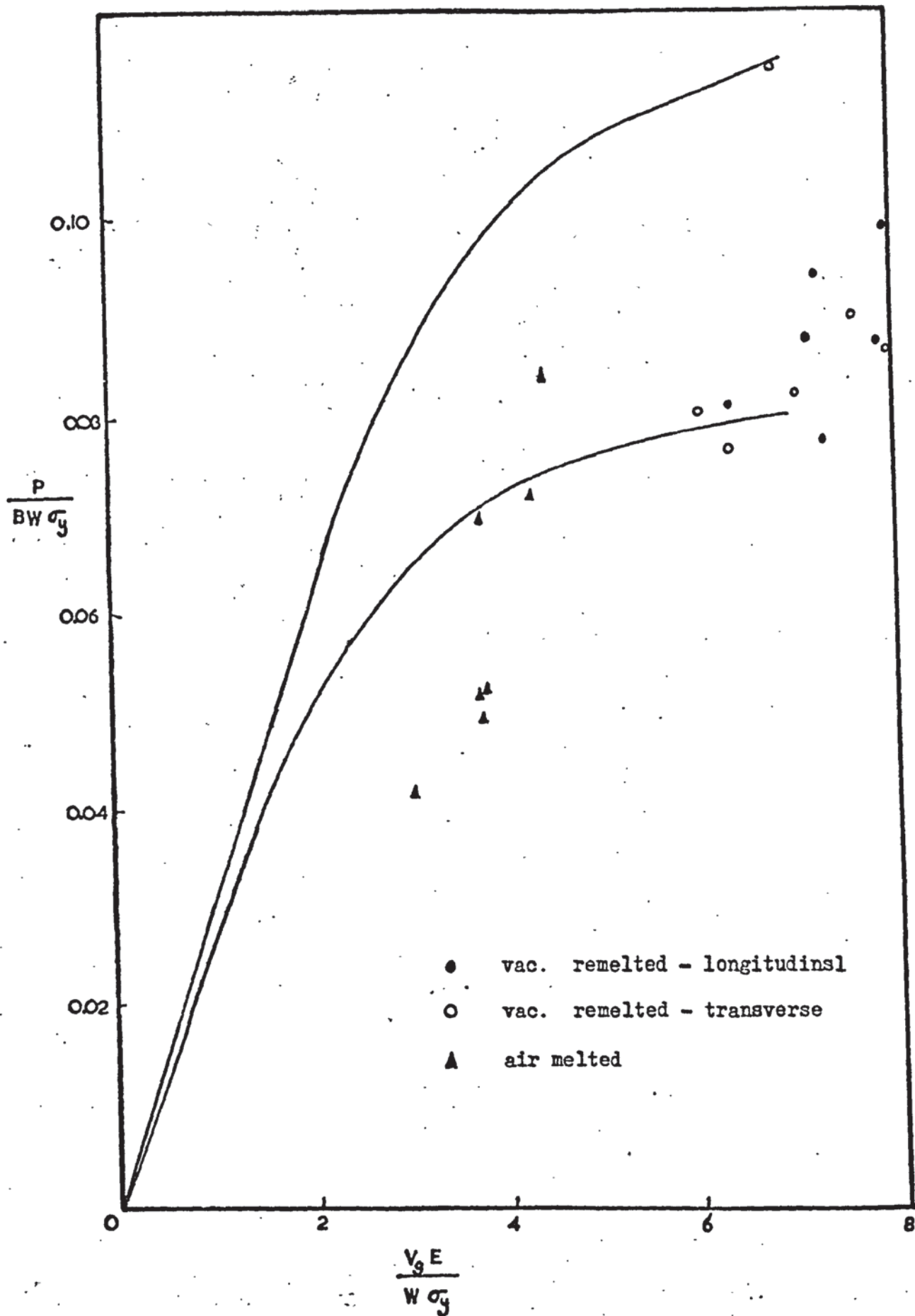
Fig. 87, Distribution of results in relation to finite element analysis.
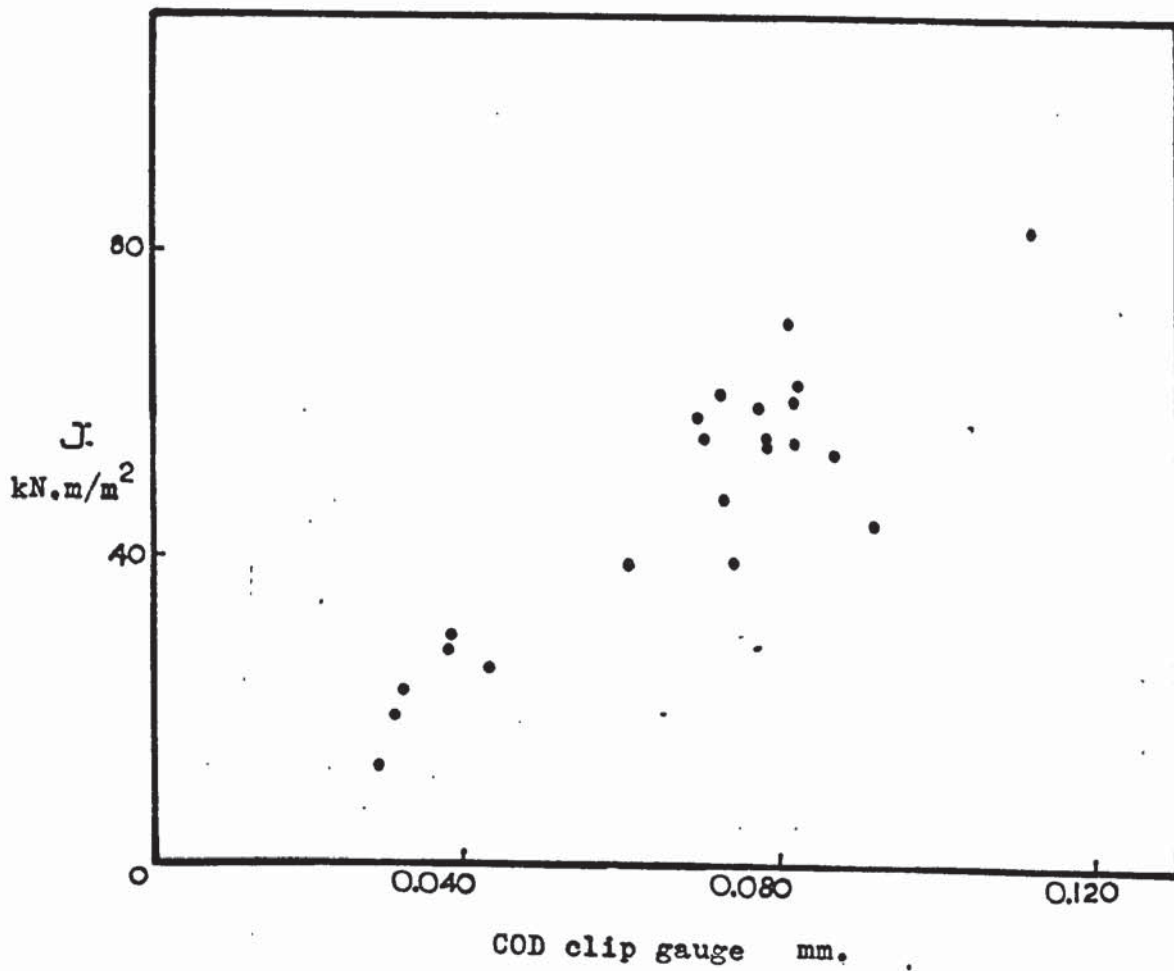
Fig. 88. Correlation of J results with clip gauge COD.
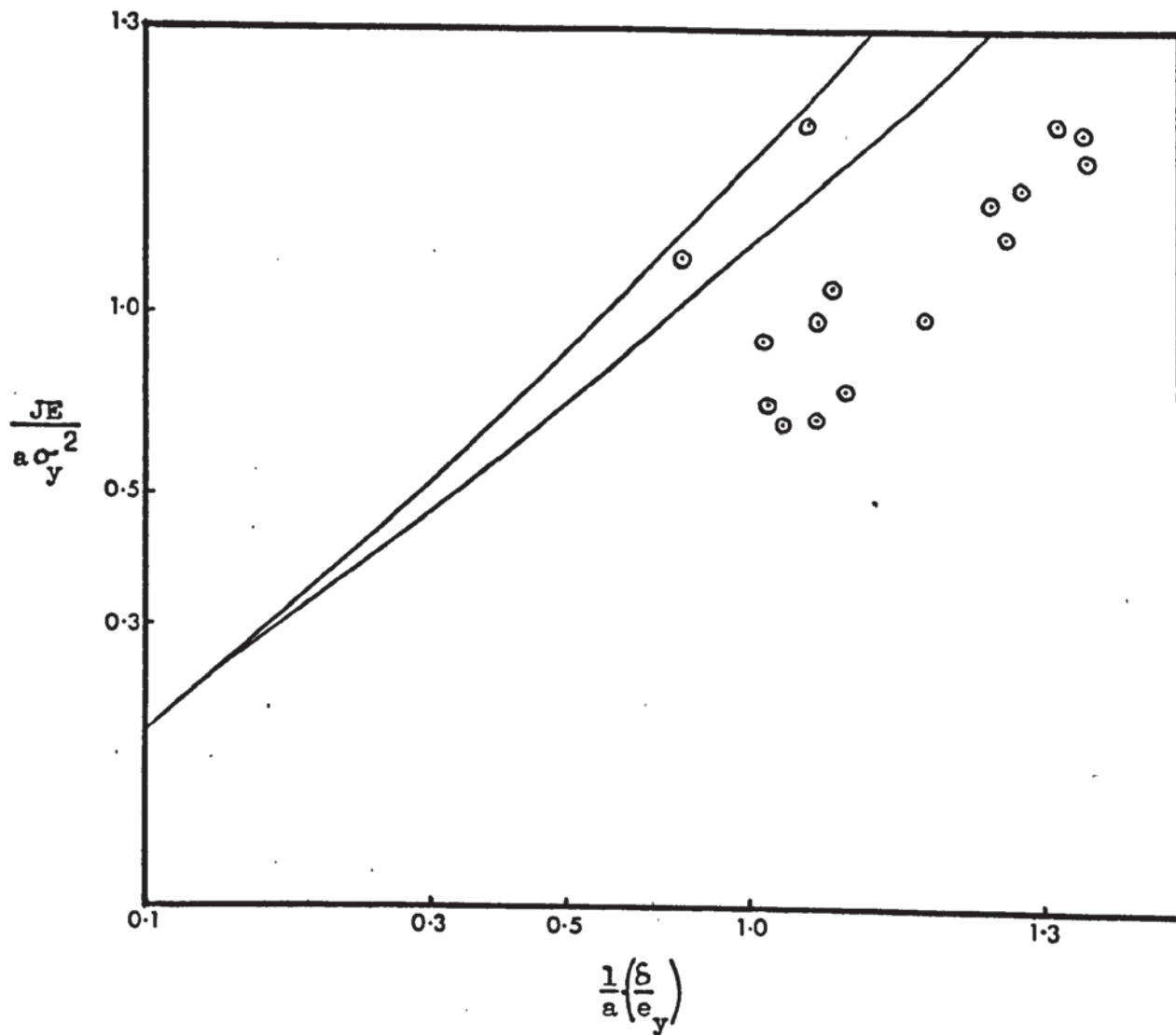
Fig. 89. Correlation of J contour integral and COD.
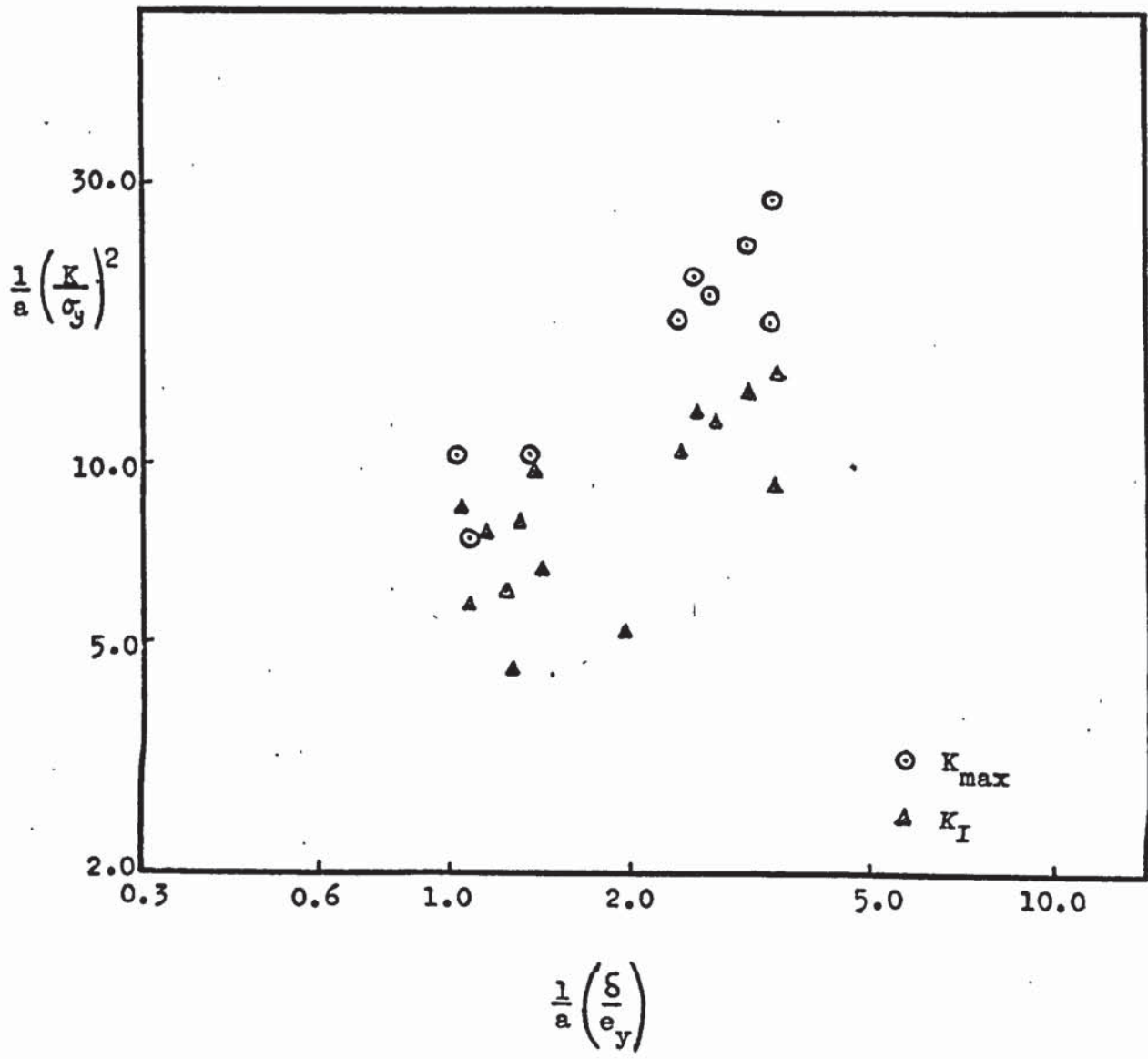
Fig. 90. Correlation of stress intensity factor and COD.
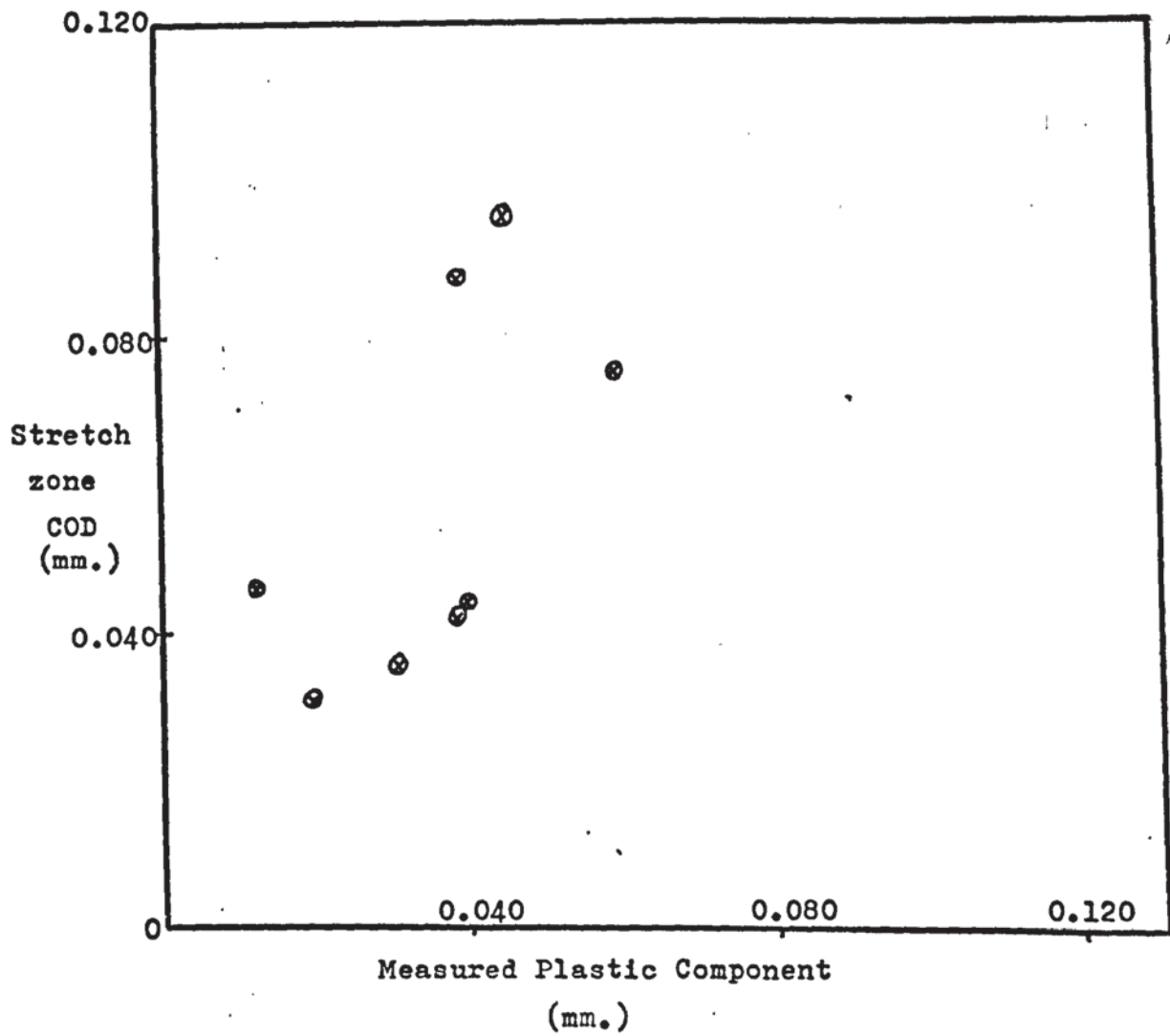
Fig. 91.   Correlation of stretch zone COD with
measured plastic component.

	C	Si	Mn	S	P	Cr	Mo	Ni	Cu	Nb	Ti	N_2	O_2
Rex 520	0.04	0.25	0.70			17.3	2.2	5.8	1.6	-	0.28		
FV520B (nom.)	0.07 max	0.6 max	1.0 max			13.5 -14.5	1.2 -2.0	5.0 -5.8	1.2 -2.0	0.2 -0.9	-		
FV520S (nom.)	0.04 -0.08	0.6 max	0.8 -1.8			15.3 -16.0	1.2 -2.0	5.0 -5.8	1.5 -2.2	-	0.02 max		
FV520B Cast 37060	0.035	0.45	0.75	0.005	0.013	13.72	1.58	5.25	1.52	0.28	-	0.024	0.007
FV520B Cast 96634	0.047	0.16	0.69			13.64	1.53	5.58	1.48	0.17	-		
FV520B (Vac.) Cast VA 12448	0.045	0.35	0.59	0.003	0.012	13.88	1.60	5.36	1.54	0.22	-		

Table I. Composition of FV 520 series steels.

Tensile Properties (room temperature)

Ageing temperature (°C)		450	550	620
Limit of proportionality	MN/m^2	621	643	139
0.5% proof stress	MN/m^2	1205	1032	936
Tensile strength	MN/m^2	1278	1102	1054
Elongation	%	22	23	27
Reduction in Area	MN/m^2	59	65	66
Izod	ft-lbs	50	75	88

Fatigue properties

10^8 reversals unbroken	MN/m^2	± 494	± 587	± 649

Fracture toughness

Condition	Section	Test temp.	K_{IC}	δ_i / δ_m
	(mm)	(°C)	$(MN.m^{-3/2})$	(mm)
1050/750/450	62.5	20	230	
1050/850/450	62.5	20	118	
950/450	16	-196	33.6	
950/525	16	-196	57.4	
950/450	16	-196		0.211/ 0.239
950/525	16	-196		0.342/ 0.442

Table II.   Mechanical properties of FV520B [134-137]

0.5% proof stress MN / m²	condition	PRIMARY HARDENED		OVERAGED 550°C	
		As-welded	Welded, then –78°C	As-welded	Welded, then –78°C
AIRMELT trans.	cycled	953 / 989 – 971	1070 / 1118 –1094	1023 / 1041 –1032	1124 / 1160 –1142
	450°C	1163 / 1235 –1199	1234 / 1317 –1276		
	550°C	1129 / 1178 –1154	1169 / 1235 –1202	1162 / 1195 –1179	1153 / 1213 –1185
	620°C	1094 / 1138 –1116	1079 / 1101 –1090	1035 / 1080 –1058	1141 / 1176 –1158
AIRMELT long.	cycled	892 / 955 – 923	859 / 936 – 898	968 / 1027 – 998	995 / 1039 –1017
	450°C	1028 / 1136 –1082	1086 / 1179 –1132		
	550°C	963 / 1055 –1009	969 / 1043 –1006	1079 / 1132 –1105	1081 / 1142 –1111
	620°C	774 / 791 – 782	825 / 903 – 864	913 / 997 – 955	935 / 1008 – 971
VACUUM REMELT long.	cycled	908 / 926 – 917	1032 / 963 – 998	957 / 974 – 965	1020 / 1046 –1033
	450°C	1203 / 1197 –1200	1173 / 1196 –1185		
	550°C	1081 / 1105 –1093	1069 / 1108 –1089	1032 / 1060 –1046	1007 / 1060 –1033
	620°C	705 / 739 – 722	981 / 1025 –1003	944 / 989 – 967	1007 / 1059 –1033

Table IIIa 0.5% Proof stress, 785°C peak.

Tensile strength MN/m²	condition	PRIMARY HARDENED				OVERAGED 550°C			
		As-welded		Welded, then -78°C		As-welded		Welded, then -78°C	
AIRMELT trans.	cycled	1165 / 1219	-1192	1243 / 1311	-1277	1183 / 1210	-1196	1132 / 1186	-1209
	450°C	1247 / 1326	-1287	1335 / 1402	-1369				
	550°C	1182 / 1241	-1212	1232 / 1307	-1270	1210 / 1253	-1231	1240 / 1279	-1259
	620°C	1146 / 1199	-1173	1117 / 1152	-1134	1104 / 1163	-1133	1156 / 1203	-1184
AIRMELT long.	cycled	1137 / 1203	-1170	1122 / 1160	-1141	1020 / 1073	-1047	1060 / 1127	-1094
	450°C	1226 / 1334	-1280	1160 / 1258	-1209				
	550°C	1108 / 1197	-1153	1151 / 1235	-1193	1127 / 1186	-1156	1167 / 1235	-1201
	620°C	1031 / 1043	-1037	1153 / 1051	-1102	981 / 1074	-1027	1046 / 1112	-1079
VACUUM REMELT long.	cycled	1208 / 1230	-1219	1193 / 1213	-1203	1157 / 1188	-1172	1163 / 1199	-1181
	450°C	1303 / 1256	-1280	1350 / 1393	-1372				
	550°C	1132 / 1170	-1151	1110 / 1155	-1133	1137 / 1186	-1161	1061 / 1144	-1102
	620°C	997 / 1009	-1003	1054 / 1092	-1073	1051 / 1120	-1086	1066 / 1142	-1104

Table IIIa (cont.)   Tensile strength, 785°C peak.

Elongation – R.A. %	condition	PRIMARY HARDENED		OVERAGED 550°C	
		As-welded	Welded, then -78°c	As-welded	Welded, then -78°c
AIRMELT trans.	cycled	12 – 42	11 – 40	13 – 41	12 – 40
	450°C	10 – 36	8 – 27		
	550°C	15 – 43	14 – 43	16 – 43	17 – 39
	620°C	18 – 40	17 – 43	18 – 46	18 – 43
AIRMELT long.	cycled	19 – 60	18 – 54	21 – 58	19 – 57
	450°C	19 – 56	22 – 46		
	550°C	22 – 60	25 – 51	23 – 55	22 – 63
	620°C	30 – 64	29 – 64	31 – 57	30 – 61
VACUUM REMELT	cycled	21 – 63	22 – 63	16 – 52	17 – 60
	450°C	17 – 57	23 – 64		
	550°C	21 – 65	14 – 64	23 – 63	16 – 63
	620°C	28 – 66	19 – 63	33 – 62	25 – 74

Table IIIb.   Ductilities, 785°C peak.

0.5% proof stress MN / m²	condition	PRIMARY HARDENED		OVERAGED 550°C	
AIRMELT trans.	cycled	833 881	– 857	869 918	– 893
	450°C	1106 1176	–1141		
	550°C	1070 1115	–1092	1103 1159	–1131
	620°C	1014 1050	–1032	1050 1075	–1062
AIRMELT long.	cycled	1301 1382	–1342	1310 1391	–1350
	450°C	1071 1167	–1119		
	550°C	1001 1073	–1037	992 1048	–1020
	620°C	982 1037	–1009	989 1008	– 998
VACUUM REMELT long.	cycled	902 911	– 906	898 956	– 927
	450°C	1241 1317	–1282		
	550°C	1201 1277	–1239	1151 1226	–1188
	620°C	1059 1100	–1080	1052 1080	–1066

Table IIIc   0.5% Proof stress, 1250°C peak.

Tensile strength MN / m²	condition	PRIMARY HARDENED		OVERAGED 550°C	
AIRMELT trans.	cycled	1239 1293	-1266	1273 1341	-1307
	450°C	1285 1323	-1304		
	550°C	1230 1304	-1267	1316 1387	-1351
	620°C	1180 1202	-1196	1195 1231	-1213
AIRMELT long.	cycled	1329 1398	-1364	1356 1399	-1377
	450°C	1257 1299	-1278		
	550°C	1155 1225	-1190	1136 1200	-1168
	620°C	1139 1220	-1179	1173 1214	-1194
VACUUM REMELT long.	cycled	1212 1248	-1230	1213 1254	-1233
	450°C	1378 1475	-1431		
	550°C	1338 1435	-1397	1268 1320	-1294
	620°C	1182 1207	-1190	1192 1230	-1211

Table IIIc (cont.)   Tensile strength, 1250°C peak.

Elongation - R.A. %	condition	PRIMARY HARDENED	OVERAGED 550°C
AIRMELT trans.	cycled	17 — 46	17 — 47
	450°C	14 — 39	
	550°C	21 — 44	22 — 38
	620°C	22 — 46	22 — 40
AIRMELT long.	cycled	17 — 57	18 — 59
	450°C	14 — 51	
	550°C	25 — 65	22 — 64
	620°C	26 — 64	23 — 63
VACUUM REMELT	cycled	22 — 72	23 — 69
	450°C	16 — 56	
	550°C	23 — 64	18 — 60
	620°C	22 — 64	22 — 62

Table IIId.   Ductilities, 1250°C peak.

	Fully Hardened 450°C	Overaged 550°C	Overaged 620°C
Transverse tensile strength MN/m^2	1016	945	659
Longitudinal tensile strength MN/m^2	1181	1039	709
Longitudinal reduction in area %	59	63	65
Longitudinal elongation %	22	25	29

Table IIIe.   Tensile properties air-melted parent plate.

Specimen gauge length 20mm

Cooling rate from 800°C peak

Finish	°C/sec
As-rolled	23.0
As-rolled + aluminium foil	31.25
As-rolled + doubled Al foil	28.0
As-rolled + linished	33.0
As-rolled + linished + Al foil	33.75
Ground surface	36.5

Table IV.   Effect of surface finish on specimen cooling rates.

COD $\delta_i - \delta_m$ mm	condition	PRIMARY HARDENED		OVERAGED 550°C	
		As-welded	Welded, then -78°c	As-welded	Welded, then -78°c
AIRMELT trans.	cycled	0.021/0.029	0.019/0.026	0.008/0.009	0.020/0.026
	450°C	0.026/0.032	0.021/0.034		
	550°C			0.015/0.026	0.017/0.026
	620°C	0.019/0.021		0.018/0.025	0.018/0.032
AIRMELT long.	cycled	0.047/0.059		0.016/0.095	0.033/0.067
	450°C	0.027/0.084	0.031/0.059		
	550°C			0.036/0.050	0.024/0.039
	620°C	0.079/0.249	0.074/0.103	0.023/0.062	
VACUUM REMELT long.	cycled	0.064/0.122	0.054/0.122	0.069/0.160	0.066/0.117
	450°C	0.026/0.153	0.070/0.081		
	550°C			0.048/0.092	0.056/0.122
	620°C		0.078/0.160		

Table Va. - COD values, photographic measurement, 785°C peak.

$\delta_i - \delta_m$ COD mm.	condition	PRIMARY HARDENED	OVERAGED 550°C
AIRMELT trans.	cycled	0.030 – 0.050	0.018 – 0.029
	450°C	0.023 – 0.026	0.024 – 0.061
	550°C		0.035 – 0.047
	620°C		
AIRMELT long.	cycled		0.039 – 0.082
	450°C	0.026 – 0.045	
	550°C		0.081 – 0.094
	620°C	0.052	0.036 – 0.115
VACUUM REMELT	cycled	0.059 – 0.159	0.084 – 0.127
	450°C	0.142 – 0.283	
	550°C		0.114 – 0.160
	620°C	0.032 – 0.127	

Table Vb.   COD values, photographic measurement 1250°C peak.

COD δ_i mm.	condition	PRIMARY HARDENED		OVERAGED 550°C	
		As-welded	Welded, then -78°C	As-welded	Welded, then -78°C
AIRMELT trans.	cycled	0.033 0.037-0.037 0.040	0.041 0.042-0.042 0.044	0.037 0.038-0.037 0.038	0.042 0.044-0.044 0.047
	450°C	0.026 0.030-0.030 0.033	0.036 0.039-0.039 0.041		
	550°C	0.033 0.034-0.034 0.035	0.041 0.044-0.044 0.048	0.036 0.038-0.039 0.042	0.034 0.036-0.036 0.039
	620°C	0.029 0.033-0.032 0.035	0.034 0.035-0.035 0.036	0.036 0.036-0.036 0.036	0.031 0.033-0.032 0.033
AIRMELT long.	cycled	0.071 0.077-0.077 0.082	0.041 0.044-0.044 0.047	0.059 0.063-0.063 0.066	0.052 0.054-0.055 0.058
	450°C	0.055 0.058-0.058 0.059	0.047 0.050-0.049 0.051		
	550°C	0.055 0.062-0.061 0.066	0.070 0.073-0.073 0.075	0.058 0.062-0.062 0.066	0.060 0.062-0.063 0.067
	620°C	0.051 0.054-0.054 0.058	0.050 0.052-0.053 0.056	0.053 0.056-0.057 0.061	0.047 0.050-0.049 0.050
VACUUM REMELT long.	cycled	0.079 0.081-0.081 0.084	0.064 0.068-0.068 0.071	0.081 0.083-0.084 0.089	0.079 0.080-0.081 0.086
	450°C	0.070 0.073-0.073 0.077	0.070 0.072-0.071 0.073		
	550°C	0.063 0.065-0.066 0.070	0.070 0.072-0.073 0.077	0.072 0.076-0.076 0.079	0.080 0.083-0.083 0.086
	620°C	0.089 0.091-0.090 0.093	0.069 0.073-0.073 0.076	0.084 0.087-0.087 0.092	0.095 0.099-0.098 0.100

Table VIa. COD values, experimental equation, 785°C peak.

COD δ_m mm.	condition	PRIMARY HARDENED		OVERAGED 550°C	
		As-welded	Welded, then −78°C	As-welded	Welded, then −78°C
AIRMELT trans.	cycled	0.035 0.038-0.039 0.043	0.043 0.044-0.045 0.047	0.040 0.043-0.043 0.047	0.045 0.049-0.049 0.051
	450°C	0.036 0.036-0.039 0.043	0.041 0.043-0.043 0.046		
	550°C	0.029 0.031-0.033 0.038	0.044 0.047-0.048 0.052	0.040 0.041-0.043 0.047	0.039 0.040-0.040 0.042
	620°C	0.035 0.037-0.038 0.038	0.037 0.039-0.039 0.041	0.039 0.039-0.040 0.041	0.033 0.035-0.035 0.036
AIRMELT long.	cycled	0.111 0.118-0.120 0.132	0.054 0.058-0.057 0.060	0.123 0.129-0.130 0.138	0.124 0.134-0.133 0.139
	450°C	0.076 0.079-0.079 0.082	0.069 0.072-0.073 0.079		
	550°C	0.074 0.078-0.077 0.079	0.090 0.094-0.095 0.099	0.068 0.072-0.072 0.075	0.069 0.070-0.072 0.077
	620°C	0.081 0.085-0.085 0.091	0.095 0.099-0.102 0.113	0.076 0.077-0.078 0.081	0.090 0.095-0.094 0.096
VACUUM REMELT long.	cycled	0.130 0.137-0.136 0.143	0.154 0.159-0.164 0.179	0.145 0.150-0.153 0.163	0.129 0.134-0.136 0.145
	450°C	0.100 0.104-0.105 0.111	0.107 0.113-0.111 0.113		
	550°C	0.091 0.094-0.095 0.099	0.156 0.160-0.162 0.171	0.136 0.139-0.142 0.151	0.153 0.158-0.158 0.164
	620°C	0.198 0.209-0.211 0.227	0.156 0.162-0.163 0.170	0.191 0.197-0.199 0.210	0.238 0.250-0.253 0.270

Table VIa (cont.). COD values, experimental equation, 785°C peak.

COD $\delta_i - \delta_m$ mm	condition	PRIMARY HARDENED		OVERAGED 550°C	
		As-welded	Welded, then −78°C	As-welded	Welded, then −78°C
AIRMELT trans.	cycled	0.033/0.036	0.038/0.040	0.034/0.042	0.040/0.046
	450°C	0.022/0.032	0.032/0.037		
	550°C	0.026/0.026	0.041/0.045	0.032/0.036	0.032/0.038
	620°C	0.026/0.032	0.030/0.035	0.031/0.036	0.033/0.036
AIRMELT long.	cycled	0.085/0.141	0.041/0.057	0.076/0.153	0.056/0.156
	450°C	0.047/0.086	0.059/0.080		
	550°C	0.065/0.086	0.080/0.108	0.064/0.076	0.066/0.077
	620°C	0.079/0.099	0.075/0.119	0.072/0.090	0.071/0.109
VACUUM REMELT long.	cycled	0.076/0.161	0.091/0.197	0.096/0.184	0.090/0.161
	450°C	0.078/0.119	0.075/0.126		
	550°C	0.073/0.110	0.079/0.194	0.083/0.169	0.090/0.186
	620°C	0.106/0.262	0.080/0.196	0.111/0.243	0.099/0.310

Table VIb. COD values, Wells' equation, 785°C peak.

COD $\delta_i - \delta_m$ mm	condition	PRIMARY HARDENED		OVERAGED 550°C	
		As-welded	Welded, then −78°C	As-welded	Welded, then −78°C
AIRMELT trans.	cycled	0.030/0.033	0.030/0.033	0.029/0.033	0.028/0.031
	450°C	0.037/0.043	0.036/0.043		
	550°C	0.032/0.035	0.030/0.032	0.030/0.035	0.028/0.033
	620°C	0.033/0.033	0.031/0.032	0.032/0.036	0.030/0.037
AIRMELT long.	cycled	0.074/0.100	0.064/0.093	0.070/0.093	0.061/0.087
	450°C	0.053/0.079	0.052/0.073		
	550°C	0.063/0.101	0.061/0.098	0.060/0.080	0.052/0.066
	620°C	0.074/0.154	0.074/0.143	0.077/0.083	0.081/0.090
VACUUM REMELT long.	cycled	0.077/0.123	0.082/0.137	0.082/0.137	0.078/0.121
	450°C	0.071/0.109	0.068/0.111		
	550°C	0.088/0.160	0.082/0.157	0.084/0.145	0.082/0.140
	620°C	0.103/0.195	0.088/0.178	0.099/0.190	0.091/0.144

Table VIc. COD values, experimental equation, 840°C peak.

COD δ_i mm.	condition	PRIMARY HARDENED	*	OVERAGED 550°C	*
AIRMELT trans.	cycled	0.031 0.033 0.034	0.032 ± 0.002	0.028 0.029 0.030	0.029 ± 0.002
	450°C	0.037 0.043 0.050	0.043 ± 0.011		
	550°C	0.037 0.039 0.041	0.039 ± 0.003	0.035 0.038 0.040	0.038 ± 0.005
	620°C	0.030 0.032 0.033	0.032 ± 0.003	0.035 0.038 0.042	0.039 ± 0.006
AIRMELT long.	cycled	0.066 0.070 0.079	0.072 ± 0.012	0.073 0.078 0.083	0.078 ± 0.007
	450°C	0.080 0.086 0.096	0.087 ± 0.014		
	550°C	0.078 0.081 0.085	0.082 ± 0.006	0.070 0.074 0.080	0.074 ± 0.009
	620°C	0.070 0.073 0.076	0.073 ± 0.005	0.057 0.060 0.066	0.061 ± 0.008
VACUUM REMELT long.	cycled	0.079 0.087 0.093	0.087 ± 0.012	0.090 0.092 0.095	0.092 ± 0.004
	450°C	0.078 0.082 0.086	0.082 ± 0.007		
	550°C	0.101 0.103 0.126	0.110 ± 0.025	0.102 0.113 0.123	0.113 ± 0.019
	620°C	0.079 0.083 0.087	0.083 ± 0.007	0.078 0.082 0.087	0.082 ± 0.008

Table VId.   COD values, experimental equation, 1250°C peak.

COD mm.	condition	PRIMARY HARDENED	*	OVERAGED 550°C	*
AIRMELT trans.	cycled	0.040 0.042 0.046	0.043 ± 0.005	0.033 0.036 0.038	0.036 ± 0.004
	450°C	0.043 0.048 0.051	0.047 ± 0.006		
	550°C	0.049 0.049 0.055	0.051 ± 0.006	0.053 0.055 0.063	0.057 ± 0.009
	620°C	0.042 0.043 0.046	0.044 ± 0.003	0.041 0.046 0.052	0.046 ± 0.010
AIRMELT long.	cycled	0.096 0.108 0.116	0.107 ± 0.017	0.094 0.102 0.104	0.100 ± 0.008
	450°C	0.089 0.096 0.105	0.097 ± 0.014		
	550°C	0.096 0.101 0.116	0.105 ± 0.015	0.101 0.110 0.128	0.113 ± 0.024
	620°C	0.069 0.073 0.078	0.073 ± 0.008	0.105 0.111 0.128	0.115 ± 0.020
VACUUM REMELT	cycled	0.161 0.171 0.178	0.170 ± 0.015	0.167 0.171 0.187	0.175 ± 0.020
	450°C	0.086 0.090 0.094	0.090 ± 0.007		
	550°C	0.131 0.142 0.154	0.143 ± 0.022	0.151 0.156 0.160	0.156 ± 0.008
	620°C	0.118 0.125 0.133	0.126 ± 0.013	0.128 0.136 0.150	0.138 ± 0.019

* 90% confidence limits

Table VId (cont.). COD values, experimental equation, 1250°C peak

K MN/m$^{3/2}$	condition	PRIMARY HARDENED		OVERAGED 550°C	
		As-welded	Welded, then −78°C	As-welded	Welded, then −78°C
AIRMELT trans.	cycled	169	165	174	170
	450°C	221	215		
	550°C	183	187	167	165
	620°C	144	143		
AIRMELT long.	cycled	205	187	199	185
	450°C	255	211		
	550°C	211	197	191	180
	620°C	179	178	178	174
VACUUM REMELT	cycled	187	178	203	197
	450°C	213	217		
	550°C	193	192	194	191
	620°C	190	188	188	186

Table VIe.   LEFM Fracture toughness, 785°C peak.

K $MN / m^{\frac{3}{2}}$	condition	PRIMARY HARDENED	OVERAGED 550°C
AIRMELT trans.	cycled	195	222
	450°C	150	171
	550°C	232	216
	620°C	216	231
AIRMELT long.	cycled	307	205
	450°C	217	225
	550°C	240	244
	620°C	230	218
VACUUM REMELT	cycled	206	198
	450°C	246	238
	550°C	251	246
	620°C	244	261

Table VIf.   LEFM Fracture toughness, 1250°C peak.

COD mm	condition	PRIMARY HARDENED		OVERAGED 550°C	
		As-welded	Welded, then -78°C	As-welded	Welded, then -78°C
AIRMELT trans.	cycled	0.020	0.013	0.019	0.009
	450°C	0.009	0.004		
	550°C	0.014	0.006	0.016	0.004
	620°C	0.018	0.008	0.018	0.007
AIRMELT long.	cycled	0.016	0.020	0.025	0.020
	450°C	0.022	0.019		
	550°C	0.022	0.030	0.018	0.021
	620°C	0.022	0.038	0.019	0.022
VACUUM REMELT long.	cycled	0.043	0.042	0.036	0.114
	450°C	0.031	0.030		
	550°C	0.032	0.043	0.097	0.089
	620°C	0.033	0.076	0.094	0.089

Table VIIa.   COD values, stretch zone measurement, 785°C peak.

COD mm	condition	PRIMARY HARDENED	OVERAGED 550°C
AIRMELT trans.	cycled	0.026	0.021
	450°C	0.021	
	550°C	0.022	0.021
	620°C	0.007	0.016
AIRMELT long.	cycled	0	0.033
	450°C	0.011	
	550°C	0.015	0.012
	620°C	0.048	0.024
VACUUM REMELT long.	cycled	0.164	0.060
	450°C	0.046	
	550°C	0.044	0.066
	620°C	0.034	0.054

Table VIIb.   COD values, stretch zone measurement, 1250°C peak.

J KNm / m^2	condition	PRIMARY HARDENED	OVERAGED 550°C
AIRMELT trans.	cycled	22.9	22.8
	450°C	26.2	
	550°C	26.0	28.3
	620°C	19.5	31.5
AIRMELT long.	cycled		55.0
	450°C	24.5	
	550°C	44.4	40.3
	620°C	48.3	40.7
VACUUM REMELT	cycled	53.5	45.1
	450°C	48.8	
	550°C	79.0	83.3
	620°C	59.7	63.4

Table VIII.   J contour values, 1250°C peak.

Table IXa.   COD values, air melted parent plate,
                  experimental equation   [94]

Ageing temperature	COD mm. Experimental equation	COD mm. Wells equation	J kN.m/$_m$2	K MN/$_m^3$2
Transverse specimens				
450°C	0.070/ 0.104	0.074/ 0.117	56.2	280
550°C	0.072/ 0.119	0.081/ 0.141	62.2	322
620°C	0.077/ 0.134	0.088/ 0.161	55.6	267
Longitudinal specimens				
450°C	0.069/ 0.156	0.077/ 0.201	59.5	273
550°C	0.080/ 0.206	0.091/ 0.252	71.4	291
620°C	0.077/ 0.205	0.093/ 0.259	60.3	263
	δ_i / δ_m	δ_i / δ_m		

Table IXb. Fracture Toughness values, vacuum remelted parent plate.

a) welds

Ageing temperature	as-welded		treated -70°C	
	δ_i (mm)	δ_m (mm)	δ_i (mm)	δ_m (mm)
3mm from fusion line				
as-welded	0.041	0.050	0.036	0.048
450°C	0.048	0.056	0.038	0.044
620°C	0.045	0.062	0.046	0.070
10mm from fusion line				
as-welded	0.041	0.052	0.030	0.034
450°C	0.057	0.075	0.043	0.057
620°C	0.078	0.118	0.072	0.106

b) effect of varying simulation time cycle

Peak	speed of cycle	δ_i (mm)	δ_m (mm)
785°C	fast	0.073	0.121
785°C	slow	0.092	0.138
1250°C	slow	0.068	0.152

Table X. Weld Fracture Toughness values.

Ageing temperature	as-welded		sub-zero treated	
	δ_i (mm)	δ_m (mm)	δ_i (mm)	δ_m (mm)
Weld HAZ, 1250°C peak				
as-welded	0.042	0.051	–	–
450°C	0.049	0.057	–	–
620°C	0.045	0.063	–	–
Weld HAZ, 785°C peak				
as-welded	0.041	0.053	0.031	0.035
450°C	0.058	0.076	0.043	0.058
620°C	0.079	0.119	0.072	0.107
Simulated HAZ, 1250°C peak				
as-welded	0.072	0.107	–	–
450°C	0.087	0.097	–	–
620°C	0.073	0.073	–	–
Simulated HAZ, 785°C peak				
as-welded	0.077	0.120	0.044	0.057
450°C	0.058	0.079	0.049	0.073
620°C	0.054	0.085	0.053	0.102
Parent plate				
450°C	0.040	0.046	–	–
550°C	0.042	0.051	–	–
620°C	0.050	0.068	–	–

Table XI. Comparison of COD values, air-melted plate

Plate	cycled and aged	Parent plate	Primary Hardened		Overaged 550°C	
			1250°C peak	785°C peak	1250°C peak	785°C peak
AIRMELT trans.	As-welded	——	0.032	0.037 / 0.042 *	0.029	0.037 / 0.044 *
	450°C	0.040	0.043	0.030 / 0.039 *	——	——
	550°C	0.042	0.039	0.034 / 0.034 *	0.038	0.039 / 0.036 *
	620°C	0.050	0.032	0.032 / 0.035 *	0.039	0.036 / 0.032 *
AIRMELT long.	As-welded	——	0.072	0.077 / 0.044 *	0.078	0.063 / 0.054 *
	450°C	0.068	0.087	0.058 / 0.049 *	——	——
	550°C	0.074	0.082	0.061 / 0.073 *	0.074	0.062 / 0.063 *
	620°C	0.076	0.073	0.054 / 0.053 *	0.061	0.057 / 0.049 *
VACUUM REMELT. long.	As-welded	——	0.087	0.081 / 0.068 *	0.092	0.084 / 0.081 *
	450°C	0.069	0.082	0.073 / 0.071	——	——
	550°C	0.081	0.110	0.066 / 0.073 *	0.113	0.076 / 0.083 *
	620°C	0.076	0.083	0.090 / 0.073 *	0.082	0.087 / 0.098 *

* sub-zero treated

Table XIIa. Fracture toughness (COD, δ_i , mm) summary table

Plate	cycled and aged	Parent plate	Primary Hardened		Overaged 550°C	
			1250°C peak	785°C peak	1250°C peak	785°C peak
AIRMELT trans.	As-welded	—	0.043	0.039 / 0.045*	0.036	0.043 / 0.048*
	450°C	0.046	0.047	0.039 / 0.043*	—	—
	550°C	0.051	0.051	0.033 / 0.048*	0.057	0.043 / 0.035*
	620°C	0.068	0.044	0.037 / 0.039*	0.046	0.040 / 0.035*
AIRMELT long.	As-welded	—	0.107	0.120 / 0.057*	0.100	0.130 / 0.133*
	450°C	0.071	0.097	0.079 / 0.073*	—	—
	550°C	0.079	0.105	0.077 / 0.095*	0.113	0.072 / 0.072*
	620°C	0.086	0.073	0.085 / 0.102*	0.115	0.078 / 0.094*
VACUUM REMELT. long.	As-welded	—	0.170	0.136 / 0.164*	0.175	0.153 / 0.136*
	450°C	0.157	0.090	0.105 / 0.111*	—	—
	550°C	0.206	0.143	0.095 / 0.163*	0.156	0.142 / 0.158*
	620°C	0.205	0.126	0.211 / 0.163*	0.138	0.199 / 0.253*

* sub-zero treated

Table XIIb. Fracture toughness (COD, δ_m , mm) summary table

Plate	cycled and aged	Parent plate	Primary Hardened		Overaged 550°C	
			1250°C peak	785°C peak	1250°C peak	785°C peak
AIRMELT trans.	As-welded	——	860	970 / *1090	890	1030 / *1140
	450°C	1020	1140	1200 / *1280	——	——
	550°C	950	1090	1150 / *1200	1130	1180 / *1190
	620°C	660	1030	1120 / *1090	1060	1060 / *1160
AIRMELT long.	As-welded	——	1340	920 / *900	1350	1000 / *1090
	450°C	1180	1120	1080 / *1130	——	——
	550°C	1040	1040	1010 / *1010	1020	1110 / *1110
	620°C	710	1010	780 / *860	1000	960 / *970
VACUUM REMELT.	As-welded	——	910	920 / *1000	930	970 / *1180
	450°C	1360	1280	1200 / *1190	——	——
	550°C	1250	1240	1090 / *1090	1190	1050 / *1100
	620°C	1100	1080	720 / *1000	1070	970 / *1100

* sub-zero treated

Table XIIc.   Tensile properties (0.5% proof stress, MN/m²)
summary table

P_1/P_m %	condition	PRIMARY HARDENED			OVERAGED 550°C	
		785°C		1250°C	785°C	1250°C
AIRMELT trans.	cycled / 450°C / 550°C / 620°C	94		91	97	92
		96		92	95	93
		97		93	96	92
		98		97	96	96
		98		97	96	
		96			97	
		99				
		Grand average 95.3				
AIRMELT long.	cycled / 450°C / 550°C / 620°C	93	94	94	94	94
		86	94	93	93	94
		88	93	94	93	93
		97	90	94	94	95
		91	92		93	
		94	89			
		93	94			
		94	92			
		Grand average 92.9				
VACUUM REMELT long.	cycled / 450°C / 550°C / 620°C	93	94	94	93	97
		87	89	97	93	94
		85	94	95	92	90
		97	94	96	96	97
		89	92	92	91	
		95	96		92	
					94	
					97	
		Grand average 93.0				

OVERALL AVERAGE 93.6

Table XIII.   Ratio of load at initiation to maximum load.